

INSTABILITY AND TRANSITION ON THE HIFIRE-5  
IN A MACH-6 QUIET TUNNEL

A Dissertation

Submitted to the Faculty

of

Purdue University

by

Thomas J. Juliano

In Partial Fulfillment of the

Requirements for the Degree

of

Doctor of Philosophy

August 2010

Purdue University

West Lafayette, Indiana

Report Documentation Page				Form Approved OMB No. 0704-0188	
Public reporting burden for the collection of information is estimated to average 1 hour per response, including the time for reviewing instructions, searching existing data sources, gathering and maintaining the data needed, and completing and reviewing the collection of information. Send comments regarding this burden estimate or any other aspect of this collection of information, including suggestions for reducing this burden, to Washington Headquarters Services, Directorate for Information Operations and Reports, 1215 Jefferson Davis Highway, Suite 1204, Arlington VA 22202-4302. Respondents should be aware that notwithstanding any other provision of law, no person shall be subject to a penalty for failing to comply with a collection of information if it does not display a currently valid OMB control number.					
1. REPORT DATE <b>27 OCT 2006</b>		2. REPORT TYPE		3. DATES COVERED <b>00-11-2005 to 00-11-2006</b>	
4. TITLE AND SUBTITLE <b>Instability and Transition on the HIFIRE-5 in a Mach-6 Quiet Tunnel</b>				5a. CONTRACT NUMBER	
				5b. GRANT NUMBER	
				5c. PROGRAM ELEMENT NUMBER	
6. AUTHOR(S)				5d. PROJECT NUMBER	
				5e. TASK NUMBER	
				5f. WORK UNIT NUMBER	
7. PERFORMING ORGANIZATION NAME(S) AND ADDRESS(ES) <b>Purdue University, School of Aeronautics Astronautics, 499 S Capitol St SW # 407, Washington, DC, 20003-4016</b>				8. PERFORMING ORGANIZATION REPORT NUMBER	
9. SPONSORING/MONITORING AGENCY NAME(S) AND ADDRESS(ES)				10. SPONSOR/MONITOR'S ACRONYM(S)	
				11. SPONSOR/MONITOR'S REPORT NUMBER(S)	
12. DISTRIBUTION/AVAILABILITY STATEMENT <b>Approved for public release; distribution unlimited</b>					
13. SUPPLEMENTARY NOTES					
14. ABSTRACT					
15. SUBJECT TERMS					
16. SECURITY CLASSIFICATION OF:			17. LIMITATION OF ABSTRACT <b>Same as Report (SAR)</b>	18. NUMBER OF PAGES <b>190</b>	19a. NAME OF RESPONSIBLE PERSON
a. REPORT <b>unclassified</b>	b. ABSTRACT <b>unclassified</b>	c. THIS PAGE <b>unclassified</b>			

## DISTRIBUTION STATEMENT

Approved for public release; distribution is unlimited.

Case Number 88ABW-2010-3955

To Mom and Dad for their love and support.



## ACKNOWLEDGMENTS

I would like to thank my advisor, Professor Steven P. Schneider, for managing the Boeing/AFOSR Mach-6 Quiet Tunnel and giving me the opportunity to work on it. The guidance and suggestions offered by my committee members, Purdue University Professors John Sullivan and Stephen Heister, Dr. Roger Kimmel from the Air Force Office of Scientific Research, and Dr. Meelan Choudhari of NASA Langley Research Center are also appreciated.

I would like to thank the ASL shop, Jerry Hahn, Robin Snodgrass, Jim Younts, John Phillips, and Madeline Chadwell, for their excellent craftsmanship and valuable advice.

I also thank the current and emeritus members of Team Schneider: Shann Rufer, Craig Skoch, Erick Swanson, Tyler Robarge, Matt Borg, Mikey Hannon, Rodrigo Segura, Katya Casper, Brad Wheaton, Dennis Berridge, Amanda Chou, Peter Gilbert, Laura Steen, Chris Ward, and Laura Letterman. It is impossible to imagine the last six years without their assistance and camaraderie.

Finally, I would like to credit the support offered by my family.

## TABLE OF CONTENTS

	Page
LIST OF TABLES . . . . .	viii
LIST OF FIGURES . . . . .	ix
SYMBOLS . . . . .	xiii
ABSTRACT . . . . .	xvi
1 BOUNDARY-LAYER TRANSITION . . . . .	1
1.1 Laminar-to-Turbulent Transition and Quiet Flow . . . . .	1
1.2 Transition Modes . . . . .	3
1.3 Transition Prediction and Computation . . . . .	5
2 ELLIPTIC CONES AND THE HIFIRE-5 . . . . .	7
2.1 Previous Work with Elliptic Cones . . . . .	7
2.1.1 AEDC Tunnel B . . . . .	7
2.1.2 Princeton Mach 8 Facility . . . . .	9
2.1.3 Purdue Quiet-Flow Ludwig Tube . . . . .	10
2.2 HIFIRE-5 . . . . .	11
2.2.1 Program Overview . . . . .	11
2.2.2 Computational Results . . . . .	12
3 THE BOEING/AFOSR MACH-6 QUIET TUNNEL — FACILITY AND HARDWARE . . . . .	17
3.1 Test Section . . . . .	19
3.2 Burst Diaphragms & Gap Pressure Management System . . . . .	21
3.3 Probe Traverse . . . . .	22
3.4 Tektronix Oscilloscopes . . . . .	24
4 THE BOEING/AFOSR MACH-6 QUIET TUNNEL — PERFORMANCE . . . . .	25
4.1 Flow Conditions . . . . .	25
4.2 Nozzle-Wall Boundary-Layer Separation . . . . .	27
4.3 Extent of Quiet Flow . . . . .	31
5 HIFIRE-5 MODEL . . . . .	39
6 TEMPERATURE-SENSITIVE PAINT MEASUREMENTS OF TRANSI- TION . . . . .	43
6.1 Instrumentation . . . . .	43
6.1.1 Paint and Insulator . . . . .	43

	Page
6.1.2 Lights and Camera . . . . .	51
6.2 Data Analysis Methodology . . . . .	53
6.2.1 TSP Calibration . . . . .	53
6.2.2 Image Registration . . . . .	54
6.2.3 Transition Threshold . . . . .	55
6.3 Results and Discussion . . . . .	58
6.3.1 Effect of Noise Level . . . . .	58
6.3.2 Effect of Angle of Attack . . . . .	66
6.3.3 Effect of Freestream Reynolds Number at Zero Angle of Attack	71
6.3.4 Effect of Freestream Reynolds Number at 4° Angle of Attack	79
6.3.5 Effect of Surface Finish (Distributed Roughness) . . . . .	86
6.3.6 Effect of Forward-Facing Step . . . . .	90
7 THERMOCOUPLES & HEAT-TRANSFER GAUGES . . . . .	92
7.1 Thermocouples . . . . .	92
7.1.1 Base Thermocouple . . . . .	92
7.1.2 Coaxial Thermocouples . . . . .	97
7.1.3 Surface Thermocouple . . . . .	98
7.2 Heat-Transfer Measurements . . . . .	99
7.2.1 Thin-Film and Schmidt-Boelter Heat-Transfer Gauges . . . .	99
7.2.2 Quantitative Heat-Flux Measurements from TSP . . . . .	102
8 MEASUREMENT OF BOUNDARY-LAYER INSTABILITIES WITH FAST PRESSURE SENSORS . . . . .	107
8.1 PCB Fast-Response Pressure Transducers . . . . .	107
8.2 Normalization of PCB Data . . . . .	108
8.3 Computation of Power Spectral Density . . . . .	108
8.4 Agreement Between TSP and PCB Indications of Transition Under Noisy Flow . . . . .	110
8.4.1 4° Angle of Attack . . . . .	110
8.4.2 0° Angle of Attack . . . . .	116
8.4.3 Second-Mode Wave Amplitudes . . . . .	119
8.5 Difficulty Interpreting PCB Sensors Under Quiet Flow . . . . .	120
8.5.1 Comparison of Experimental and Computational Disturbance Frequencies . . . . .	128
9 HOT-WIRE MASS FLUX PROFILES . . . . .	134
9.1 Instrumentation . . . . .	134
9.1.1 Hardware . . . . .	134
9.1.2 Mass Flux Calibration . . . . .	136
9.1.3 Hot Wire Location and Spatial Accuracy . . . . .	142
9.2 Results and Discussion . . . . .	145
9.2.1 4° Angle of Attack . . . . .	145
9.2.2 0° Angle of Attack . . . . .	149

	Page
10 SUMMARY AND CONCLUSIONS . . . . .	151
10.1 Recommendations for Future Work . . . . .	153
LIST OF REFERENCES . . . . .	155
A Figure Source Data . . . . .	163
B Model Final Drawings . . . . .	166
VITA . . . . .	171

## LIST OF TABLES

Table	Page
6.1 Summary of paint roughness and step for TSP data . . . . .	50
6.2 Summary of centerline transition locations for $\alpha = 0^\circ$ . . . . .	79
6.3 Summary of centerline transition locations for $\alpha = 4^\circ$ . . . . .	85
8.1 Computed mean wall pressures used in PCB normalization . . . . .	108
A.1 Figure source data . . . . .	163

## LIST OF FIGURES

Figure	Page
1.1 Computational and experimental heat flux [4] . . . . .	2
1.2 Shadowgraph of sharp cone at $M = 4.31$ (Ref. 4) . . . . .	4
1.3 Boundary layer profiles illustrating inflection point arising from pressure-gradient-induced crossflow [15] . . . . .	5
2.1 Oil streak flow visualization on sharp 2:1 elliptic cone at $M = 8$ , $\alpha = 0$ [29]	8
2.2 CFD prediction of static pressure for $\alpha = 0^\circ$ . . . . .	14
2.3 CFD prediction of surface $T_0$ , streamwise velocity, and selected streamlines for $\alpha = 0^\circ$ . . . . .	15
2.4 CFD centerline mass flux profile . . . . .	16
3.1 BAM6QT schematic . . . . .	17
3.2 Schematic of Mach-6 quiet nozzle with $7.5^\circ$ cone model. Dimensions are inches [meters]. . . . .	19
3.3 Test section with blank insert . . . . .	20
3.4 Probe traverse . . . . .	23
4.1 Hot-film array installed in Section 8. View from upstream. Ref. 56 . .	27
4.2 Comparison of centerline pitot pressure and nozzle-wall hot film . . . .	28
4.3 Hot-film traces indicating attached and separated flow on the nozzle wall	30
4.4 Pitot-mounted Kulite. 2.38 m from the throat, 76.2 mm below the centerline. . . . .	32
4.5 Hot-film traces for run in Figure 4.4 . . . . .	34
4.6 Impact of flow quality on TSP results . . . . .	36
4.7 Hot-film traces for run in Figure 4.6 . . . . .	37
5.1 Exploded assembly drawing of HIFiRE-5 model . . . . .	40
6.1 Photographs of first TSP application showing ‘orange-peel’ roughness .	44
6.2 Photograph of orange peel paint finish through microscope . . . . .	45

Figure	Page
6.3 Photographs of second TSP application showing heterogeneous insulator	46
6.4 Photographs of final TSP application on spray-paint insulator . . . . .	48
6.5 Profile of forward-facing step at nosetip/frustum junction . . . . .	50
6.6 Camera and light source setup in the BAM6QT with HIFiRE-5 model visible through big window . . . . .	52
6.7 Representative TSP contour and centerline profile . . . . .	57
6.8 Effect of tunnel noise level. $\alpha = 0^\circ$ , $Re = 10.2 \cdot 10^6$ /m . . . . .	59
6.9 Effect of tunnel noise level at high pressure. $\alpha = 0^\circ$ , $Re = 11.8 \cdot 10^6$ /m	61
6.10 Spanwise temperature profile . . . . .	63
6.11 Effect of tunnel noise level. $\alpha = 4^\circ$ , $Re = 9.5 \cdot 10^6$ /m . . . . .	64
6.12 Effect of tunnel noise level at high pressure. $\alpha = 4^\circ$ , $Re = 11.9 \cdot 10^6$ /m	65
6.13 Effect of angle of attack. Quiet flow, $M = 6.0$ , $t = 0.5$ s . . . . .	67
6.14 Effect of angle of attack on spanwise temperature profile . . . . .	68
6.15 Effect of angle of attack. Noisy flow, $M = 5.8$ , $Re = 9.5 \cdot 10^6$ /m . . . .	69
6.16 Effect of tunnel noise and angle of attack . . . . .	70
6.17 Effect of varying freestream $Re$ . Quiet flow, $M = 6.0$ , $\alpha = 0^\circ$ . . . . .	72
6.18 Centerline temperatures for $\alpha = 0^\circ$ under quiet flow . . . . .	75
6.19 Effect of varying freestream $Re$ . Noisy flow, $M = 5.8$ , $\alpha = 0^\circ$ . . . . .	76
6.20 Centerline temperatures for $\alpha = 0^\circ$ under noisy flow . . . . .	78
6.21 Effect of varying freestream $Re$ . Quiet flow, $M = 6.0$ , $\alpha = 4^\circ$ . . . . .	80
6.22 Centerline temperatures for $\alpha = 4^\circ$ under quiet flow . . . . .	82
6.23 Effect of varying freestream $Re$ . Noisy flow, $M = 5.8$ , $\alpha = 4^\circ$ . . . . .	83
6.24 Centerline temperatures for $\alpha = 4^\circ$ under noisy flow . . . . .	85
6.25 Effect of surface finish . . . . .	88
6.26 Effect of surface finish on spanwise temperature profile . . . . .	89
6.27 Effect of forward-facing step at $x = 76$ mm . . . . .	91
7.1 Base thermocouple attachment with extra insulation from caulking tape	93
7.2 Base thermocouple temperature . . . . .	94

Figure	Page
7.3 Pre-run model temperature measured by thermocouple on model base for the twenty runs of the 2010-2-8 tunnel entry . . . . .	95
7.4 Long-duration record of stagnation pressure and model temperature . .	96
7.5 Surface thermocouple (upper left) and thin-film heat-transfer gauge attachment . . . . .	98
7.6 Typical heat-flux and surface temperature under quiet flow . . . . .	100
7.7 TSP contour for comparison with heat transfer gauges . . . . .	101
7.8 Time history of heat flux during a noisy run . . . . .	103
7.9 Global heat flux during a noisy run . . . . .	104
7.10 Time history of heat flux during a quiet run . . . . .	105
7.11 Global heat flux during a quiet run . . . . .	106
8.1 Representative PCB power spectra . . . . .	111
8.2 TSP for comparison to PCB power spectra under noisy flow, $\alpha = 4^\circ$ . .	112
8.3 PCB power spectra under noisy flow, $\alpha = 4^\circ$ . . . . .	114
8.4 PCB power spectra under noisy flow, $\alpha = 4^\circ$ . . . . .	115
8.5 TSP for comparison to PCB power spectra under noisy flow, $\alpha = 0^\circ$ . .	117
8.6 PCB power spectra under noisy flow, $\alpha = 0^\circ$ . . . . .	118
8.7 Quiet flow, $M = 6.0$ , $\alpha = 4^\circ$ , $Re_i = 12.0 \cdot 10^6 / \text{m}$ , $p_{0i} = 1120 \text{ kPa}$ . . .	121
8.8 Quiet flow, $M = 6.0$ , $\alpha = 4^\circ$ , $Re_i = 3.0 \cdot 10^6 / \text{m}$ , $p_{0i} = 280 \text{ kPa}$ . . . . .	121
8.9 Quiet flow, $M = 6.0$ , $\alpha = 0^\circ$ , $Re_i = 6.7 \cdot 10^6 / \text{m}$ , $p_{0i} = 630 \text{ kPa}$ . . . . .	122
8.10 Quiet flow, $M = 6.0$ , $\alpha = 4^\circ$ , $Re(t = 3) = 10.3 \cdot 10^6 / \text{m}$ , $p_0(t = 3) = 890 \text{ kPa}$	123
8.11 Quiet flow, $M = 6.0$ , $\alpha = 0^\circ$ , $Re(t = 3) = 10.2 \cdot 10^6 / \text{m}$ , $p_0(t = 3) = 890 \text{ kPa}$	124
8.12 Quiet flow, $M = 6.0$ , $\alpha = 0^\circ$ , $Re(t = 3) = 6.9 \cdot 10^6 / \text{m}$ , $p_0(t = 3) = 600 \text{ kPa}$	124
8.13 TSP for comparison to PCB power spectra under quiet flow . . . . .	126
8.14 PCB power spectra under quiet flow . . . . .	127
8.15 PCB output under quiet flow, $\alpha = 4^\circ$ . . . . .	128
8.16 Computational prediction of disturbance amplification spectra, $\alpha = 4^\circ$ [92]	129
8.17 PCB and LST comparison, $\alpha = 4^\circ$ . . . . .	130
8.18 PCB output under quiet flow, $\alpha = 0^\circ$ . . . . .	131



Figure	Page
8.19 Computational prediction of disturbance amplification spectra, $\alpha = 0^\circ$ .	132
8.20 PCB and LST comparison, $\alpha = 0^\circ$ . . . . .	133
9.1 Photograph of a broken hot wire through microscope . . . . .	135
9.2 Hot wire calibration data . . . . .	140
9.3 Hot wire calibration data converted to non-dimensional parameters . .	141
9.4 Hot wire calibration data converted to non-dimensional parameters. Linear independent axis . . . . .	142
9.5 Mass flux measured by hot wire. $\alpha = 4^\circ$ , $x = 250$ mm, $y = 0$ mm . . .	146
9.6 Mass flux boundary layer profile. $\alpha = 4^\circ$ , $x = 250$ mm, $y = 0$ mm . . .	148
9.7 Mass flux measured by hot wire. $\alpha = 0^\circ$ , $x = 250$ mm, $y = 0$ mm . . .	149
9.8 Mass flux boundary layer profile. $\alpha = 0^\circ$ , $x = 250$ mm, $y = 0$ mm . . .	150
B.1 Frustum end view . . . . .	166
B.2 Frustum top and side views . . . . .	167
B.3 Nosetip . . . . .	168
B.4 Nosetip and glow perturber access hatch . . . . .	169
B.5 Glow perturber insert . . . . .	169
B.6 Top spacer for vertical nosetip steps . . . . .	170
B.7 Side spacer for horizontal nosetip steps . . . . .	170

## SYMBOLS

$a$	ellipse semi-major axis
$b$	ellipse semi-minor axis
$C$	hot wire calibration offset
$D$	hot wire calibration slope
$d$	hot wire diameter
$e$	ellipse aspect ratio $a/b$ ; $e = 2.0$ for the HIFiRE-5
$f$	frequency
$I$	temperature sensitive paint intensity
$Kn$	Knudsen number
$k$	thermal conductivity
$L$	model length or paint thickness
$l$	hot wire length
$M$	freestream Mach number
$N$	disturbance amplification factor
$Nu$	Nusselt number
$n$	hot wire calibration exponent
$p$	pressure
$\dot{q}$	heat transfer
$\dot{q}''$	heat flux (heat transfer per unit area)
$R$	resistance
$R_a$	constant resistance in CTA circuit
$R_{\text{bridge}}$	bridge resistance in CTA circuit
$Re$	freestream unit Reynolds number
$Re_d$	Reynolds number based on $d$ and $\mu(T_0)$
$Re_x$	Reynolds number based on length $x$ and freestream conditions

$r_n$	nose radius
$T$	temperature
$T_{\text{model}}$	model temperature
$t$	time
$u$	streamwise velocity (parallel to $x$ )
$V$	voltage (e.g., hot wire output)
$v$	spanwise velocity (parallel to $y$ )
$x$	axial distance parallel to model centerline; $x = 0$ at nosetip
$y$	spanwise distance; $y = 0$ on model centerline
$z$	vertical distance from model surface, normal to tunnel axis
$\alpha$	angle of attack or thermal coefficient of resistance
$\eta$	hot wire recovery ratio, $T_{\text{rec}}/T_0$
$\theta$	minor axis half-angle
$\mu$	dynamic viscosity
$\rho$	density
$\rho u$	mass flux
$\tau$	hot wire overheat ratio, $(T_{\text{wire}} - T_{\text{rec}})/T_0$

#### Superscripts

$\sim$	root-mean-square (rms)
$-$	mean
$'$	fluctuation

#### Subscripts

0	stagnation
1	pre-shock
2	post-shock
$i$	initial
$\infty$	freestream

dark	without illumination
e	at the boundary-layer edge
off	flow off (before the tunnel run)
on	flow on (while the tunnel is running)
max	maximum
rec	recovery
ref	reference
wall	at the model wall
wire	hot wire

## ABSTRACT

Juliano, Thomas J. Ph.D., Purdue University, August 2010. Instability and Transition on the HIFiRE-5 in a Mach-6 Quiet Tunnel. Major Professor: Steven P. Schneider.

A 2:1 aspect-ratio elliptic cone with a blunt nosetip was tested in the Boeing/AFOSR Mach-6 Quiet Tunnel to investigate the effects of freestream noise level, surface roughness, angle of attack, and freestream Reynolds number on laminar-to-turbulent boundary layer transition on the windward surface. The cone had a minor axis half-angle of  $7^\circ$  and a nose radius of 0.95 mm. Temperature-sensitive paint enabled a global measurement of the temperature distribution and detection of the transition front. Transition apparently arising from two mechanisms was observed: transition along the centerline suspected to arise from the amplification of second-mode waves in the inflected boundary layer, and transition roughly halfway between the centerline and leading edges probably due to the breakdown of crossflow vortices. Reducing noise level from conventional (root-mean-square pressure 3% of the mean) to quiet (root-mean-square pressure less than 0.1% of the mean) substantially delayed transition due to both mechanisms. Increasing the angle of attack from  $0^\circ$  to  $4^\circ$  delayed the crossflow transition mode on the windward side. Transition moved forward as freestream unit Reynolds number increased from  $2.6 \cdot 10^6$  /m to  $11.9 \cdot 10^6$  /m. PCB fast-response pressure transducers installed along the model centerline detected apparent instabilities at frequencies from 50 to 150 kHz prior to transition under noisy flow; quiet-flow results are less clear. Mass flux profiles along the centerline were measured with a calibrated hot wire.

## 1. BOUNDARY-LAYER TRANSITION

### 1.1 Laminar-to-Turbulent Transition and Quiet Flow

Fluid flow in a boundary layer can exist in two regimes, laminar and turbulent, usually separated by a transitional phase. In natural transition, disturbances in the laminar flow, such as free-stream turbulence, free-stream vorticity disturbances, or surface roughness, excite instability waves which are amplified through various instabilities and lead to transition to turbulent flow. [1]. Larger initial disturbances will bypass the linear growth mechanisms and lead directly to turbulent flow. This process is not well understood and the prediction of bypass transition is therefore difficult.

The streamlines of particles in a laminar boundary layer are smoother and straighter than those in turbulent flow and result in less friction and heat flux at the wall [2]. The prediction and control of transition is an important factor in the design of hypersonic vehicles due to its effect on surface heating, skin friction, separation, aero-optical distortion, and other boundary-layer properties [3]. This issue is especially pressing at hypersonic velocities, Mach number greater than 5, due to the high energies and heating involved.

Aeroheating can often be predicted accurately for both laminar and turbulent flow. The largest source of uncertainty in calculating heat flux is then the transition location, as illustrated in Figure 1.1 [4]. Reentry-heating flight data and a computational prediction are plotted as a function of distance along the body. The transition location for the computational prediction was chosen to match the flight data. The laminar and turbulent heating levels match the predicted level fairly well (within 20%), but the uncertainty in transition location can cause large errors. Present empirical correlations for transition are uncertain by a factor of three for this case. If

heating is more than predicted (i.e., transition is earlier than predicted), the vehicle might burn up; if it is less than predicted, there would be a performance penalty due to an unnecessarily heavy thermal protection system.

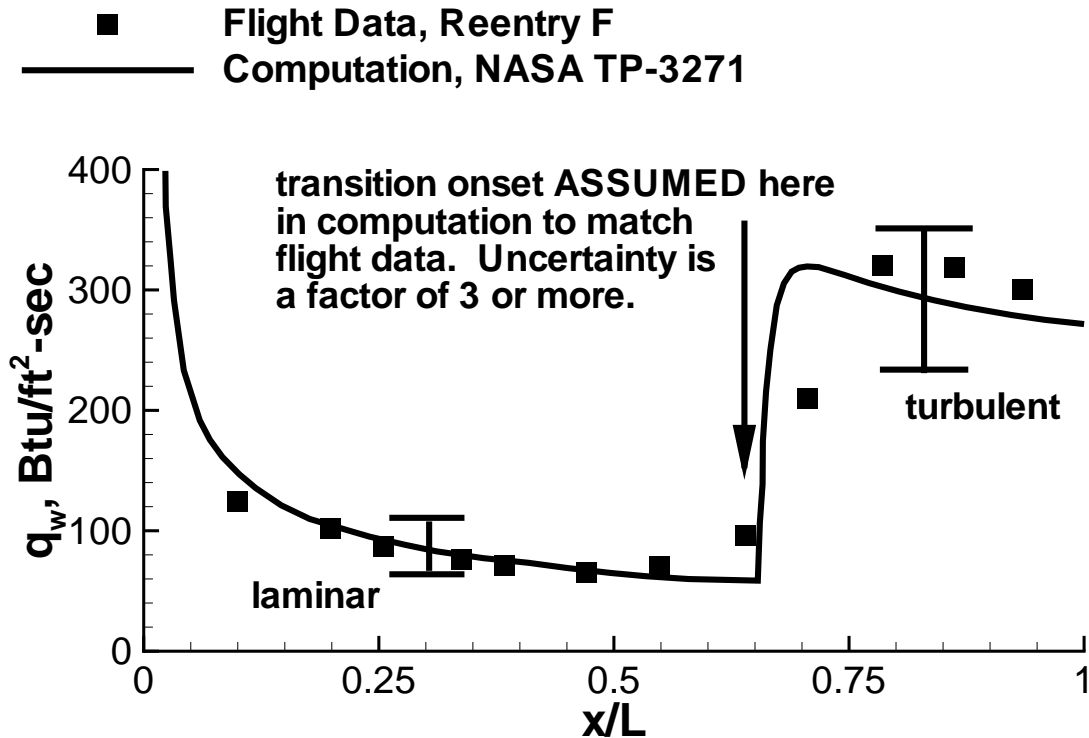


Figure 1.1.: Computational and experimental heat flux [4]

Many factors influence transition, including Reynolds number, surface roughness, and atmospheric conditions such as freestream noise level [1,5,6]. The noise level of a flow can be defined as the ratio of root-mean-square (rms) pitot stagnation pressure to mean pitot stagnation pressure. Atmospheric levels are typically  $< 0.05\%$  [7]. Such low levels are regarded as “quiet”. Accurate wind-tunnel testing requires matching as many flight parameters as possible, but achieving this low noise level in a wind tunnel has been particularly difficult [8]. Conventional tunnels have noise levels of 1–3%. Reference 7 contains a thorough discussion of the influence of tunnel noise on boundary-layer transition. The higher noise levels in a conventional ground-test

facility have been shown to lead to early transition as well as to changes in the parametric trends of transition. Thus, ground tests in a quiet tunnel are necessary in order to obtain more accurate transition estimates [9].

The primary reason for the difference in noise levels between conventional and quiet tunnels is that conventional tunnels have turbulent boundary layers whereas quiet tunnels have laminar boundary layers [10, 11]. Turbulent boundary layers produce unsteady Mach waves that cause fluctuations in the pressure downstream in the test section [4]. The control of transition on the nozzle walls is a problem that needs to be overcome in order to study transition on the test articles.

Figure 1.2 is a shadowgraph of a  $5^\circ$  sharp cone at Mach 4.31 that illustrates many transition-related phenomena [4]. The cone is at approximately zero angle of attack in air with a unit Reynolds number of  $105 \cdot 10^6$  /m ( $2.66 \cdot 10^6$  /in.). This image was obtained in the Naval Ordnance Lab ballistics range. The upper surface of the cone is mostly laminar with two turbulent spots. An oblique shock emanates from each of these spots. The lower surface is fully turbulent. The noise radiated into the flow by the turbulent boundary layer is visible as diagonal striations not present near the laminar boundary layer on the upper surface. Similar noise radiates from wind tunnel nozzle boundary layers into the air that subsequently passes through the test section.

## 1.2 Transition Modes

Several modes of boundary-layer instability causing linear disturbance growth have been identified. They include first mode (Tollmein-Schlichting), second mode (Mack), Görtler vortices, and crossflow vortices [12]. Second mode and crossflow instabilities are the most likely to be encountered for this geometry and flight regime. Mack demonstrated that the second mode is more amplified than the first mode in flat plate boundary layers for edge Mach numbers greater than about 4 [13]. Görtler vortices only develop on concave surfaces. Second-mode waves are acoustic waves



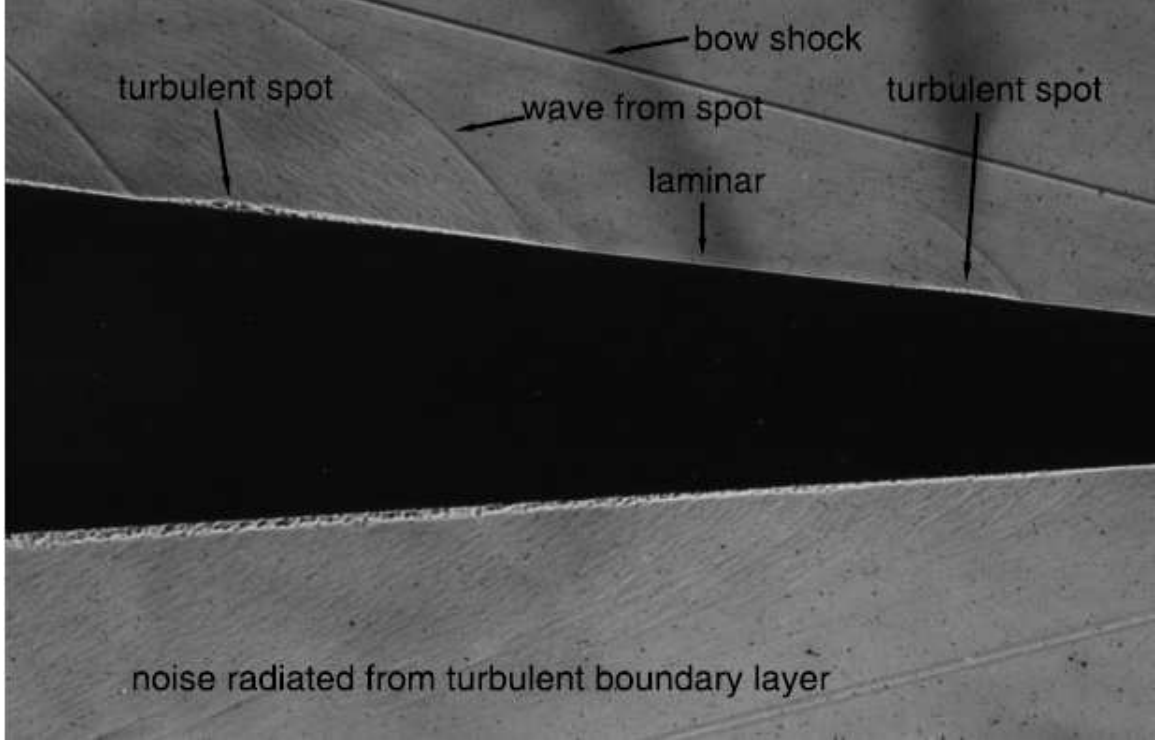


Figure 1.2.: Shadowgraph of sharp cone at  $M = 4.31$  (Ref. 4)

reflecting within the boundary layer. They are most unstable as a 2-D disturbance (with a wavefront perpendicular to the mean flow direction) [14].

The crossflow instability, on the other hand, is strictly a three-dimensional flow phenomenon. A pressure gradient, such as the one that exists along a swept wing, will induce crossflow perpendicular to the inviscid streamline. Figure 1.3, reprinted from Reference 15, shows the streamwise, spanwise, and net velocity profiles within a 3-D boundary layer. An inviscidly unstable inflection point necessarily exists in the velocity profile due to the boundary conditions: zero spanwise velocity at the surface and in the freestream, and spanwise velocity derivative of zero in the freestream.

Reference 16 is a comprehensive review of the effect of roughness on hypersonic boundary-layer transition. Radeztsky et al. showed that isolated roughness elements near the attachment line on a swept wing can strongly influence crossflow-dominated transition in subsonic flow [17]. The three-dimensional roughness is a source of vortic-

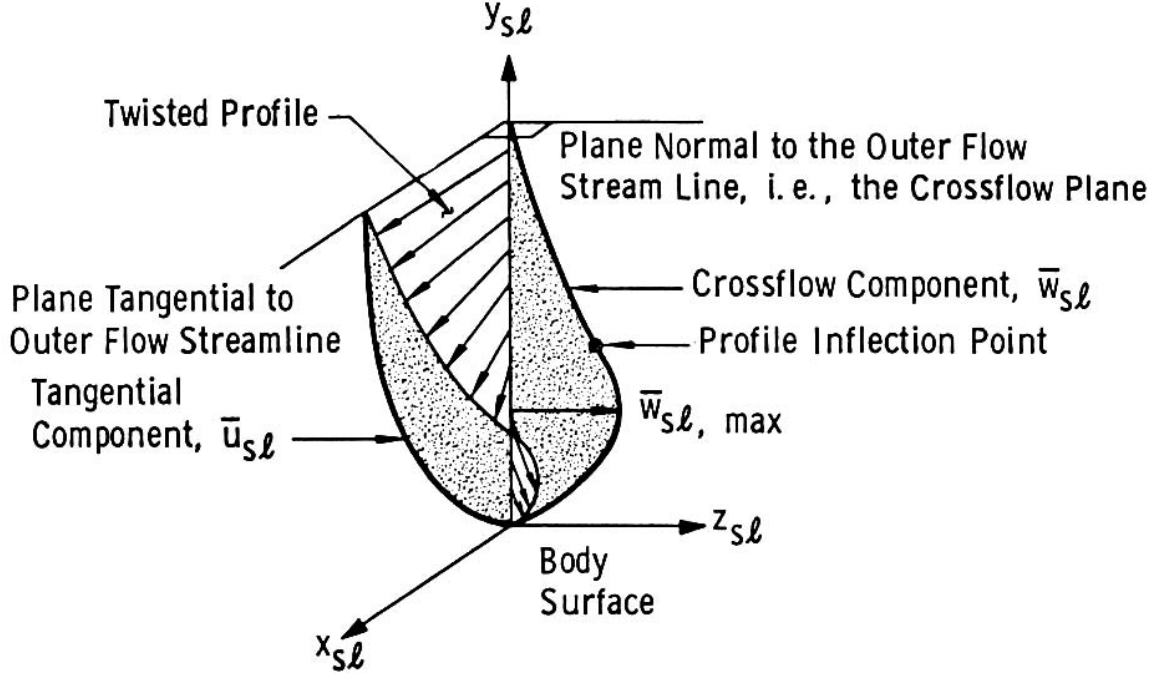


Figure 1.3.: Boundary layer profiles illustrating inflection point arising from pressure-gradient-induced crossflow [15]. In this figure,  $y$  is the wall-normal coordinate, while  $z$  and  $w$  are the spanwise coordinate and velocity.

ity affecting the initial disturbance amplitudes (receptivity), which causes transition to occur earlier.

### 1.3 Transition Prediction and Computation

Linear stability theory (LST) provides a theoretical underpinning that has been successful at predicting transition location as a function of flow parameters and the disturbance environment [18]. It can be combined with the semi-empirical  $e^N$  method to predict transition location. Disturbance amplification  $A/A_0 = e^N$ , where  $A$  is a disturbance amplitude and  $A_0$  is its initial amplitude before amplification, can be computed, given a geometry and the flow parameters. Transition location is then related empirically to a critical value of  $N$ . LST and its similar but improved successor, parabolized stability equations (PSE), are of crucial importance because they enable

the extrapolation of limited experimental test conditions to a wider range of cases. For instance,  $N \approx 5.5$  correlates well with transition location on a nearly sharp cone under noisy flow in multiple facilities [19]. Sharp cones in low-noise facilities typically exhibit transition for  $N = 8\text{--}11$  [20]. These methods are not applicable for disturbances of large initial amplitude that bypass the linear growth regime [21].

Current experimental research aims to improve the accuracy and extend the applicability of these computational methods. The preponderance of previous experiments have studied axisymmetric and two-dimensional geometries such as circular cones, capsules, and flat plates. A similar dataset for three-dimensional geometries, with the addition of crossflow, would enable development and verification of stability and transition CFD for a broader range of future vehicles.

Assessing the effect of roughness is another critical issue for hypersonic boundary-layer transition prediction [22]. Numerous experimental efforts are presently underway to better understand isolated and distributed roughness [23–26].

Experimental measurements of boundary-layer disturbances prior to transition are needed for comparison with LST and PSE computations of wave growth. Measuring disturbance frequencies is more difficult than identifying their breakdown into turbulence; measuring disturbance amplitudes is even more challenging. Hot wires have been used since the earliest tests of boundary-layer stability and transition [27], but they are fragile and difficult to use, particularly at hypersonic speeds. Recent work with surface-mounted fast-response pressure sensors have demonstrated their ability to detect second-mode waves, but these sensors are presently too large to measure boundary layer profiles with the necessary spatial resolution [28].

## 2. ELLIPTIC CONES AND THE HIFIRE-5

### 2.1 Previous Work with Elliptic Cones

#### 2.1.1 AEDC Tunnel B

Elliptic cones have been the subject of previous studies of three-dimensional hypersonic flow. Kimmel and Poggie tested a sharp elliptic cone in the Arnold Engineering Development Center von Karman Facility Tunnel B at Mach 8 [29, 30]. The nose radius was 0.4 mm, the cross section aspect ratio  $e$  was 2:1, and the half angle along the minor axis was  $7^\circ$ . The model overall length  $L$  was 1.016 m. The majority of their data were collected at  $Re = 1.79 \cdot 10^6$  /m and  $x/L = 0.8$ , so  $Re_x = 1.6 \cdot 10^6$ . The model wall was adiabatic and  $T_0$  in the settling chamber was 728 K. The model was instrumented with 1-mm-diameter pressure taps and 4.8-mm-diameter Schmidt-Boelter heat-transfer gauges. Hot-film probes with constant-current anemometers were used to measure boundary-layer disturbance frequencies and amplitudes. Oil flow and schlieren provided flow visualization.

Parabolized Navier-Stokes and linear stability computations were made in support of these measurements. Three different aspect ratios — 1.5, 2, and 4:1 — were computed. The maximum  $N$ -factor for the  $e = 1.5$  geometry was less than 5, making transition unlikely. For  $e = 4$ , crossflow amplification  $N$  reached 5 at  $x/L = 0.3$ . Thus early transition was possible, which would make it difficult to probe the laminar and transitional boundary layer. Therefore, the 2:1 configuration was chosen for further computational as well as experimental study.

Figure 2.1, a reproduction of Figure 7-3 in Reference 29, is an example of surface oil streak flow visualization from these tests. The middle portions of the third and fourth oil bands have been moved further downstream than the outboard portions. The increased dragging of the oil is indicative of increased shear from flow that has

become turbulent. Oil streaks in the second and outboard areas of the third bands are angled toward the centerline. These streaks, which match the computed laminar flow surface streamlines, are evidence of crossflow. The streaks were deemed unlikely to be crossflow vortices because computations indicated that crossflow vortices would have greater spacing and be more closely aligned with the inviscid streamlines [31]. That the oil streaks are not as long as those near the centerline indicates this crossflow has not yet led to turbulence.

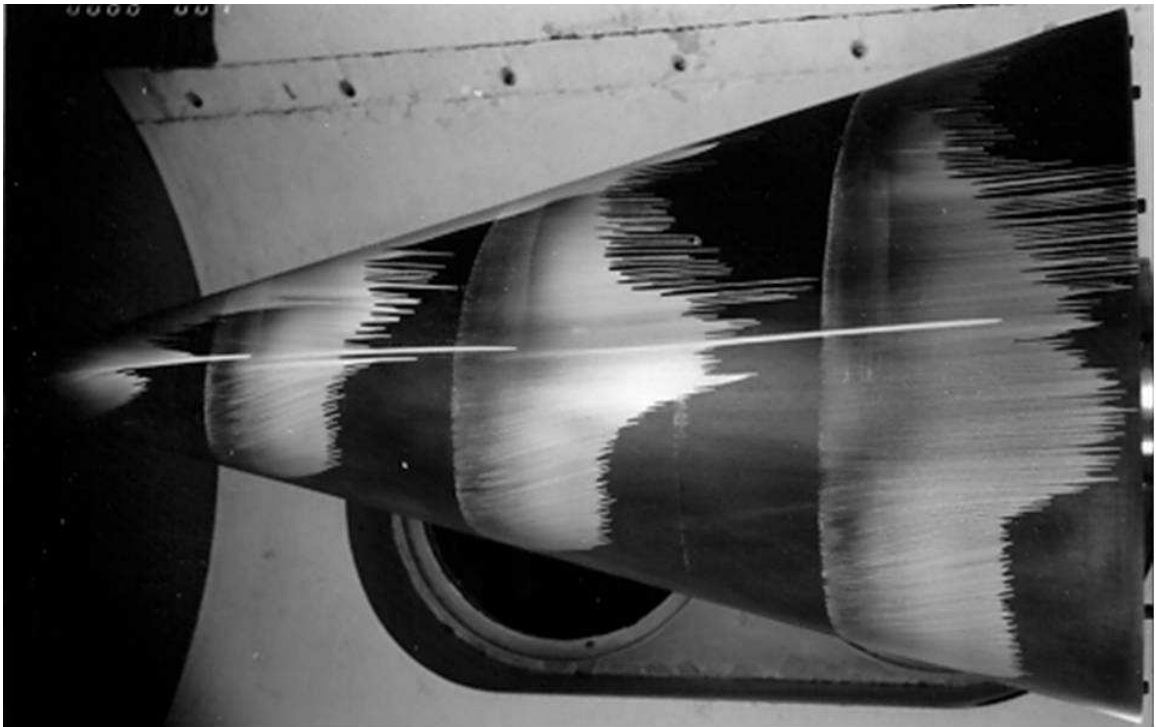


Figure 2.1.: Oil streak flow visualization on sharp 2:1 elliptic cone at  $M = 8$ ,  $\alpha = 0$  [29]

The hot-film probes were able to detect disturbances over a range of azimuths. Low frequency ( $f \approx 20$  kHz) peaks were associated with crossflow instability, whereas higher frequency (80 kHz) peaks match the predicted frequency of second-mode instability. Broadband noise replaced the peaks at azimuths near the centerline, which corroborated the oil flow and heat-transfer gauges indicating a turbulent boundary layer.

### 2.1.2 Princeton Mach 8 Facility

Huntley and Smits conducted numerous flow visualization experiments on sharp 2:1 and 4:1 elliptic cones at the Princeton Mach 8 Facility [32, 33]. The minor axis half-angle  $\theta$  was  $9^\circ$  for the 4:1 elliptic cone, compared to  $7^\circ$  for the Tunnel B tests and the HIFiRE-5. The model length was 0.242 m and the nominal nose radius was  $200\ \mu\text{m}$  on the major axis. Freestream Reynolds number ranged from 2.0 to  $21 \cdot 10^6$  /m. Stagnation temperature  $T_0$  was 780 K. The model temperature was 0.50–0.56 times  $T_0$ .

Remarkable images of boundary-layer instability and transition along the model centerline were obtained with Filtered Rayleigh Scattering in the centerline plane (for example, Figures 4b and 4c in Ref. 32). Prior to transition, traveling waves of density fluctuations with a wavelength 4–5 times the boundary layer thickness were imaged. Waves with such a long wavelength are unlikely to have been second-mode waves. At higher  $Re$  nearer to transition onset, the fluctuation wavelength decreased to twice the boundary layer thickness, which agrees with the measurements in Tunnel B as well as theoretical predictions for second-mode waves.

The same technique was used to image the boundary layer in a plane perpendicular to the model axis (Figure 5 in Ref. 32). The centerline ballooning of the boundary layer predicted by the computations of Kimmel et al. was observed [31]. As  $Re$  was increased to  $6.5\text{--}8.0 \cdot 10^6$  /m, vortical structures were visible on either side of the centerline bulge. At yet higher  $Re = 10.5 \cdot 10^6$  /m, flow near the centerline was late-transitional, and vortices had begun to develop further from the centerline.

Similar results were observed for the 2:1 elliptic cone. They were inclined more toward the centerline for the 4:1 than the 2:1 aspect ratio, which was attributed to the stronger crossflow for the higher eccentricity cross section.

### 2.1.3 Purdue Quiet-Flow Ludwig Tube

Schmisseur et al. tested a 4:1 elliptic cone in the Purdue Quiet-Flow Ludwig Tube at Mach 4 [34,35]. The major and minor axes at the base were 80 and 20 mm, respectively. The minor-axis half-angle was  $4.5^\circ$  and the nose radius was less than 0.051 mm along the minor axis. The primary goal of these tests was to investigate boundary-layer receptivity with controlled perturbations from a thermal spot generated by a pulsed laser. Constant-temperature and constant-current hot wires were used to probe the flowfield away the cone and a hot-film array provided surface measurements.

The surface hot films nearest the minor axis (7 mm from the centerline) indicated the strongest response to the laser perturber. Two possible explanations for this finding were provided. One suggestion is that the crossflow convects the disturbance towards the centerline, concentrating the disturbance near the centerline. The other explanation is that the boundary layer above the minor axis is less stable than elsewhere around the elliptic cone.

Mean-flow mass-flux profiles from calibrated hot wires are presented in Reference 35. The hot wires indicate a highly inflected mass-flux profile above the centerline with a very steep velocity gradient near the outer edge of the boundary layer. The experimental data were compared with computations from Reference 36. The experimental and computed profile shapes matched well, but the boundary layer thicknesses differed by about 28% (see Figure 12 in Ref. 35). The measured mass flux was about 20% below the theoretical values obtained from oblique shock relations for the computed shock angle. This difference was attributed to errors in the hot-wire calibration.

These measurements were supported by mean-flow and stability computations by Lyttle and Huang et al. [36,37]. Lyttle applied the crossflow transition correlation developed by Reed and Haynes in Reference 38 and found that transition would not be expected for the conditions in the Mach-4 Tunnel for  $e = 2, 3$ , or 4. Huang et

al. reached the opposite conclusion from their PSE computations: using  $N = 10$  as the transition threshold, transition is predicted to occur for the 4:1 elliptical cone. They found that the logarithmic amplification factors for traveling crossflow modes are comparable to that of the stationary crossflow vortex.

## 2.2 HIFiRE-5

### 2.2.1 Program Overview

The Hypersonic International Flight Research and Experimentation (HIFiRE) program is a joint effort of the U.S. Air Force Research Laboratory (AFRL) and the Australian Defence Science and Technology Organization (DSTO) [39]. Its goal is to develop necessary knowledge and technologies required for future global reach and reusable space access vehicles. To this end, a coordinated set of computational, ground, and flight tests are planned.

The HIFiRE program is organized as a collection of up to ten research projects, each of which has a unique subset of goals regarding aerodynamics, propulsion, navigation, control, materials, and others. Aerothermodynamics, including boundary-layer transition, is a primary goal of the HIFiRE-1 and -5 tests. HIFiRE-1, a cone-cylinder-flare geometry, examined natural and roughness-induced transition [19, 40, 41]. Tests in the BAM6QT showed a significant transition delay under quiet flow, reinforcing the necessity of quiet-flow testing as a component of transition studies [23].

The second HIFiRE test examining boundary-layer stability and transition is HIFiRE-5. An elliptic cone was chosen as the geometry because of its resemblance to practical geometries, the body of previous work on such shapes, and the presence of three-dimensional flow. Unlike previous elliptic cones tested, the HIFiRE-5 has a small bluntness nosetip ( $r_n = 2.5$  mm) to moderate heating. Three-dimensional flow introduces transition mechanisms not present in axisymmetric or two-dimensional flow. Improved understanding of these transition modes is essential to the prediction



of transition on complicated geometries, which in turn is an important facet of the design of future vehicles.

This series of tests on the HIFiRE-5 follows tests done for the DARPA/USAF FALCON HTV-2 (Hypersonic Test Vehicle-2) program [42]. The HTV-2 was tested in the BAM6QT between November 2006 and April 2008. HIFiRE-5 is expected to exhibit much of the transition flow physics seen on hypersonic glide vehicles like HTV-2.

### 2.2.2 Computational Results

Computational analysis of the HIFiRE-5 was conducted for selected wind tunnel test cases as well as the proposed flight conditions [43, 44]. Among the cases tested were two simulating the HIFiRE-5 at 0 and 4° angle of attack in the BAM6QT near the maximum quiet pressure achieved at that time (970 kPa in December 2008). Unsurprisingly, the computations predict many of the same interesting flow features encountered in the experiments discussed above.

The CFD mean-flow results were a very helpful tool in understanding the overall flowfield because they provided a more complete picture than the experimental data from any single instrument. Stability computations were also executed and will be discussed in conjunction with the relevant experimental results.

These computations were made by Jeff White and Meelan Choudhari of the NASA Langley Computational Aerosciences Branch using VULCAN. They supersede preliminary results obtained with LAURA. The following flow conditions were selected: freestream  $M = 6.0$ ,  $p_0 = 970$  kPa,  $T_0 = 433$  K,  $Re = 10.2 \cdot 10^6$  /m, and model wall  $T = 300$  K. These parameters were the same for both the 0° and 4° angle of attack cases. The computational domain was extended to  $x = 381$  mm (the model length is 328 mm) to mitigate the effects of the outflow boundary condition.

Dr. Choudhari provided these data directly to the author. These figures were then created from those data.

Figure 2.2 shows the static pressure 20 gridpoints (0.076 mm) above the surface of the HIFiRE-5 at  $\alpha = 0^\circ$ . Only one quarter of the surface is shown, from leading edge to centerline. The units shown in the legend are Pascals. The crossflow-inducing spanwise pressure gradient is clear. The pressure along the leading edges is twice that along the centerline. It arises from the azimuthal variation in the shock angle around the elliptic cone. The pressure in the vicinity of the blunt nosetip is high for the same reason — the flow there has passed through the nearly-normal detached shock ahead of the tip. Several streamlines exhibiting the spanwise velocity component within the boundary layer are shown as well.

Figure 2.3 presents the computed stagnation temperature  $T_0$  near the surface, streamwise velocity  $u$ , and a few streamlines for  $\alpha = 0^\circ$ . The temperature units are K, and  $u$  is in m/s. The  $T_0$  contour shows the data for 40 gridpoints (0.18 mm) above the surface. These data are useful because they are qualitatively similar to the output from Temperature-Sensitive Paint. The spanwise slices (showing  $u$ ) occur every 50 mm starting at  $x = 50$  mm. The data in the immediate vicinity of the nosetip was suppressed to reduce the computer memory needed to display these contours.

One significant effect of the crossflow is the accumulation of low-momentum fluid near the HIFiRE-5 centerline, as shown by the velocity contours. A vortex is predicted to form on each side of this bulge. In an approximate and qualitative way, these results resemble those from the several sources discussed in Section 2.1.

The thick boundary layer near the centerline substantially reduces the heat flux into the wall because of the reduced temperature gradient, as expressed by Fourier's law [45]:

$$\dot{q}'' = -k \frac{\partial T}{\partial z} \quad (2.1)$$

where  $\dot{q}''$  is the heat flux (rate of heat transfer per unit area) and  $k$  is the thermal conductivity (with units of W/m·K). The heat flux into the wall depends on  $\frac{\partial T}{\partial z}$  evaluated at  $z = 0$  and the thermal conductivity of the fluid (air in this case) at the temperature of the wall. This reduced heating is apparent in the near-surface  $T_0$  contour and figures prominently in the TSP data presented in Chapter 6. The

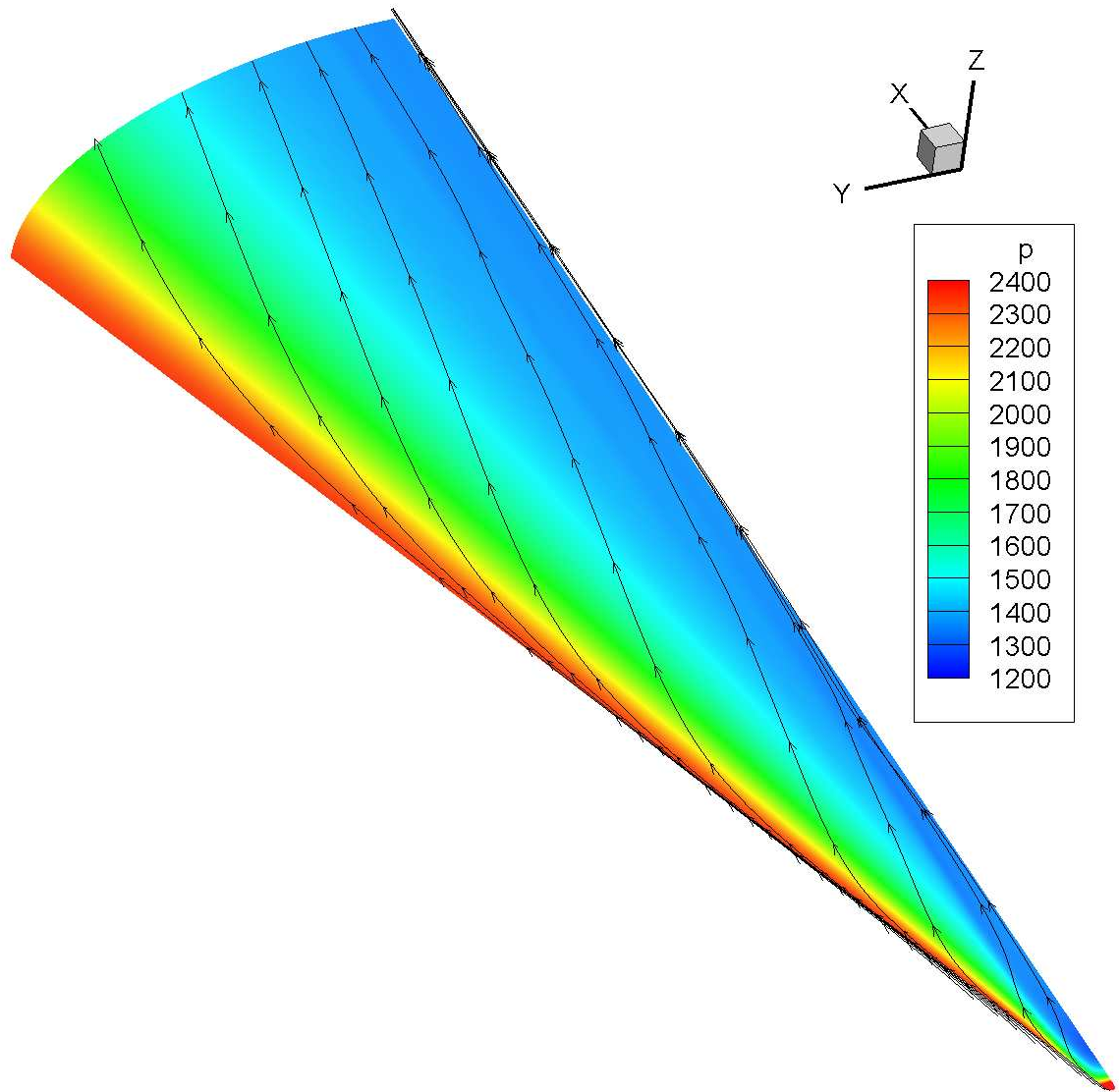


Figure 2.2.: CFD prediction of static pressure and selected streamlines for  $\alpha = 0^\circ$ . Units are Pa. Computation by J. White and M. Choudhari

vortices on either side of the centerline bulge convect high-momentum fluid closer to the wall, thereby thinning the boundary layer and increasing the heat flux. These off-centerline hot streaks are even more prominent at  $\alpha = 4^\circ$ .

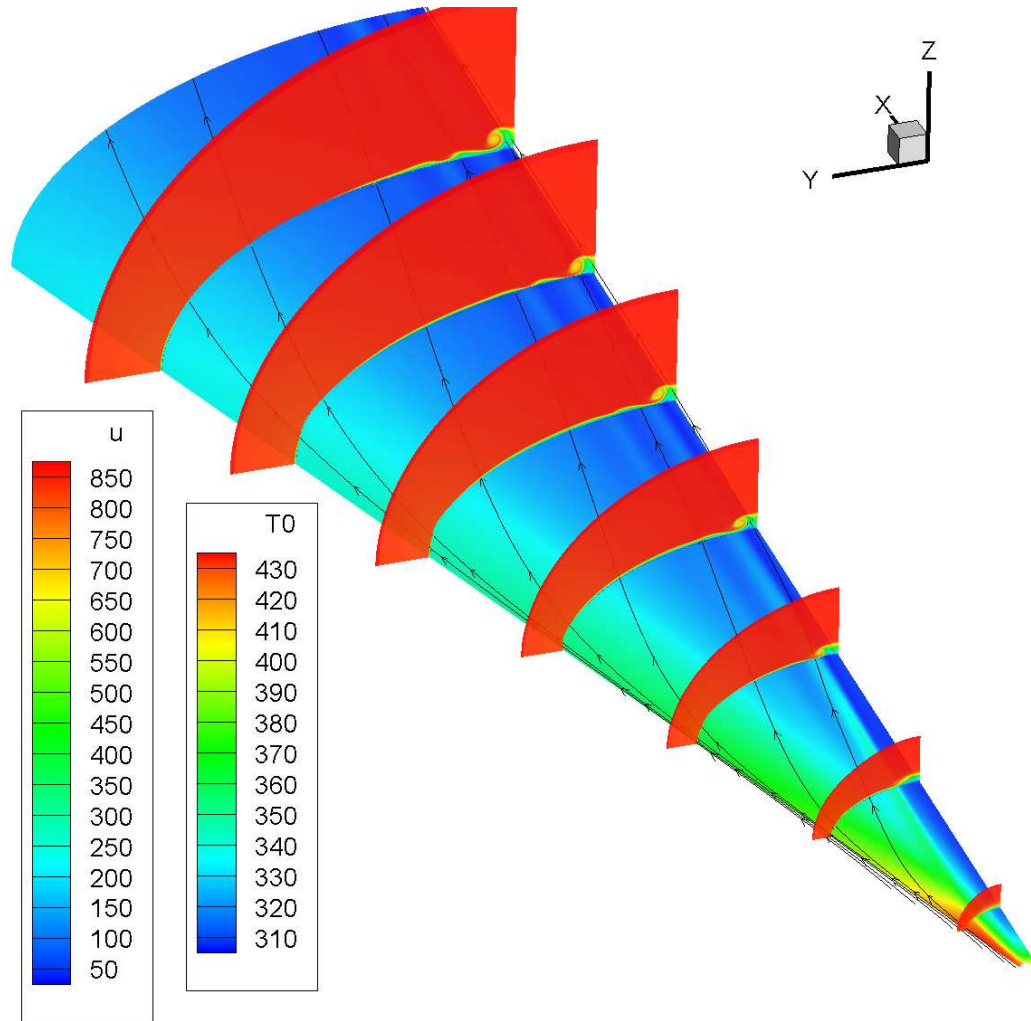


Figure 2.3.: CFD prediction of surface stagnation temperature  $T_0$ , streamwise velocity  $u$ , and selected streamlines for  $\alpha = 0^\circ$ . Surface contour is  $T_0$  in K and spanwise slices show  $u$  in m/s. Computation by J. White and M. Choudhari

Accurately simulating the velocity profile within the centerline bulge is a difficult problem and part of the motivation for the hot-wire mass flux profiles presented in Chapter 9. Figure 2.4 shows the centerline mass flux profile at  $x = 285$  mm extracted from an earlier mean flow solution using LAURA. The mass flux was normalized by its freestream value and the black circle denotes the boundary layer edge location, which is assumed to be where  $\rho u = 0.99(\rho u)_{\max}$ .

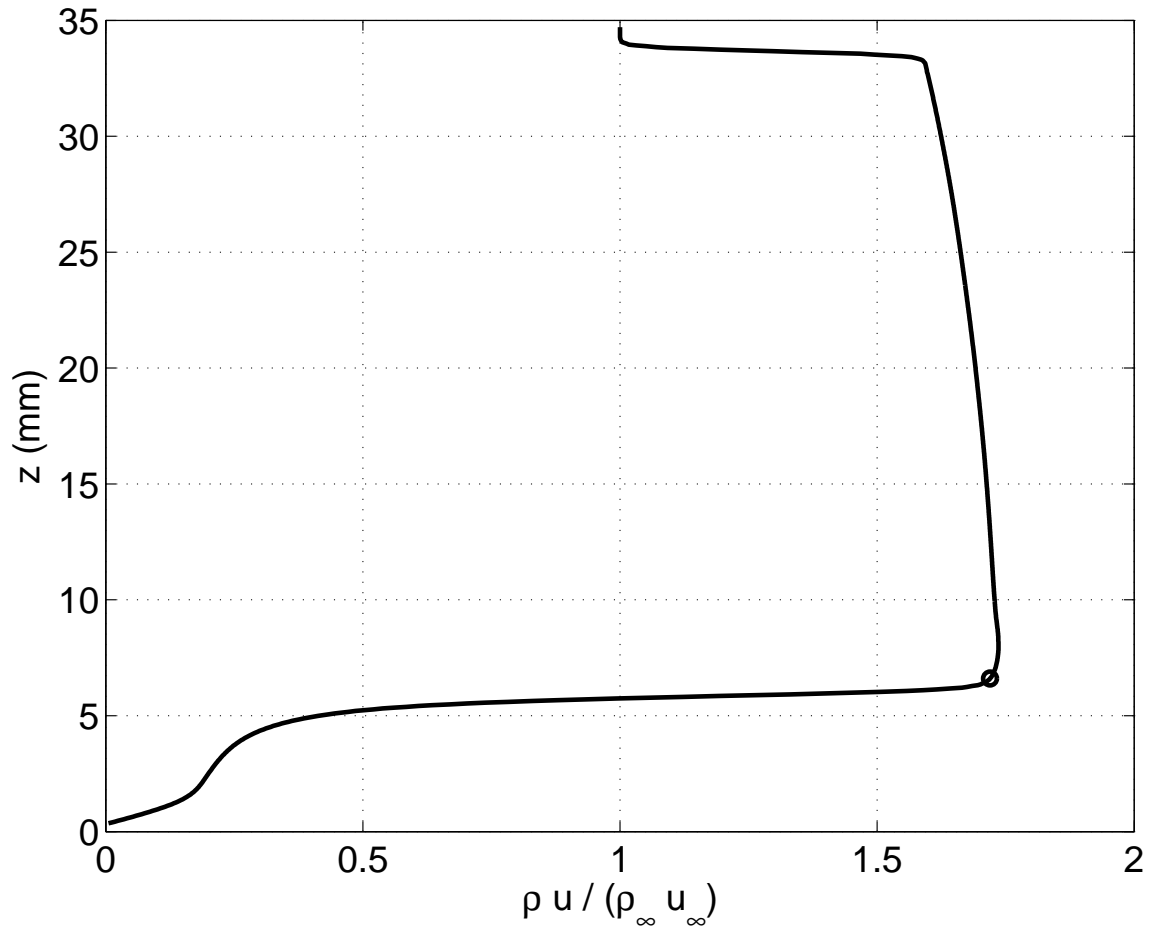


Figure 2.4.: CFD prediction of mass flux normalized by freestream value at  $x = 285$  mm,  $y = 0$  mm,  $\alpha = 0^\circ$

### 3. THE BOEING/AFOSR MACH-6 QUIET TUNNEL — FACILITY AND HARDWARE

The Boeing/AFOSR Mach-6 Quiet Tunnel (BAM6QT) at Purdue University is one of two hypersonic quiet tunnels in operation anywhere in the world, and the only one offering optical access to the test section. In order to minimize complexity and cost, a Ludwieg-tube design was chosen for the BAM6QT. A Ludwieg tube is a high-pressure driver tube connected to a converging-diverging nozzle that accelerates the flow to the desired Mach number, which is set by the ratio between the test section and throat areas [46]. The tunnel configuration is shown in Figure 3.1. The maximum stagnation pressure for the BAM6QT is 2.0 MPa, although the design maximum quiet pressure is 1.0 MPa. This goal was not achieved until November 2006 [47]. While running quietly, the noise level is less than 0.05%, and it increases to about 3% when noisy [48].

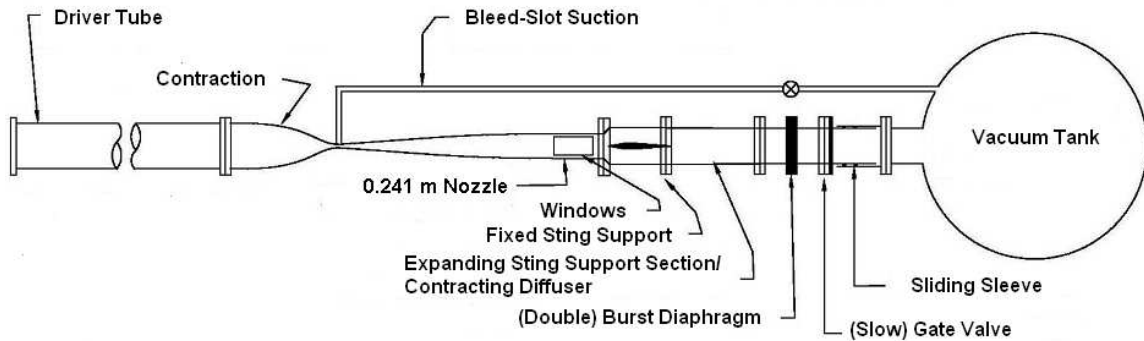


Figure 3.1.: BAM6QT schematic

Air entering the driver tube and the driver tube itself are heated to a nominal temperature of 433 K (160 °C) to avoid nitrogen liquefaction in the nozzle, where the static temperature decreases to 53 K when expanded to Mach 6. A 6-volt electric potential across the tube draws approximately 2000 amps of current from a series of DC power supplies to maintain the driver-tube temperature.

The BAM6QT employs many features to maintain a laminar nozzle-wall boundary layer, thereby achieving quiet flow [48]. Among these features is a suction slot upstream of the throat that removes the boundary layer on the contraction, allowing a fresh laminar boundary layer to grow on the expanding portion of the nozzle. In order to run quietly, a valve must be opened connecting the bleed slot to the vacuum tank. Thus, the BAM6QT can be run with a conventional noise level by leaving the bleed line closed. A more comprehensive discussion of the components of the BAM6QT is contained in Reference 49.

The nozzle-wall boundary layer is more likely to transition to turbulent (resulting in noisy flow) at higher stagnation pressures. Thus, the performance of the BAM6QT is typically expressed in terms of its maximum quiet pressure — the highest stagnation pressure that will result in quiet flow. Due to the sensitivity of the BAM6QT nozzle to dust or other imperfections, the maximum quiet pressure has varied over the last few years (Reference 9 summarizes progress through 2007; References 50–53 provide updates through mid-2010). Increasing the tunnel’s maximum quiet pressure was a primary goal for the first several years after its completion (2001–2006) and efforts to enable low-noise testing at ever-higher  $Re$  are ongoing. For the results herein, the maximum quiet pressure was consistently above 1000 kPa.

At the time that HIFiRE-5 testing was performed, the run duration was about 6 s for quiet flow (with the contraction bleed lines open) and 10 s for noisy flow (bleed lines closed). The increased mass flux through the bleed lines results in a faster emptying of the driver tube and decreased run time for quiet-flow testing. The run time also depends on the efficiency of the diffuser; HIFiRE-5 tests were conducted with the second-generation sting-support section and diffuser described in Reference 54. The

pipe insert was installed in the sting-support section, with no gap between it and the test section. The pipe insert extension described in Reference 51 was also installed for most tests because it was found to inhibit separation of the nozzle-wall boundary layer (see Section 4.2).

### 3.1 Test Section

Figure 3.2 shows Section 8, the last nozzle section. The region of useful quiet flow lies between the characteristics marking the onset of uniform flow and the characteristics marking the upstream boundary of acoustic radiation from the onset of turbulence in the nozzle-wall boundary layer. A  $7.5^\circ$  half-angle sharp cone is drawn on the figure. The rectangles are drawn on the nozzle at the location of window openings.

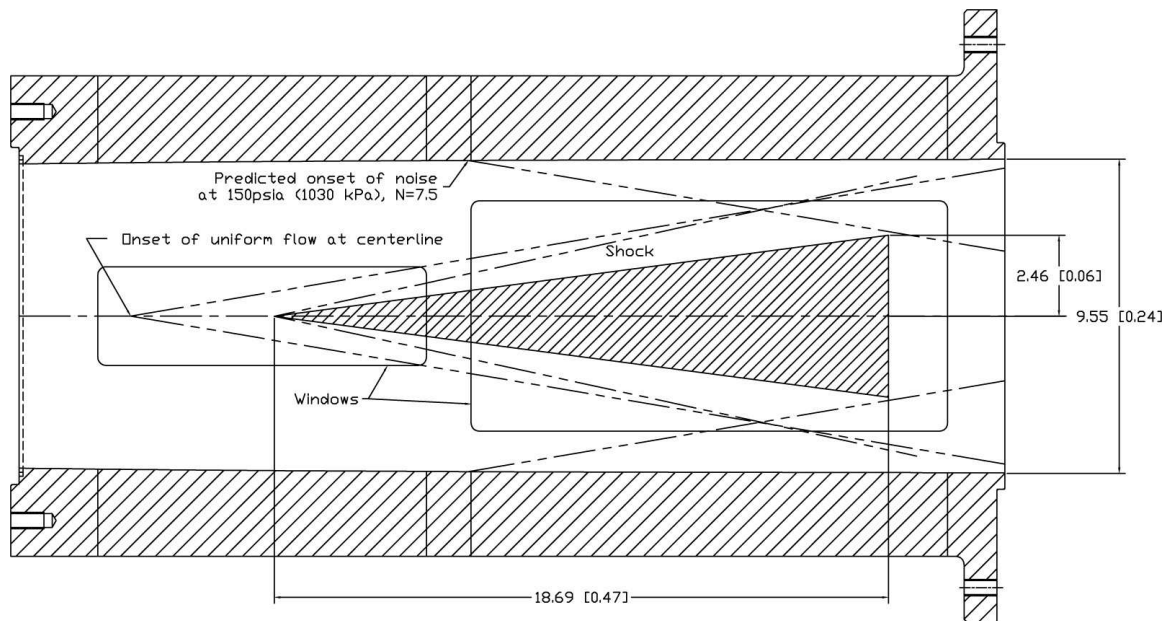


Figure 3.2.: Schematic of Mach-6 quiet nozzle with  $7.5^\circ$  cone model. Dimensions are inches [meters].

Section 8 has several ports for various instruments and windows (Figure 3.3). A solid steel blank, a large acrylic window, and a pair of smaller porthole windows



can be inserted in the large side port. The large acrylic window was used for most HIFiRE-5 temperature-sensitive-paint tests because the model was large enough to benefit from the good field of view (see Section 6.1). The traverse system is installed in the aft-upper window slot. Except for the hot-wire tests, the traverse slot plug was installed to fill and eliminate any effects from the traverse slot cavity. The hot-film array was installed in the forward-lower or a forward-side port. During every run, the uncalibrated output from the nozzle-wall hot-films were recorded in order to verify whether the flow was noisy, quiet, or separated [47, 49, 55, 56]. Section 4.2 contains more details about these measurements.

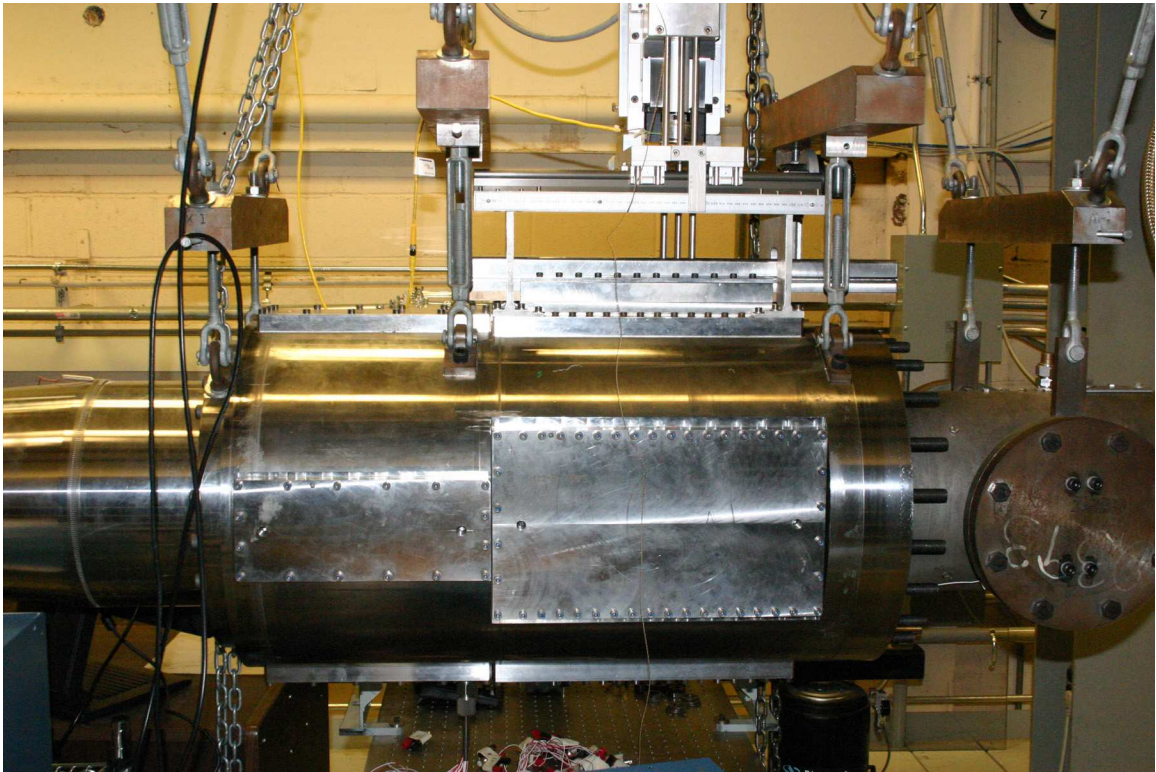


Figure 3.3.: Test section with blank insert

### 3.2 Burst Diaphragms & Gap Pressure Management System

The BAM6QT employs a double diaphragm system to separate the upstream (pressurized) and downstream (vacuum) ends of the Ludwig tube prior to the run. The space between the diaphragms, referred to as the ‘gap’, is maintained at half of the upstream pressure. Diaphragm material, alloy, and thickness is chosen so that they can each withstand half of the stagnation pressure, but rupture when exposed to the full pressure. Compared to a single-diaphragm system, the double-diaphragm setup allows more precise control over the upstream conditions. It also enables the driver tube to be isolated from the air supply after filling, prior to the run, while the driver air settles.

Piping and high-pressure hoses connect the diaphragm gap to the diffuser upstream and the pipe leading to the gate valve downstream. These lines are closed with valves that permit control of the gap pressure. Opening the valve from upstream allows air into the gap, thereby increasing the gap pressure; opening the downstream valve decreases gap pressure by releasing air from the gap to the vacuum tank. Adjusting these valves was a manual job for whoever is running the tunnel. It could take a large share of attention if running near the upper limit of a diaphragm’s pressure range or if the diaphragms were particularly leaky. The penalty for failing to maintain the gap pressure within limits is an early diaphragm burst and likely a wasted run.

The idea to automate the regulation of the gap pressure was first conceived in the summer of 2005, when the author was training to run the BAM6QT. More urgent work took priority, and the idea was not revisited until the spring of 2008, when the decision was made to hire Alexander Cartagena on a Summer Undergraduate Research Fellowship. He assisted in selecting the components of the system and wrote the first draft of the software that controls it, based on the framework provided by the author [57]. Significant additional work on the system was contributed by Amanda Chou, who completed and debugged the control software and aided in assembly of the plumbing [58]. John Phillips, the electronics technician for the School of Aeronautics

and Astronautics, designed and assembled the electronic circuitry that controls the hardware.

The centerpiece of the system is a Proportion Air QB1 Electronic Pressure Regulator. This device regulates the pressure in the gap by allowing air in from the driver tube or exhausting it out to the room. It interfaces with a control computer running LabVIEW through a National Instruments 6229 M Series USB DAQ Card. The contraction Kulite signal is also digitized by the computer — the control program endeavors to maintain half of the upstream pressure as the gap pressure. The other significant piece of hardware added is a Parker 3-Way Electronic Directional Control Valve. This valve toggles between connecting the driver tube and regulator with the gap and venting the gap to the vacuum tank. When the tunnel is ready to be run, the user flips a switch in the control software, this valve switches, the gap evacuates, and the diaphragms burst. This automated system is much easier to use and also more reliable.

### 3.3 Probe Traverse

The hot wire is mounted on a Parker Square Rail Positioner that is driven by a Parker stepper motor (Figure 3.4) [59]. The hardware is controlled by Parker Compumotor Motion Planner software running on an attached PC. A Fortran script was obtained from Erick Swanson to create the series of instructions for Motion Planner to move the probe. When the oscilloscope triggers from the drop in diffuser pressure, it sends a signal to the Motion Planner software to execute the program.

When the traverse was originally installed, a Renishaw Model RGH22 X30F00 linear encoder was attached to the square rail positioner, the first step towards enabling the measurement of the traverse probe’s location with 1- $\mu\text{m}$  precision. Unfortunately, developing a means to read and record the encoder’s output remained on the research group’s collective ‘to-do’ list for the eight years since 2002. During this time, a traversing probe’s location was predicted by assuming it followed accurately the

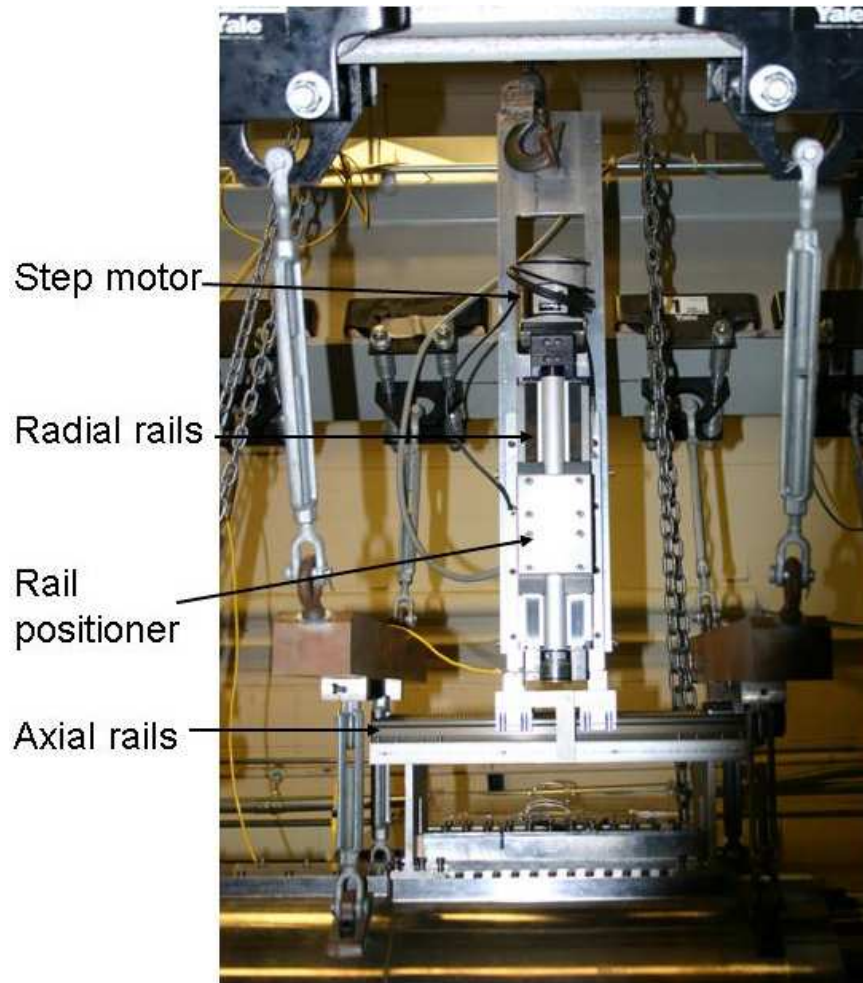


Figure 3.4.: Probe traverse

Motion Planner instructions. Accounting for the finite acceleration and deceleration of the motor proved tedious, especially for hot-wire profiles incorporating numerous short segments.

At the author's request, John Phillips researched what additional equipment was necessary to complete the traverse position measurement system. He chose a Laurel Electronics, Inc. Laureate Quadrature Encoder Position & Rate Meter model number L61010QD, Box1 [60]. The output of the quadrature reader is logged by one of the oscilloscopes commonly used with the BAM6QT. The hot-wire mass flux profiles measured on the HIFiRE-5 were the first use of this new hardware.

### 3.4 Tektronix Oscilloscopes

All data except for the temperature-sensitive paint images were recorded on Tektronix oscilloscopes in Hi-Res mode. When an oscilloscope is set to Hi-Res mode, it samples at its highest rate (1 GHz for a DPO 7054) then averages the data on the fly and saves it at the set sampling frequency, supplying 11-12 bits of resolution and digital filtering. Two Tektronix DPO 7054, one TDS 7104, and one TDS 5034 were used depending on availability. The DPO 7054 oscilloscopes have 50 Mb of memory per channel, enabling 5 MHz sampling of the PCB sensors for a 10-s run. Typically, lower sampling rates of 200 kHz–2 MHz were used to ease file storage difficulties. The thermocouples and heat-transfer gauges were sampled at 50–100 kHz because they have a slower time response and benefitted from additional averaging to reduce noise (Chapter 7).

The oscilloscopes were set to record ten seconds of data. The drop in pressure detected by a Kulite pressure transducer in the diffuser was used to set  $t = 0$ , the beginning of the run. The drop of the diffuser pressure as the diverging portion of the nozzle evacuates is very good for triggering oscilloscopes because it is rapid and large. Additional oscilloscopes were triggered from the first using the auxiliary output and input channels. One second of pre-run data was saved as a reference for electronic noise.

## 4. THE BOEING/AFOSR MACH-6 QUIET TUNNEL — PERFORMANCE

### 4.1 Flow Conditions

The stagnation pressure decreases quasi-statically during the run as the expansion wave reflects back and forth within the driver tube, dropping to about 70% of its initial value after 5 s [47]. The stagnation temperature at the beginning of each run is nominally 433 K. Like the stagnation pressure, the stagnation temperature decreases quasi-statically during the run to 400 K after 5 s [61,62].

For  $M = 6.0$ , a stagnation pressure of 1030 kPa, and a stagnation temperature of 433 K, the corresponding static temperature is 52.8 K and the unit Reynolds number is  $11 \cdot 10^6$  /m. Sutherland's Law based on the freestream static temperature was used to compute the dynamic viscosity  $\mu$  of air (Reference 12, Table 1-2):

$$\mu = 1.716 \cdot 10^{-5} \cdot \left( \frac{T}{273} \right)^{3/2} \cdot \frac{384}{T + 111} \quad (4.1)$$

with units of kg/(m·s) (or equivalently Pa·s or N·s/m<sup>2</sup>), where  $T$  is in Kelvin. The viscosity was found to be  $3.42 \cdot 10^{-6}$  kg/(m·s).

Sutherland's Law is of dubious accuracy at these low temperatures (Ref. 12 states  $\pm 2\%$  error down to 170 K and no estimate for lower temperatures). The  $Re$  values presented herein are limited to two or three significant digits because of the acknowledged error in viscosity. The trends observed as a function of  $Re$  should be unaffected by these errors because the same method was used to calculate all BAM6QT Reynolds numbers. A recent formulation of the viscosity by Lemmon and Jacobsen and computed for conditions in the BAM6QT by Gilbert shows  $\mu = 3.6 \cdot 10^{-6}$  kg/(m·s) when

extrapolated to this temperature, which is 5–6% higher than the value obtained from Sutherland’s Law [63, 64].

The changing stagnation conditions during the run result in a unit Reynolds number sweep down to about 80% of its initial level after 5 s.  $M = 6.0$  was assumed for quiet-flow Reynolds number calculations and  $M = 5.8$  was used for noisy-flow calculations. The Mach number is higher under quiet flow because the laminar nozzle-wall boundary layer is thinner, increasing the effective area ratio between the test section and the throat. The Mach number decreases slightly during the run as the stagnation pressure decreases and the nozzle-wall boundary layer thickens [49].

The stagnation pressure was measured during every run by a Kulite pressure transducer flush-mounted on the wall at the inlet of the BAM6QT contraction, where the Mach number is low so the static and stagnation pressures are essentially equal. The initial stagnation temperature, measured by a thermocouple on the driver tube centerline extending from its upstream end, was typically  $433 \pm 4$  K. This sensor location is not ideal for measuring the temperature of the air entering the nozzle because it is at the far end of the driver tube, but a sensor at the downstream end of the driver tube would disrupt the air entering the nozzle and threaten to increase the noise level. The isentropic relation

$$T_0(t) = T_{0i} \cdot \left( \frac{p_0(t)}{p_{0i}} \right)^{\frac{\gamma-1}{\gamma}} \quad (4.2)$$

was used to compute the stagnation pressure during the run, where  $T_{0i}$  was assumed to be 433 K and  $p_0(t)$  was measured by the contraction Kulite (equation 7.32 in Reference 65). The static temperature was calculated from the stagnation temperature as derived above and the assumed Mach number:

$$T(t) = T_0(t) / \left( 1 + \frac{\gamma-1}{2} \cdot M^2 \right) \quad (4.3)$$

## 4.2 Nozzle-Wall Boundary-Layer Separation

During every run, the uncalibrated output from a hot-film array on the nozzle wall is recorded in order to verify whether the flow is noisy, quiet, or separated [47,49,55,56]. The hot-film array is mounted on one of the test section small window inserts (Figure 4.1). The output of hot films located 1.89 and 2.07 m downstream of the tunnel throat were recorded. The hot films are controlled by Bruhn-6 Constant Temperature Anemometers built at Purdue.



Figure 4.1.: Hot-film array installed in Section 8. View from upstream. Ref. 56

A pitot probe in the test section is nominally a better instrument for measuring flow quality, but unlike the hot-film array, the pitot probe cannot be used at the same time as testing a model because of the probe's interference. Figure 4.2 compares nozzle-wall hot-film data with measurements by a pitot probe mounted on the tunnel centerline. The hot film was located 1.89 m from the throat. The centerline pitot was 2.38 m from the throat, with an acoustic origin  $\approx 1.7$  m from the throat. The initial stagnation pressure, 1100 kPa, was greater than the maximum quiet pressure at that time (1010 kPa in September 2006). This figure illustrates the agreement



between the instruments identifying startup, noisy flow (0.2–1.1 s), quiet flow (1.1–7.1 s), shutdown (7.1 s), and turbulent bursts (several during the first 0.2 s of quiet flow, then five more at 2.8, 3.7, 5.2, 5.4, and 5.6 s). Note that the hot films show 0.2-V variations that do not register on the pitot away from the wall.

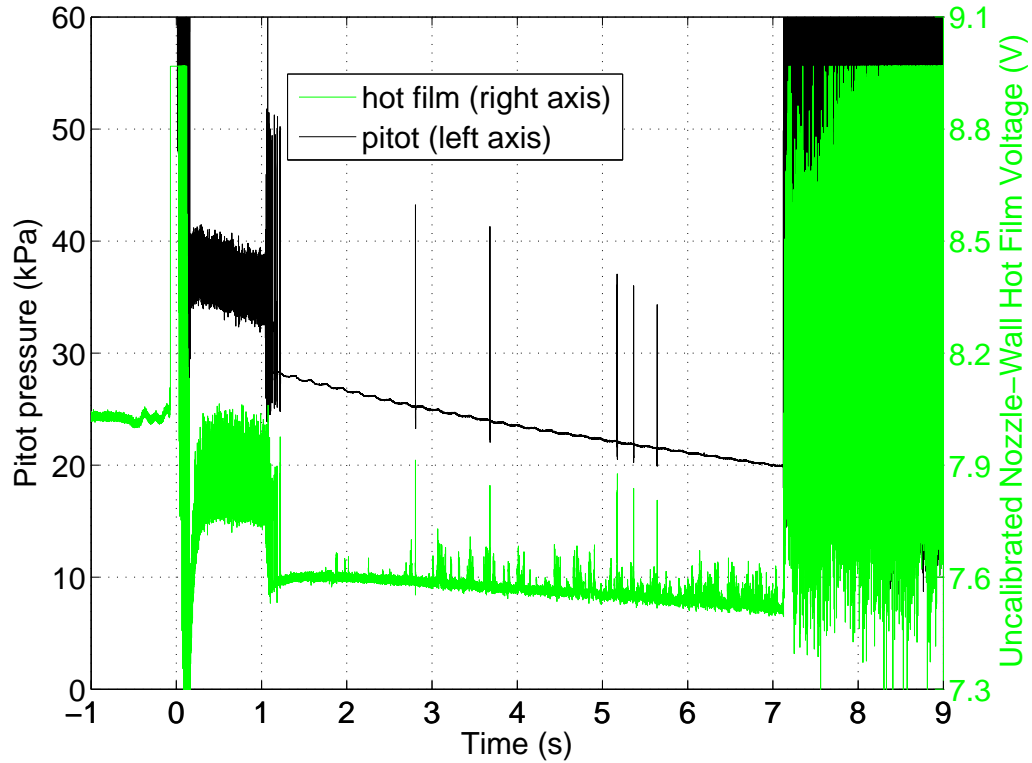


Figure 4.2.: Comparison of centerline pitot pressure (2.38 m from throat) and nozzle-wall hot film (1.89 m from throat). Empty test section except for pitot probe.

Originally, the model was designed to be at 35% scale, resulting in a base area of  $89.7 \text{ cm}^2$ . This is slightly more than the  $81.1 \text{ cm}^2$  base area of 4.0 in.- (101.6 mm-) base-diameter slender cones that commonly run in the BAM6QT. The model scale was subsequently increased to 38.1% scale to match the LaRC model (see Chapter 5). The base area is thus  $106.3 \text{ cm}^2$ , which is smaller than the  $153 \text{ cm}^2$  base area for 5.5 in.- (139.7 mm-) base-diameter slender cones that are used on occasion. However, the major axis length of 164 mm exceeds the diameter of the larger cones. It was thus a possibility that the model would have difficulty starting in the BAM6QT.

Improving the ability of the BAM6QT to start with larger models is an area of ongoing work [54, 66]. For the first HIFiRE-5 tests, the pipe insert was installed in the new sting-support section with no gap between the insert and the test section. Previous tests have shown that this configuration is successful for slender models [50]. The quiet-flow run duration with the pipe insert installed was 2–4 s — much less than the 8–10 s typical with the original sting-support section and diffuser. In later tests, the pipe insert extension was installed in the diffuser. This modification extended the run time to  $6.0 \pm 0.2$  s when the contraction bleed valve was open (i.e., for quiet-flow testing) and  $> 9$  s when the bleed valve was closed. With the exception of Figure 6.25 in Section 6.3.5, all HIFiRE-5 data presented herein is with the pipe insert extension installed.

The set of conditions most likely to result in a separated nozzle-wall boundary layer is quiet flow at low pressure and the model at higher angle of attack. Hannon found that larger blunt models would start under quiet flow than under noisy flow, perhaps because of the larger core flow with a thinner laminar nozzle-wall boundary layer [50, 54]. However, in this author’s experience, slender models at  $\alpha = 0\text{--}8^\circ$  have never separated under noisy flow, only quiet flow [47, 49]. Quiet flow is more likely to separate because the laminar nozzle-wall boundary layer that makes quiet flow possible separates more readily than a turbulent boundary layer [65]. Lower pressure corresponds to thicker boundary layers and an increased possibility of disturbances traveling upstream in otherwise supersonic flow. A higher angle of attack results in a greater shock angle and higher pressure increase across the shock; increasing the strength of an adverse pressure gradient also increases the threat of separation.

Figure 4.3 is representative of nozzle-wall hot-film data for the HIFiRE-5 with the pipe insert and pipe insert extension installed. The test conditions for this run were: quiet flow (except during separation), nominal  $M = 6.0$ ,  $\alpha = 4^\circ$ ,  $Re_i = 12.1 \cdot 10^6$  /m,  $p_{0i} = 1130$  kPa, and  $T_{0i} = 433$  K. This stagnation pressure was slightly less than the BAM6QT maximum quiet pressure. The run begins at  $t = 0$  s and startup lasts 0.3 s. There are 0.3 s of quiet, attached flow after startup for  $t = 0.3\text{--}0.6$  s. The jump

(up or down) in hot-film voltage during  $0.6 < t < 2.0$  s is indicative of separation on the nozzle-wall boundary layer (see References 49 and 47 for a discussion of hot-film interpretation). Thereafter the flow reattaches until the run ends at  $t = 6.1$  s. Several turbulent bursts pass through the nozzle and are detected by the hot films — 18 in the 4 s after reattachment, plus two during separation. No effect of these turbulent bursts is observed in TSP data, but PCB sensor power spectra over a window containing a burst show high-power broadband noise (see Chapter 8). Apart from the 18 turbulent bursts, which correspond to hot-film voltage spikes of 0.4–0.5 V, there are lower-voltage ( $\approx 0.2$  V) fluctuations after reattachment. Based on the pitot probe data described above (Figure 4.2) and the lack of effect on PCB power spectra, those 0.2-V variations are ignored, and the flow is thought to be quiet.

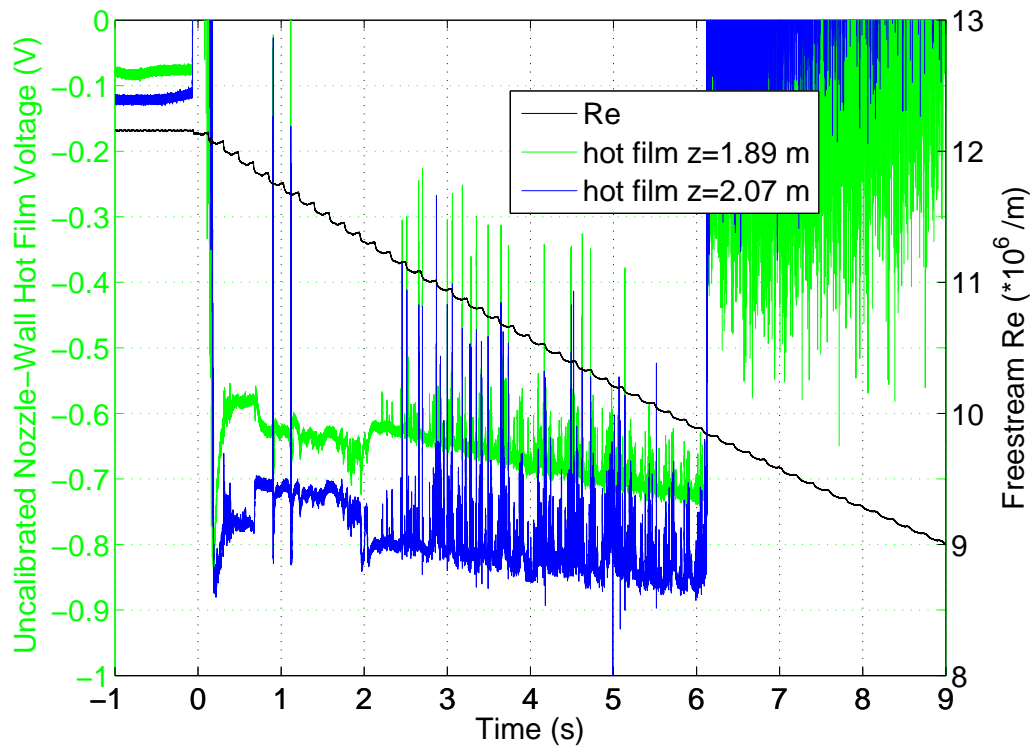


Figure 4.3.: Hot-film traces indicating attached and separated flow on the nozzle wall. Quiet flow, nominal  $M = 6.0$ ,  $\alpha = 4^\circ$ ,  $Re_i = 12.1 \cdot 10^6$  /m,  $p_{0i} = 1130$  kPa,  $T_{0i} = 433$  K

### 4.3 Extent of Quiet Flow

A careful characterization of the quality, extent, and uniformity of quiet flow in the BAM6QT test section has not been conducted since quiet-flow operation at high freestream Reynolds number ( $Re > 10.7 \cdot 10^6$  /m,  $p_0 > 1000$  kPa) was achieved in September 2006. Prior to the entry into service of the polished electroform nozzle with recut elliptical bleed lip, nozzle-wall boundary-layer transition appeared to result from a bypass mechanism far upstream in the nozzle [49]. This conclusion was drawn because pitot probe measurements indicated that the maximum quiet pressure was independent of axial location. The transition mechanism that applied to the original flawed electroform nozzle and surrogate aluminum nozzle is not necessarily the same for the improved nozzle, especially considering that the improvements were directed against bypass transition [48, 67, 68].

Measuring the extent of the quiet-flow test core is a special concern for the HIFiRE-5 because it was far back in the test section to inhibit separation and its semi-major axis was larger than the radius of most models typically run in the tunnel (82 mm, compared to 70 mm for a large circular cone). The radius at the exit of the test section is 120 mm, so the model is as close as 38 mm to the tunnel wall (at  $x = L = 328$  mm,  $y = a = 82$  mm). The acoustic origin of the flow at this location is only 0.22 m upstream from the model base (2.28 m downstream from the tunnel throat). For comparison, the acoustic origin of the model tip is 1.47 m from the throat. It is thus a distinct possibility that the noise level near the tunnel centerline would be low (with its origin upstream of nozzle-wall boundary-layer transition) while the back of the model is exposed to high noise radiated from a turbulent boundary layer.

Laura Steen is working on describing and improving the BAM6QT performance for her forthcoming master's thesis [69]. The full report is not yet available, but she provided some preliminary measurements with a pitot-mounted Kulite sensor. Amongst the data she collected were some pitot-mounted Kulite measurements made

2.38 m from the throat, 76 mm below the centerline. The tunnel test section was empty except for the pitot. The short 38-mm- (1.50-in.-) diameter cone ('spike') was installed in the sting mount. Figure 4.4 shows the pitot pressure (black line, left axis) and noise level (red diamonds, right axis) as a function of time during the run. For this run, the contraction bleed was open, so the flow is nominally quiet with  $M = 6.0$ , and the conditions at  $t = 0$  s were  $Re_i = 11.9 \cdot 10^6$  /m,  $p_{0i} = 1090$  kPa, and  $T_{0i} = 430$  K.

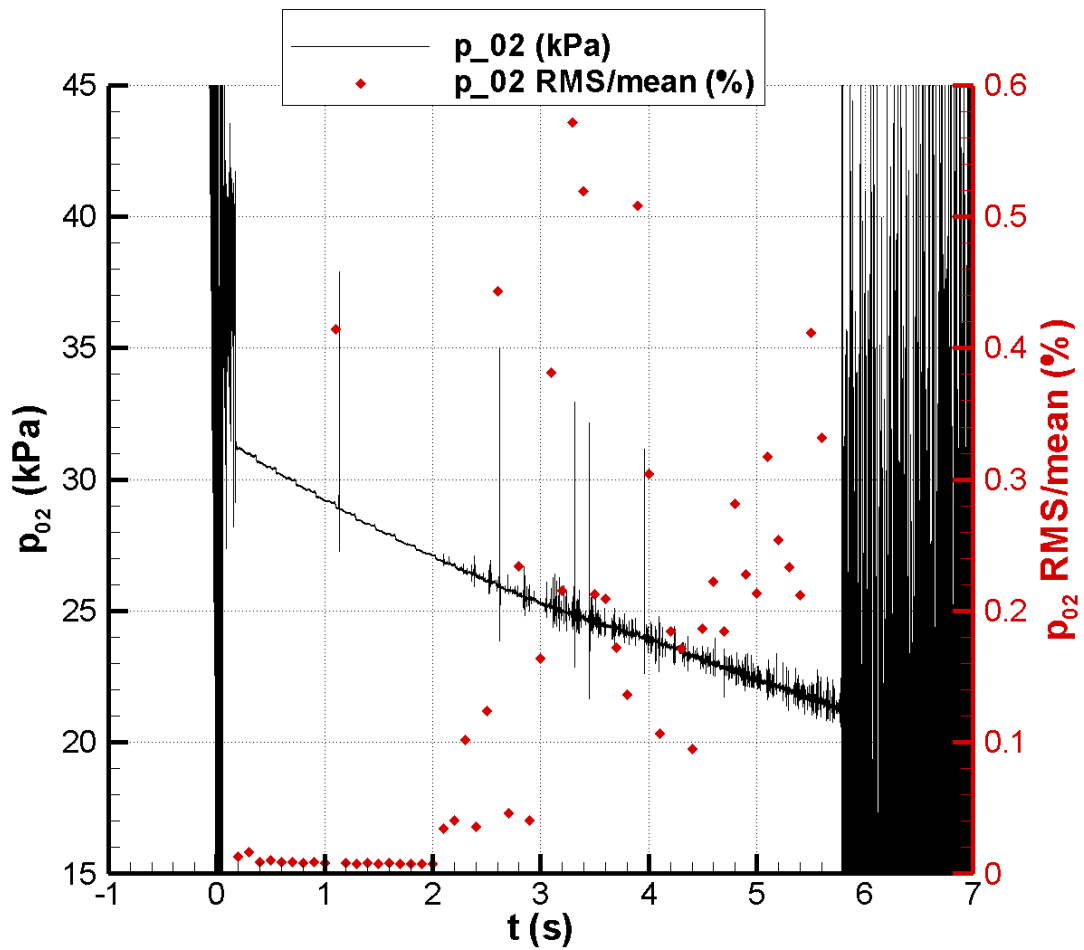


Figure 4.4.: Pitot-mounted Kulite. 2.38 m from the throat, 76.2 mm below the centerline. Contraction bleed open, nominal  $M = 6.0$ ,  $Re_i = 11.9 \cdot 10^6$  /m,  $p_{0i} = 1090$  kPa,  $T_{0i} = 430$  K

Except for a turbulent burst, the first two seconds of this run demonstrated a noise level of 0.01%, well below the quiet threshold of 0.06% [70]. This result suggests that the nozzle-wall boundary layer was laminar at least to the acoustic origin of this probe, 0.26 m upstream of its tip, 2.12 m from the throat. The noise level detected by the pitot probe increases for  $t > 2$  s, however. The change is plainly visible in the pitot trace and results in noise levels of 0.04–0.6%.

The cause of the elevated noise is unclear. There are some instances of the nozzle-wall boundary layer becoming turbulent during a run (for example, Figure 14 in Reference 47). However, this pitot pressure trace does not resemble the typical result encountered previously in the BAM6QT for turbulent boundary layers, which indicate higher pitot pressures and noise levels of 1–3% instead of 0.1–0.6%. For these reasons, it does not appear that the increased noise is due to turbulence on the nozzle wall. It remains a possibility that the boundary layer is transitional, but that would be surprising because the nozzle-wall boundary layer is less likely to transition during the run as the stagnation pressure and freestream unit Reynolds number decrease.

Another more likely explanation is that some sort of disturbance is feeding forward. The flow in the new sting-support section and diffuser is even less well understood than that in the original diffuser. Naiman et al. evaluated the redesigned diffuser using CFD, but these results are of limited usefulness because they simulate a model mostly located in the sting-support section, far downstream of its typical location in the test section [71]. Furthermore, they model the new sting-support section without the pipe insert that is now typically in use. Skoch found that disturbances in the original diffuser could feed upstream into the nozzle [55, 56, 72], and similar behavior is plausible for the new one. This explanation accounts for the increased disturbances later in the run — as  $Re$  decreases, the subsonic portion of the boundary layer thickens, enabling flow disturbances to propagate further upstream. More work is needed to understand and predict the performance of the new diffuser.

Based on these pitot measurements, it appeared that the flow near the wall (76 mm from the centerline, 44 mm from the wall) and far downstream (2.38 m from the

throat) in the test section may be quiet at high Reynolds number (as it is for  $t \leq 2$  s) or it may not be. Running TSP and other experiments with a pitot probe installed at the same time is not desirable because the added blockage would compound the nozzle-wall boundary-layer separation problem and because the probe's wake would disrupt the flow over the model.

As described in the previous section, the nozzle-wall hot-film array is a typical choice for non-intrusive measurement of the BAM6QT flow quality. Figure 4.5 contains the uncalibrated hot-film traces collected during the run shown in Figure 4.4. The hot films show a few small spikes starting at  $t = 2$  s and a slightly bigger noise increase at  $t = 3$  s. Perhaps these weak indications in the hot film are related to the noise increase at  $t = 2$  s detected by the pitot located near the wall at the downstream end of the nozzle, as shown in Figure 4.4.

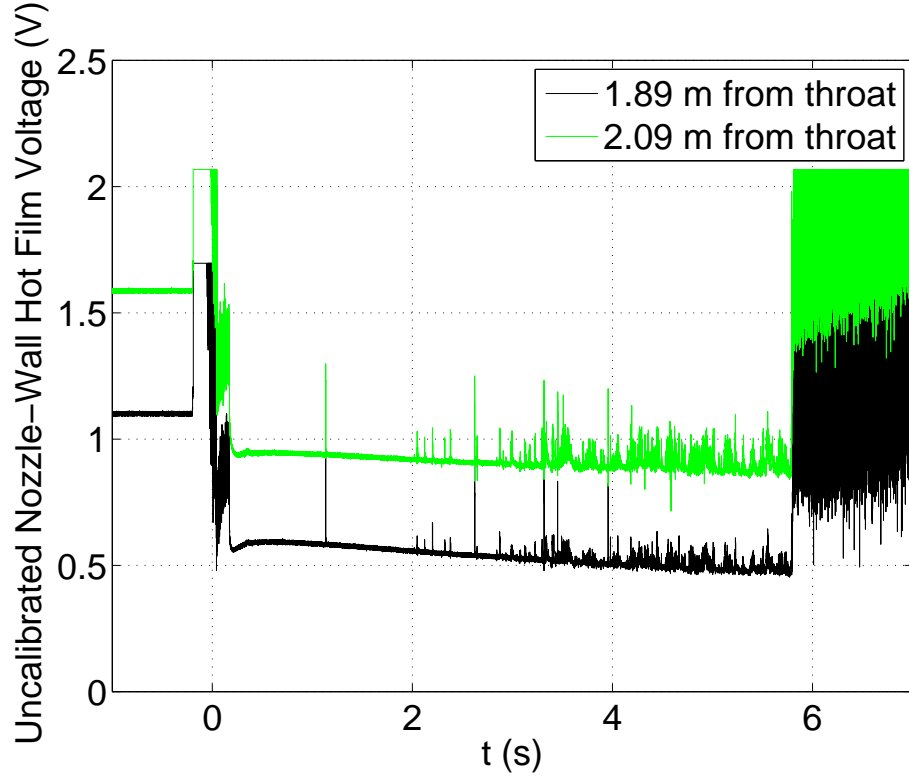


Figure 4.5.: Hot-film traces for run in Figure 4.4. Contraction bleed open, nominal  $M = 6.0$ ,  $Re_i = 11.9 \cdot 10^6 / \text{m}$ ,  $p_{0i} = 1090$  kPa,  $T_{0i} = 430$  K

There is evidence that the problem can be seen in the temperature-sensitive paint (TSP) data. The TSP instrumentation and data reduction is described in detail in Section 6.1. Figure 4.6 shows two TSP images from a run that demonstrated a transient flow quality issue. At  $t = 0.65$  s after startup, the lower corner of the model shows a temperature increase, presumably due to transition on the model boundary layer (Figure 4.6a). A similar increase is not observed on the upper corner. Later, at  $t = 2.8$  s, the image is essentially symmetric, as expected (Figure 4.6b).

The white rectangle superimposed on the TSP shows the location of the pitot probe used to take data shown in Figure 4.4 relative to the HIFiRE model. Note that the pitot Kulite and TSP data are from different runs. No pitot was installed with the HIFiRE-5 model, and no model was installed when the pitot data were collected. The initial flow conditions for the run shown in Figure 4.6 are  $Re_i = 10.4 \cdot 10^6$  /m and  $p_{0i} = 970$  kPa. These values are about 12% lower than for the run shown in Figures 4.4 and 4.5. It appears that the pitot would be in position to detect whatever flow disturbance led to transition on that corner of the model. The pitot data showing intermittent noise near the wall may well be connected to the occasional hot corner appearing in the TSP, which otherwise remains a mystery.

Figure 4.7 shows the hot-film traces for the run in Figure 4.6. There is nozzle-wall boundary-layer separation for  $t = 0.7$ – $2.1$  s. The hot films show less noise at  $t = 0.65$  s, where the TSP indicated transition on a portion of the model, than at  $t = 2.80$  s. This result suggests that the nozzle-wall hot films may not be suitable for identifying this particular flow quality problem, perhaps because it arises well downstream of the hot films.

The pitot data indicated quiet flow initially, then higher noise later. HIFiRE-5 TSP tests showed the opposite: some sort of flow disruption early but not later, segregated by separation of the nozzle-wall boundary layer. The presence of a model in the test section, the resulting separation, and the slightly different flow conditions could account for the different chronology. On the other hand, perceiving the pitot and TSP data as symptoms of the same problem may be misguided.



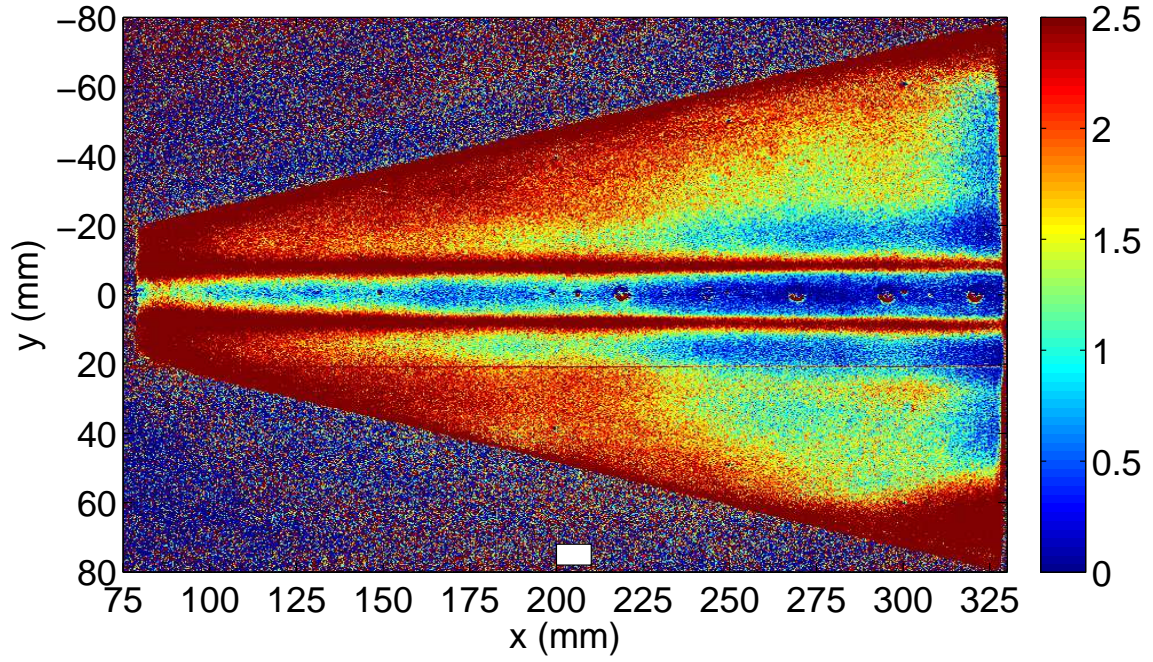
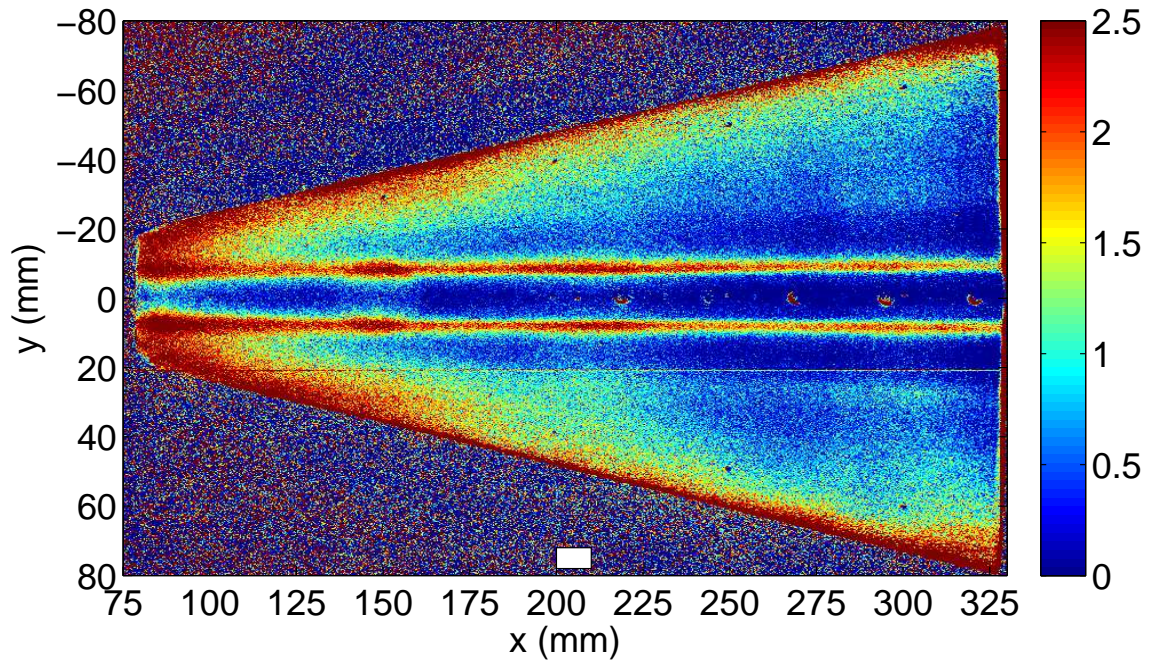
(a)  $t = 0.65$  s(b)  $t = 2.80$  s

Figure 4.6.: Impact of flow quality on TSP results. Contraction bleed open, nominal  $M = 6.0$ ,  $\alpha = 4^\circ$ ,  $Re_i = 10.4 \cdot 10^6$  /m,  $p_{0i} = 970$  kPa,  $T_{0i} = 432$  K

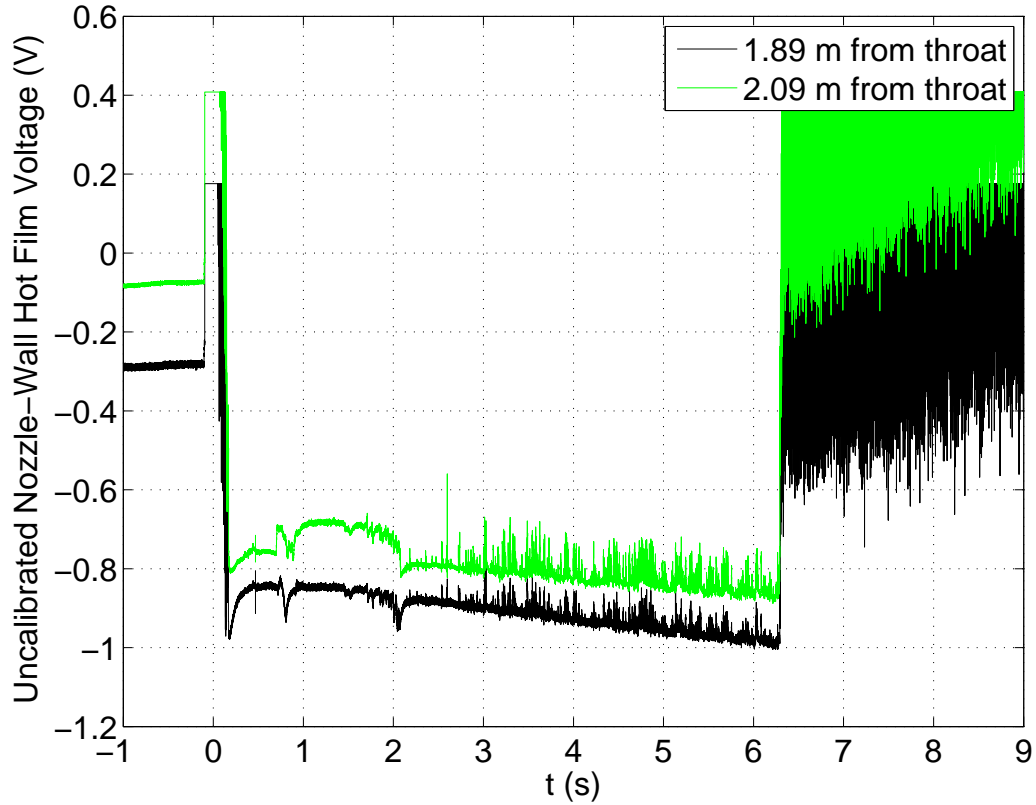


Figure 4.7.: Hot-film traces for run in Figure 4.6. Contraction bleed open, nominal  $M = 6.0$ ,  $Re_i = 10.4 \cdot 10^6 / \text{m}$ ,  $p_{0i} = 970 \text{ kPa}$ ,  $T_{0i} = 432 \text{ K}$

This disruption was observed in approximately one-third of quiet-flow runs and sometimes was visible even after reattachment. For example, Figure 6.21 contains several images from late in the run ( $t = 3.0\text{--}4.2 \text{ s}$ ). These frames were selected because the hot corner existed immediately after reattachment and only decreased after another 1–2 s.

It is proposed that a disturbance occasionally develops far downstream in the nozzle. A pitot Kulite near the wall (with a far downstream acoustic origin) can detect it and indicates a higher noise level as a result. This higher noise level equates to the end of the quiet-flow test core. The higher noise leads to transition on the HIFiRE-5, which is detected by TSP. Seeing and avoiding the data corrupted by the

higher noise level appears to be a simple and effective means of dealing with this disturbance.

However, it is also possible that this far-downstream disturbance affects the model boundary layer in a subtler way. Perhaps the transition that is observed under nominally quiet flow (contraction bleed valve open and stagnation pressure less than the maximum quiet pressure) is in fact promoted by higher noise levels that may be present on the downstream ends of the model. *Thus, the quiet-flow transition results should be regarded as under ‘presumed’ or ‘nominally’ quiet flow.* Further experiments with additional hot films farther downstream in Section 8 and the sting-support section are recommended to allay flow quality concerns for almost all BAM6QT projects.

## 5. HIFIRE-5 MODEL

The HIFiRE-5 model tested in the BAM6QT was designed by the author during May–July 2008 to match the geometry provided by Dr. Roger Kimmel, the HIFiRE-5 principal investigator. The scale of the model tested in the BAM6QT was chosen to be 38.1% to match the model tested at the NASA Langley Research Center. Only the first 861 mm of the full-scale vehicle is modeled (model length  $L = 328$  mm). The full vehicle has an elliptical-to-circular adapter at this location to fair the elliptic cone to the 355.6-mm-diameter sounding rocket, but this portion is omitted from the BAM6QT model so that the model was not too long for the test section. The base semi-major axis is 82 mm, the base semi-minor axis is 41 mm, the length from nosetip to base is 328 mm, and the nosetip radius along the minor axis is 0.95 mm. When the preliminary design was completed, it was sent to Tri-Models, Inc. of Huntington Beach, CA for final design and fabrication. The model was completed in December, 2008. Appendix B contains the final drawings provided by Tri-Models.

Many previous models studied with temperature-sensitive paint in the BAM6QT have been fabricated with nylon in the regions where TSP is applied, whereas the HIFiRE-5 model has an aluminum frustum. Nylon provides superior insulation, resulting in higher temperature change and a better signal-to-noise ratio. However, it is more difficult to calculate heat transfer for the nylon model than for a thin insulator on aluminum [73]. Aluminum has several other advantages over nylon — it is more dimensionally stable for varying temperature, fewer mating parts need to be machined and assembled, thermocouples can more nearly match its thermal properties, etc. For these reasons, 7075T6 aluminum was chosen for the frustum.

The model has numerous features that allow testing for different configurations and several sensors (Figure 5.1). The flight vehicle will have a break between the nosetip and frustum at approximately  $x = 200$  mm. Thermal expansion at this loca-

tion could potentially create roughness that would trip the boundary layer. Differential ablation could create a similar effect, but the HIFiRE-5 will not be hot enough to exhibit this phenomenon. Thus, the model was designed with a 76.2-mm-long nosetip (38.1% of 200 mm) that can attach to the frustum forming backward- and forward-facing steps. Steps along the major and minor axes can be created. Spacers in 1-mm increments are included with the model. A maximum step of 2 mm along the major or minor axis can be accommodated. The nosetip and the cover that allows access to the nosetip/frustum attachment are fabricated from 15-5 stainless steel.

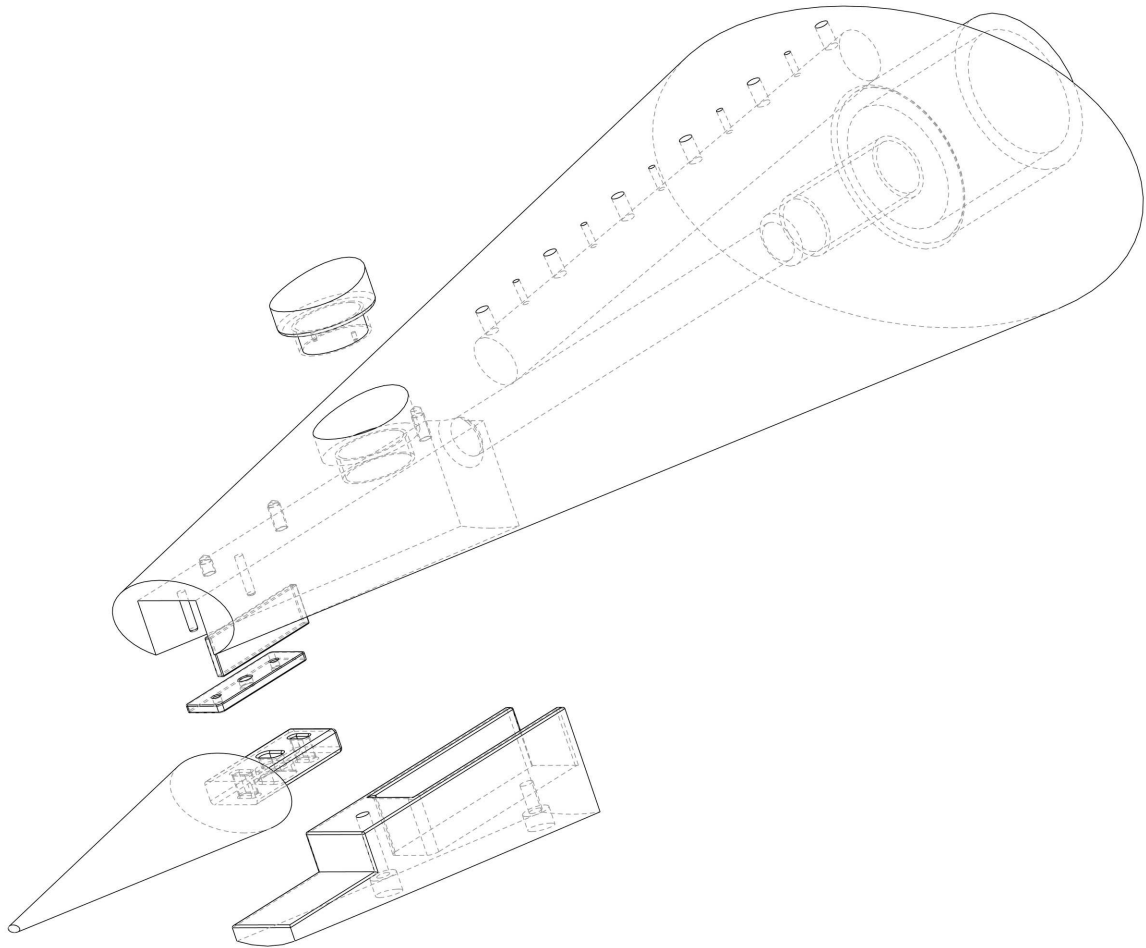


Figure 5.1.: Exploded assembly drawing of HIFiRE-5 model

A glow perturber can be installed on the centerline at  $x = 150$  mm. A blank plug made of 15-5 stainless steel occupies the 24-mm-diameter port in lieu of a perturber. Access to the back side of the perturber is possible through the same hatch that permits nosetip adjustments. A 9.65-mm-diameter hole runs along the model axis for glow perturber wire access through a hollow sting.

Eleven sensor holes are on the centerline starting at  $x = 195$  mm. Their centers are evenly spaced in 12.5-mm increments (measured parallel to the model axis). The hole diameters alternate between 3.28 and 1.60 mm, starting with the larger diameter. The 3.28-mm-diameter holes are appropriate for 1/8-in.-diameter sensors such as PCB fast pressure sensors and Schmidt-Boelter heat transfer gages. The 1.60-mm-diameter holes fit 1/16-in.-diameter coaxial thermocouples and heat transfer gages. A 12.7-mm-diameter hole parallel to the model surface provides passage for the sensor leads out the back of the model. The wall thickness is reduced to 6.2 mm between the outer surface and the access hole. Dowel pins were used to plug the holes when sensors were not installed.

For most tests, three 1/8-in.- (3.2-mm-) diameter PCB model 132A31 pressure transducers were installed along the model centerline at  $x = 220$ , 270, and 320 mm (see Chapter 8) and a 1/8 in.- (3.2-mm) diameter Medtherm 8-2FSB-0.25-36-20835 Schmidt-Boelter heat transfer gauge was installed at  $x = 295$  mm (Section 7.2). When using PCB and Schmidt-Boelter gauges, blanks were installed in the model before applying the temperature-sensitive paint. Care was taken to ensure the blanks were as flush as possible with the model surface. After the painting was finished, these blanks were carefully removed and the PCBs and Schmidt-Boelter were installed. The goal was then to install the sensors flush with the paint. The sensors were secured with nail polish, which has been found to be a strong enough adhesive to keep the sensors in place, but easy enough (with careful application of acetone) to remove that the sensors are usually not damaged. The nail polish is also thick enough that it fills in the gap between the sensor and its surrounding sensor hole and paint, resulting in a smoother contour between the sensor and paint.

A Mitutoyo Surftest SJ-301 profilometer was used to measure the surface defect. Typical steps were 15–50  $\mu\text{m}$  between the model and sensor surface, with a gap of 100  $\mu\text{m}$  between the sensor side wall and its hole. The PCB faces cannot be contoured, so there is some deviation from the true surface shape. The sensor holes are normal to the model surface, not the model axis. The HIFiRE-5 model has no streamwise curvature and has 56-, 68-, and 88-mm radii of curvature in the spanwise direction at these locations. At the farthest upstream sensor, the deviation between the model centerline contour and sensor face is 20  $\mu\text{m}$ , and the difference is less for the farther-aft sensors where the radius of curvature is less.

A 50- $\mu\text{m}$  roughness is less than 2% of the boundary layer thickness predicted by CFD at this location for  $\alpha = 4^\circ$  (Section 2.2.2). Thus, the effect of the sensors on the flow is neglected in this report. However, the impact of these discrete roughnesses upon transition is not well understood and may have influenced these results. Attempted measurements of smooth(er)-wall transition using only coaxial thermocouples were unsuccessful, as described in Section 7.1. Measurements on the HIFiRE-1 in the BAM6QT by Casper et al. under quiet flow at similar freestream Reynolds numbers to these tests found that a 360- $\mu\text{m}$  roughness (height more than twice the boundary-layer thickness) did not lead to transition before the end of the model [23].

## 6. TEMPERATURE-SENSITIVE PAINT MEASUREMENTS OF TRANSITION

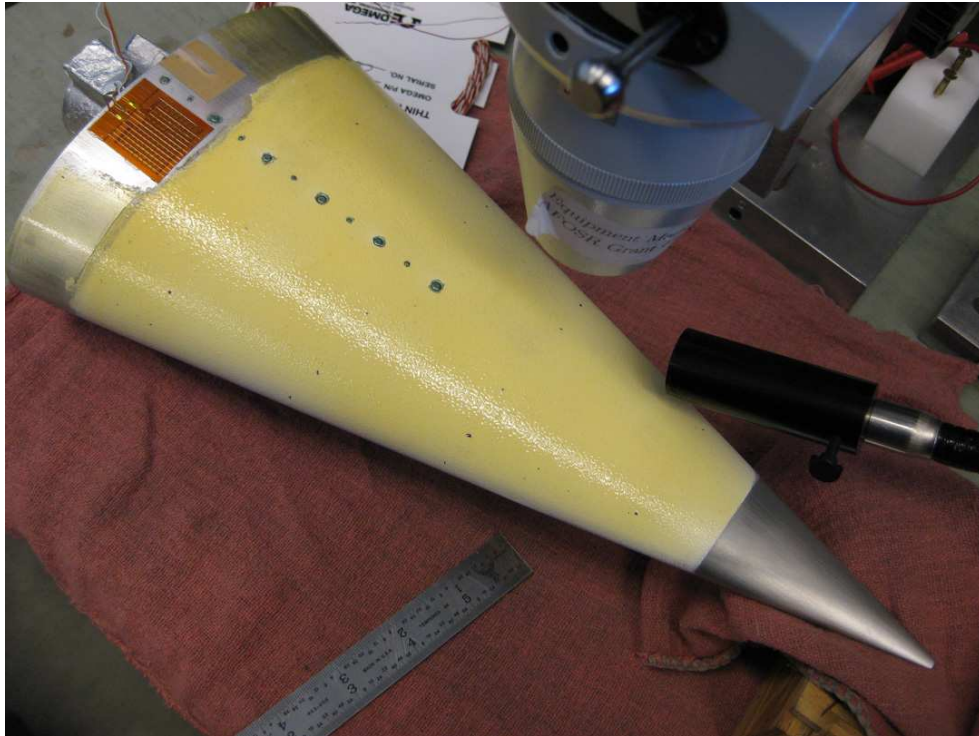
### 6.1 Instrumentation

#### 6.1.1 Paint and Insulator

Three different airbrush insulators and a fourth spray-paint insulator were tested on the HIFiRE-5. The first three were applied by Justin Rubal, a student working on temperature-sensitive paint (TSP) for Professor John Sullivan. The fourth was applied by the author with Justin's advice. Justin's help preparing the model for testing assisted the HIFiRE-5 project, and testing these insulator candidates provided him more opportunities to gather data for his TSP project.

The first insulator tested, in January 2009, was Industrial Nanotech Inc. (INI) Nansulate Home Protect Interior thinned with tap water. The first two attempts to apply this insulator were frustrated by poor adherence to the model. Continued adjustments to the paint/thinner ratio resulted in an insulator that would stick, but was not very smooth. The texture resembled that of an orange peel, a common problem for airbrushed paints (Figure 6.1). Time to prepare the model for the first tunnel entry was running low, so it was decided to continue with this substandard paint job. This insulator proved to be the roughest surface finish tested. Not realizing its significance, a measurement of the finish with the group's Mitutoyo SurfTest SJ-301 profilometer was not made. Photographs of the painted surface were taken through a microscope at  $40\times$  magnification (Figure 6.2). The left edge of the image is a ruler with lines engraved at  $1/64$  in. (0.397 mm) intervals. The bumps are spaced about 1 mm from one another and are roughly 0.2 mm high. See Section 6.3.5 for discussion of the effect of the orange-peel finish.





(a)



(b)

Figure 6.1.: Photographs of first TSP application showing ‘orange-peel’ roughness

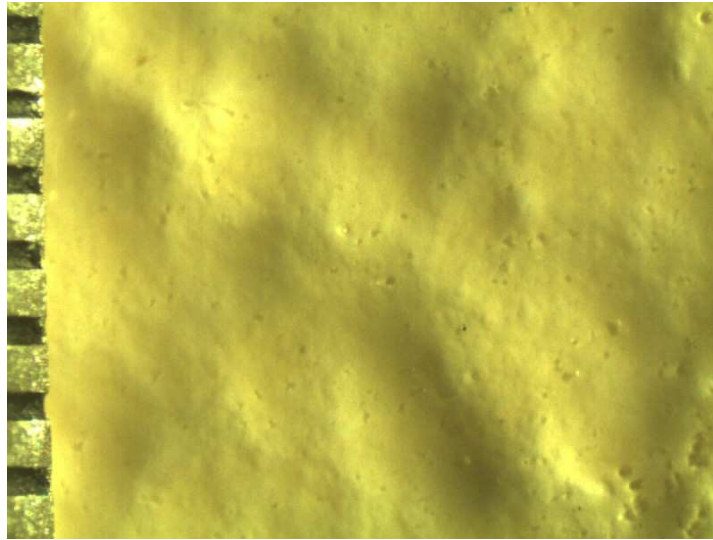


Figure 6.2.: Photograph of orange peel paint finish through microscope at  $40\times$  magnification. Left side of image shows a ruler with  $1/64$ -in. (0.397-mm) engravings. Individual bumps have  $\approx 1$ -mm spacing.

The second insulator was Hy-Tech Thermal Solutions ThermaCels insulating paint additive, used in March 2009. These particles were mixed into DuPont ChromaClear paint, the standard clear coat used in the lab for TSP. Unfortunately, the particles did not mix well into the ChromaClear and would begin to separate as soon as stirring stopped. The effect was that the insulator was somewhat heterogeneous (Figure 6.3). Splotches of higher or lower concentration of the additive were visible on the model even under the TSP. Furthermore, a mistake was made when allowing this paint to dry. While painting, the model was left upright (standing on its base), so that the airbrush was spraying onto a vertical surface. Rather than leaving the model in this orientation to dry, so that the paint pooled at the bottom, it was propped so that the windward ray was parallel with the ground. The result was a very smooth paint finish over most of the windward face, but lumpy rivulets of dried paint near the leading edges. Anticipating a substantial impact on transition of these 1–2-mm-high ridges, sandpaper, a razor blade, and acetone were used to fair the insulator onto the model as smoothly as possible. The final result was much smoother, but the leading edges were still somewhat ragged.



(a)



(b)

Figure 6.3.: Photographs of second TSP application showing heterogeneous insulator

Two tunnel entries in July and August 2009 used Sherwin-Williams Pro-Cryl acrylic primer airbrushed onto the model. This insulator had several good traits — it adhered well, did not bubble, and was smooth with uniform thickness. Unfortunately, its thermal conductivity is higher than desirable, so it does not insulate as well, resulting in relatively low signal-to-noise ratios.

The final and most effective insulator is Top Flite LustreKote spray paint. Three coats of the white primer were followed by three or four coats of the jet white top

coat. The spray paint is quicker and easier to apply than any airbrush formulation because no mixing is required beforehand and cleanup is trivial. Good uniformity is achieved after several even, thin coats (Figure 6.4). The thermal conductivity  $k$  is not as low as the best insulator (INI Nansulate) but much better than the worst (ThermaCels).

The TSP itself was a Ru(bpy) luminophore dissolved in ethanol and mixed into clear paint and applied by an airbrush. DuPont ClearCote was the original clear paint of choice, but it was discontinued by the manufacturer. BASF LIMCO LC4000 Clearcoat with LIMCO LHM hardener was selected as the replacement, but it seems to respond to pressure as well as temperature changes (see Reference 73 and Section 6.2 below).

### **Paint Roughness and Thickness**

The surface finish for the LustreKote spray paint was on par with the smooth portions of the ThermaCels and Pro-Cryl insulators. The profilometer found root-mean-square surface finishes of 0.17–0.42  $\mu\text{m}$  for the final TSP application on the HIFiRE-5. All TSP images reported herein except Figure 6.25b use this insulator. They all are regarded as having a ‘smooth’ finish.

The multiple layers of spray paint necessarily have some finite thickness. These layers consist of not only the TSP insulator but also several coats of the TSP itself. This thickness creates a forward-facing step at the front edge of the frustum. One option to mitigate this step is to paint the entire model, adding some thickness to the entire surface. Perhaps this thickness would have some variation, but at least there would be no discontinuities. This approach was considered for the HIFiRE-5, but was rejected because of the uncertain effect it would have on the nosetip geometry. The nosetip was machined carefully to be a 0.381 scale match of the true shape, and applying paint to this sensitive region would have an unknown influence on the BAM6QT results.





(a)



(b)

Figure 6.4.: Photographs of final TSP application on spray-paint insulator

Instead, the decision was made to paint only the aluminum frustum (and its inserts), leaving the steel nosetip unpainted. The thickness of the final TSP application (LustreKote spray paint plus TSP) was measured with gauge blocks and found to be 0.33 mm (0.013 in.). Until the final session of TSP data collection, this forward-facing step existed at  $x = 76.2$  mm. Before the final set of TSP data was gathered, fine-grit sandpaper was used to taper the upstream edge of the paint. The Mitutoyo profilometer was used to measure the step before and after sanding, but it proved to be ineffective for the steeper pre-sanded step because the profilometer's read head is too large and would be in contact with the surface instead of the needle. Spurious peaks, valleys, and slopes would appear in the profile depending on which part of the read head was actually in contact.

Figure 6.5 shows profiles of the forward-facing step at the nosetip/frustum junction. The pre-sanding profile (dotted line) is an estimate based on the initial slope determined by the profilometer and the paint thickness measured by the gauge blocks. The after-sanding profile (solid line) is the profilometer measurement. A side-by-side comparison of TSP data for these two step profiles is presented in Section 6.3.6.

Almost all TSP data presented in this report was collected with a relatively smooth paint finish. The only exception is Figure 6.25b, part of the Section 6.3.5 assessment of the effect of surface finish on transition. Most of the 'smooth'-finish data was collected with the tapered step. The data from high-pressure runs (any images through the porthole windows) were collected with the unsanded paint edge. Except for Figures 6.27a (which illustrates the negligible effect of the step) and 6.25b, all TSP images through the large window are with the tapered paint edge. All hot-wire and PCB data except for the high-pressure runs were also recorded with the 'smooth' finish and tapered edge. Table 6.1 summarizes the paint roughness for all the TSP data.

The Top Flite LustreKote spray paint has been used successfully for several subsequent TSP tests on various models [53]. Among the students in this research group, Chris Ward has the most experience applying this paint and found that the final

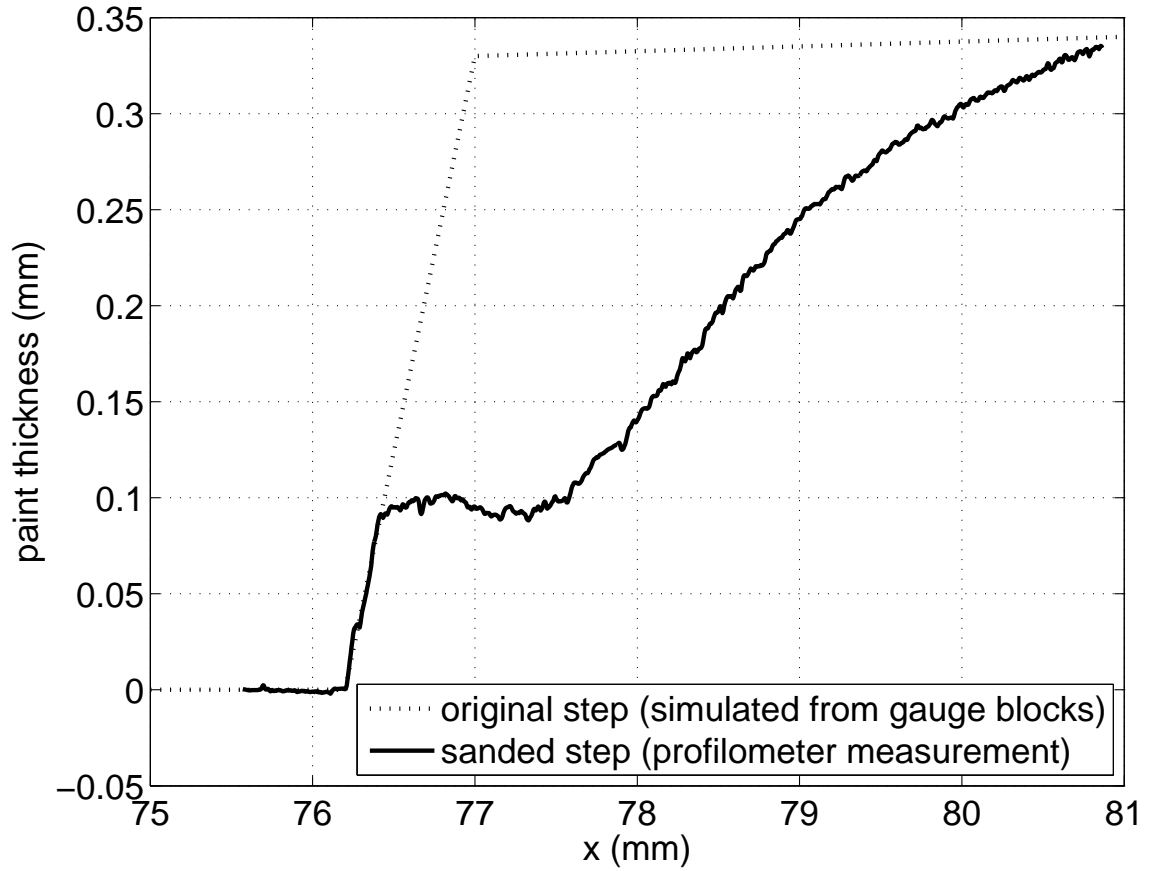


Figure 6.5.: Profile of forward-facing step at nosetip/frustum junction. LustreKote spray paint plus TSP

Table 6.1: Summary of paint roughness and step for TSP data

Figure	Surface Finish		Step
	Qualitative	Quantitative	
6.25b	orange peel	0.2-mm high lumps with 1-mm spacing	untapered
6.27a and all high-pressure ( $p_0 > 1050$ kPa)	‘smooth’	rms surface finish 0.17–0.42 $\mu\text{m}$	untapered
all others	‘smooth’	rms surface finish 0.17–0.42 $\mu\text{m}$	tapered

thickness over a model is typically within 15% of the mean, with the thickest build-up at the bottom [74]. He reports root-mean-square surface finishes of 0.25–0.38  $\mu\text{m}$ . The similarity of his finish to that on the HIFiRE-5 suggests that the TSP can be applied consistently and these results could be repeated.

### 6.1.2 Lights and Camera

The paint was excited by two blue (465 nm wavelength) light emitting diode (LED) arrays. Originally, a single Innovative Scientific Solutions, Inc. (ISSI) LMA LM4 array was employed. A second, more powerful ISSI LM2xLZ-465 LED array was subsequently acquired. Once the necessary water cooling lines were installed, the two LED arrays were employed together. The new LED array has significantly more brightness, enabling shorter exposure times and/or smaller apertures (yielding improved depth-of-field [75]). Using the two lights in conjunction also provided more uniform illumination and reduced shadows from the window frame that would otherwise obscure portions of the model.

$\text{Ru}(\text{bpy})$  is excited by blue light and fluoresces orange. Thus, an orange filter (556 nm wavelength high-pass) was used to limit the incident light entering the camera, leaving only the fluoresced output.

A Cooke Corporation PCO.1200 14-bit CCD camera controlled by CamWare software was used. Its array is nominally  $1600 \times 1200$  pixels, but  $2 \times 2$  binning was selected, reducing the image size to  $800 \times 600$  pixels. Binning reduces noise in the image and reduces the image size, allowing a faster frame rate with the limited transmission speed between camera and computer. Spatial resolution is reduced, but is still sufficient at 3.0 pixels per mm (0.33 mm per pixel) in streamwise and spanwise directions. When using the porthole window with the smaller field of view, the camera was moved closer and spatial resolution was 4.2 pixels per mm (0.24 mm per pixel).

Figure 6.6 is a photograph of the TSP hardware set up for the BAM6QT. The  $7 \times 14$  in. ( $0.18 \times 0.36$  m) plexiglass window is installed in the north large window



opening in the test section. The HIFiRE model is visible through the window. The camera (blue box) and one LED array (black cylinder) are in the foreground. The LEDs were placed on the optical bench as far as possible from the window (1.1 m) to maximize uniformity of the illumination. The camera was placed between them with a 50-mm-focal-length lens so that the model nearly filled the field of view.

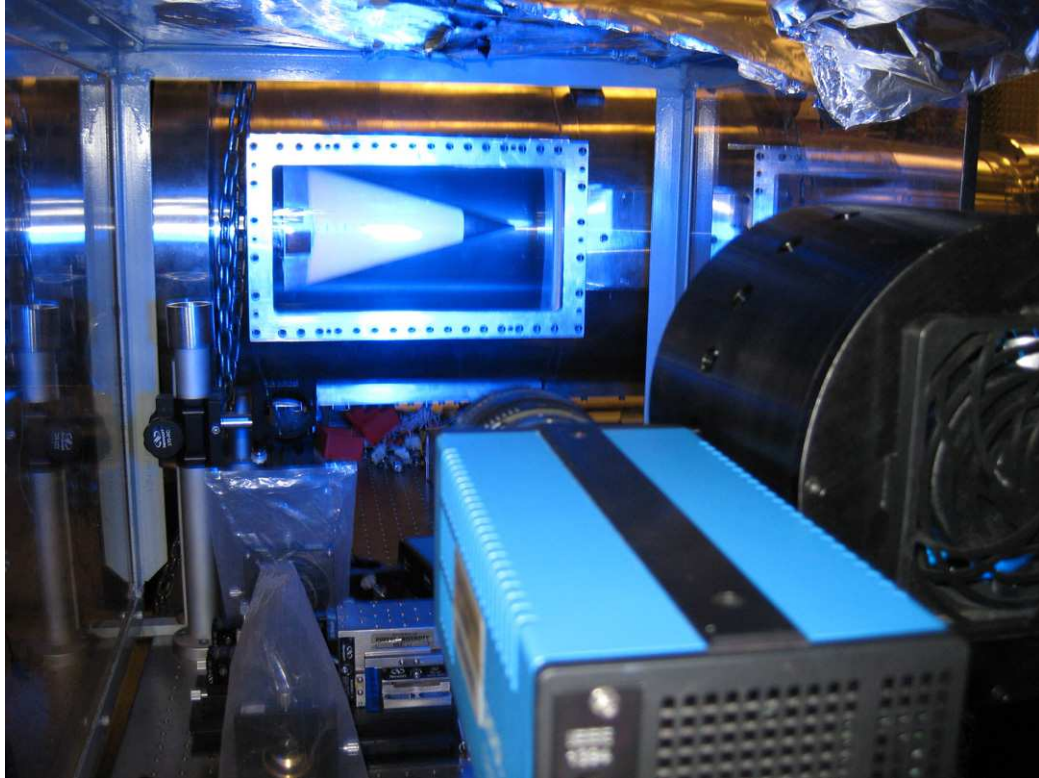


Figure 6.6.: Camera and light source setup in the BAM6QT with HIFiRE-5 model visible through big window

The large rectangular window has the obvious benefit that the entire model is visible. However, it is limited to a maximum working pressure of 950 kPa (138 psi) gauge, or 1050 kPa (153 psi) absolute. In the terminology of the BAM6QT research group, runs at  $p_0 > 1050$  kPa are regarded as ‘high-pressure’ because they require switching to porthole windows with a higher maximum allowable working pressure and using a boost pump to reach pressures in excess of the main air compressor’s  $\approx$

1000 kPa output [76]. The TSP images from the several high-pressure runs conducted have a limited field of view circumscribed by a circular window frame.

The exposure time was varied from run to run to fill most of the CCD's bit depth. The most common exposure was 10 ms, but it sometimes varied within  $\pm 2$  ms. These changes in the settings are not expected to affect the output temperature as long as the settings were consistent for the dark, flow-off, and flow-on images (see below). The camera was set to record at 20 Hz (near the maximum data transfer rate), starting with the run start. Ten frames recorded within a minute before the run were averaged and used as the flow-off image. The camera shutter-open signal was recorded on an oscilloscope to verify the camera frame rate.

## 6.2 Data Analysis Methodology

### 6.2.1 TSP Calibration

Temperature sensitive paint intensity ratios are proportional to the temperature ratio between the two images [77]. For each run, a 'dark' image was recorded with the LED array off. A few seconds before the run, the LED array was turned on and an image was recorded with the flow 'off'. Then during the run, 'on' images were recorded. The contour plots display the temperature difference between the 'on' and 'off' images:

$$\Delta T = T_{\text{on}} - T_{\text{off}} = f \left( \frac{I_{\text{on}} - I_{\text{dark}}}{I_{\text{off}} - I_{\text{dark}}} \right) \quad (6.1)$$

A thermocouple attached to the base of the model typically indicated  $T_{\text{off}} = 290$ – $320$  K (see Section 7.1). As discussed above, the insulator applied for these tests did not insulate as well as desired, resulting in low values for  $\Delta T$ . It is surprising that  $\Delta T < 0$  occasionally. Investigating this anomaly is another topic in Rubal's research. It appears that some batches of TSP are sensitive to pressure as well as temperature. When each tunnel run began, the paint intensity changed in response to the large pressure drop from stagnation to static. The static pressure also varies during a run,

but the change at startup is the larger effect. Rubal found that a +2–3 K correction to BAM6QT TSP data is in order (that is, if the TSP indicates  $\Delta T = 1$  K, the true  $\Delta T$  on which to base heat-flux computation is 3–4 K) [78]. Because the proper means of reducing TSP contours to heat flux has yet to be determined with confidence, uncorrected  $\Delta T$  is presented herein.

The TSP calibration was based on Figure 3.13 ‘Temperature dependencies of the luminescence intensity for TSP’ from Reference 77. A linear fit to the  $I/I_{\text{ref}}$  vs.  $T$  curve for Ru(bpy) between 15 and 60 °C (288–333 K) was computed. This approximation has the benefit of a simple implementation and is accurate over the temperature range encountered. The resulting calibration equation is:

$$\Delta T = (362 - T_{\text{ref}}) \cdot \left( 1 - \left( \frac{I_{\text{on}} - I_{\text{dark}}}{I_{\text{off}} - I_{\text{dark}}} \right) \right) \quad (6.2)$$

where  $T_{\text{ref}}$  is the wind-off (or pre-run) model temperature measured by the thermocouple on the model base with units of Kelvin. When the pre-run model temperature was unavailable, 310 K was used as an estimate because it is in the middle of the typical range. As is discussed in Section 7.1, several unsuccessful methods of attaching the base thermocouple were attempted before finding one that worked.

The scale of the temperature contour for each figure was adjusted to maximize the detail both before and after transition. Also, note that the insulator is not a factor in the TSP calibration. The properties of the insulator are required for calculation of the heat flux.

### 6.2.2 Image Registration

In order to properly find the TSP intensity ratio, the flow-on and flow-off images need to be aligned with one another. An ultra-fine-point Sharpie permanent marker was used to place registration marks on the painted model surface for reference when aligning the images. Placing the marks by hand is sufficient for registering images. This method was used for the first two paint applications. Later versions were instead

marked with the model mounted in a mill vise and the marker placed in the spindle. The precision afforded by the mill table's traverse enabled the marks to be used as reference points usually with 1-mm or less accuracy. A mistake was made mounting the model in the vise for the final set of registration marks and the marks nominally at  $y = 0$  are off by 1–3 mm in the spanwise direction. The error is evident because they do not align with the centerline sensors. The  $x$ -coordinate for these points is accurate.

Typically, only a small shift was needed to align the images (3 pixels or less). ISSI OMS Lite 1.2 Beta was used to register most of the images in this report. OMS Lite is labor-intensive, so only one frame per run was processed in this way. Matlab was used to pre- and post-process the data and was used to get a quick look at all frames for each run. Since the adjustments needed to register the images were so small, unregistered ratios still provide a clear image. The images were also flipped left-to-right so that the flow is from the left.

A 1/8-in.- (3.2-mm-) diameter Schmidt-Boelter heat transfer gauge is on the centerline at  $x = 295$  mm and three 1/8-in.- (3.2-mm-) diameter pressure sensors are on the centerline at  $x = 220, 270$ , and 320 mm. They are described in Chapter 8.

### 6.2.3 Transition Threshold

Transition onset was inferred from a temperature rise along the centerline. The centerline profiles presented in Section 6.3.3 were used in conjunction with the overall temperature contour plots. There was typically some variation in the temperature profile, so a simple search for the minimum temperature was not sufficient. The temperature rise at higher freestream Reynolds number tended to be steeper, whereas at low  $Re$  the rise might be very gradual with a greater uncertainty in transition location.

Figure 6.7 presents a typical TSP contour plot as well as the temperature profile along the centerline extracted from the global contour. The centerline trace enables

greater precision in finding streamwise location, but the TSP images are essential to identifying the effects of unpainted sensors and sensor blanks, registration marks, window frame shadows, and any other stray influences. To reduce noise in the data, the paint intensity was averaged within 3.5 mm (12 pixels) of the centerline. This width was chosen so that only the data between the off-centerline hot streaks were included. These spanwise strips were then smoothed further with a streamwise 3-pixel moving average ( $\pm 0.33$ -mm for the big window, 0.25-mm for the smaller field-of-view porthole). Gaps in the profiles exist where the data from the sensor locations (centered at  $x = 220, 270, 295$ , and  $320$  mm) were excised. The temperature along the centerline starts increasing at  $x \approx 145$  mm, so this location is reported for the onset of transition. Note that due to the limits inherent in contour plots, the temperature rise is not apparent in the contour until the temperature has risen by  $\approx 0.4$  K at  $x = 165$  mm.

Under noisy flow, the transition location is accurate within less than 10% — roughly  $150 \pm 10$  mm at higher  $Re$  and  $250 \pm 20$  mm at lower  $Re$ . The percent error in transition location is slightly reduced under quiet flow because the uncertainty is proportional to  $Re$ . Therefore the uncertainty under quiet flow was similarly  $\pm 10$  mm, but relative to a larger value of approximately 250 mm, or less than 5%.

Identifying the onset of crossflow transition is somewhat more difficult, especially under quiet flow. The crossflow transition front is not a straight line perpendicular to the centerline, so a single number would not fully characterize its location. As will be seen, under quiet flow numerous streamwise hot streaks are evident over a long distance. Eventually their temperature increases more rapidly, but it does not reach a minimum beforehand. Whereas amplifying second-mode waves would not be expected to significantly impact heating, crossflow vortices would influence heating by virtue of their effect upon the boundary layer thickness even prior to their breakdown to turbulence due to secondary instabilities. Thus the effect of crossflow can be qualitatively perceived by TSP, but a quantitative determination of the location of crossflow transition is not made.

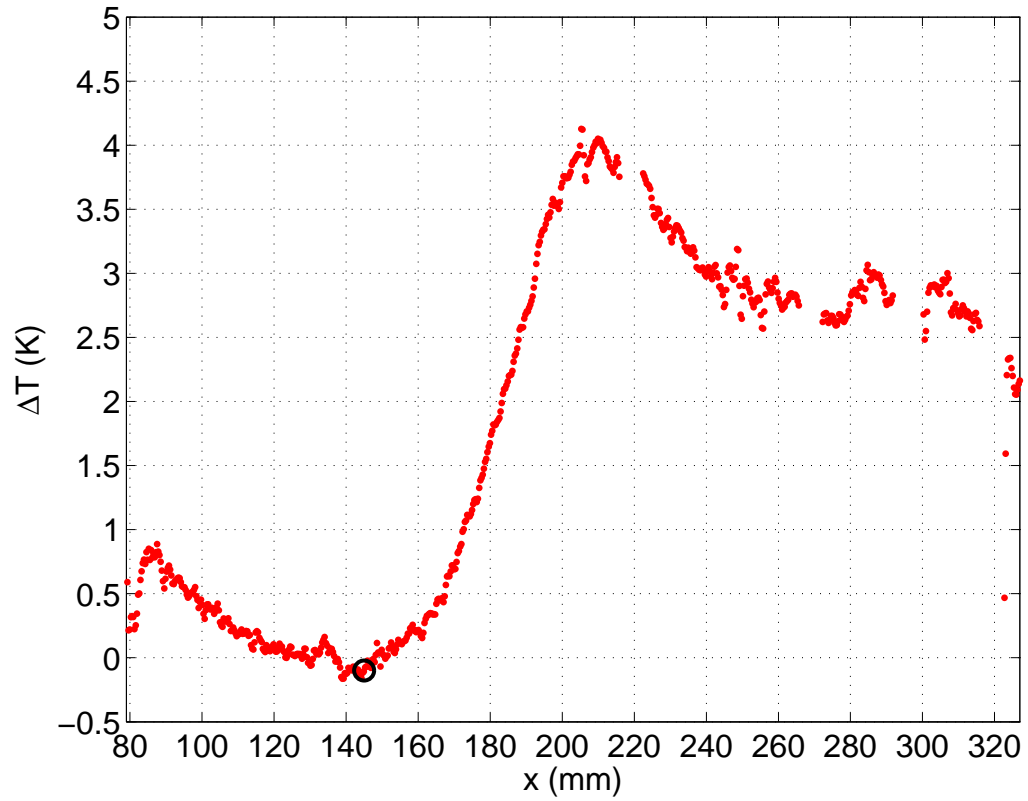
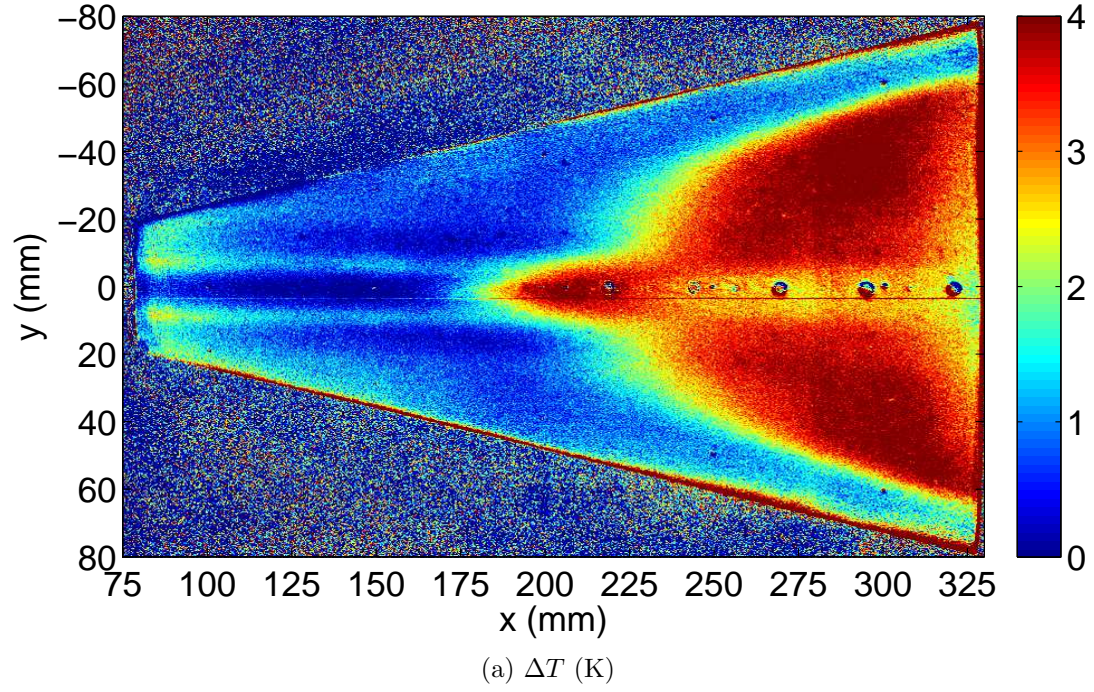


Figure 6.7.: Representative TSP contour and centerline profile. Noisy flow,  $M = 5.8$ ,  $\alpha = 4^\circ$ ,  $Re = 8.1 \cdot 10^6$  /m,  $p_0 = 610$  kPa

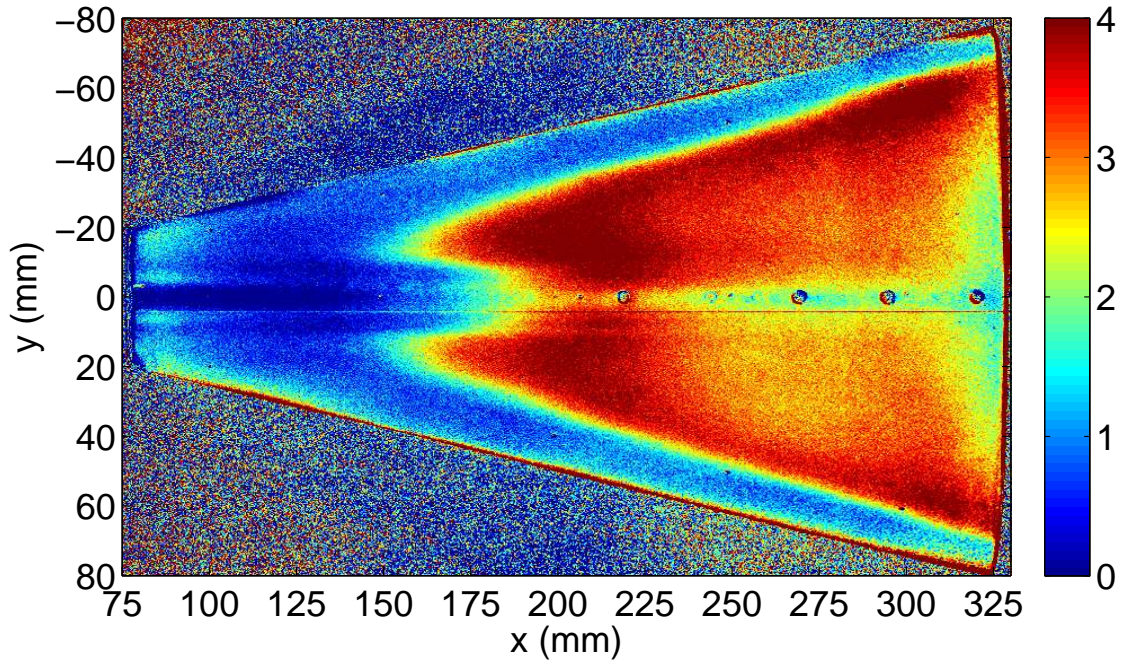
## 6.3 Results and Discussion

### 6.3.1 Effect of Noise Level

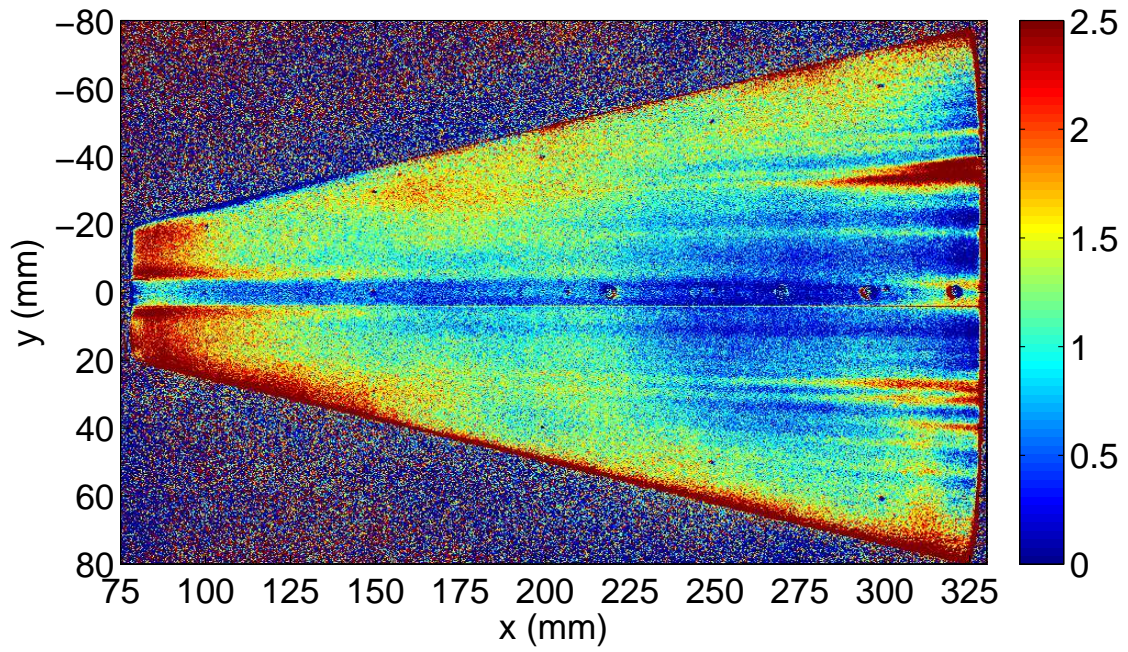
Figure 6.8 illustrates the effect of tunnel noise level on the HIFiRE-5 at  $\alpha = 0^\circ$  and  $Re = 10.2 \cdot 10^6$  /m. Transition onset on the centerline is delayed from  $x = 130$  mm under noisy flow to  $x = 270$  mm under quiet flow. The streamwise profiles used to judge transition location are contained Section 6.3.3. As discussed in Section 6.2.3, the line plots show earlier transition than the contour plots. Centerline transition is presumed to be due to the amplification and breakdown of second-mode waves (Section 1.2). Crossflow is absent on the centerline because it is an axis of symmetry without a spanwise velocity component. Computations predict a Mach number at the boundary layer edge of about 5 for this case (see Section 2.2.2); second-mode waves are more amplified than first-mode for an edge Mach number this large and a cold model wall ( $T_{\text{wall}} \approx 0.7T_0$ ) [79]. Furthermore, disturbance frequencies measured along the centerline match computational predictions of second-mode frequencies more closely than first mode (see Chapter 8).

Under noisy flow, transition appears to initiate off the centerline as well as on it, resulting in a three-lobed transition front. This transition away from the centerline is presumed to arise from the amplification and breakdown of crossflow vortices. Under quiet flow at this  $Re$ , it is not clear whether the onset of crossflow transition has begun. Streamwise streaks of elevated heating are visible. It is suspected that these streaks are due to crossflow vortices that have not yet broken down to turbulence. They are roughly aligned with the inviscid streamlines. The streaks do not broaden into a turbulent wedge, but instead remain distinct to the back end of the model. It is anticipated that a secondary instability would ultimately lead to breakdown of the stationary crossflow vortices into turbulence, but this process was not observed even at the highest  $Re$  achievable under quiet flow. Perhaps the low tunnel noise has reduced the amplitude of the traveling secondary instability. There is no local





(a) Noisy flow,  $M = 5.8$ ,  $p_0 = 810$  kPa,  $T_0 = 410$  K,  $t = 4.5$  s



(b) Quiet flow,  $M = 6.0$ ,  $p_0 = 940$  kPa,  $T_0 = 429$  K,  $t = 0.5$  s

Figure 6.8.: Effect of tunnel noise level.  $\alpha = 0^\circ$ ,  $Re = 10.2 \cdot 10^6$  /m



maximum of heating that would indicate a fully-turbulent boundary layer. It is difficult to determine the location of transition onset or fully-turbulent flow.

Unlike the second-mode waves, which are traveling waves, stationary crossflow vortices under quiet flow are detected by TSP, which is monotonic in the mean heat transfer. Although crossflow-induced transition is evident under noisy flow, individual streaks are only visible under quiet flow. This difference may arise from the relative stability of traveling and stationary crossflow vortices. References 80 and 81 explain that stationary waves are dominant in low-noise environments, at least at low speeds.

The centerline transition result is significant because it is the first evidence in the BAM6QT of transition under quiet flow that is not induced by deliberately-generated roughness. Until now, quiet-flow transition had been detected only on vehicles with isolated roughness elements intended to trip the boundary layer, such as the X-51 [82,83] and HIFiRE-1 [23]. Conclusions regarding the effect of noise level on (relatively) smooth walls had been limited to setting a lower bound on the delay.

A noise level comparison at a higher freestream Reynolds number shows the same effect of tunnel noise, but more features are visible in the model boundary layer under (nominally) quiet flow (Figure 6.9). Centerline transition is delayed from  $x = 125$  to 255 mm. Crossflow transition is evident under noisy flow; hot streaks thought to arise from crossflow vortices and possible transition from these vortices exists under quiet flow, but further from the nose. At the time these data were collected, the maximum useful quiet pressure of the BAM6QT was 1170 kPa (169 psia) [52]. As discussed above in Section 4.3, low noise levels at this high pressure this far back in the nozzle have not been proven.

Tests at these high pressures necessitate use of the porthole windows, which restrict the field of view (see Section 6.1). Note that the noisy-flow image is viewing the front half of the frustum, roughly the middle third of the model, whereas the range of the image under quiet flow is the aft third. The model was repositioned between tunnel runs so that the transition front was visible through the downstream porthole window. The TSP contour plots for images through the porthole windows are shown

on the same axes as the images through the big window. This presentation makes the relative locations of the images easier to see.

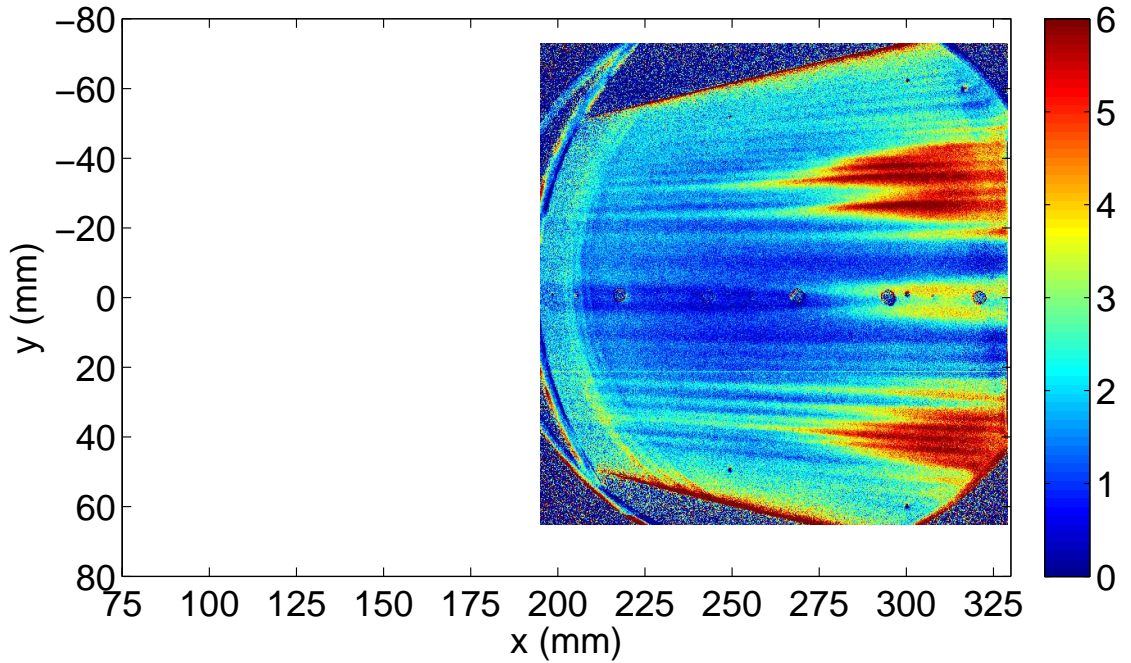
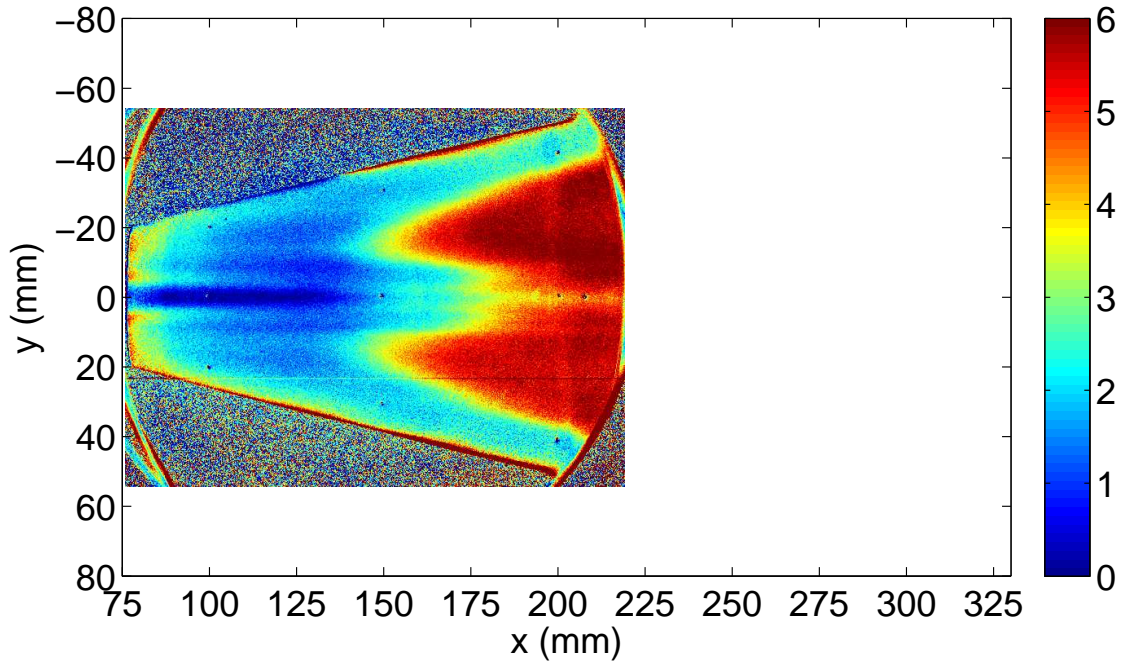


Figure 6.9.: Effect of tunnel noise level at high pressure.  $\alpha = 0^\circ$ ,  $Re = 11.8 \cdot 10^6$  /m

Figure 6.10 shows a spanwise temperature profile for the contour plot shown in Figure 6.9b at  $x = 255$  and  $305$  mm. This case (maximum quiet pressure,  $\alpha = 0^\circ$ ) is particularly interesting because it exhibits the maximum impact of crossflow encountered. The upstream location coincides with the apparent onset of transition along the centerline. The data was averaged over  $\pm 2$  mm (8 pixels) in the streamwise direction and  $\pm 0.24$  mm ( $\pm 1$  pixel, or a 3-pixel-wide strip) in the spanwise direction.

The centerline and off-centerline temperature increases are visible. The hot streaks thought to arise from crossflow vortices persist into the region of presumed turbulent or transitional flow. These streaks are spaced about 3.0 mm from one another at  $x = 305$  mm and they are inclined  $4\text{--}5^\circ$  away from the centerline. As discussed in Section 6.2.3, it is unclear what is an appropriate threshold for transition onset or end for crossflow transition, especially under quiet flow.

Figure 6.11 shows a noise comparison for  $\alpha = 4^\circ$  on the windward side at  $Re = 9.5 \cdot 10^6$  /m. The significant effect of noise level on transition is again obvious. Under noisy flow, both second-mode- and crossflow-induced transition appear to occur. Transition onset due to second-mode waves begins on the centerline at approximately  $x = 140$  mm for these conditions (see Section 6.3.3). Crossflow transition begins at roughly 180 mm, but it is again difficult to set a threshold. Upstream of  $x = 140$  mm, the temperature contours are very similar for both noise levels.

Under quiet flow, on the other hand, transition does not occur as a result of either instability. Two hot streaks parallel with the centerline run the entire length of the painted portion of the model. The streaks are approximately 4 mm wide and centered 9 mm from the centerline. The temperature between these streaks is lower than elsewhere on the surface. The explanation for this temperature distribution is not obvious from the TSP data, but the CFD simulations (Section 2.2.2) and Princeton Filtered Rayleigh Scattering experiments (Section 2.1.2) are helpful. They both show a thicker boundary layer along the centerline, which would result in lower heat flux. Vortices form on each side of the centerline bulge, which cause the boundary layer to be thinner and would appear as a higher temperature.

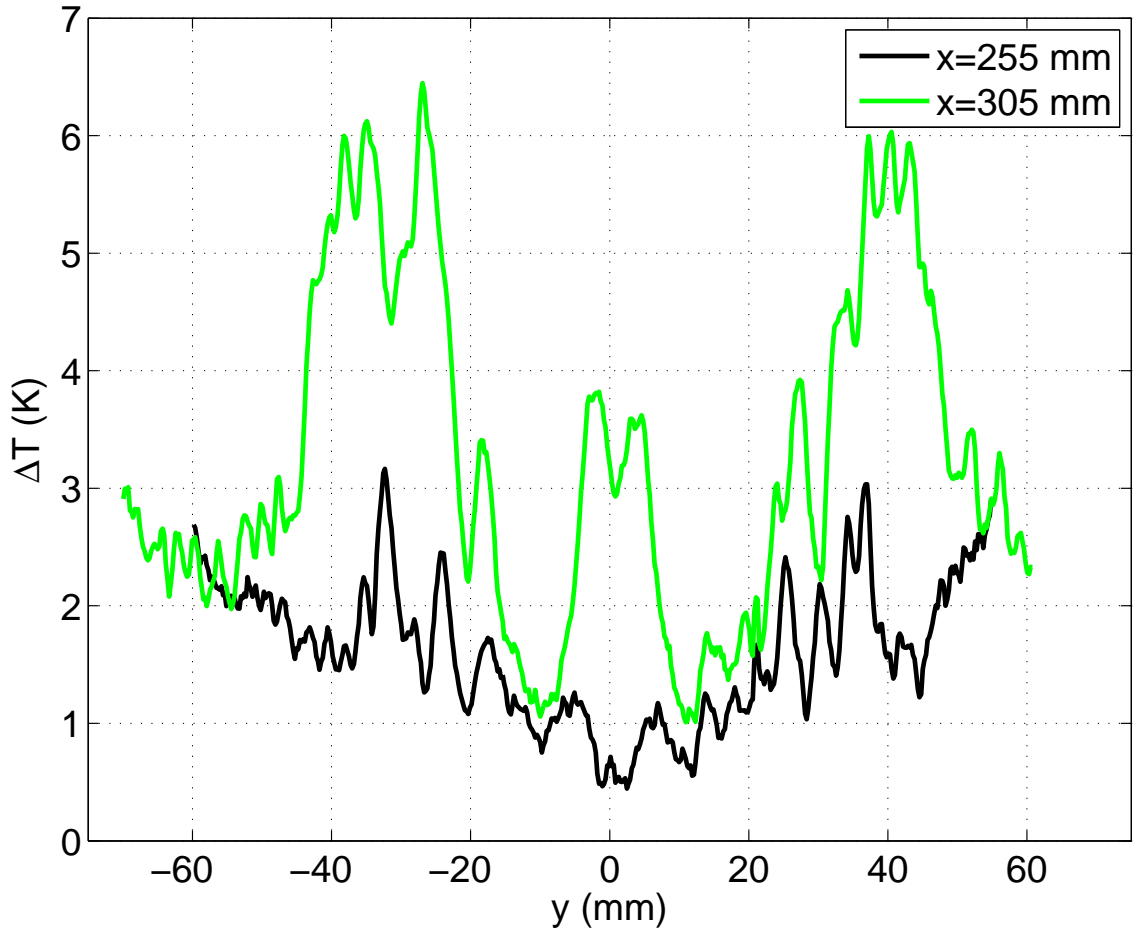
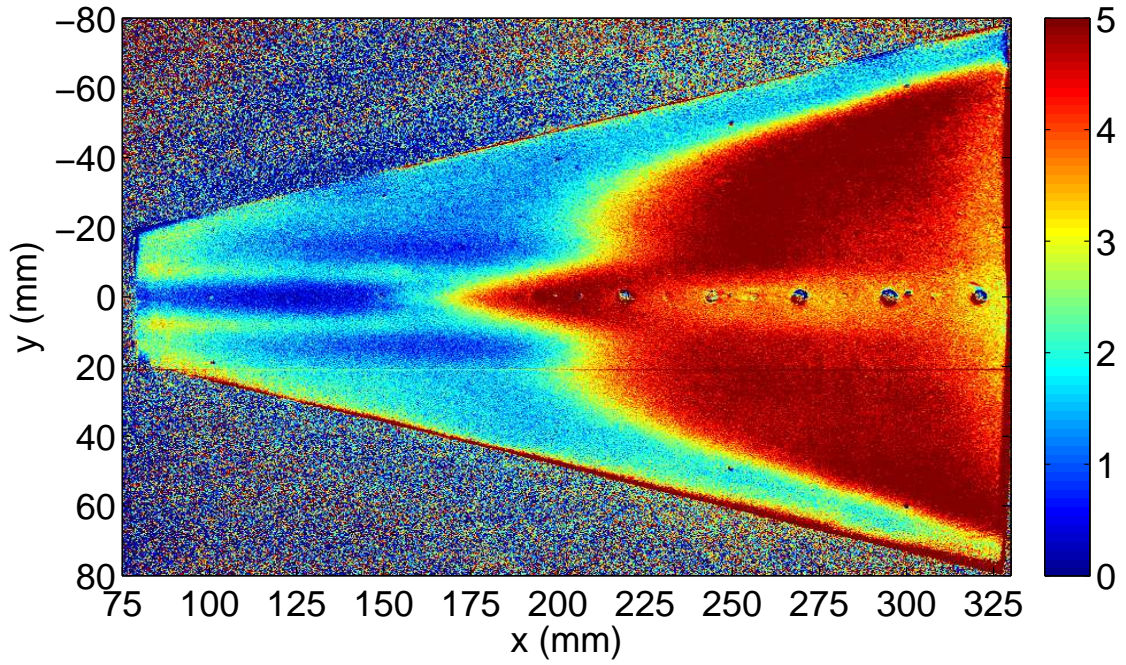


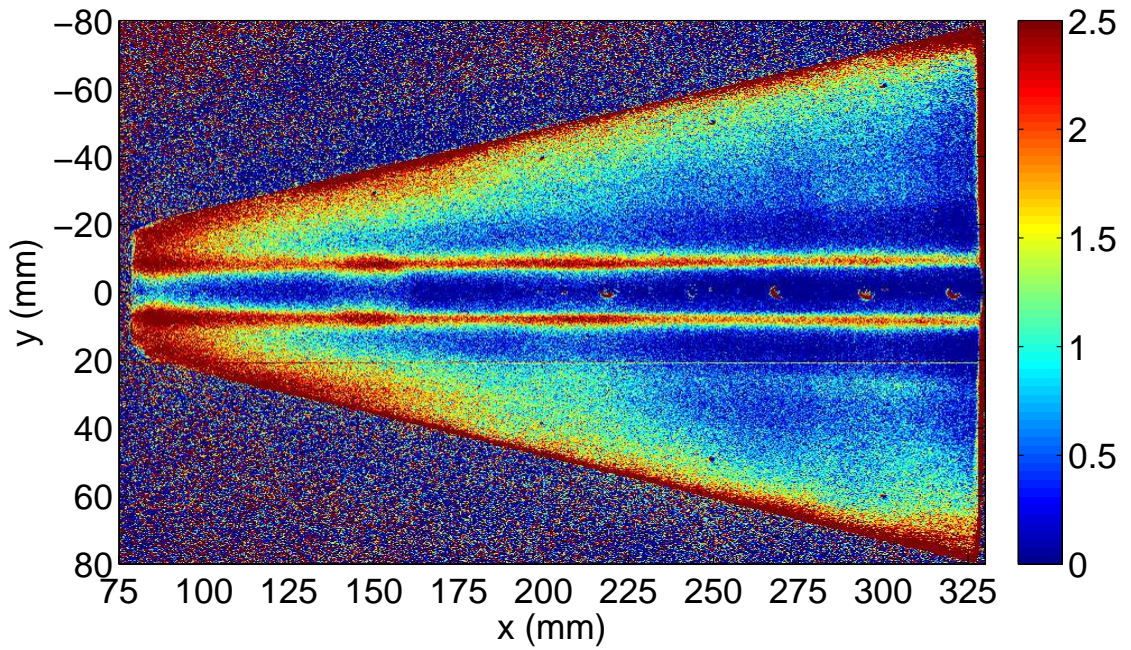
Figure 6.10.: Spanwise temperature profile. Quiet flow,  $M = 6.0$ ,  $\alpha = 0^\circ$ ,  $Re = 11.8 \cdot 10^6 / m$ ,  $p_0 = 1090$  kPa

Figure 6.12 illustrates a similar noise effect as Figure 6.11, except at  $p_0$  near the tunnel's maximum quiet pressure. Note that the horizontal scales for these two subfigures differ because, as with Figure 6.9, the model was repositioned between runs so different portions were visible through the porthole windows. The most significant difference observed at this higher  $Re$  is the evidence of centerline transition under quiet flow. Transition onset occurs at  $x \approx 275$  mm under quiet flow in Figure 6.12b. Unlike the hot streaks on either side of centerline, the elevated centerline heating widens downstream in the classic turbulent wedge. The apparently higher and wider





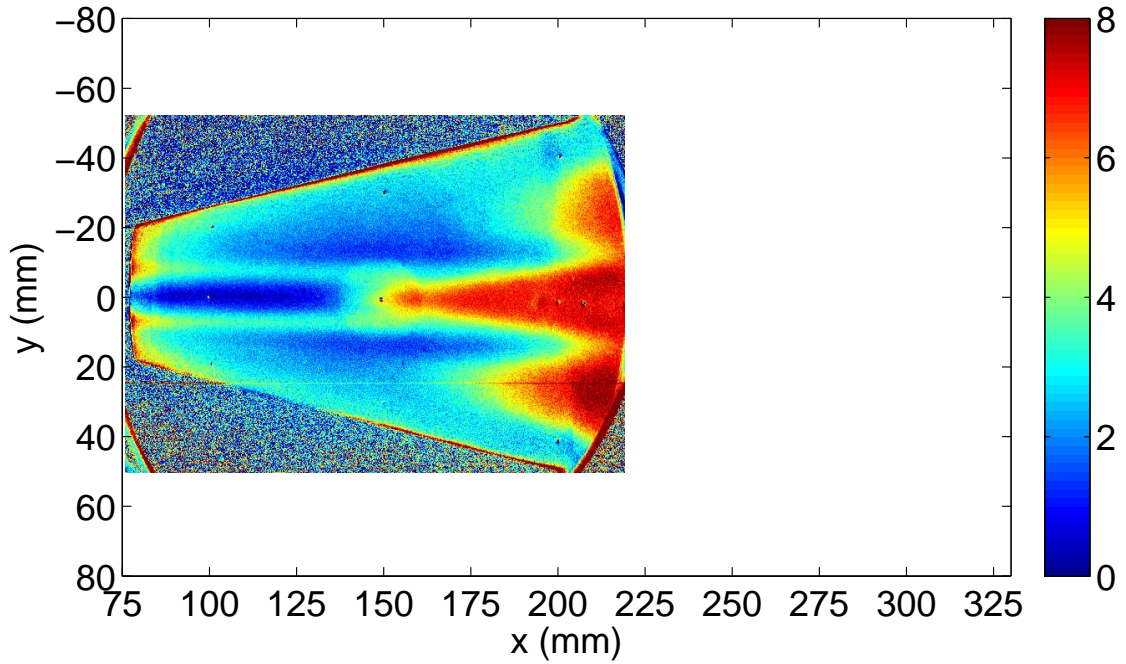
(a) Noisy flow,  $M = 5.8$ ,  $p_0 = 720$  kPa,  $T_0 = 397$  K,  $t = 7.5$  s



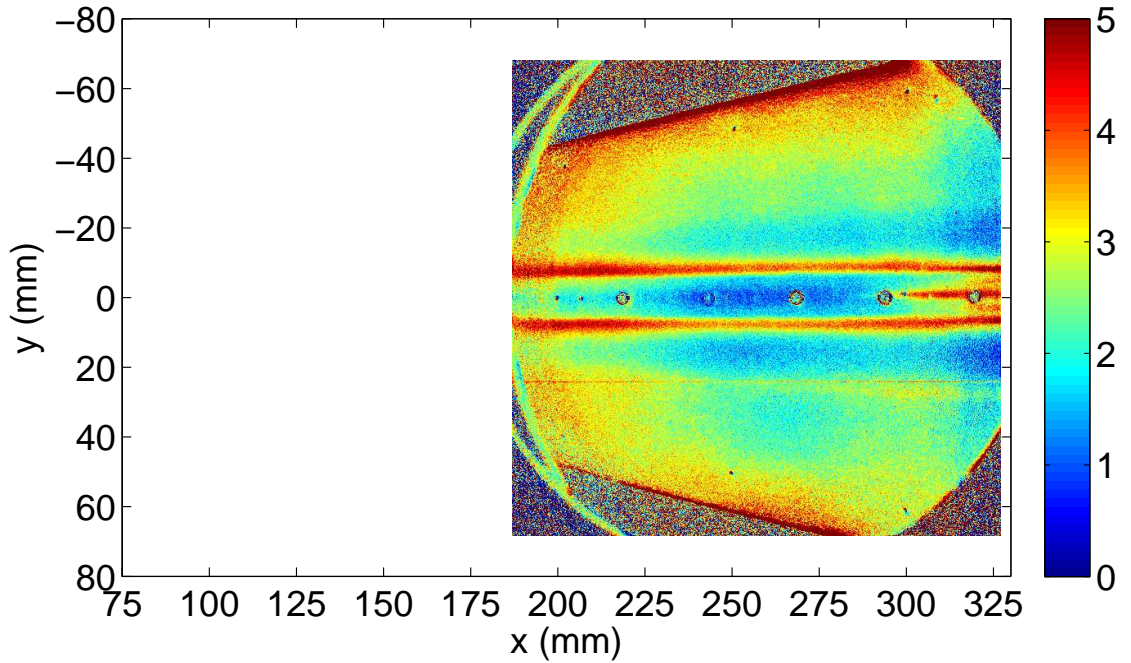
(b) Quiet flow,  $M = 6.0$ ,  $p_0 = 810$  kPa,  $T_0 = 410$  K,  $t = 2.8$  s

Figure 6.11.: Effect of tunnel noise level.  $\alpha = 4^\circ$ ,  $Re = 9.5 \cdot 10^6$  /m

heating at the tip of the centerline transition under noisy flow is an artifact arising from the steel insert for the glow perturber, which is centered at  $x = 150$  mm.



(a) Noisy flow,  $M = 5.8$ ,  $p_0 = 950$  kPa,  $T_0 = 410$  K,  $t = 4.5$  s



(b) Quiet flow,  $M = 6.0$ ,  $p_0 = 1100$  kPa,  $T_0 = 428$  K,  $t = 0.5$  s

Figure 6.12.: Effect of tunnel noise level at high pressure.  $\alpha = 4^\circ$ ,  $Re = 11.9 \cdot 10^6$  /m

### 6.3.2 Effect of Angle of Attack

Tests were run at 0 and 4° (windward side) angle of attack. Figure 6.13 shows the TSP result from two runs at  $Re \approx 11.8 \cdot 10^6$  /m under quiet flow. The most striking difference due to angle of attack is that the streaks suspected to arise from crossflow vortices at  $\alpha = 0$  are entirely absent at  $\alpha = 4^\circ$ . This observation can be explained by the altered pressure gradient when  $\alpha$  changes. On the windward face, as angle of attack increases, the centerline static pressure increases relative to the leading edge pressure, thereby weakening the pressure gradient that creates crossflow vortices and causes ballooning of the centerline boundary layer. This trend is the opposite of what is encountered when studying crossflow on circular cones, for which increasing angle of attack corresponds to increasing crossflow. Centerline transition is delayed from  $x = 255$  mm for  $\alpha = 0^\circ$  to  $x = 275$  mm for  $\alpha = 4^\circ$ . The centerline temperature profiles used to gauge transition location appear in Section 6.3.3.

Figure 6.14 shows the spanwise temperature profiles at  $x = 305$  mm for the two images in Figure 6.13. It was constructed the same as Figure 6.10 — the data was averaged over  $\pm 2$  mm (8 pixels) in the streamwise direction and  $\pm 0.24$  mm (1 pixel) in the spanwise direction. Both angles of attack demonstrated elevated heating along the centerline at this location, suggesting that the boundary layer is transitional or turbulent. The narrow off-centerline hot streaks stand out clearly for  $\alpha = 4^\circ$  at  $y = \pm 8$  mm. The temperature for  $y = 20$ – $50$  mm on both sides of the centerline is much higher for  $\alpha = 0^\circ$ , which agrees with the observation that crossflow transition has begun only for this angle of attack.

Similar trends were observed when varying angle of attack under noisy flow, as seen in Figure 6.15. As under quiet flow, crossflow transition is delayed under noisy flow at higher angle of attack. The centerline transition delay is again much smaller, from  $x = 130$  to  $140$  mm.

Regardless of noise level, both angles of attack show low temperatures near the centerline prior to transition. For  $\alpha = 4^\circ$ , the low-temperature region is wider and



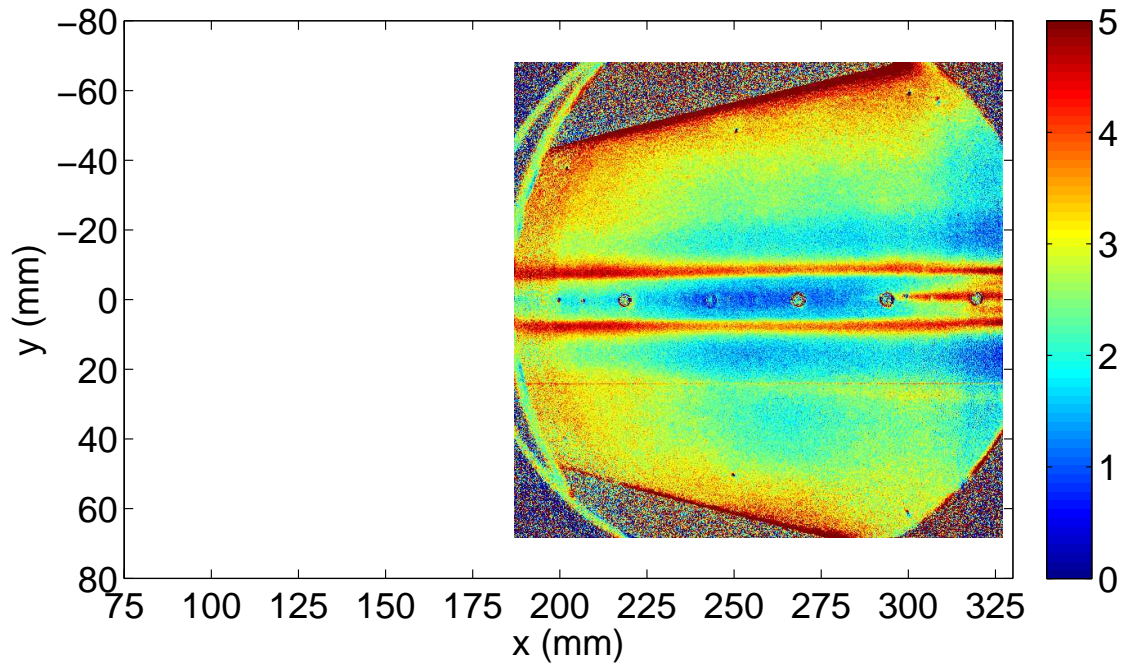
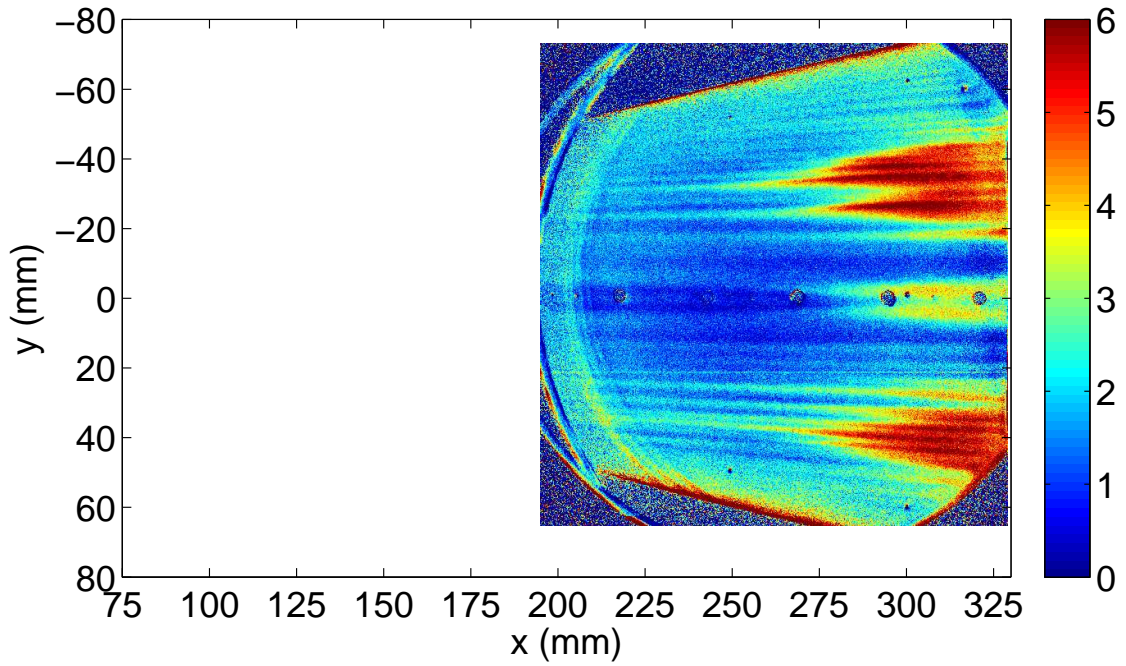


Figure 6.13.: Effect of angle of attack. Quiet flow,  $M = 6.0$ ,  $t = 0.5$  s



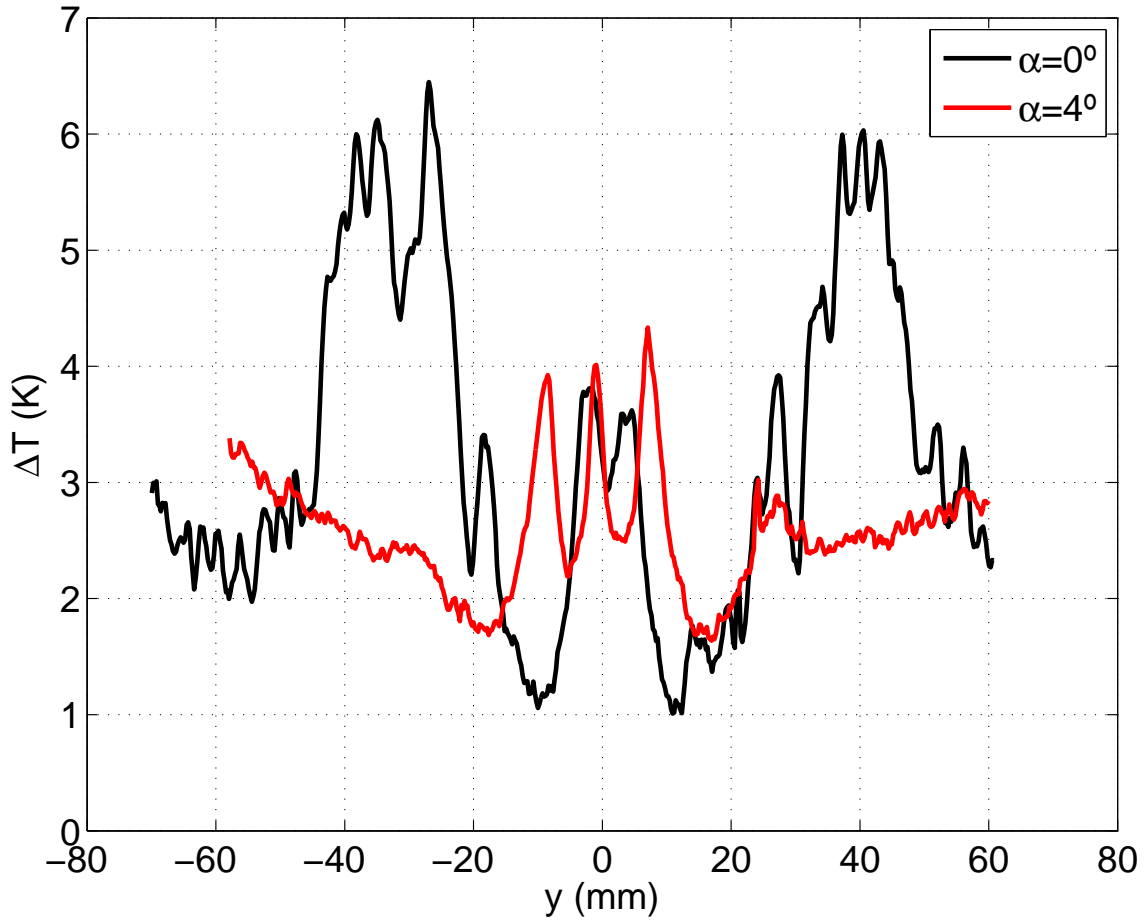


Figure 6.14.: Effect of angle of attack on spanwise temperature profile. Quiet flow,  $M = 6.0$ ,  $x = 305$  mm

bordered by hot streaks. For both quiet and conventional noise levels, the overall temperatures are higher at higher angle of attack, which is attributed to the thinner boundary layer on the windward side.

Whereas most temperature-rise contour plots presented have had their ranges adjusted to show the most detail, the four contour plots in Figure 6.16 have identical scales to highlight the higher temperatures encountered at higher angle of attack and under noisy flow when the model boundary layer becomes turbulent. The freestream Reynolds number does not match for all cases, but this figure provides a qualitative illustration of the effect of  $\alpha$  and freestream noise on heating.

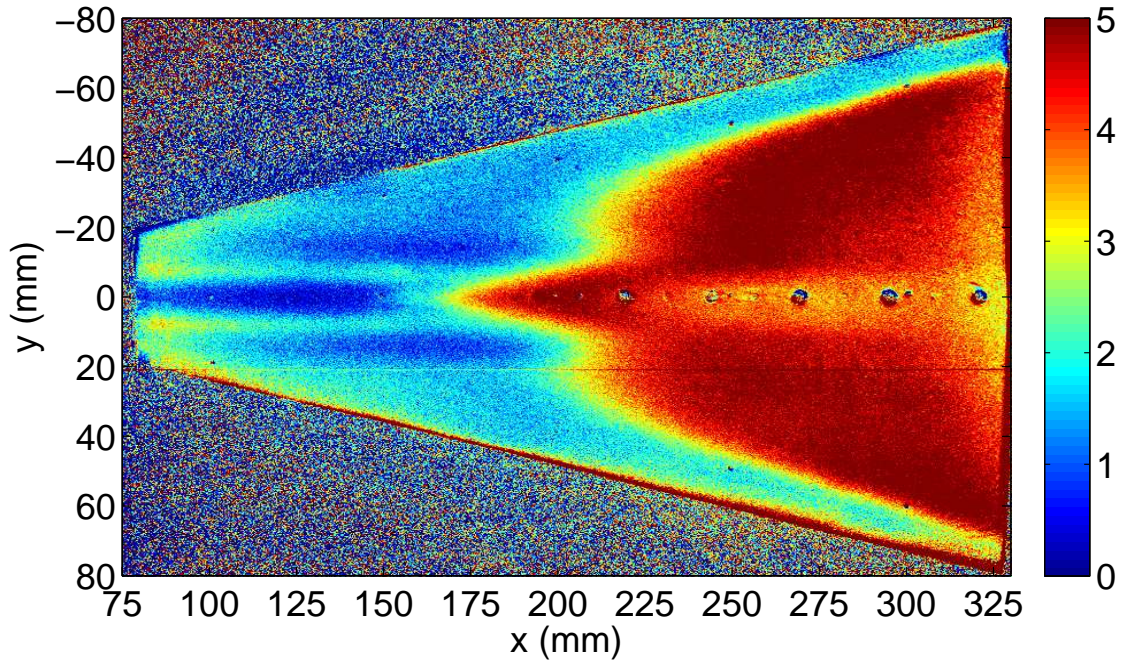
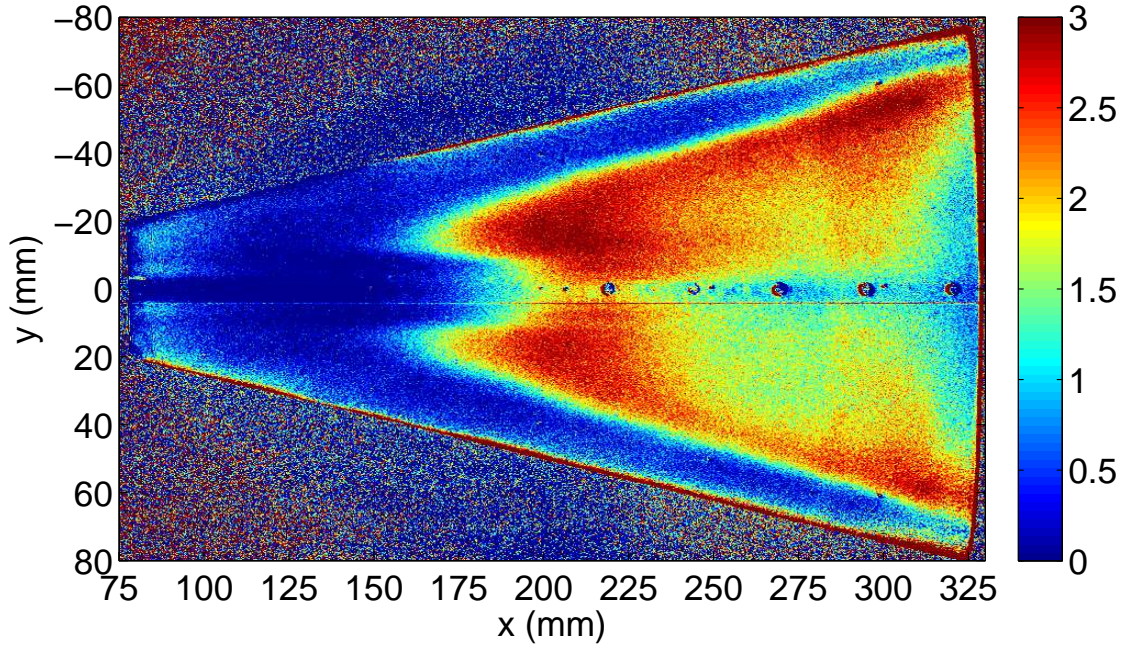


Figure 6.15.: Effect of angle of attack. Noisy flow,  $M = 5.8$ ,  $Re = 9.5 \cdot 10^6$  /m



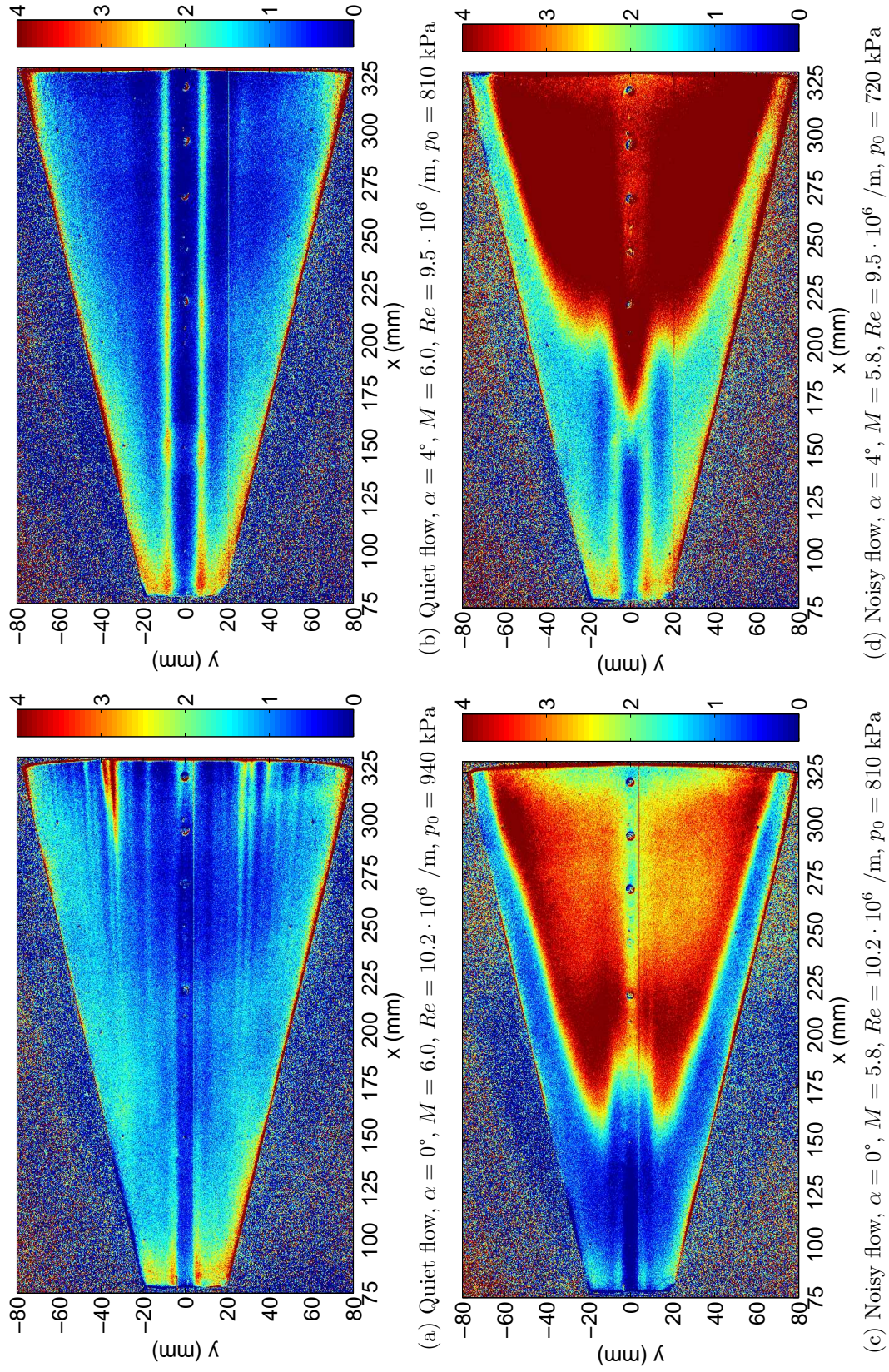


Figure 6.16.: Effect of tunnel noise and angle of attack. Same temperature scale for all subfigures

### 6.3.3 Effect of Freestream Reynolds Number at Zero Angle of Attack

Figure 6.17 illustrates the effect of freestream  $Re$  on transition under quiet flow for  $\alpha = 0$ . The scale of the temperature contours was adjusted for each subfigure to make flow features more perceptible at the expense of a direct temperature comparison. For all cases, heating is lower on the centerline and highest near the leading edges. Off-centerline heating decreases as the boundary layer thickens downstream. No transition is present for the three lower- $Re$  cases shown. Centerline transition onset is detected at  $x = 270$  mm for  $Re = 10.2 \cdot 10^6$  /m or  $Re_x$  of  $2.8 \cdot 10^6$ . For the highest  $Re$  shown,  $11.8 \cdot 10^6$  /m, transition on the centerline begins at  $x \approx 255$  mm. This location corresponds to  $Re_x = 3.0 \cdot 10^6$ . This 7% difference in  $Re_x$  at transition is not much larger than the 5% error in transition location as estimated in Section 6.2.3. As discussed in Section 4.3, it cannot be stated with complete confidence that flow is completely quiet throughout the nozzle at these high  $Re$ . Thus, the quiet-flow transition locations are in fact the transition locations where the flow is presumed to still be quiet.

The temperature contours indicate higher  $T$  for the  $Re = 6.0$  and  $8.0 \cdot 10^6$  /m cases for approximately  $285 < x < 315$  mm. These images are taken from later during their runs, after the nozzle-wall boundary layer has separated and reattached. These regions experienced higher heating under a turbulent model boundary layer during the period of separated flow and the TSP still exhibits the residual heating.

Streaks due to crossflow vortices are barely visible at  $Re = 8.0 \cdot 10^6$  /m and become more obvious at higher  $Re$ . More streaks appear at the highest  $Re$  and they appear farther upstream. It is not clear whether the boundary layer transitions to turbulent before the end of the model as a result of these streaks or if the higher temperatures are due to increased laminar heating. The temperature increase is consistent with a transitional or turbulent boundary layer, but the streaks remain distinct, suggesting that the vortices have not broken down completely. It appears



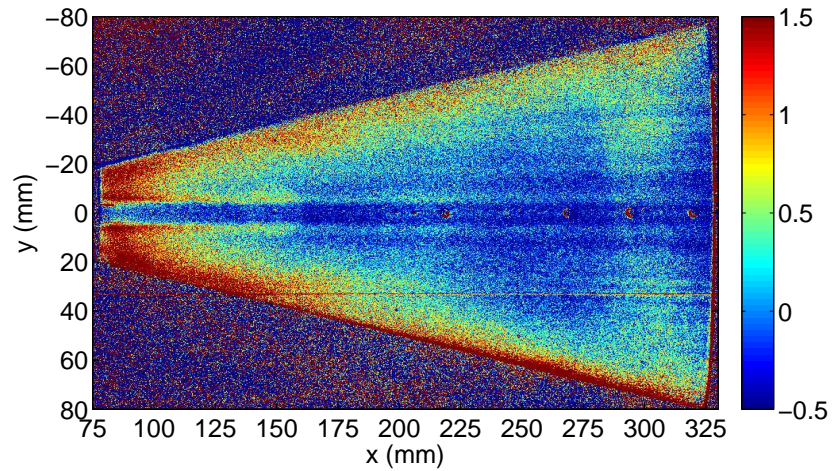
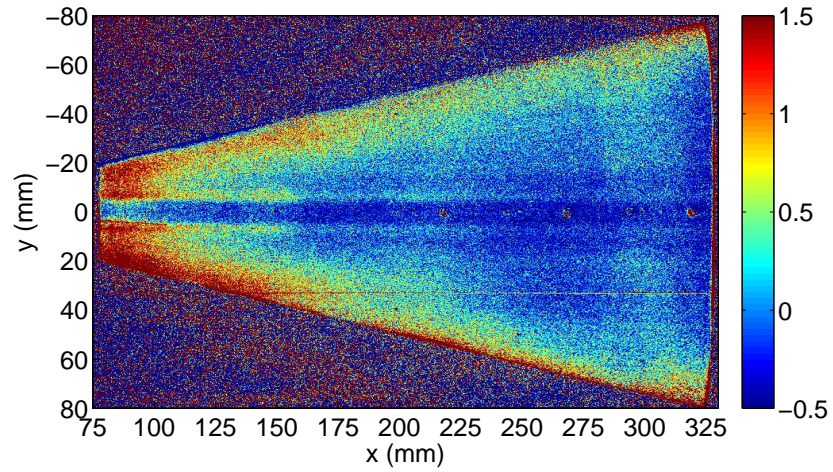
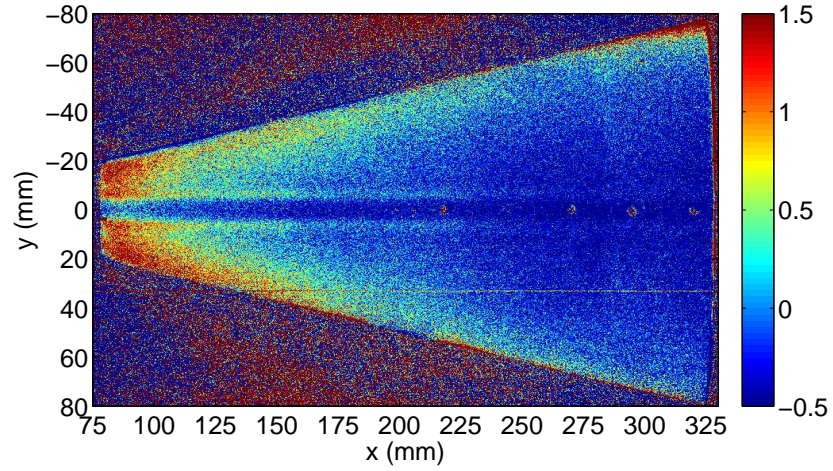
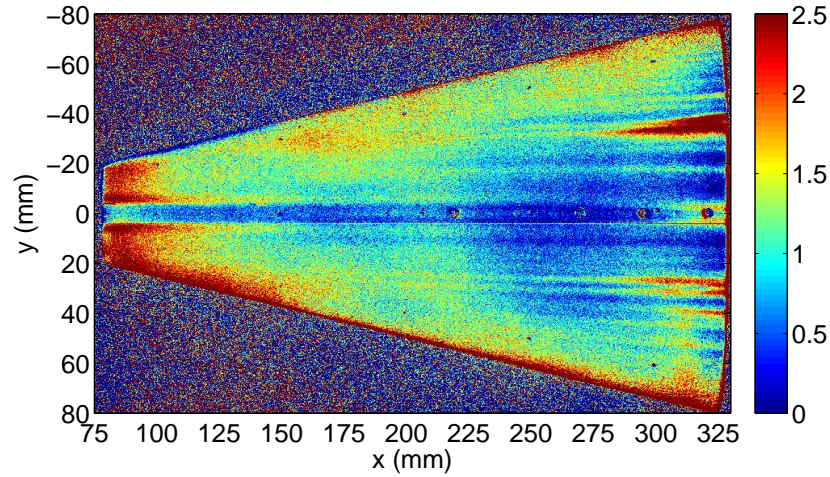
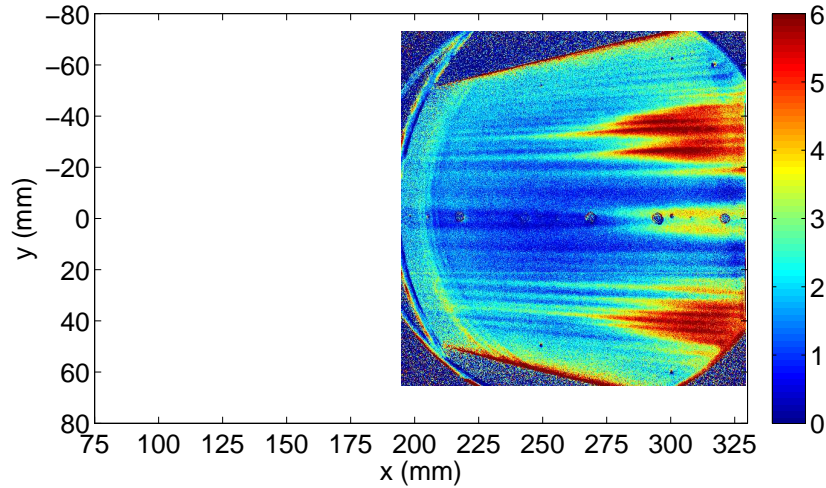


Figure 6.17.: Effect of varying freestream  $Re$ . Quiet flow,  $M = 6.0$ ,  $\alpha = 0^\circ$



(d)  $Re = 10.2 \cdot 10^6 / \text{m}$ ,  $p_0 = 940 \text{ kPa}$ ,  $t = 0.5 \text{ s}$



(e)  $Re = 11.8 \cdot 10^6 / \text{m}$ ,  $p_0 = 1090 \text{ kPa}$ ,  $t = 0.5 \text{ s}$

Figure 6.17.: Effect of varying freestream  $Re$  (continued). Quiet flow,  $M = 6.0$ ,  $\alpha = 0^\circ$

likely that the boundary layer has become turbulent due to the breakdown of crossflow vortices at this highest  $Re$ .

Figure 6.18 shows the centerline temperature rise for the five images in Figure 6.17. The centerline temperature rise was averaged within 3.5 mm (12 pixels) of the centerline. This width was chosen so that only the data between the off-centerline hot streaks were included. The data were then smoothed in the streamwise direction with a 3-pixel moving average ( $\pm 0.33\text{-mm}$  for the big window,  $0.25\text{-mm}$  for the smaller

field-of-view porthole). Gaps in the profiles exist where the data from the sensor locations (centered at  $x = 220, 270, 295$ , and  $320$  mm) were excised. Narrow spikes occasionally appear at the registration mark locations ( $x = 100, 150, 200, 250$ , and  $300$  mm).

Figure 6.18 was used in conjunction with the whole-surface images to judge transition locations, which were determined as described above in Section 6.2.3. They are marked with black circles and are summarized below in Table 6.2 after noisy-flow results are presented.

Naturally, there is some scatter and random variation in the temperature profile. For the three lower freestream unit Reynolds numbers ( $2.7, 6.0$ , and  $8.0 \cdot 10^6$  /m), the temperature is mostly decreasing over the entire model length. It is thus concluded that the centerline transition does not occur in these cases. For  $Re = 10.2 \cdot 10^6$  /m,  $\Delta T$  begins to rise downstream of the sensor at  $x = 270$  mm. The effect of the sensors on the surface contour was described in Chapter 5. It is possible that the sensor affected transition in this or other cases, but its impact is unknown. Attempts to measure smoother-wall transition with coaxial thermocouples were unsuccessful (Section 7.1). Transition onset occurs at  $x = 255$  mm for the  $Re = 11.8 \cdot 10^6$  /m case. The temperature reaches a maximum at  $x = 310$  mm, which is assumed to coincide with the beginning of fully-turbulent flow. The transitional region in this case is 55-mm in length.

Figure 6.19 contains TSP images at a range of freestream Reynolds numbers under noisy flow at  $\alpha = 0$ . It is uncertain whether second-mode and crossflow transition occur independently or crossflow transition propagates to the centerline. As in Figure 6.17, the scale was varied to enhance detail at the expense of an easier temperature comparison. The signal-to-noise ratio is particularly poor for the  $Re = 2.8 \cdot 10^6$  /m case, but the temperature does indeed increase starting near  $x = 270$  mm. As expected, transition onset occurs farther forward as  $Re$  increases. The shape of the transition front is essentially the same for all  $Re$ , which suggests that the two transition modes are affected more or less equally by changing  $Re$ .

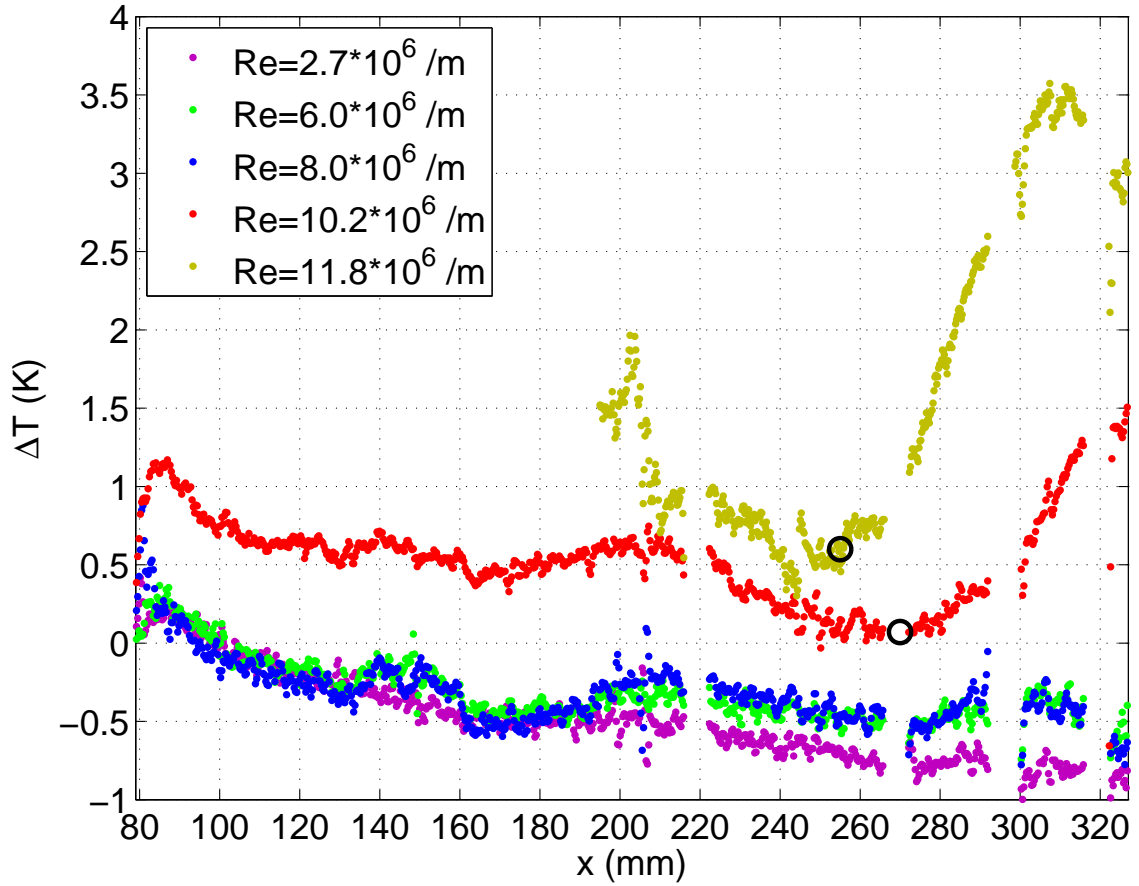
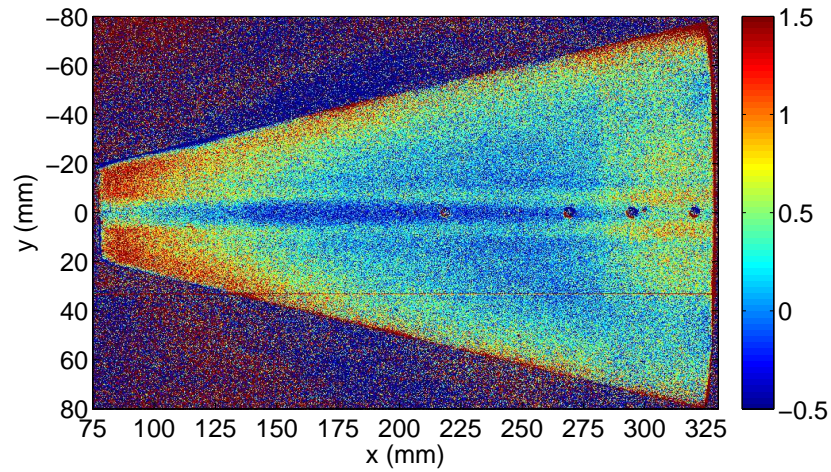


Figure 6.18.: Centerline temperatures for  $\alpha = 0^\circ$  under quiet flow

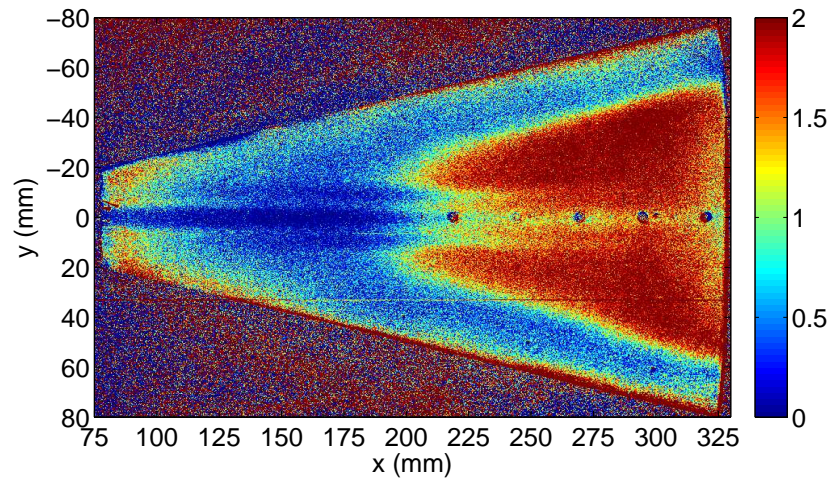
Figure 6.20 shows the centerline temperature distribution for the  $\alpha = 0^\circ$  noisy-flow results gleaned from the images in Figure 6.19. It was constructed the same way as Figure 6.18. Unlike under quiet flow, centerline transition appears before the end of the model at all  $Re$  tested. The expected trend of earlier transition as  $Re$  increases is evident. Little importance should be given to the actual  $\Delta T$  values reported because of the pressure dependence discussed in Section 6.2.

Table 6.2 presents the transition locations measured with TSP for  $\alpha = 0^\circ$  under quiet and noisy flow. The freestream Reynolds numbers were matched as closely as possible when choosing the images to present, but it was not possible to match conditions within  $0.1 \cdot 10^6$  /m for the low- $Re$  quiet cases. Images early in the run

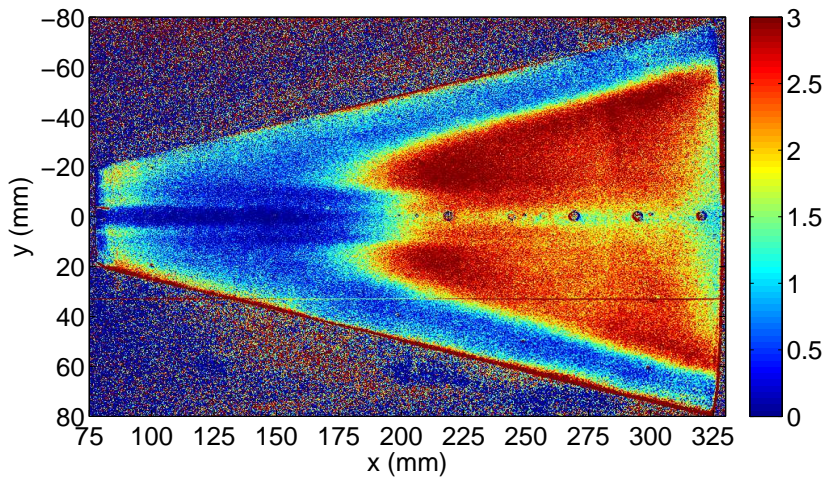




(a)  $Re = 2.8 \cdot 10^6$  /m,  $p_0 = 210$  kPa,  $t = 7.95$  s

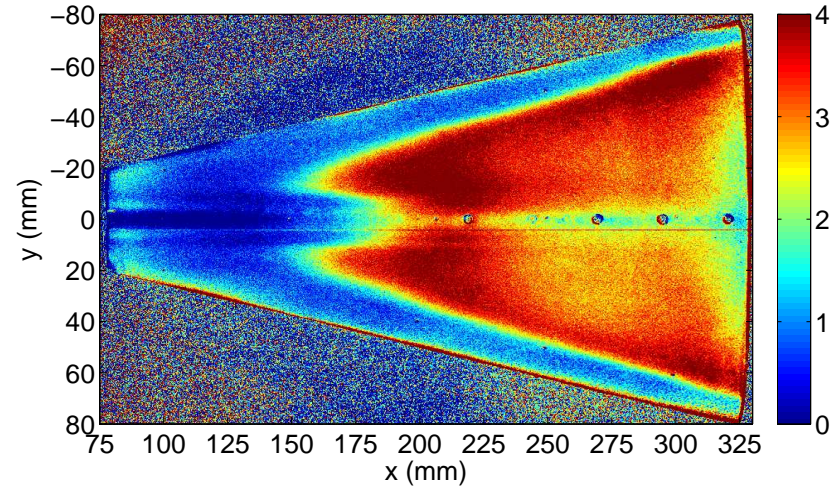


(b)  $Re = 6.1 \cdot 10^6$  /m,  $p_0 = 460$  kPa,  $t = 7.95$  s

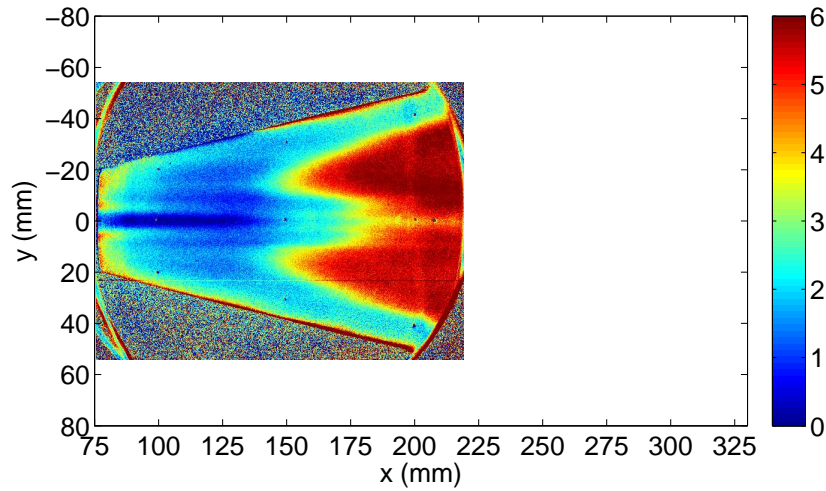


(c)  $Re = 8.1 \cdot 10^6$  /m,  $p_0 = 610$  kPa,  $t = 7.95$  s

Figure 6.19.: Effect of varying freestream  $Re$ . Noisy flow,  $M = 5.8$ ,  $\alpha = 0^\circ$



(d)  $Re = 10.2 \cdot 10^6$  /m,  $p_0 = 810$  kPa,  $t = 4.5$  s



(e)  $Re = 11.8 \cdot 10^6$  /m,  $p_0 = 930$  kPa,  $t = 5.0$  s

Figure 6.19.: Effect of varying freestream  $Re$  (continued). Noisy flow,  $M = 5.8$ ,  $\alpha = 0^\circ$

were contaminated by nozzle-wall boundary-layer separation or other flow-quality problems (see Chapter 4 for more information), so images at later times were used (generally after reattachment at  $t = 3$ – $5$  s). Noisy-flow runs did not achieve these lower  $Re$  until after data collection had ended, so the latest (lowest- $Re$ ) image is used for comparison. The difference in  $Re$  is only  $0.1 \cdot 10^6$  /m, a 1–4% discrepancy.

The transition delay shown in the final column is the ratio between transition  $Re_x$  under quiet and noisy flow. It is unclear if  $Re_x$  is a proper scaling for transition

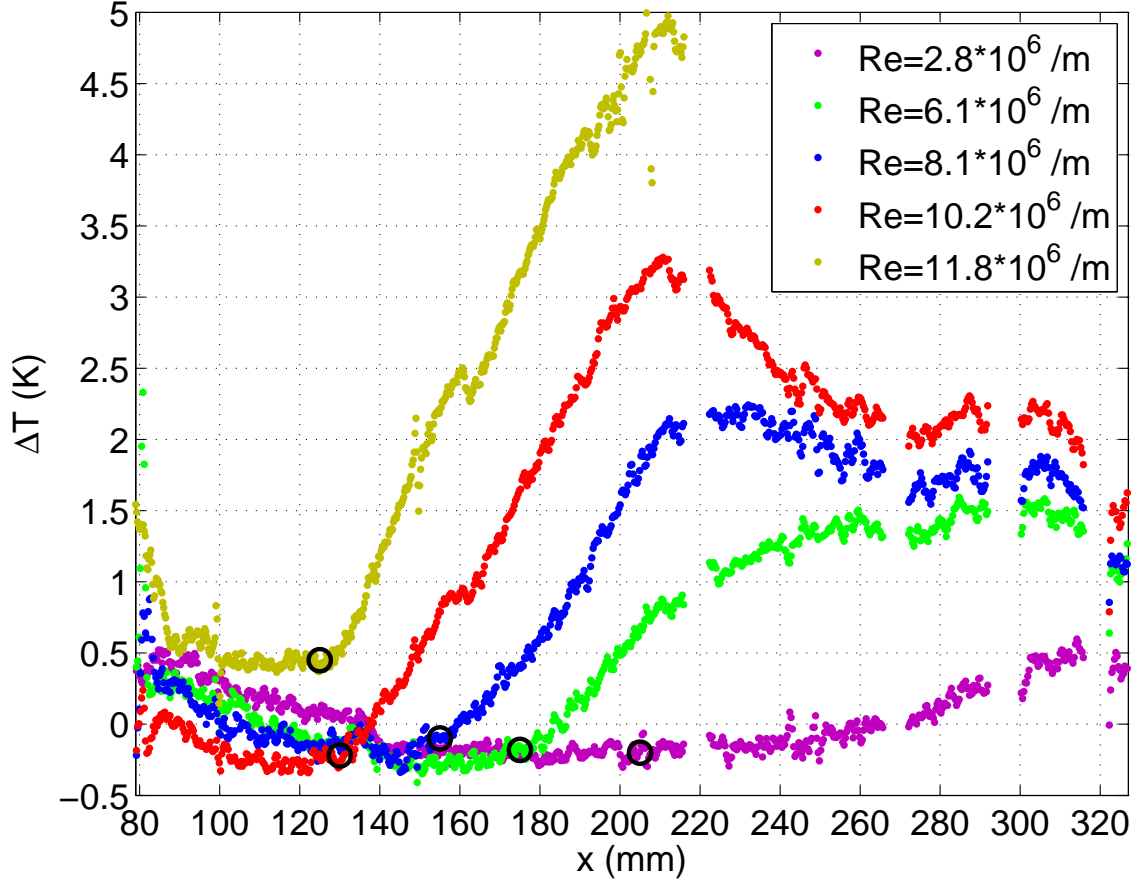


Figure 6.20.: Centerline temperatures for  $\alpha = 0^\circ$  under noisy flow

location for this geometry, but these values at least give a rough assessment of the significant impact of tunnel noise on transition. Because transition is not observed for the three lower- $Re$  cases shown, only a lower bound on the transition delay can be stated for them. It bears repeating that the higher- $Re$  cases are significant because they are the first evidence in the BAM6QT of transition under quiet flow not induced by deliberately-generated roughness. In other words, the actual ratio between transition  $Re_x$  can be stated, rather than just a lower bound.

Once again it is warned that the quiet-flow transition results may have been contaminated by higher-than-quiet noise levels at the end of the test section. Even if the flow along the tunnel centerline was quiet, disturbances may propagate through the

Table 6.2: Summary of centerline transition locations for  $\alpha = 0^\circ$ 

$Re$ ( $\cdot 10^6$ /m)	Location (mm)		Transition $Re_x$ ( $\cdot 10^6$ )		Transition Delay quiet $Re_x$ / noisy $Re_x$
	Quiet	Noisy	Quiet	Noisy	
2.7–2.8	> 328	205	> 0.89	0.57	> 1.6
6.0–6.1	> 328	175	> 2.0	1.1	> 1.8
8.0–8.1	> 328	155	> 2.6	1.3	> 2.0
10.2	270	130	2.8	1.3	2.1
11.8	255	125	3.0	1.5	2.0

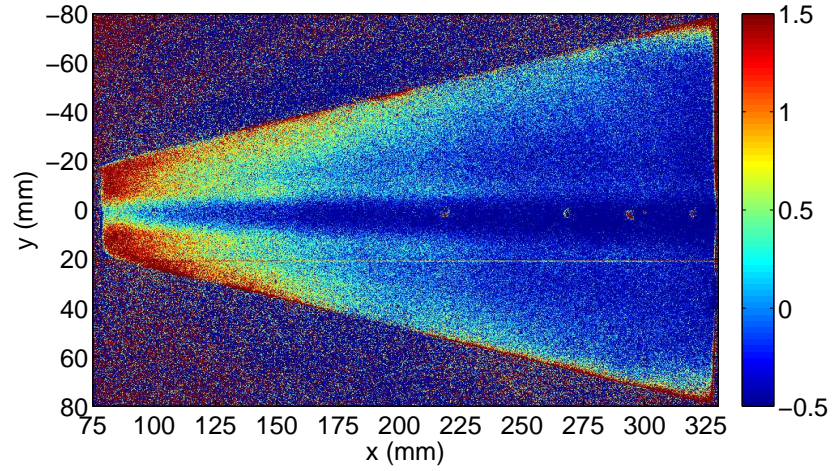
model boundary layer to affect transition. Also note that these results for transition delay may not apply to other flows and modes of transition.

#### 6.3.4 Effect of Freestream Reynolds Number at $4^\circ$ Angle of Attack

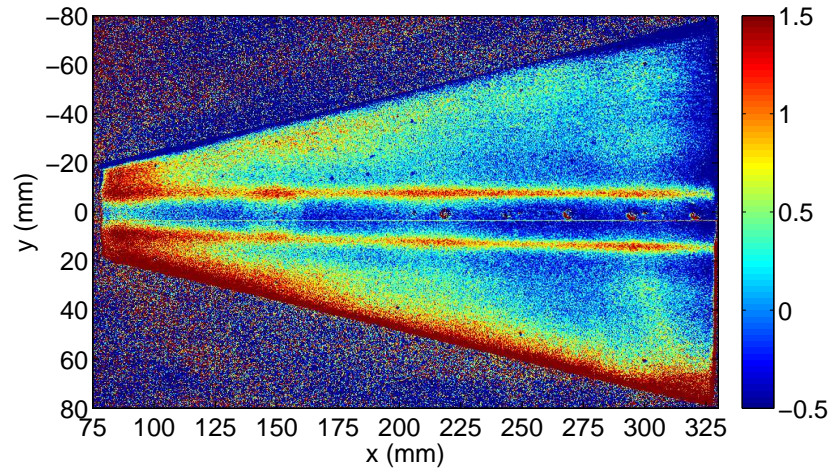
Figure 6.21 illustrates the effect of freestream  $Re$  on transition under quiet flow for  $\alpha = 4^\circ$ . The boundary layer appears to be laminar over the entire model except for the highest  $Re$  tested,  $11.9 \cdot 10^6$  /m, for which centerline transition occurs. There is no evidence of crossflow transition (or even crossflow vortices) at any  $Re$  tested. The relatively low-temperature centerline occurs as it did for  $\alpha = 0^\circ$ . The distinct off-centerline hot streaks are not clear at the lowest  $Re$  shown ( $2.6 \cdot 10^6$  /m), but are evident at all higher  $Re$ . At  $Re$  between the formation of the hot streaks and transition onset, there is very little change observed in the overall temperature distribution.

Figure 6.22 shows the centerline TSP intensity ratios for the five images in Figure 6.21. As with the other streamwise profiles, the paint intensity was averaged within 3.5 mm (12 pixels) of the centerline and then the spanwise strips were smoothed further with a 1-mm (3-pixel) moving average. Figure 6.22 corroborates the conclusion drawn from analyzing the TSP contour plots: the boundary layer is laminar for all cases except the highest. For  $Re = 11.9 \cdot 10^6$  /m, centerline transition begins at  $x = 275$  mm. The higher temperatures for  $x = 180$ – $200$  mm arise from reflections from the window frame.

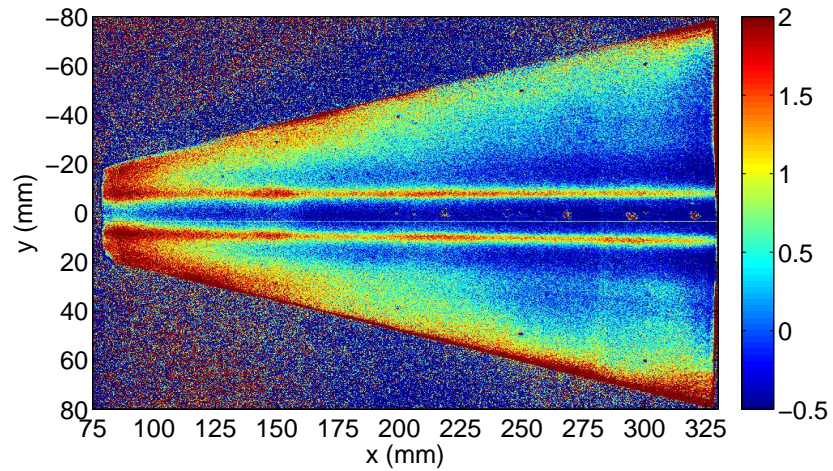




(a)  $Re = 2.6 \cdot 10^6 /m$ ,  $p_0 = 220$  kPa,  $t = 4.2$  s

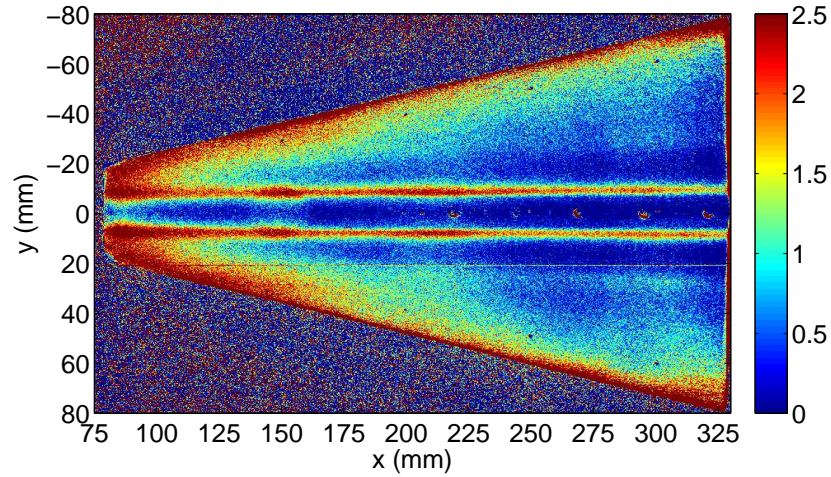


(b)  $Re = 6.0 \cdot 10^6 /m$ ,  $p_0 = 500$  kPa,  $t = 3.6$  s

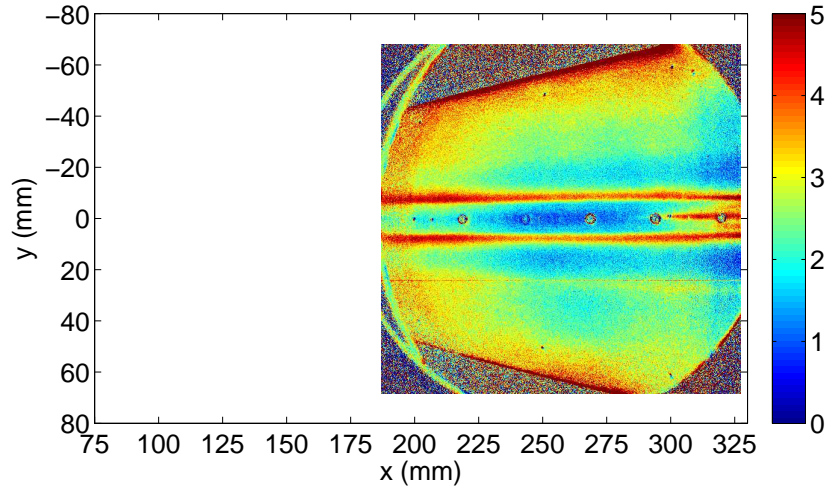


(c)  $Re = 8.0 \cdot 10^6 /m$ ,  $p_0 = 680$  kPa,  $t = 3.0$  s

Figure 6.21.: Effect of varying freestream  $Re$ . Quiet flow,  $M = 6.0$ ,  $\alpha = 4^\circ$



(d)  $Re = 9.5 \cdot 10^6 / \text{m}$ ,  $p_0 = 810 \text{ kPa}$ ,  $t = 2.8 \text{ s}$



(e)  $Re = 11.9 \cdot 10^6 / \text{m}$ ,  $p_0 = 1100 \text{ kPa}$ ,  $t = 0.5 \text{ s}$

Figure 6.21.: Effect of varying freestream  $Re$  (continued). Quiet flow,  $M = 6.0$ ,  $\alpha = 4^\circ$

The elevated temperature at  $x = 150 \pm 12 \text{ mm}$  in Figure 6.22 is due to the steel glow perturber insert. These images were all collected after the nozzle-wall boundary layer had reattached; prior to reattachment, the model boundary layer was turbulent at that location. The turbulent model boundary layer caused higher heating, the steel insert's temperature rose more than the surrounding aluminum, and it was still cooling at the times of these images. This effect is visible in several images (e.g., Figure 6.12), but is clearest here.

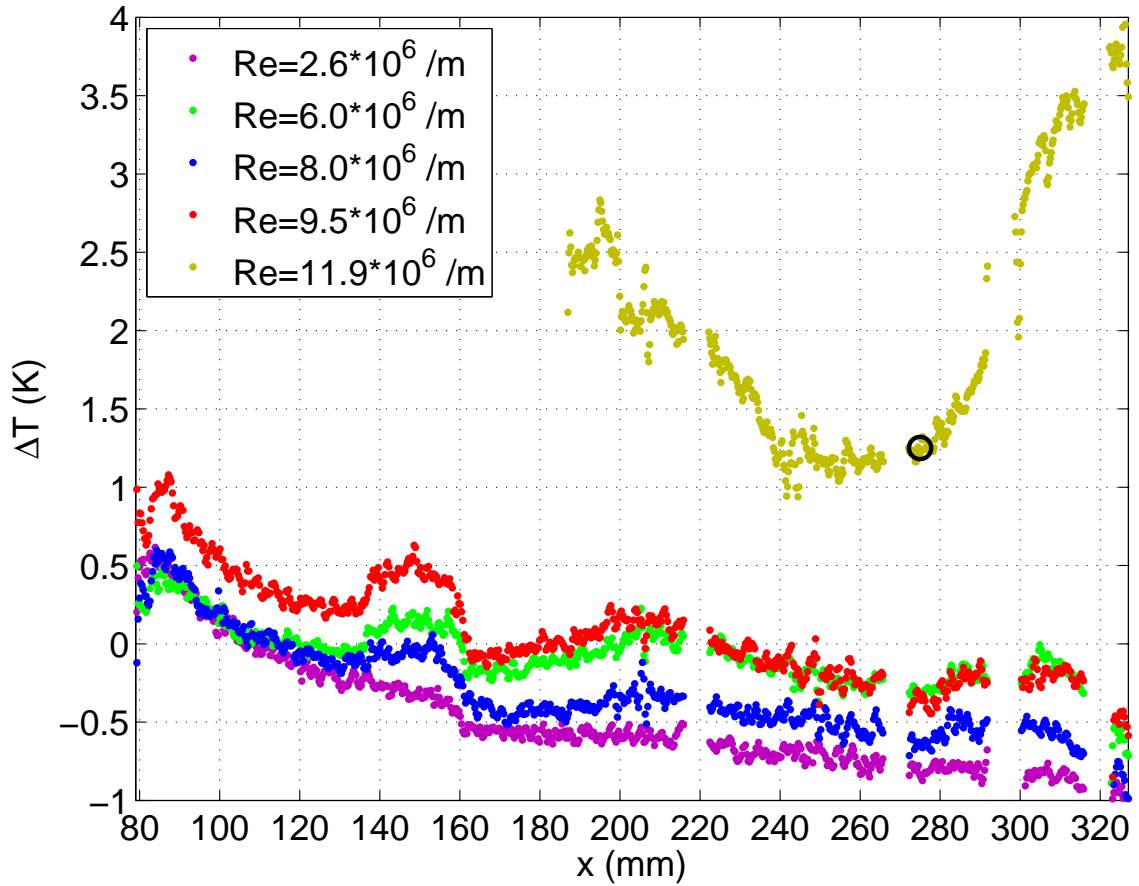
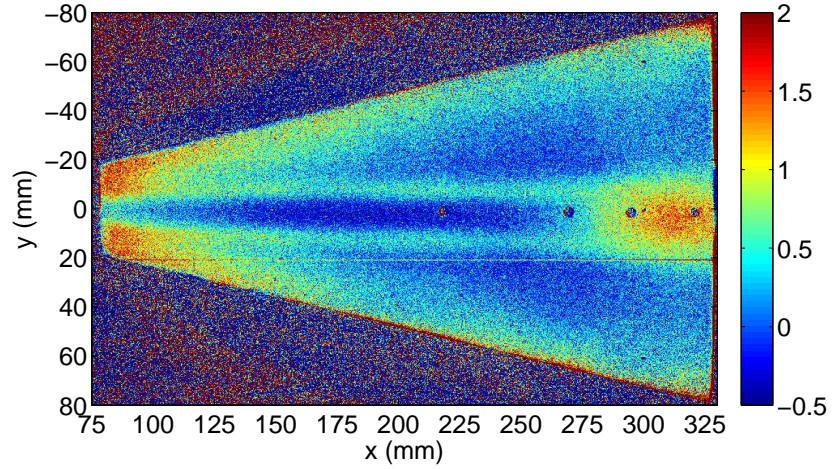


Figure 6.22.: Centerline temperatures for  $\alpha = 4^\circ$  under quiet flow

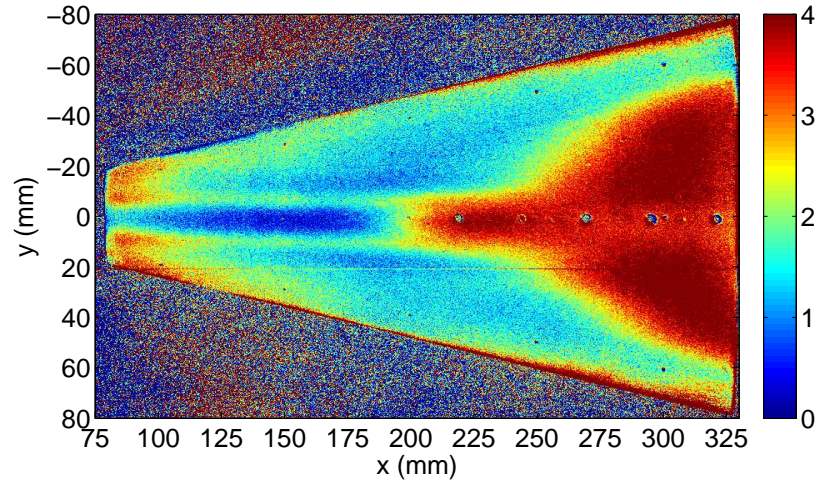
Under noisy flow, the effect of  $Re$  at  $\alpha = 4^\circ$  is comparable to the effect at  $\alpha = 0^\circ$  (Figure 6.23). The shape of the transition front is consistent and it moves upstream at higher  $Re$ . As discussed in Section 6.3.2, centerline transition is ahead of crossflow at  $\alpha = 4^\circ$ . At  $Re = 2.8 \cdot 10^6/m$ , only centerline transition is present.

The trend of transition moving closer to the nosetip as  $Re$  increases is apparent in Figure 6.24, the streamwise temperature profiles from the images in Figure 6.23. The temperature profiles show the classic trend, as demonstrated in Figure 1.1 — temperature decreases slowly as  $x$  increases until transition onset, where  $T$  increases rapidly until reaching a maximum where turbulence is fully developed, and then shows another slow decrease as the turbulent boundary layer thickens.

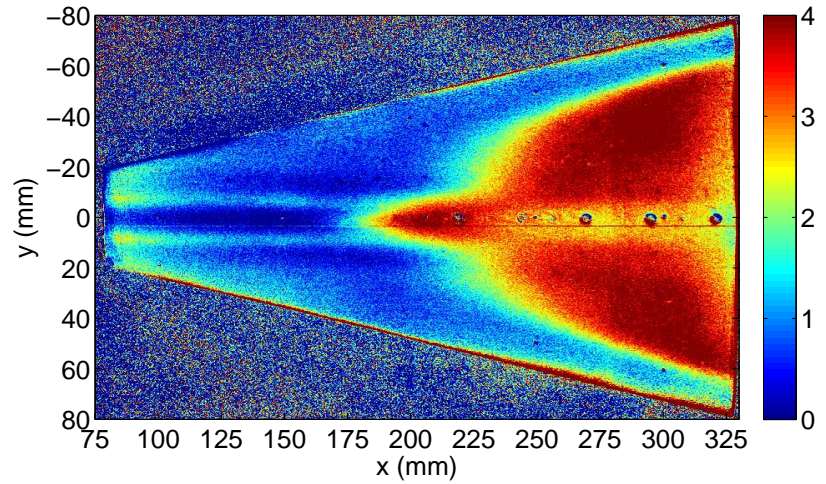




(a)  $Re = 2.8 \cdot 10^6 /m$ ,  $p_0 = 210$  kPa,  $t = 7.95$  s



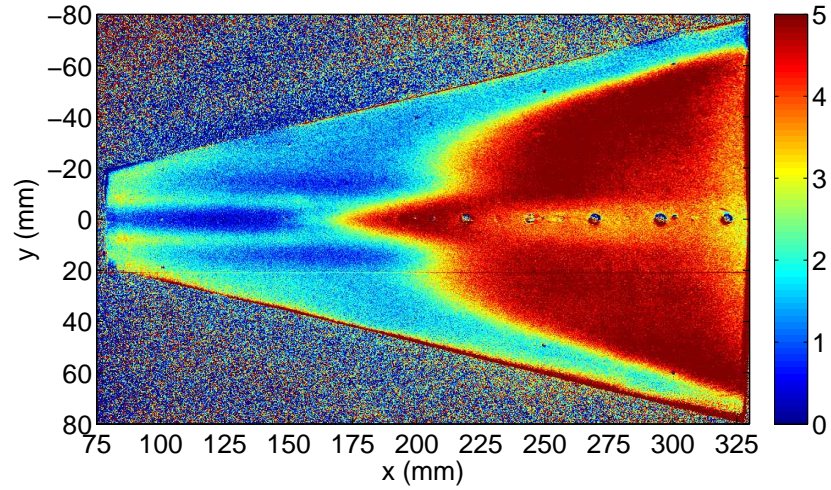
(b)  $Re = 6.1 \cdot 10^6 /m$ ,  $p_0 = 460$  kPa,  $t = 7.95$  s



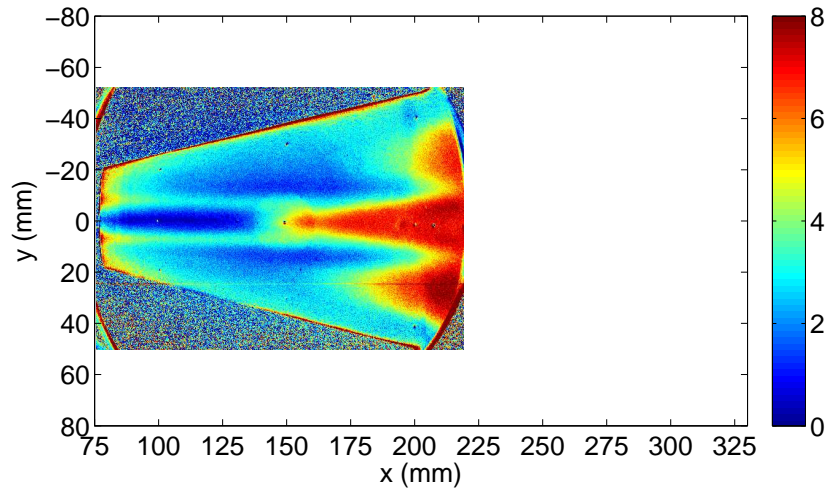
(c)  $Re = 8.1 \cdot 10^6 /m$ ,  $p_0 = 610$  kPa,  $t = 7.95$  s

Figure 6.23.: Effect of varying freestream  $Re$ . Noisy flow,  $M = 5.8$ ,  $\alpha = 4^\circ$





(d)  $Re = 9.5 \cdot 10^6 / \text{m}$ ,  $p_0 = 720 \text{ kPa}$ ,  $t = 7.5 \text{ s}$



(e)  $Re = 11.9 \cdot 10^6 / \text{m}$ ,  $p_0 = 950 \text{ kPa}$ ,  $t = 4.5 \text{ s}$

Figure 6.23.: Effect of varying freestream  $Re$  (continued). Noisy flow,  $M = 5.8$ ,  $\alpha = 4^\circ$

Table 6.3 summarizes the transition locations assessed from Figures 6.21, 6.23, and 6.24 using the method described in Section 6.2.3. The results are comparable to those at  $\alpha = 0^\circ$  (Table 6.2). The  $2.2\times$  delay under quiet flow for  $Re = 11.9 \cdot 10^6 / \text{m}$  is the delay between noisy flow and the flow suspected to be quiet. Once again, there may be some influence of tunnel noise on transition this far downstream in the nozzle.

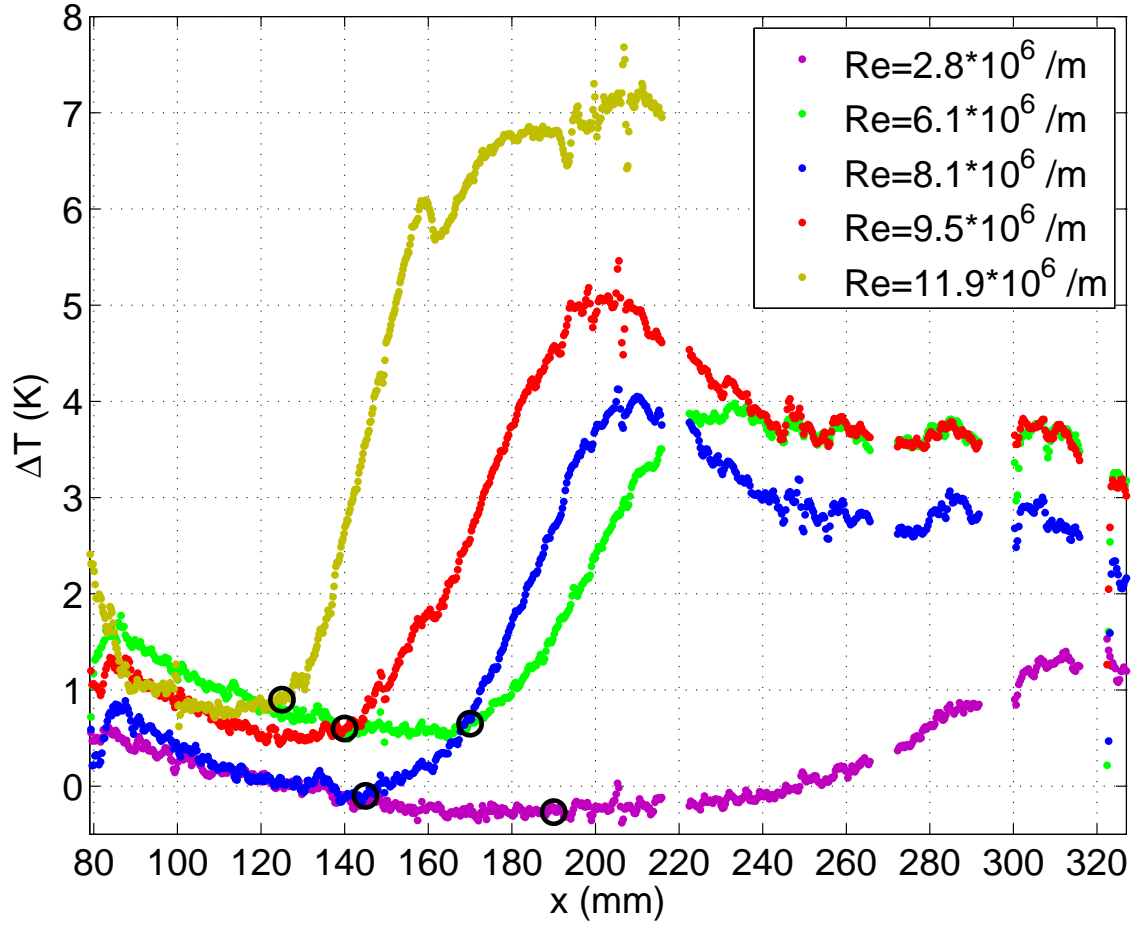


Figure 6.24.: Centerline temperatures for  $\alpha = 4^\circ$  under noisy flow

Table 6.3: Summary of centerline transition locations for  $\alpha = 4^\circ$

$Re$ ( $\cdot 10^6$ /m)	Location (mm)		Transition $Re_x$ ( $\cdot 10^6$ )		Transition Delay quiet $Re_x$ / noisy $Re_x$
	Quiet	Noisy	Quiet	Noisy	
2.6–2.8	> 328	190	> 0.85	0.53	> 1.6
6.0–6.1	> 328	170	> 2.0	1.0	> 1.9
8.0–8.1	> 328	145	> 2.6	1.2	> 2.2
9.5	> 328	140	> 3.1	1.3	> 2.3
11.9	275	125	3.3	1.5	2.2

### 6.3.5 Effect of Surface Finish (Distributed Roughness)

The painted finish on the HIFiRE-5 model necessarily changed the surface roughness from that of a machined aluminum or steel model. Chapter 7 describes fruitless attempts to measure the centerline transition front using coaxial thermocouples mounted flush to the model surface.

A significant error was committed in the preliminary analysis of HIFiRE-5 TSP data. In the first data set, the nozzle-wall boundary layer had separated for a large proportion of each quiet-flow run. The pipe insert was installed in the sting-support section, but the pipe insert extension had not yet been fabricated and installed. This configuration resulted in short run times (3–5 s for quiet flow) and confusing hot-film readings. The separated nozzle flow went undetected until June 2009 when the pipe insert extension was installed. When comparing temperature contours on the HIFiRE-5 under separated and attached nozzle flow, a dramatic difference in transition location was seen — but it was wrongly attributed to the model finish, not rejected because it arose from unacceptable flow quality.

A careful reexamination of earlier data found 0.6 s of attached, quiet flow in one run with the orange-peel finish. Figure 6.25 is a comparison of TSP data from that run with a later smoother-finish paint under otherwise similar conditions. The profilometer found root-mean-square surface finishes of 0.17–0.42  $\mu\text{m}$  for the ‘smooth’ finish. All TSP data in this report except Figure 6.25b has the ‘smooth’ finish. It is unclear whether and where transition occurs for the rough finish. Transition is not apparent on the centerline for the orange-peel finish, but the aft portion of the model ( $x > 290$  mm) was not painted. Because centerline transition cannot be discerned clearly with the rough finish, no conclusion regarding centerline transition can be made.

Crossflow transition or elevated heating from crossflow vortices is present for the rough finish, however. For the smoother finish, crossflow streaks are visible and remain distinct to back edge of model. Elevated heating occurs in the same spanwise

location for both, but the rise becomes larger farther upstream for the rough finish. It is thus concluded that the roughness promoted the amplification of crossflow vortices. However, no quantitative conclusion can be drawn. The  $\Delta T$  range in Figure 6.25b is much larger because the original insulator (INI Nansulate) has a lower thermal conductivity than the LustreKote spray paint.

Figure 6.26 shows the spanwise temperature profiles at  $x = 280$  mm for the two contour plots in Figure 6.25. At this downstream location, both images show temperature peaks at  $y = \pm 30$  mm. However, for the rough finish, the peak is much larger relative to the baseline level. This difference suggests that transition is further advanced for the rough finish.



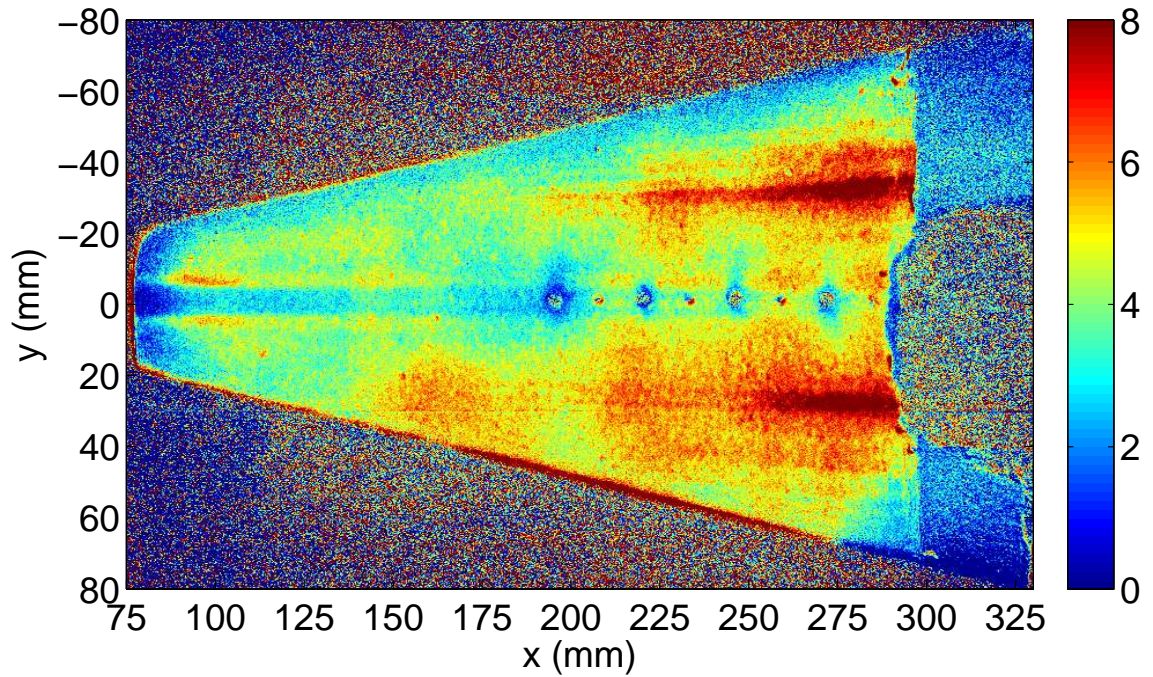
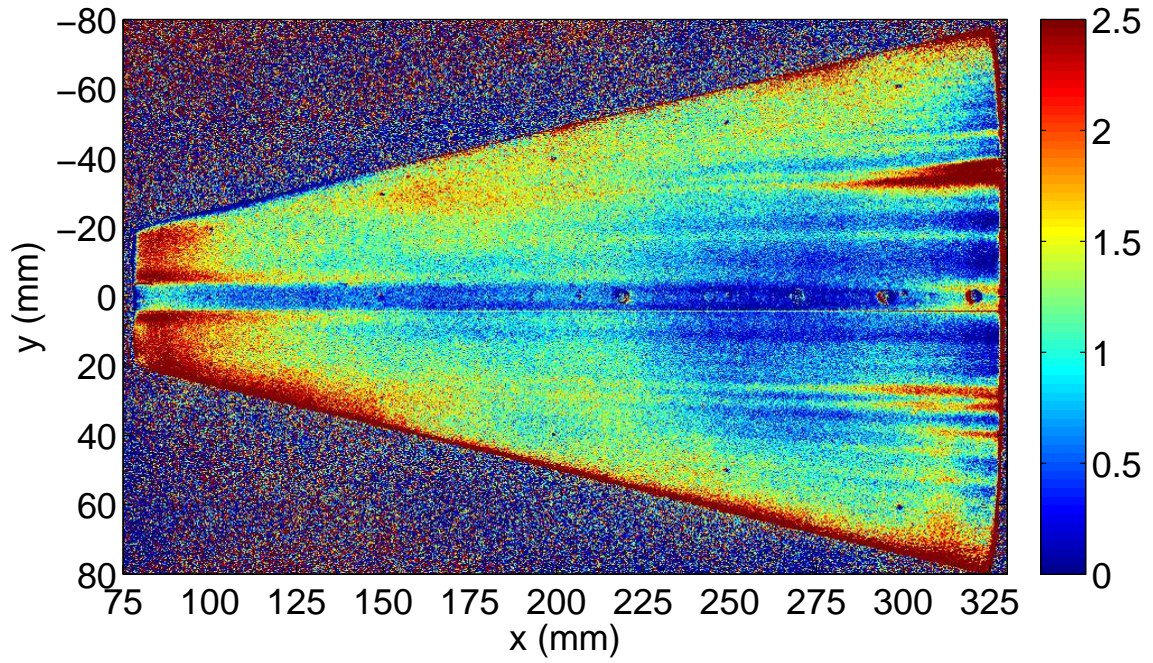


Figure 6.25.: Effect of surface finish. Quiet flow,  $M = 6.0$ ,  $\alpha = 0^\circ$

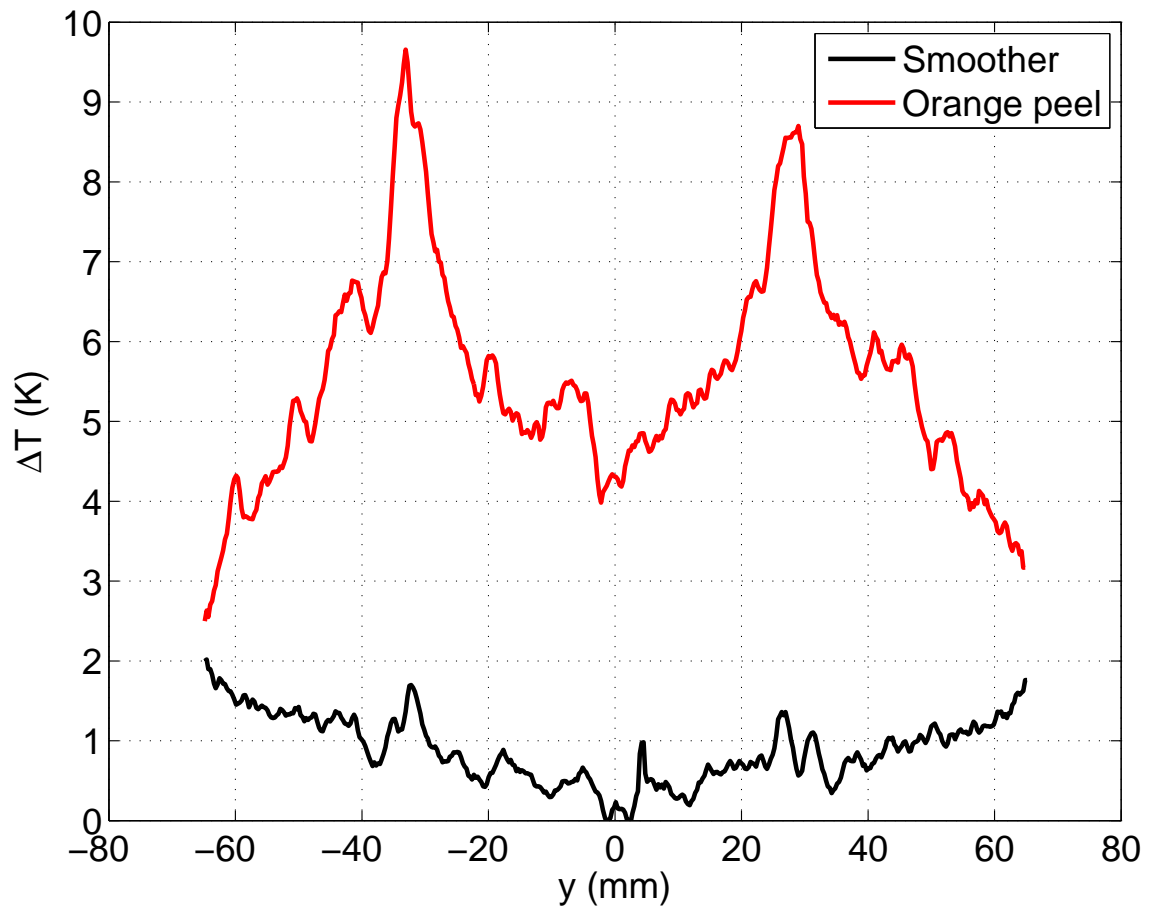


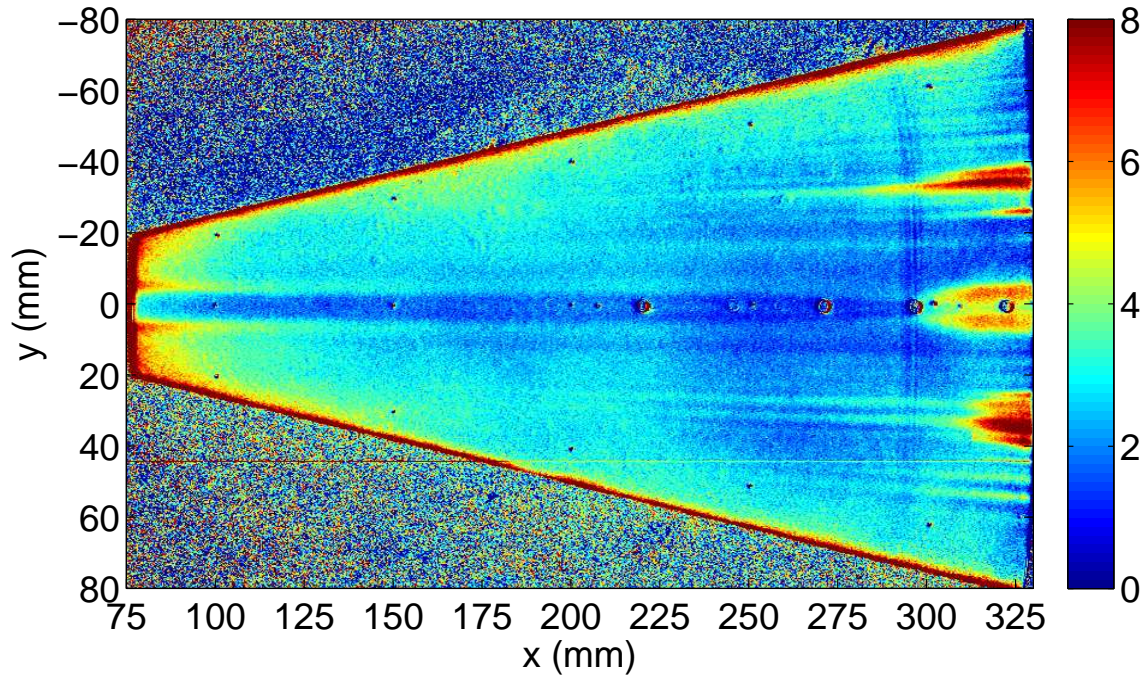
Figure 6.26.: Effect of surface finish on spanwise temperature profile. Quiet flow,  $M = 6.0$ ,  $\alpha = 0^\circ$ ,  $x = 280$  mm

### 6.3.6 Effect of Forward-Facing Step

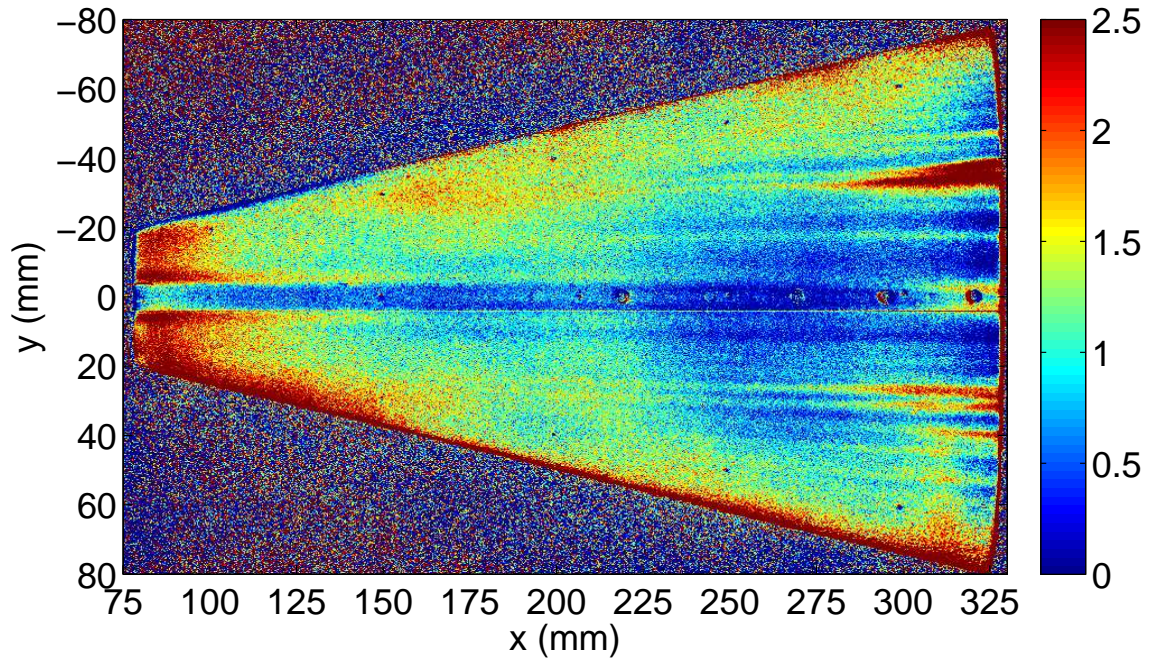
The effect of reducing the forward-facing step at the nosetip/frustum junction ( $x = 76.2$  mm) is illustrated in Figure 6.27. As shown in Figure 6.5, the step is not eliminated entirely but rather the paint was sanded so that its thickness increases more gradually. The paint was tapered over a length of about 6 mm. The overall temperature distributions, and in particular the location of centerline transition onset and hot streaks induced by crossflow vortices, are essentially the same. It is thus concluded that the difference between the steeper step and the smoother fairing of the paint at that location does not substantially affect the boundary layer stability at these flow conditions. On the basis of this similarity, results with the unsanded step are considered comparable to subsequent tests with the edge smoothed. The data from high-pressure runs presented herein (any images through the porthole windows) were collected with the unsanded paint edge. Except for Figures 6.27a and 6.25b, all TSP images through the large window are with the tapered paint edge.

The scale differs significantly between the two subfigures in Figure 6.27. It was surprising that the temperature range would be so different for these two runs — the test conditions are the same, and the paint was not changed. The test with the sanded step was conducted about two months after the earlier tests, which was made one month and several high-pressure runs after the paint was originally applied. The model was stored in its carrying case to prevent extended exposure to light. The difference is probably due to the natural decay in TSP sensitivity.





(a) Original untapered step,  $Re = 10.3 \cdot 10^6 / \text{m}$ ,  $p_0 = 950 \text{ kPa}$



(b) Reduced step,  $Re = 10.2 \cdot 10^6 / \text{m}$ ,  $p_0 = 940 \text{ kPa}$

Figure 6.27.: Effect of forward-facing step at  $x = 76 \text{ mm}$ . Step profiles are presented in Figure 6.5. Quiet flow,  $M = 6.0$ ,  $\alpha = 0^\circ$ ,  $T_0 = 429 \text{ K}$ ,  $t = 0.5 \text{ s}$



## 7. THERMOCOUPLES & HEAT-TRANSFER GAUGES

### 7.1 Thermocouples

#### 7.1.1 Base Thermocouple

Omega Engineering, Inc. SA1-T-72 self-adhesive and COCO-005 Type T beaded thermocouples were used to measure the model temperature before and during runs. To obtain accurate heat transfer calculations from TSP data, it is necessary to know the underlying model temperature. The beaded thermocouple was the first configuration used, but the leads would contact the metal model and the signal would be overridden by electronic noise. The self-adhesive thermocouple's leads were insulated and the sensing head was isolated from the model by the adhesive pad. Although this insulator probably degrades the time response of the thermocouple, it should provide a reliable pre-run measurement. It is uncertain how this one thermocouple's output characterizes the overall model temperature.

The thermocouples were connected to Omega MCJ-T Miniature Electronic Ice point reference junctions. Their output was recorded by the digital oscilloscopes used with other sensors. These reference junctions were used for the base, surface, and coaxial thermocouples. The thermocouple output voltage for the temperatures encountered (roughly 280–330 K) is very small — 0–2.5 mV. Amplifiers were purchased to improve future thermocouple data collection, but they arrived too late for the HIFiRE-5 tests.

Figure 7.1 is a photograph of the base of the model showing the attachment of the base thermocouple. The hollow cylinder at the center of the base is the sting connection. The hole to the left of center is for attaching the leveling block. Above the center of the back end is a hole through which sensor leads pass. The three PCB leads are protected by translucent spiral wrap and terminated by threaded connectors.

The leads from the Schmidt-Boelter gauge and paste-on thermocouple pass through the black tubing, which protects the fine wires. The off-white rectangle above and left of the center is a piece of caulking tape (see below). The paste-on thermocouple is beneath it.

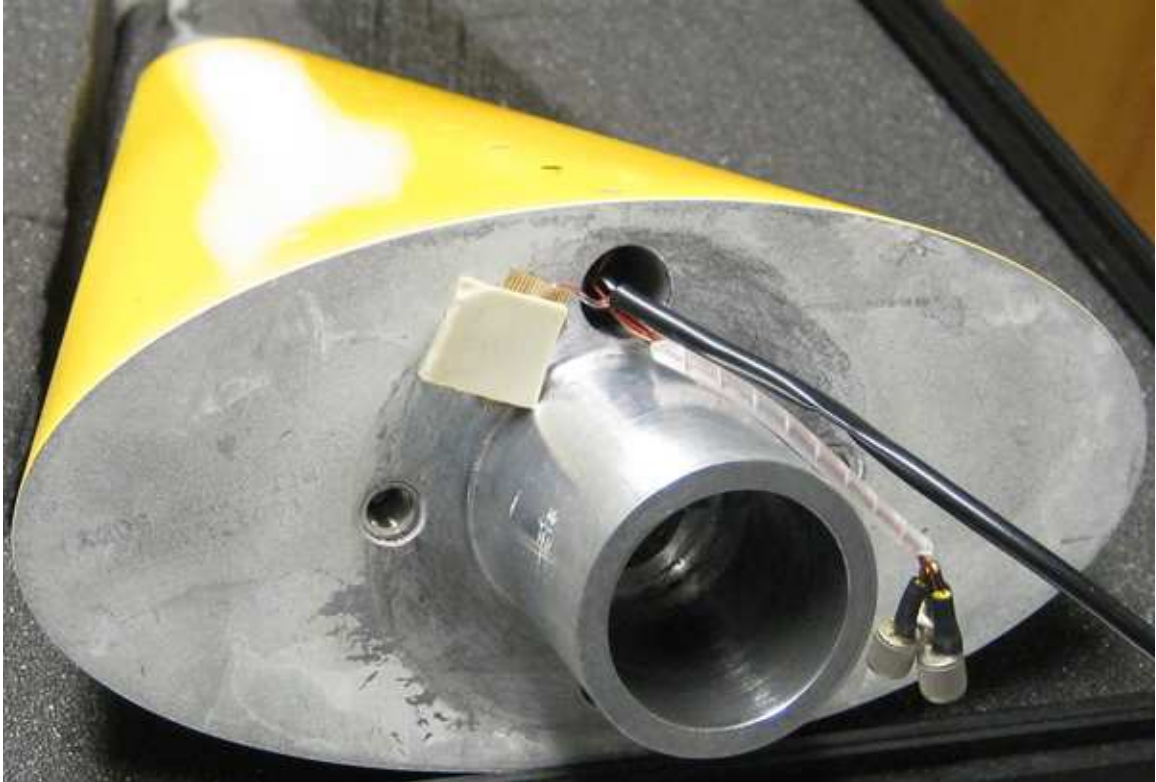


Figure 7.1.: Base thermocouple attachment with extra insulation from caulking tape

Tests were conducted with the base thermocouple insulated by only its built-in adhesive pad and also with a piece of caulking tape applied on the outer surface. The intent of the caulking tape was to insulate the thermocouple from the tunnel flow. Figure 7.2 shows typical thermocouple traces with and without the caulking tape. The conditions were the same for both runs: noisy flow,  $M = 5.8$ ,  $\alpha = 0^\circ$ ,  $Re_i = 11.2 \cdot 10^6$  /m,  $p_{0i} = 980$  kPa, and  $T_{0i} = 433$  K. After startup, the temperature variation was less than 1 K during a run. The caulking tape reduced sensitivity of the thermocouple to tunnel startup and shutdown. The pre-run variation is the same

magnitude as during the run because the small thermocouple signal of about 1 mV is nearing the oscilloscope's resolution limit.

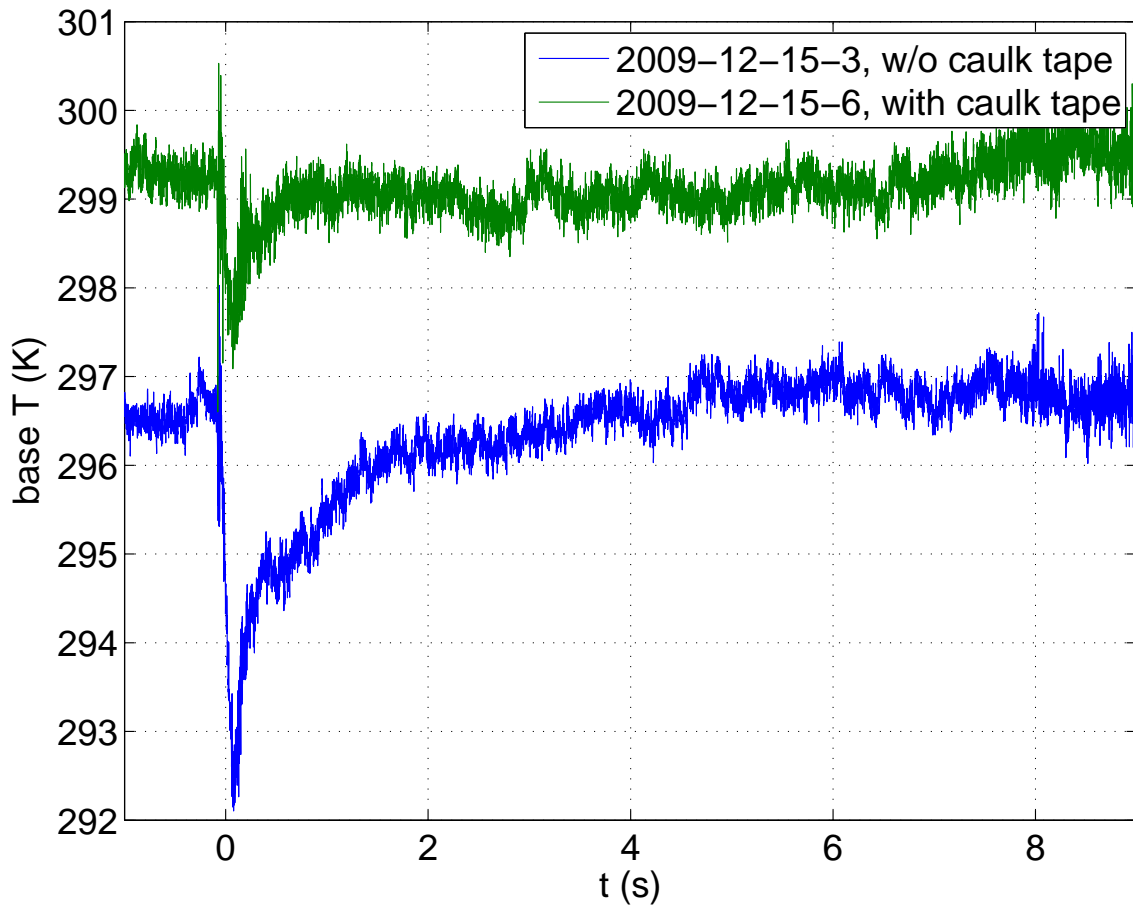


Figure 7.2.: Base thermocouple temperature

The initial temperature generally varies from 285 to 320 K. Figure 7.3 shows the pre-run model temperatures for the twenty runs during one week of HIFiRE-5 testing. The variation during a run (Figure 7.2) is small relative to the variation between runs (Figure 7.3). This comparison indicates that it is important to check the model temperature prior to every run, but perhaps not essential to record temperature *during* every run to have a good estimate of the model temperature for heat-flux calculations. However, the heat flux calculations described below indicate that differences of only  $\approx 1$  K can have an effect.

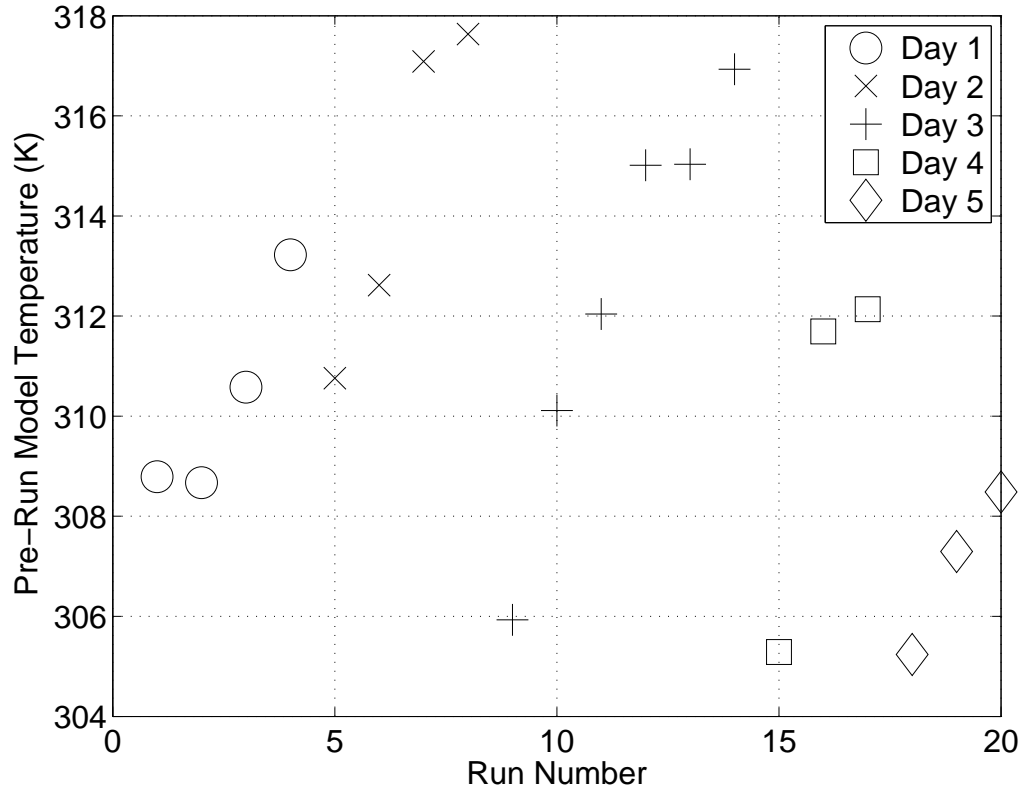


Figure 7.3.: Pre-run model temperature measured by thermocouple on model base for the twenty runs of the 2010-2-8 tunnel entry

It is also noteworthy that the first run each day has a lower temperature than the subsequent runs. The only exception is that the first run on the first day is warmer than the second run. After a model is installed in the BAM6QT, it is customary to open the gate valve to evacuate the atmospheric-pressure air in the tunnel so that the first real tunnel run is conducted exclusively with air that has entered through the filters. The second run is no warmer than the first because the first was already heated by the passing air as the tunnel was evacuated.

After the 6–10-s hypersonic portion of each run, there is a long period of transonic flow until the gate valve closes. The gate valve takes 60 s to close once the control button is pushed, which is usually about 10 s after the run begins. To investigate the effect of this prolonged heating on the model temperature, several runs were conducted with oscilloscopes set to record 100 s of data (of which 2 s were pre-run).

Figure 7.4 shows the stagnation pressure and model temperature for one such run. The diaphragms burst at  $t = 0$  s and the hypersonic flow ends at  $t = 6$  s. The thermocouple temperature drops by 1 K once the run begins, which is unexpected. Perhaps the cold flow is affecting the thermocouple despite the caulking tape. There are several short spikes in the thermocouple signal that appear to be electronic noise. As mentioned above, the thermocouple outputs very small voltages. A mere  $0.04\text{-mV}$  ( $4 \cdot 10^{-5}\text{-V}$ ) fluctuation would cause the 1-K temperature spike. By  $t = 9$  s, when recording of sensor signals usually ceases, the model temperature has risen 3 K from 293 to 296 K. The model temperature continues to climb, however, reaching a peak of 299 K after 28 s and eventually 298 K after 98 s. It is suggested that this 5-K temperature rise is representative of the difference from one run to the next as a result of the heating under transonic flow after the hypersonic portion of the run ceases.

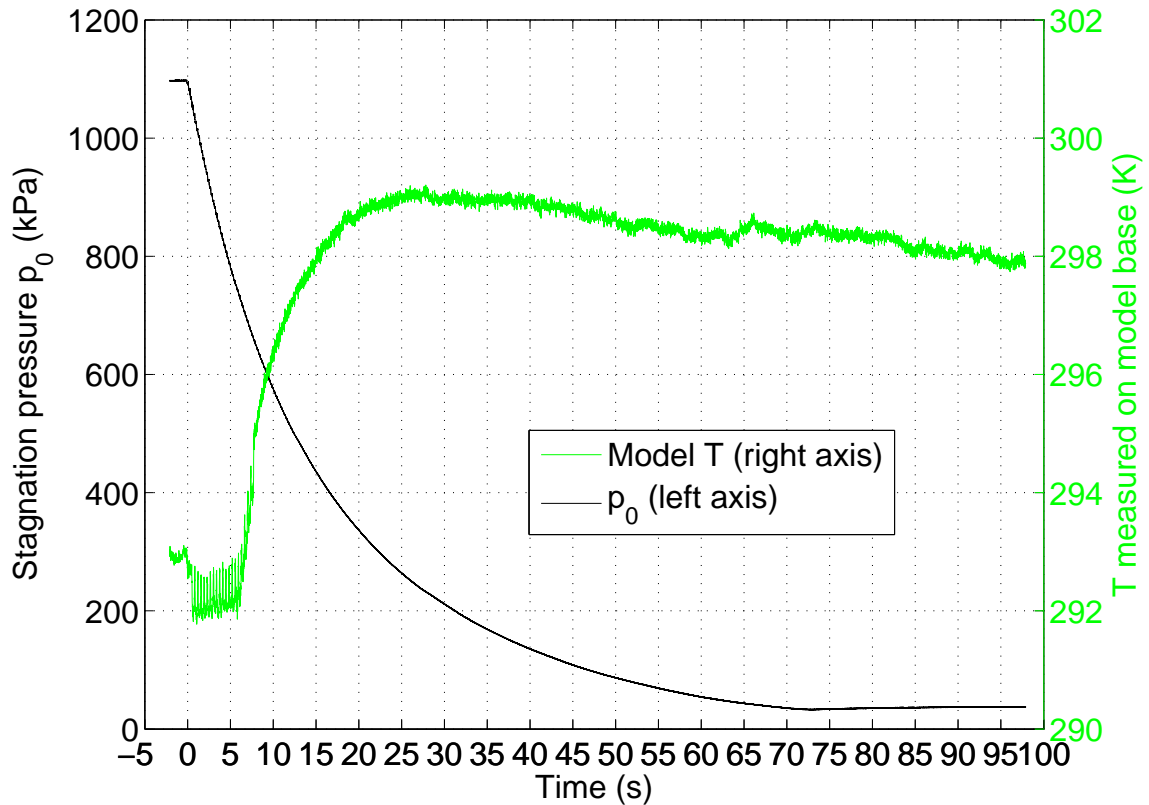


Figure 7.4.: Long-duration record of stagnation pressure and model temperature

### 7.1.2 Coaxial Thermocouples

Coaxial type T (copper/constantan) thermocouples (TCS-T-061-0.25-36-10370) were purchased from Medtherm Corporation of Huntsville, AL. Type T was chosen because the heat transfer properties of the materials most nearly match those of the aluminum model, thereby reducing error due to two-dimensional heat transfer from the surrounding model. The thermocouples are 1/16 in. (1.6 mm) diameter. The model was designed with holes along the centerline for these sensors (see Chapter 5). The heads of these sensors can be shaped to match the contour of the model surface. The original intent for the thermocouples was to use them in conjunction with TSP. The output of the thermocouples would anchor the TSP data enabling quantitative, rather than qualitative, temperature distributions.

The coaxial thermocouples suffered from a very low signal-to-noise ratio. A complicated set of connections was required to avoid ground loops. The expected temperature rise during the run of only a few degrees C corresponds to less than a millivolt of output. The model is too small to fit amplifiers close to the thermocouples, before the signal degrades. Using an amplifier on the thermocouple leads outside of the tunnel succeeded only in increasing the baseline output voltage. For these reasons, the coaxial thermocouples were deemed unsatisfactory for determining transition location. They were uninstalled from the HIFiRE-5 and 1/16-in.-diameter (1.60 mm) dowel pins were used as blanks to plug the holes.

### 7.1.3 Surface Thermocouple

The self-adhesive thermocouple was also used in an effort to measure surface temperature as an alternative to the coaxial thermocouples. It was affixed to the model surface near the aft end 12 mm from the model centerline (Figures 6.1, 6.3, and 7.5).

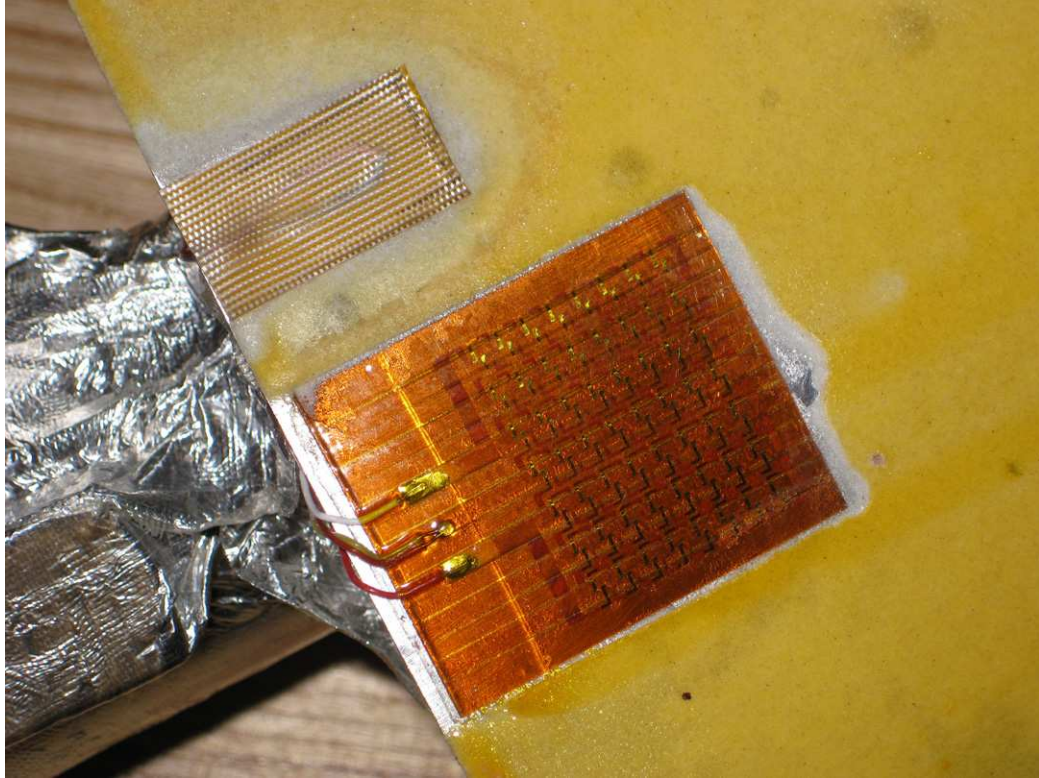


Figure 7.5.: Surface thermocouple (upper left) and thin-film heat-transfer gauge attachment

Although the surface thermocouple output appeared reasonable, showing the expected trends and generally corroborating the heat-transfer gauges (see Section 7.2, below), their use was discontinued. Their effect on the model boundary layer is unknown and their location obstructed important TSP data. Furthermore, it is not understood how the temperature of the thermocouple under its pad compares with the TSP signal, so it could not be used to anchor TSP results with great confidence. The Schmidt-Boelter gauge (see below) had more promise for this purpose.

## 7.2 Heat-Transfer Measurements

### 7.2.1 Thin-Film and Schmidt-Boelter Heat-Transfer Gauges

Fast-response Schmidt-Boelter heat-transfer gauges were ordered from Medtherm in addition to the coaxial thermocouples. Schmidt-Boelter gauges consist of a series of thermocouple junctions on either side of an insulating wafer. The temperature difference across the wafer is proportional to the heat flux into the sensor. They can be used to infer whether the boundary layer is laminar or turbulent due to the increased heat transfer under a turbulent boundary layer. Two models were ordered: 1/16 in. (1.6 mm) diameter 4-30FSB-0.125-36-SJ-21636 and 1/8 in. (3.2 mm) diameter 8-2FSB-0.25-36-20835. The smaller sensor offers better spatial resolution but reduced sensitivity.

An Omega HFS-4 thin-film heat transfer gauge with a  $1 \times 1$  in. ( $2.54 \times 2.54$  cm) area was also applied to the windward surface near the back end off the centerline (Figure 7.5). It appears in older TSP images as the rectangular area of noise below the centerline. The thin-film gauge is more sensitive than the Schmidt-Boelter gauge but has much lower spatial resolution. It also has a faster time response than the Schmidt-Boelter gauge. It was removed for the later sets of tunnel runs so that TSP data could be collected all the way to the back edge of the model.

Unlike the coaxial thermocouples, the Schmidt-Boelter heat-transfer gauge did generate a useful signal. Only one Schmidt-Boelter gauge was installed. A set of these gauges would be able to identify the transition front with spatial resolution equal to the spacing of the sensors. A single heat transfer gauge can be used to anchor the heat transfer calculated from TSP (see below), replacing the disappointing thermocouples.

Figure 7.6 shows the Schmidt-Boelter, thin-film, and surface thermocouple outputs for the run corresponding to the TSP contour plot in Figure 7.7. The sensors are all visible in the image and their locations are as follows: Schmidt-Boelter gauge centered at  $x = 295$  mm,  $y = 0$  mm; thin-film heat transfer gauge sensitive over  $295 < x < 315$  mm,  $5 < y < 30$  mm; and surface thermocouple with its junction



at  $x = 310$  mm,  $y = -10$  mm but a larger footprint due to the adhesive pad. The nozzle-wall hot-film (not shown) detected nozzle-wall boundary-layer separation from 1.6 to 2.2 s (Section 4.2). This separation caused the model boundary layer to become turbulent, resulting in increased heat flux as indicated by the two heat transfer gauges. The run ends at  $t = 6.0$  s, prompting the higher heating described above in Section 7.1 and visible in all three sensors. The surface temperature lags behind the heat flux as expected. The large negative and positive heat fluxes during startup are typical. Their origin and effect upon heat transfer calculations from TSP is unclear.

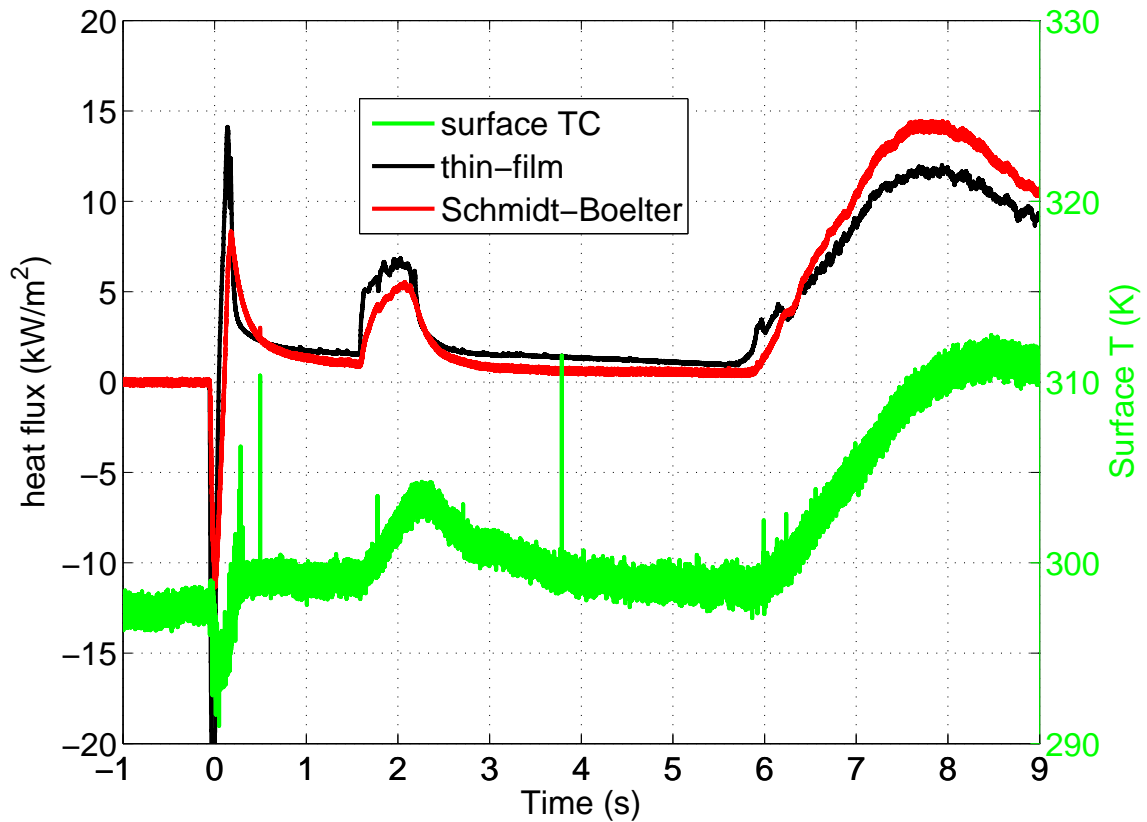


Figure 7.6.: Typical heat-flux and surface temperature under quiet flow

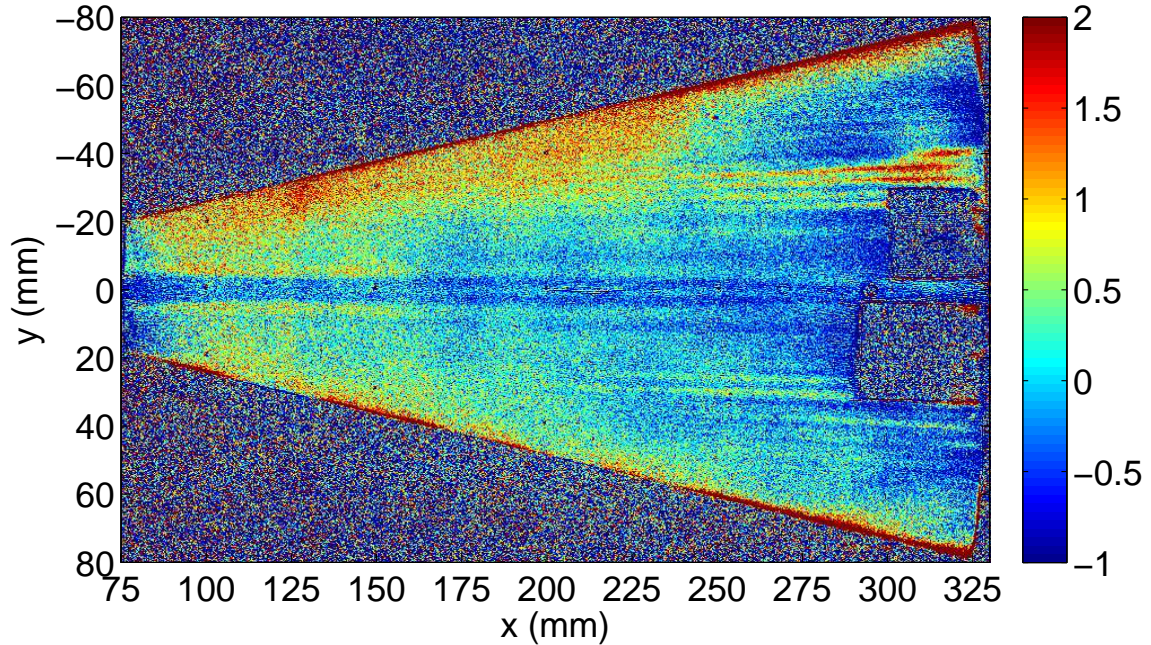


Figure 7.7.: TSP contour for comparison with heat transfer gauges. Thin-film heat transfer gauge outline is larger than that of the surface thermocouple. Quiet flow,  $M = 6.0$ ,  $\alpha = 0^\circ$ ,  $Re = 10.8 \cdot 10^6$  /m,  $p_0 = 980$  kPa,  $T_0 = 425$  K,  $t = 1.0$  s

The two heat-transfer gauges agree regarding the timing of separation (and the resultant turbulent model boundary layer), reattachment, and the end of the run. They do not agree on the heat flux level during the quiet-flow portion of the run, but the discrepancy is probably due to the different locations of the sensors. The Schmidt-Boelter gauge is on the model centerline, where laminar heating is lowest. The thin-film gauge, on the other hand, is off centerline and may additionally encounter higher heating due to crossflow vortices. Figure 7.7 shows the temperature distribution at  $t = 1.0$  s, before separation occurs.

### 7.2.2 Quantitative Heat-Flux Measurements from TSP

The Schmidt-Boelter (S-B) heat-transfer gauge was employed as an *in situ* calibration point in calculating heat flux from TSP data. This technique only became practical after the full TSP data analysis had been completed; in the future, it is recommended to interpret TSP data by calculating global heat flux contours from the beginning. This description is an extension of work with Professor Sullivan [84].

A square patch of TSP data within 5 pixels (1.7 mm) of  $x = 290$ ,  $y = 0$  mm was chosen for comparison to the circular Schmidt-Boelter gauge centered at  $x = 295$ ,  $y = 0$  mm with a 1.6-mm radius. In other words, the TSP data is from a square with sides of 3.3 mm whereas the S-B data is from a circle with a sensing area slightly less than its 3.2-mm diameter. The installation location for the S-B was chosen so it would be useful in identifying transition along the centerline. In retrospect, it was realized that this location is poorly suited to this application — the heating is lowest on the centerline, there is no TSP patch mirrored across a plane of symmetry for comparison, the streamwise heat-flux gradient may be significant, and the spanwise heat-flux gradient is large near the centerline. This location for the TSP patch was selected because it was the best of several poor options. The potential difference between the true heat fluxes at the locations of the TSP and S-B gauge is a source of error in these results that can be reduced easily in future experiments with a better S-B gauge location.

The heat flux computed from Fourier's law adjusted for the finite paint thickness:

$$\dot{q}'' = -k \frac{\partial T}{\partial z} \approx -\frac{k}{L} \Delta T \quad (7.1)$$

where  $k$  is the thermal conductivity of the paint and insulator and  $L$  is their thickness. In practice, another parameter was included to account for the changing model temperature during startup:

$$\dot{q}'' = \frac{k}{L} (\Delta T + T_{\text{ref}} - T_{\text{model}}) \quad (7.2)$$

where  $T_{\text{ref}}$  is the pre-run model base thermocouple temperature and  $T_{\text{model}}$  was measured during the run.

The result of this equation is that there were two parameters, the  $k/L$  ratio and  $T_{\text{model}}$ , that could be adjusted to achieve agreement between the heat flux measured by the Schmidt-Boelter gauge and calculated from the TSP. In theory, the time-dependent thermocouple output  $T_{\text{model}}(t)$  should be used; however, it was found that choosing a constant  $T_{\text{model}}$  gave better agreement. The heat flux during a run was plotted and  $k/L$  and  $T_{\text{model}}$  were adjusted until the Schmidt-Boelter measurement and TSP calculation agreed, as shown in Figure 7.8. In this case,  $k/L = 960 \text{ W/m}^2/\text{K}$ ,  $T_{\text{ref}} = 317.6 \text{ K}$ , and  $T_{\text{model}} = 316.0 \text{ K}$ .

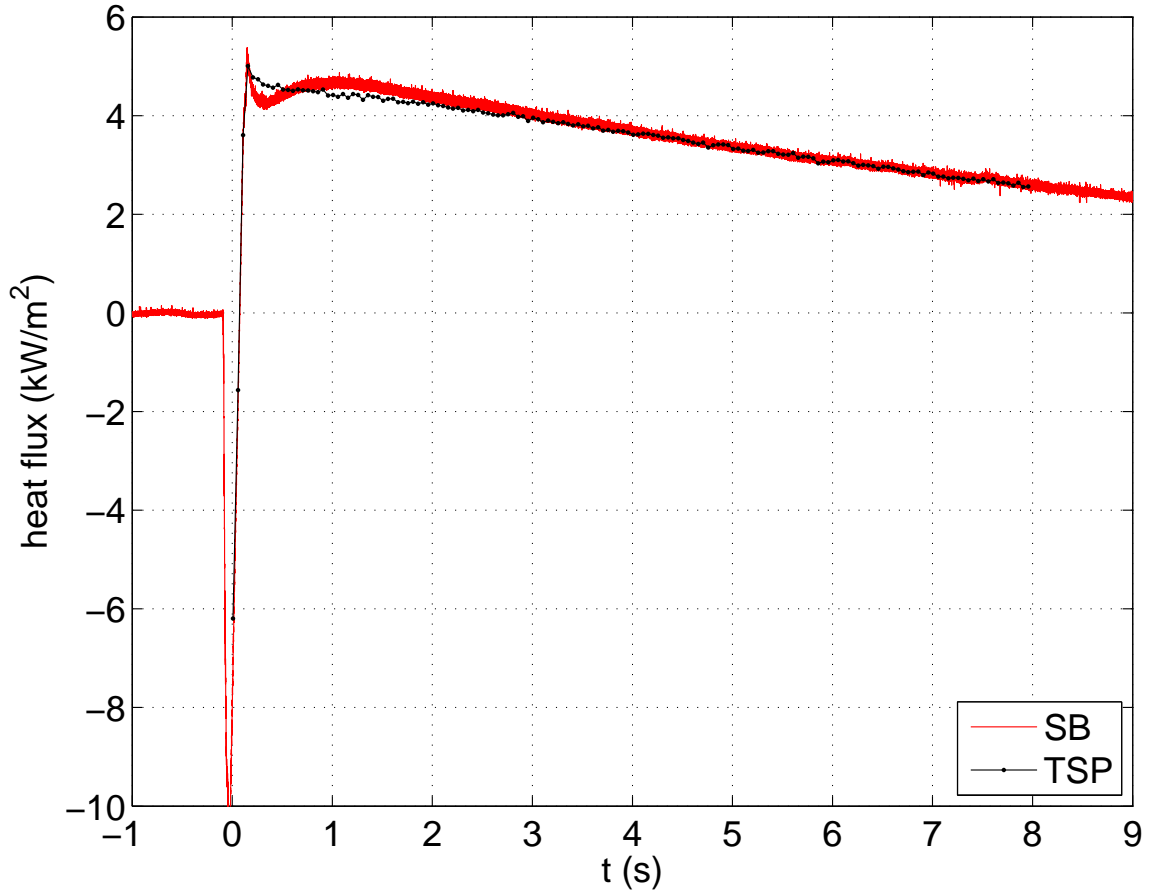


Figure 7.8.: Time history of heat flux during a noisy run.  $M = 5.8$ ,  $\alpha = 0^\circ$ ,  $Re(4.5) = 10.2 \cdot 10^6 / \text{m}$ ,  $p_0(4.5) = 810 \text{ kPa}$ ,  $T_0(4.5) = 410 \text{ K}$

Figure 7.9 shows the global heat flux contour as calculated from the TSP data for this run. This image is essentially the same as Figure 6.8a, but the contours show heat flux in  $\text{kW/m}^2$  instead of temperature in Kelvin. The images look slightly different because the MATLAB script `dftregistration` was employed to register this image using cross correlation instead of the more cumbersome OMS Lite used previously.

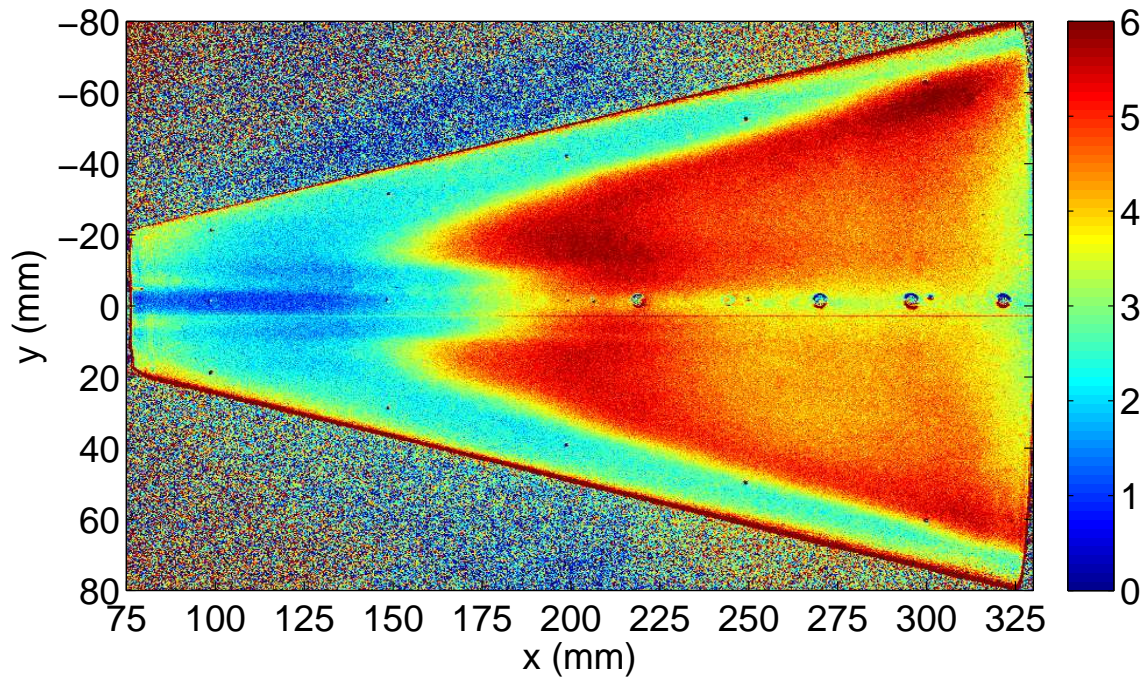


Figure 7.9.: Global heat flux during a noisy run. Contour units are  $\text{kW/m}^2$ .  $M = 5.8$ ,  $\alpha = 0^\circ$ ,  $Re = 10.2 \cdot 10^6 / \text{m}$ ,  $p_0 = 810 \text{ kPa}$ ,  $T_0 = 410 \text{ K}$ ,  $t = 4.5 \text{ s}$

Figure 7.10 shows the heat flux history for a quiet-flow run. The nozzle-wall boundary-layer separates for  $t = 0.9\text{--}2.2 \text{ s}$  and the run ends at  $t = 6.0 \text{ s}$ ; both of these events cause much higher heating on the model, as detected by both the Schmidt-Boelter gauge and TSP. Good agreement was achieved with the same  $k/L = 960 \text{ W/m}^2/\text{K}$  as before. The  $k/L$  ratio should not change from run to run because it is a property of the paint application, so this consistency is reassuring. The reference temperature for this case was  $317.1 \text{ K}$  and  $T_{\text{model}}$  was chosen to be  $315.2 \text{ K}$ . The heat flux measurements have slightly different slopes for  $t = 4\text{--}6 \text{ s}$ , where the TSP shows

a steady decrease while the S-B gauge's output is more nearly constant. It is possible to adjust the calibration constants to match the slope for this portion, but then the agreement is less good at other times. The maximum difference between the TSP and S-B heat fluxes is  $0.12 \text{ kW/m}^2$ , or 25%.

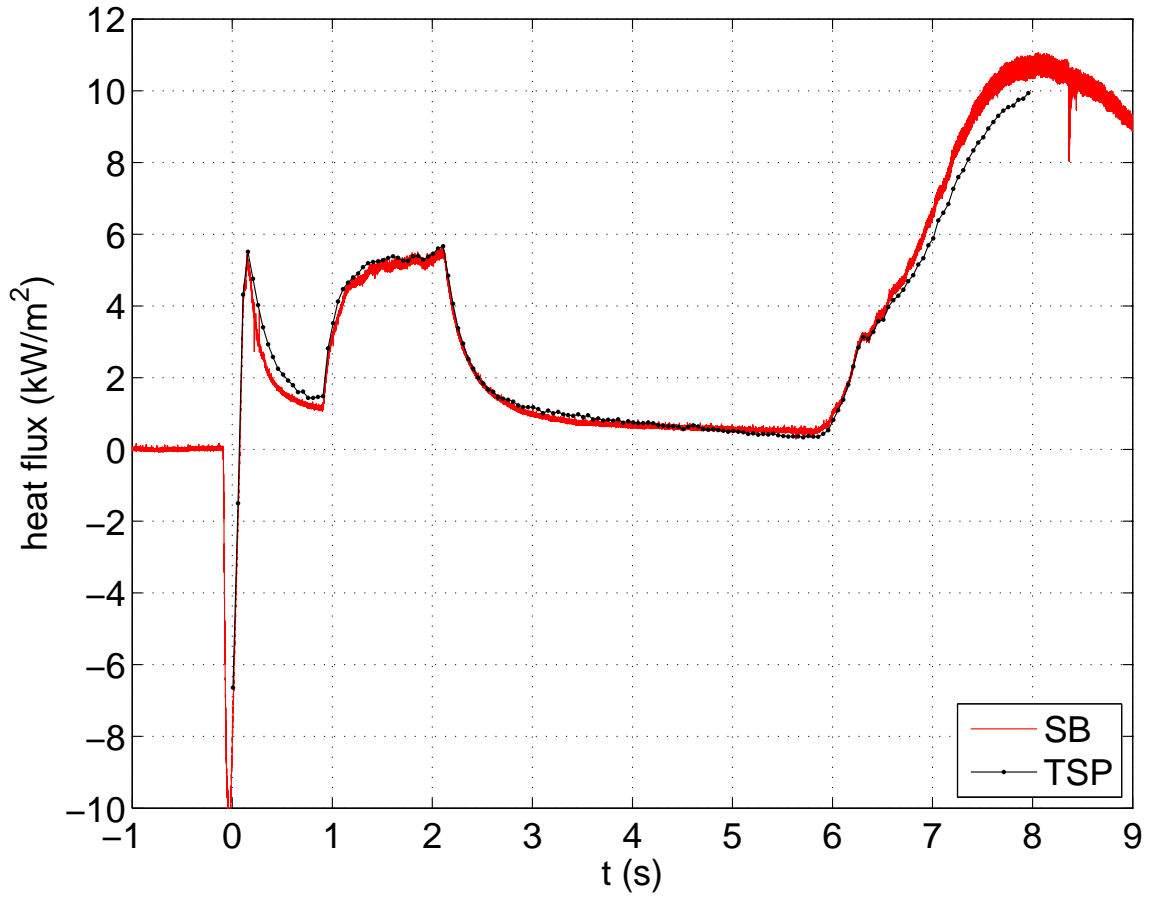


Figure 7.10.: Time history of heat flux during a quiet run.  $M = 6.0$ ,  $\alpha = 0^\circ$ ,  $Re(0.5) = 10.2 \cdot 10^6 / \text{m}$ ,  $p_0(0.5) = 940 \text{ kPa}$ ,  $T_0(0.5) = 429 \text{ K}$

The global heat flux contour for this quiet-flow case is shown in Figure 7.11. The color scale units are  $\text{kW/m}^2$ . Its temperature-contour analog is Figure 6.8b.



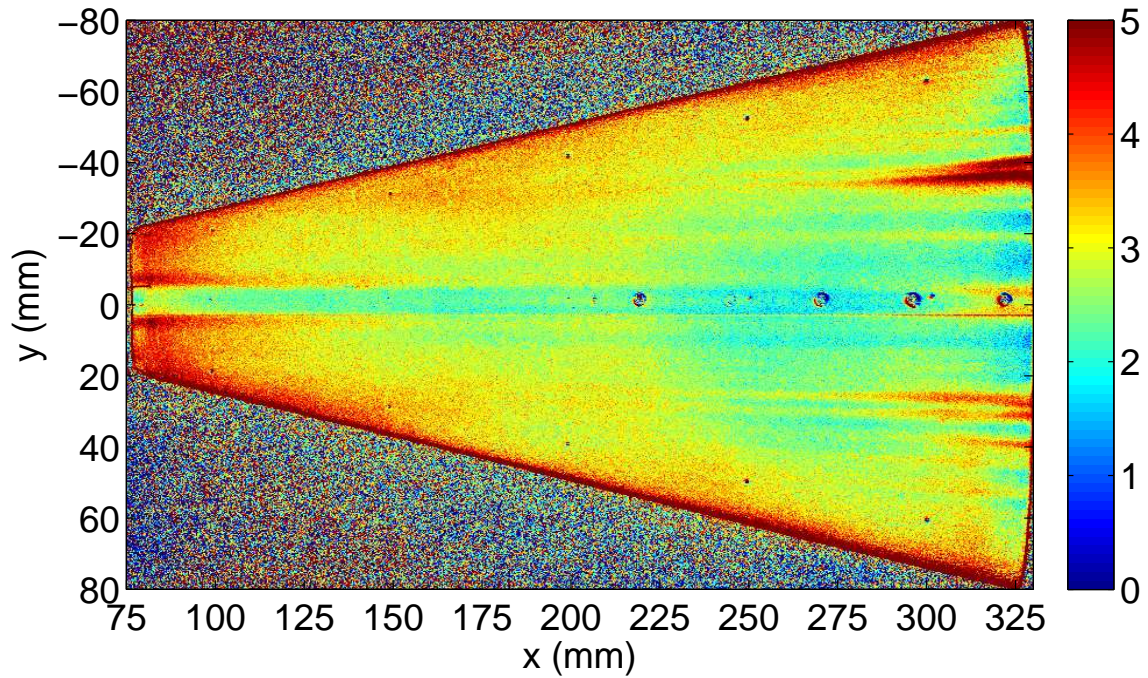


Figure 7.11.: Global heat flux during a quiet run. Contour units are  $\text{kW/m}^2$ .  $M = 6.0$ ,  $\alpha = 0^\circ$ ,  $Re = 10.2 \cdot 10^6 / \text{m}$ ,  $p_0 = 940 \text{ kPa}$ ,  $T_0 = 429 \text{ K}$ ,  $t = 0.5 \text{ s}$

It is clear that work remains to improve this technique and resolve problems such as the impact of the changing model temperature on TSP output. However, it appears that the tandem employment of TSP and a Schmidt-Boelter gauge can be an effective tool to measure heat flux quantitatively.



## 8. MEASUREMENT OF BOUNDARY-LAYER INSTABILITIES WITH FAST PRESSURE SENSORS

### 8.1 PCB Fast-Response Pressure Transducers

The use of PCB fast-response piezoelectric pressure transducers in the BAM6QT is a fairly recent development, first accomplished by Estorf and developed further by Casper [28, 85, 86]. The analysis and interpretation of their output is still a work in progress at this facility [87]. These sensors were first employed to measure second-mode disturbances by Fujii in the Japan Aerospace Exploration Agency’s 0.5 m Hypersonic Wind Tunnel (JAXA HWT1) [88].

The sensors were designed as time-of-arrival sensors, so they produce accurate frequency measurements within a large range — 11 kHz to 1 MHz. The factory-provided shock-tube calibrations unique to each sensor were used to convert the output voltage to pressure. Compared to disturbance frequency measurement by these sensors, their magnitude output is somewhat questionable. Efforts to dynamically calibrate these sensors are ongoing [89].

The PCB sensors were powered by a PCB 482A22 four-channel signal conditioner. The signal conditioner output was then recorded by a Tektronix DPO 7054 oscilloscope (described in Section 3.4) at a 2-MHz sampling rate. This sampling rate is more than 10 times the expected frequency of the disturbances to be measured. A higher sampling rate yielded data files too large to be worked with by MATLAB. The range of the AC-coupled signal was typically on the order of 10–50 mV, so sensitive oscilloscope ranges of 1–5 mV/division were used.

## 8.2 Normalization of PCB Data

After the PCB voltage was converted to pressure with the factory calibration, these fluctuation magnitudes were normalized by the mean wall pressure as computed by Meelan Choudhari. Dr. Choudhari extracted the pressure from the LAURA computations described in Reference 44. As discussed in Section 2.2.2, the conditions simulated were: freestream  $M = 6.0$ ,  $p_0 = 970$  kPa,  $T_0 = 433$  K,  $Re = 10.2 \cdot 10^6$  /m, and model wall  $T = 300$  K. Table 8.1 lists the values of  $p_{\text{wall}}$  that were used.

Table 8.1: Computed mean wall pressures used in PCB normalization

$x$ (mm)	$\overline{p_{\text{wall}}} \text{ (kPa)}$	
	$\alpha = 0^\circ$	$\alpha = 4^\circ$
220	1.369	2.054
270	1.369	2.053
320	1.366	2.053

For other conditions, it was assumed that the mean wall pressure is proportional to the stagnation pressure, so  $p_{\text{wall}}$  was multiplied by  $p_0(t)/970$  (where 970 kPa is  $p_0$  for the computed case). The power spectral density was calculated on a signal with dimensions of  $p'/p_{\text{wall}}$ , where  $p'$  signifies that the PCB signal is the fluctuating component of the pressure.

## 8.3 Computation of Power Spectral Density

A frequency spectrum analysis of PCB data was performed to determine which disturbance frequencies are amplified within the boundary layer. Because these naturally-occurring disturbances are continuous in the frequency domain, power spectral densities were computed [90]. A power spectral density (PSD) is a measurement of power per unit bandwidth — [units]<sup>2</sup> per Hz.

A separate PSD was computed for each 0.1-s segment of PCB data. Longer segments enable more averaging and/or higher frequency resolution, but shorter time segments yields greater uniformity of flow conditions and reduce the probability of

interference from a turbulent burst. This duration was chosen as a balance between these two considerations. Because the BAM6QT produces quasi-steady flow in 0.2-s steps, a 0.1-s segment ensures that at most two stagnation pressure steps will be averaged together, and that a careful selection of the window could realize constant freestream conditions.

Each 0.1-s segment was then divided into 1024-point-long samples, or 1024 points / 2 MHz sampling rate = 512  $\mu$ s per sample, with 50% overlap from one sample to the next. Thus each 0.1-s segment contained 390 512- $\mu$ s samples. The power spectra for each sample was computed, then these spectra were averaged together to produce the PSD for that 0.1 s. The 1024-point sample was selected because it was found to provide an optimal balance of noise reduction and frequency resolution (which is 1.953 kHz).

These calculations were made using built-in functions in MATLAB Version 7.6.0 (R2008a). First,

```
H = spectrum.welch('Blackman', segment_length, 50)
```

was used to create a Welch spectrum estimator using a Blackman window, a 1024-point-long sample (`segment_length`), and 50% overlap between segments. Then

```
psd(H, PCB, 'Fs', sampling_PCB)
```

is used to calculate the power per unit frequency for each 0.1-s sample, where `PCB` is the calibrated PCB data for that sample and `'Fs'`, `sampling_PCB` specifies the PCB sampling rate (2 MHz) in Hz.

The base-10 logarithm of the PSD is computed and plotted to improve the visibility of data over several orders of magnitude. One segment of pre-run data (starting at  $t = -0.2$  s) is shown to establish a baseline electronic noise level. PSD are not calculated for the tunnel startup ( $-0.1 < t < 0.2$ ). Data during nozzle-wall boundary-layer separation are similarly omitted. Finally, segments corrupted by the passage of turbulent bursts were deleted. Waterfall plots such as Figure 8.1a were constructed to facilitate rapid assessment of flow and data quality over the duration of the run. Because details in the signal amplitude are harder to discern, regular line plots such

as Figure 8.1b are used for the rest of the data presented. Each curve in a set of power spectra corresponds to 0.1 s of attached flow between startup and shutdown. During the run, the power decreases steadily as the stagnation pressure decreases.

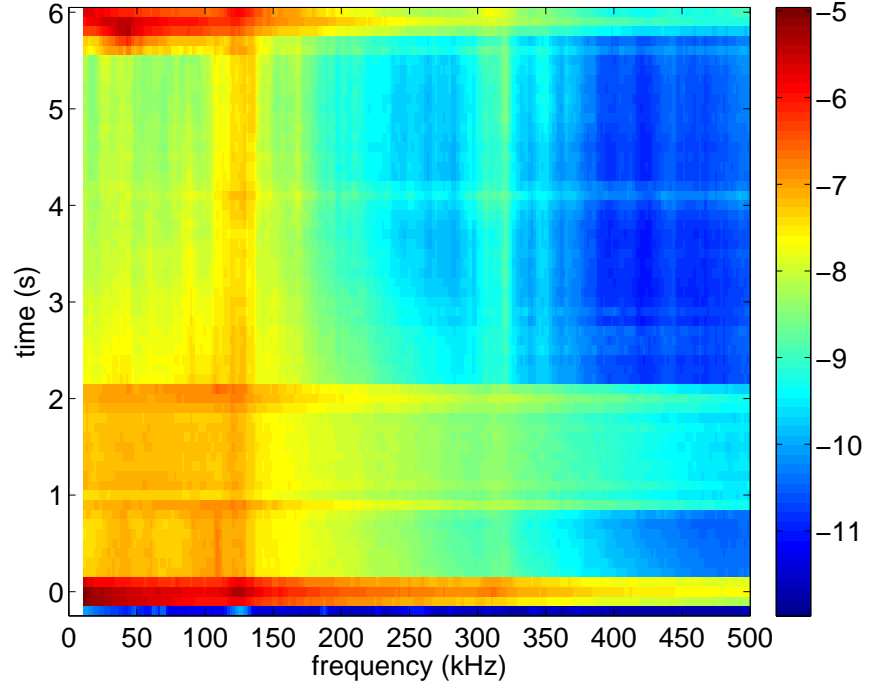
## 8.4 Agreement Between TSP and PCB Indications of Transition Under Noisy Flow

For the majority of BAM6QT HIFiRE-5 tests, temperature-sensitive paint data were collected concurrently with the PCBs. The PCB sensor locations ( $x = 220, 270$ , and  $320$  mm) are visible in the TSP images. The circle centered at  $x = 295$  mm is the Schmidt-Boelter heat-transfer gauge discussed in Chapter 7. This setup enables an outstanding opportunity for side-by-side comparison of the TSP and PCB output. Inferring transition from TSP and interpreting PCB power spectra are both works in progress, so these results are not definitive, but they do provide compelling evidence of agreement between the techniques under noisy flow.

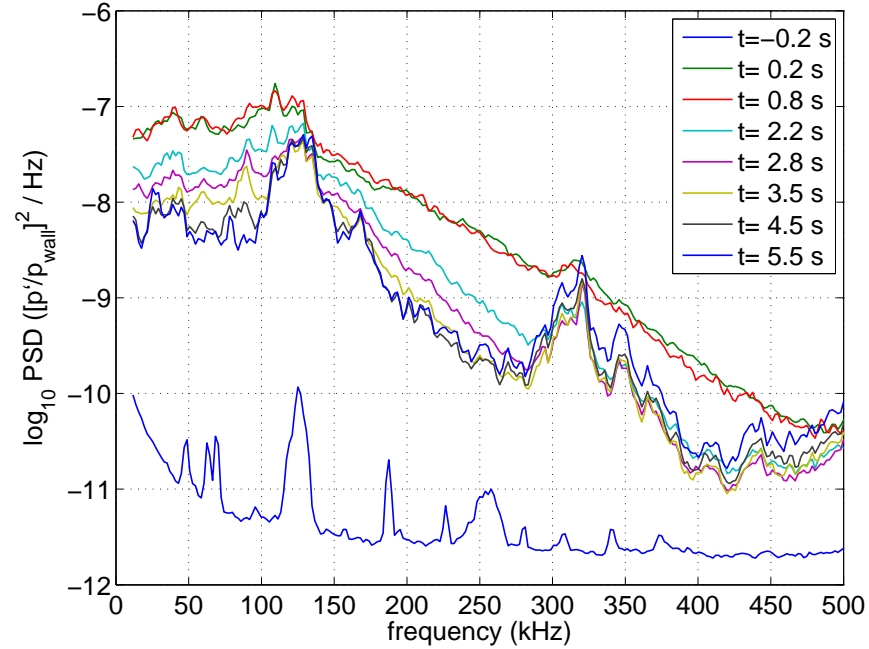
### 8.4.1 4° Angle of Attack

Figures 8.2 and 8.3 show TSP and PCB data, respectively, from one run under noisy flow at 4° angle of attack. Figure 8.2b shows the centerline temperature profile from the global contour in Figure 8.2a. These data are from the lowest pressure case in Figures 6.23 and 6.24. Using the method described in Section 6.2.3, the TSP indicates transition onset at  $x = 190$  mm. The maximum centerline temperature, which is taken to correspond to fully-turbulent flow, occurs at  $x = 310$  mm.

The PCB at  $x = 220$  mm shows disturbances centered at 100 to 110 kHz with a 60-kHz width, which are suspected to be due to second-mode waves. This sensor's location is 30 mm downstream of the initial temperature rise, but  $\partial T/\partial x$  is still very small and the location is well ahead (90 mm) of the end of transition, so it is not surprising that these disturbances are visible in the power spectra. The peak's frequency decreases as stagnation pressure decreases, which is expected [85,86]. Lower

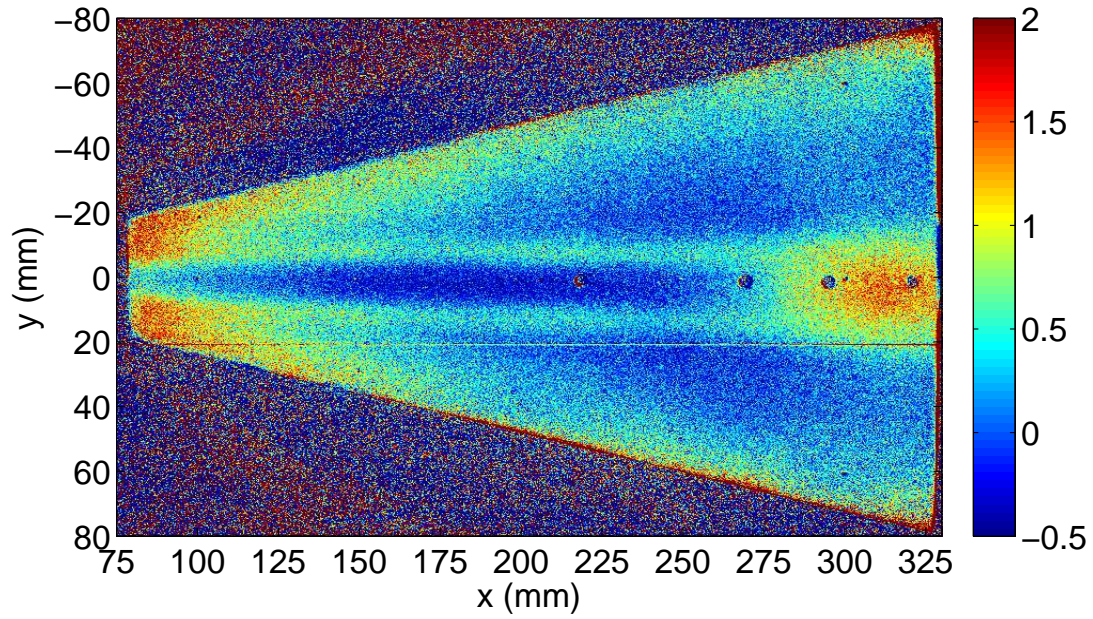
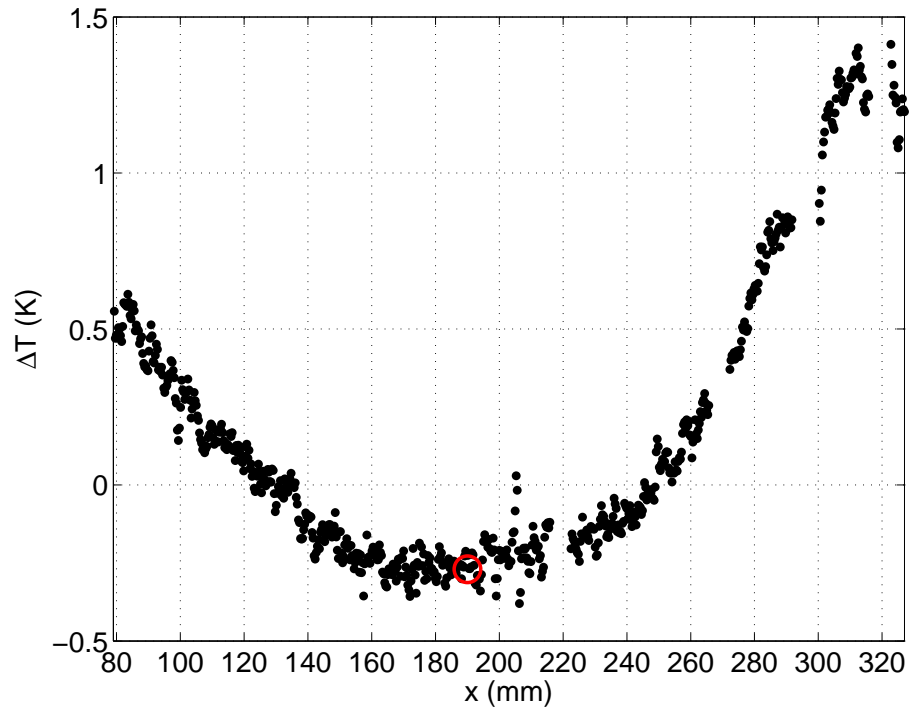


(a) Waterfall plot. Colorbar on right indicates amplitude, the  $\log_{10}$  PSD ( $[p'/p_{\text{wall}}]^2/\text{Hz}$ ). Startup for  $-0.1 < t < 0.2$ , separation for  $t = 0.9\text{--}2.1$ , turbulent bursts at  $t = 2.5\text{--}2.7, 2.9, 4.1\text{--}4.2$ , shutdown at  $t = 5.6$  s



(b) Line plot. Amplitude decreases as time increases. Startup, separation, and turbulent bursts are excised.

Figure 8.1.: Representative PCB power spectra. Quiet flow,  $M = 6.0$ ,  $\alpha = 0^\circ$ ,  $Re_i = 10.4 \cdot 10^6 / \text{m}$ ,  $p_{0i} = 970$  kPa,  $T_{0i} = 433$  K,  $x = 320$  mm

(a) TSP  $\Delta T$  (K)

(b) Centerline temperature profile. Red circle marks inferred transition onset location

Figure 8.2.: TSP for comparison to PCB power spectra under noisy flow.  $M = 5.8$ ,  $\alpha = 4^\circ$ ,  $Re = 2.8 \cdot 10^6$  /m,  $p_0 = 210$  kPa,  $T_0 = 396$  K,  $t = 7.95$  s

stagnation pressure corresponds to lower Reynolds number and a thicker boundary layer, which in turn would have a lower associated second-mode wave frequency. Lower stagnation pressure also implies lower initial disturbance amplitudes. This factor may explain the interesting finding that the peak amplitudes do not collapse when normalized by stagnation pressure.

The PCB at  $x = 270$  mm shows higher noise levels over a broad range of frequencies, suggesting that the boundary layer is more turbulent (Figure 8.3b). A hump centered at  $\approx 100$  kHz is visible, but it does not rise as far above the signal at other frequencies (less than half of an order of magnitude, rather than more than one order). No evidence of the 100 kHz peak is visible in the third PCB ( $x = 320$  mm, Figure 8.3c). This result is consistent with the TSP indication of fully-turbulent flow. The sensor does, however, exhibit a peak at 125 kHz that appears to be an amplification of some noise detected during the pre-run as well. The significance of this peak will be discussed further in Section 8.5.

Under noisy flow, transition occurred ahead of the first PCB sensor for all stagnation pressures tested except the lowest. As expected, the PCB power spectra exhibited broad-frequency noise for these cases. Figure 8.4, which presents power spectra for the three PCBs for a run with  $Re_i = 7.2 \cdot 10^6$  /m, is exemplary of this result. A TSP contour plot from this run is presented in Figure 6.23b. Figure 8.4c shows the same 125 kHz peak as Figure 8.3c. The 300-kHz peak in Figures 8.3a and 8.4a is thought to be spurious because of its invariance with  $Re$  and presence for both laminar and turbulent boundary layers.



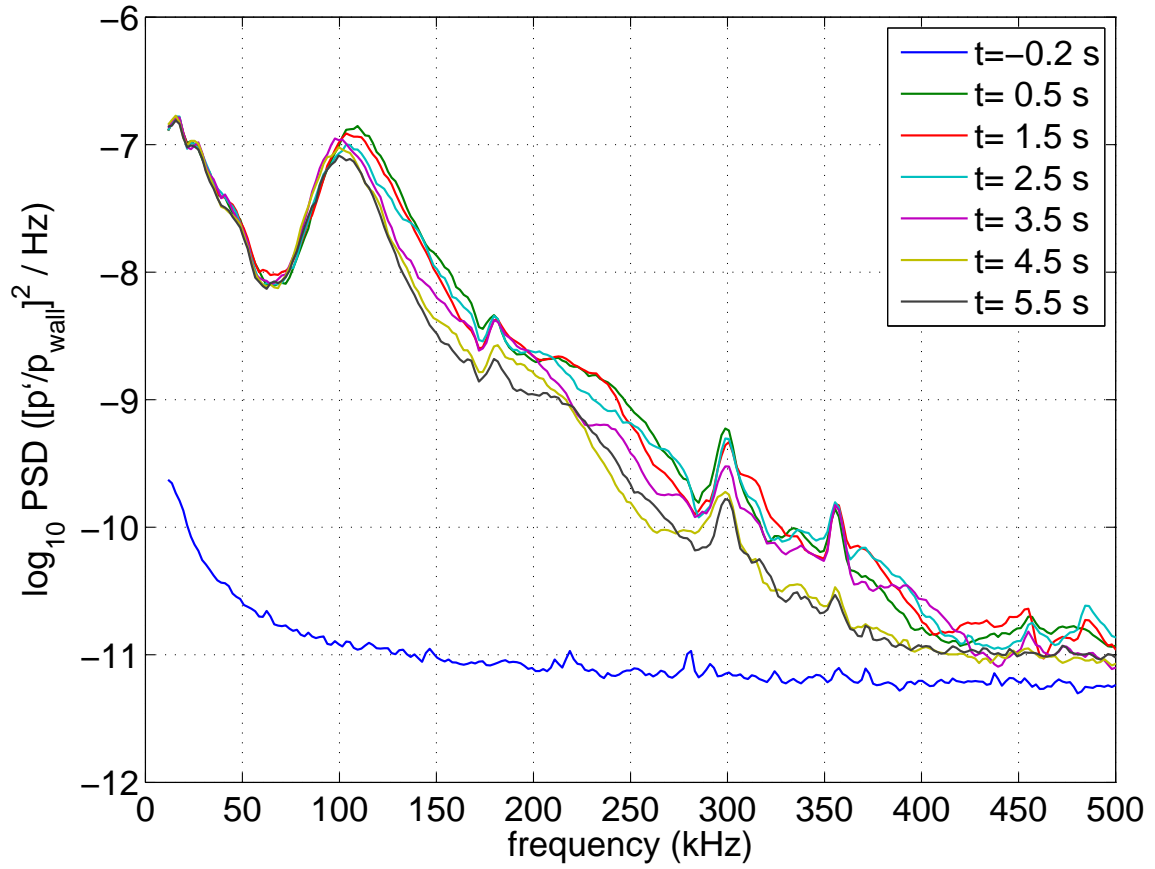
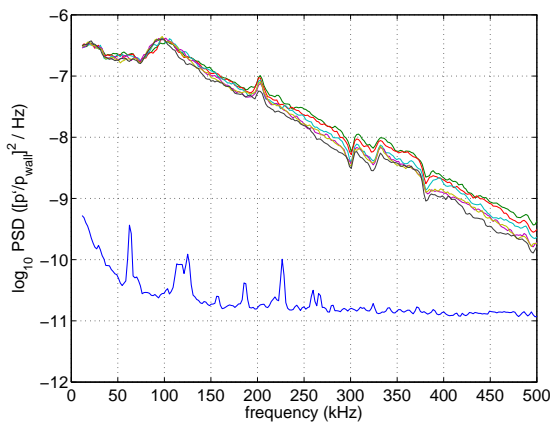
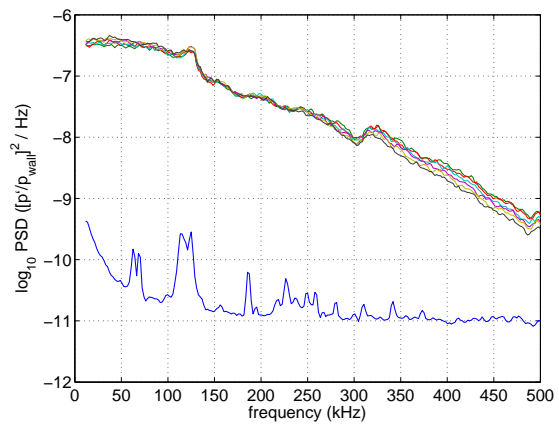
(a)  $x = 220$  mm(b)  $x = 270$  mm(c)  $x = 320$  mm

Figure 8.3.: PCB power spectra under noisy flow. Legend common to all subfigures.  $M = 5.8$ ,  $\alpha = 4^\circ$ ,  $Re_i = 3.3 \cdot 10^6$  /m,  $p_{0i} = 280$  kPa,  $T_{0i} = 433$  K

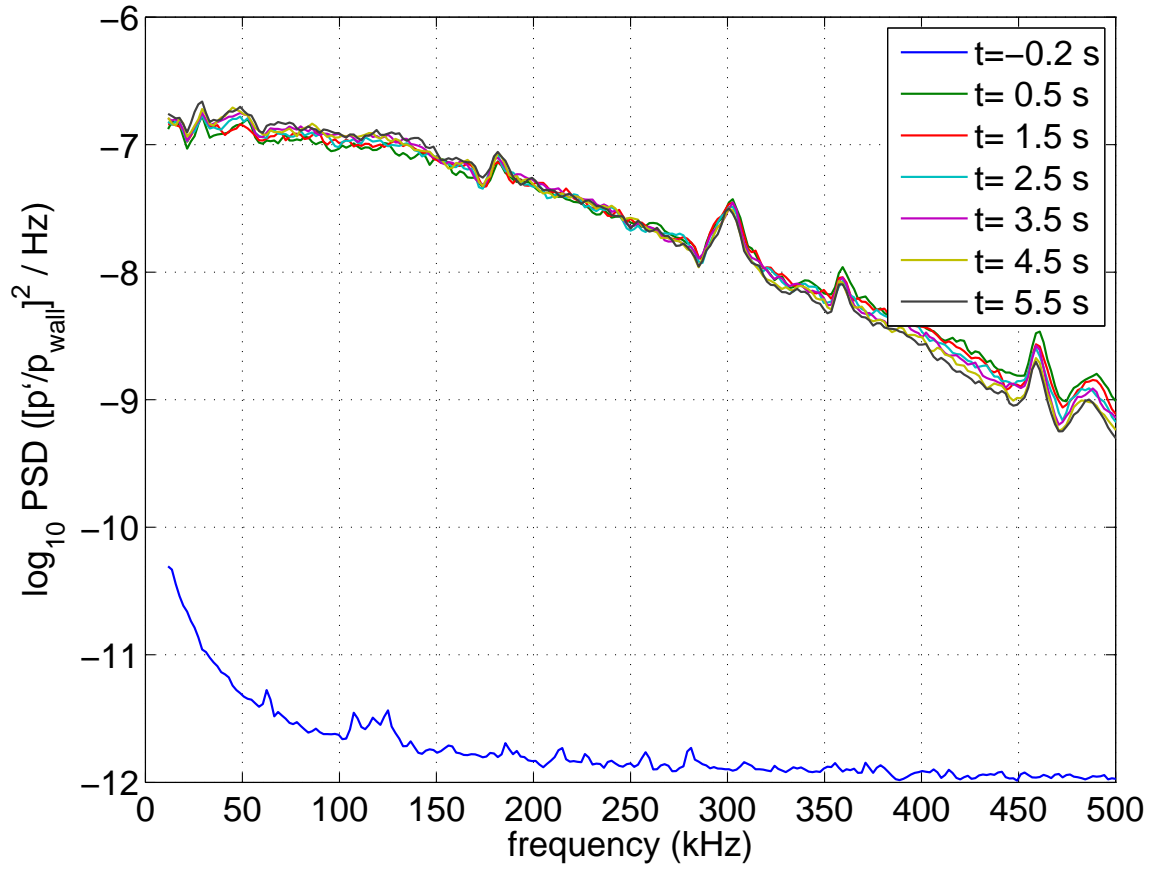
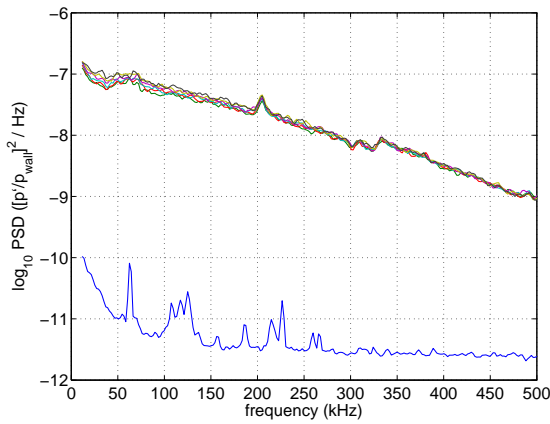
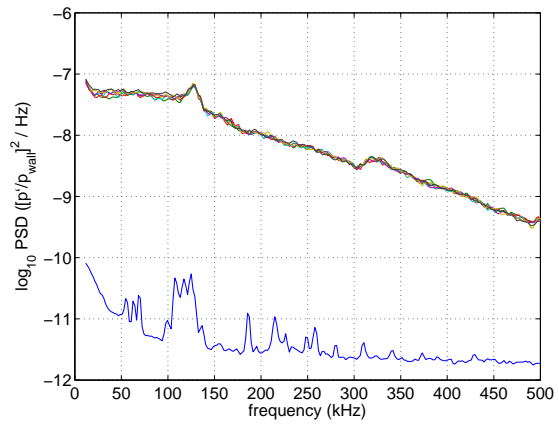
(a)  $x = 220$  mm(b)  $x = 270$  mm(c)  $x = 320$  mm

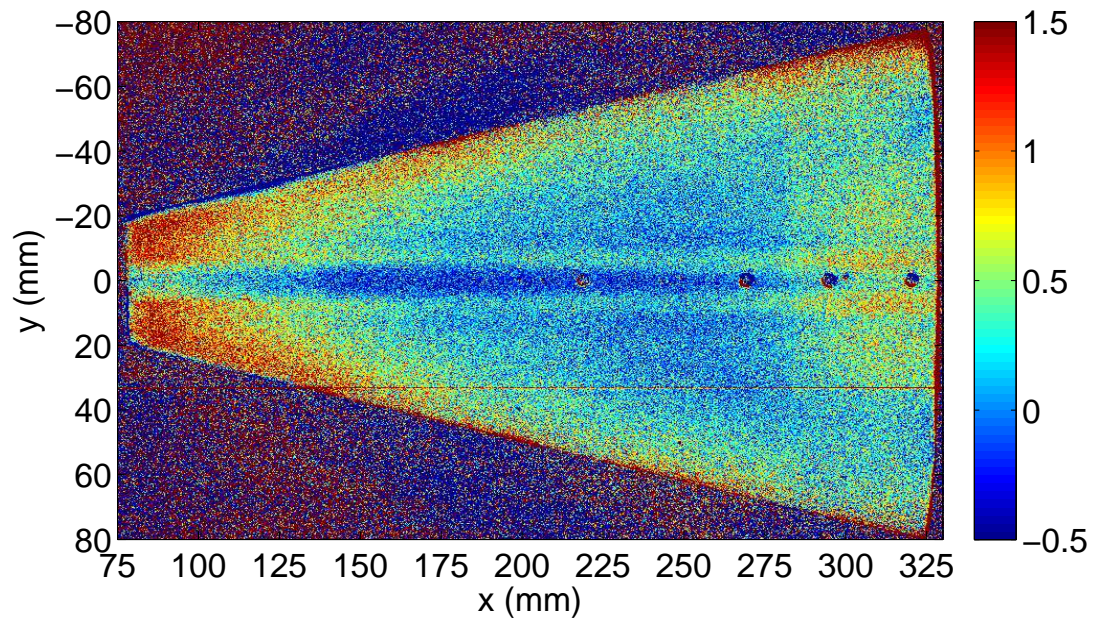
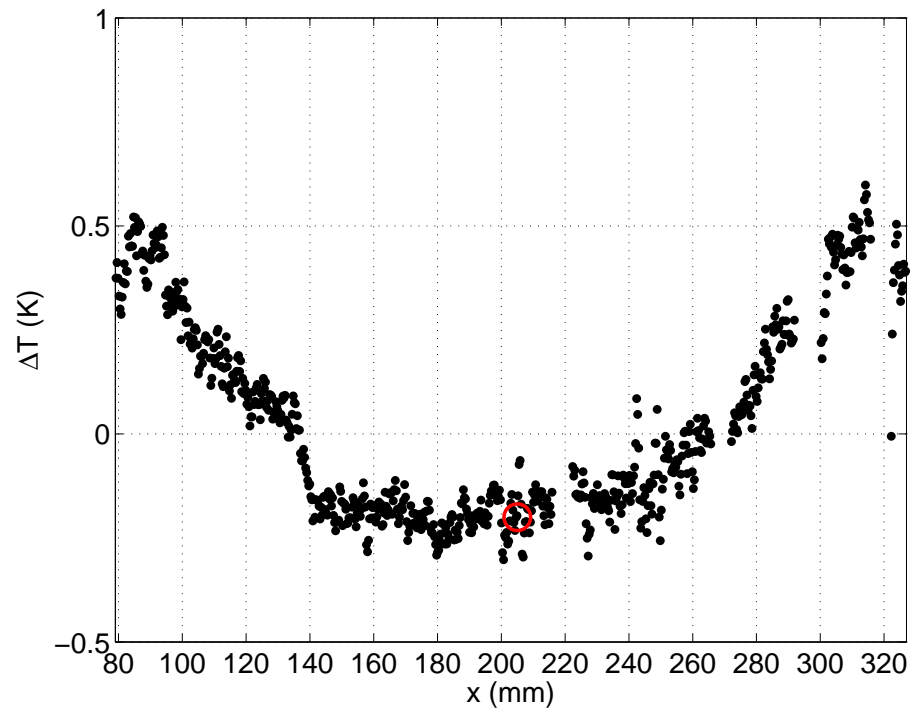
Figure 8.4.: PCB power spectra under noisy flow. Legend common to all subfigures.  $M = 5.8$ ,  $\alpha = 4^\circ$ ,  $Re_i = 7.2 \cdot 10^6$  /m,  $p_{0i} = 630$  kPa,  $T_{0i} = 433$  K

### 8.4.2 $0^\circ$ Angle of Attack

Figures 8.5 and 8.6 are analogous to 8.2 and 8.3 except they show data for  $0^\circ$  instead of  $4^\circ$  angle of attack. Figure 8.5b shows the centerline temperature profile from the global contour in Figure 8.5a. These data are from the lowest-pressure case in Figures 6.19 and 6.20. The TSP indicates transition onset at  $x = 205$  mm. The temperature rise is very gradual and the TSP signal-to-noise ratio is not very good at this low pressure, so the transition location is very hard to judge. Any estimate from 180 to 240 mm seems reasonable, which is an uncertainty of  $\pm 15\%$ .

The PCB at  $x = 220$  mm (Figure 8.6a) shows disturbance frequencies of 60–65 kHz. Similar frequencies are detected further downstream at  $x = 270$  mm (Figure 8.6b). According to the TSP data, these sensors both appear to be under a transitional boundary layer. Figure 8.6b exhibits a large pre-run peak at  $f = 62$  kHz, so there is some concern that the peak observed during the run could be affected by noise evident in the prerun signal. However, during the run the peak frequency decreases by about 10%, which meets with the expectation of a thickening boundary layer as  $Re$  decreases. For the PCB at  $x = 320$  mm (Figure 8.6c), where the TSP indicates a turbulent boundary layer, the power spectra no longer display the distinct peak at 60–65 kHz. Figure 8.6c bears a strong resemblance to 8.3c despite the different angle of attack. The peak at 125 kHz is once again present before and during the run.

For  $\alpha = 0^\circ$ , the TSP indicates that the boundary layer transitions to turbulent ahead of the first PCB sensor at the other (higher) Reynolds numbers tested. The PCB power spectra exhibit high-amplitude disturbances over a large frequency range. This result is the same as for  $\alpha = 4^\circ$ .

(a) TSP  $\Delta T$  (K)

(b) Centerline temperature profile. Red circle marks inferred transition onset location

Figure 8.5.: TSP for comparison to PCB power spectra under noisy flow.  $M = 5.8$ ,  $\alpha = 0^\circ$ ,  $Re = 2.8 \cdot 10^6$  /m,  $p_0 = 210$  kPa,  $T_0 = 396$  K,  $t = 7.95$  s

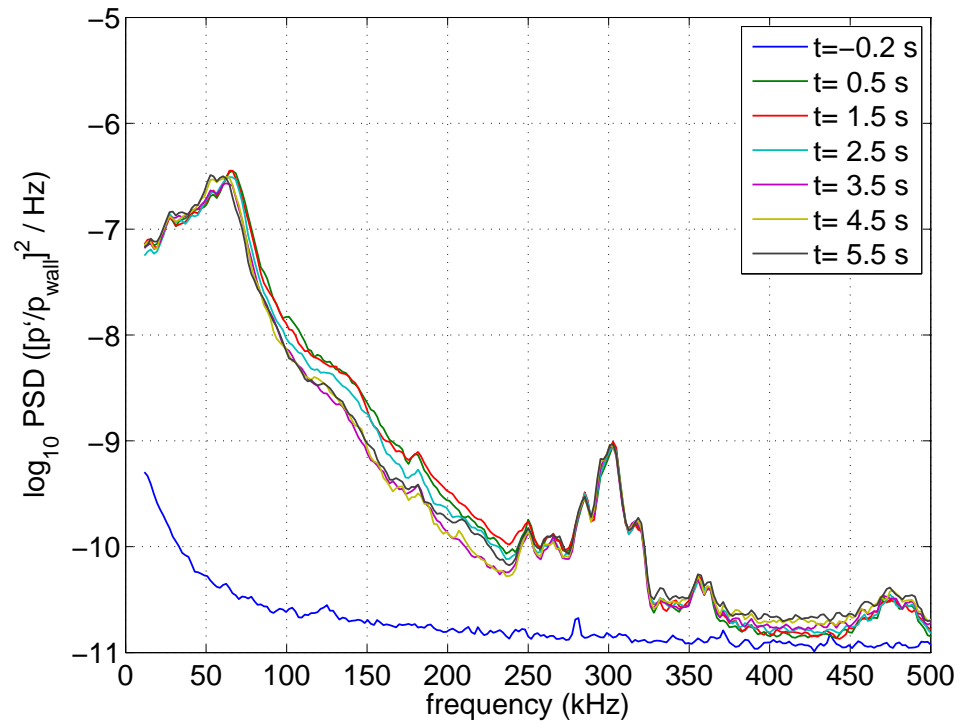
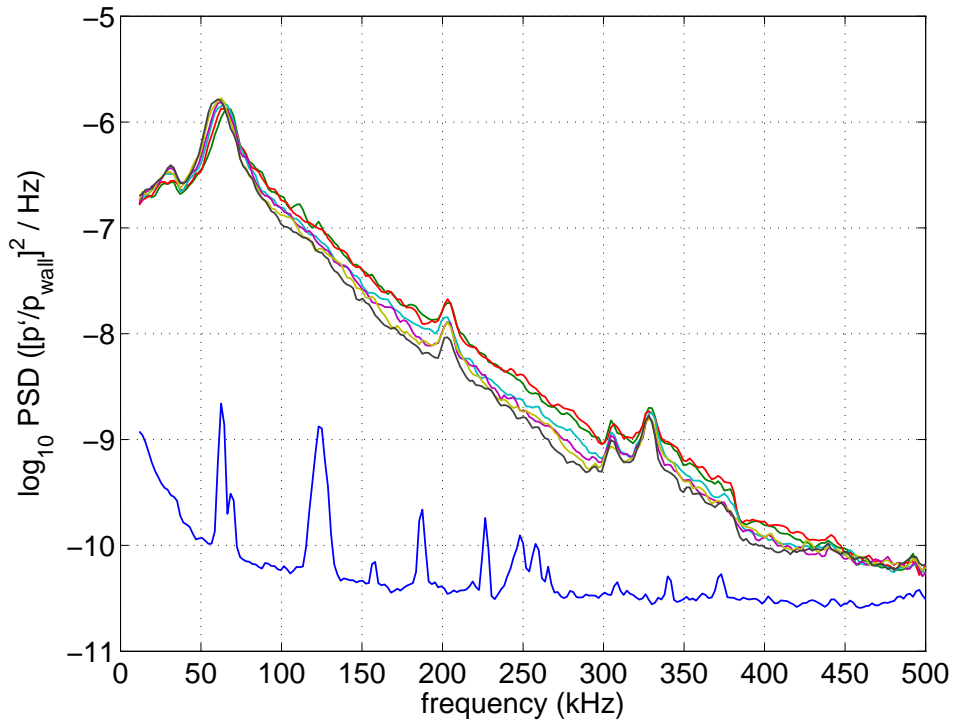
(a)  $x = 220$  mm(b)  $x = 270$  mm

Figure 8.6.: PCB power spectra under noisy flow. Legend common to all subfigures.  $M = 5.8$ ,  $\alpha = 0^\circ$ ,  $Re_i = 3.3 \cdot 10^6$  /m,  $p_{0i} = 280$  kPa,  $T_{0i} = 433$  K

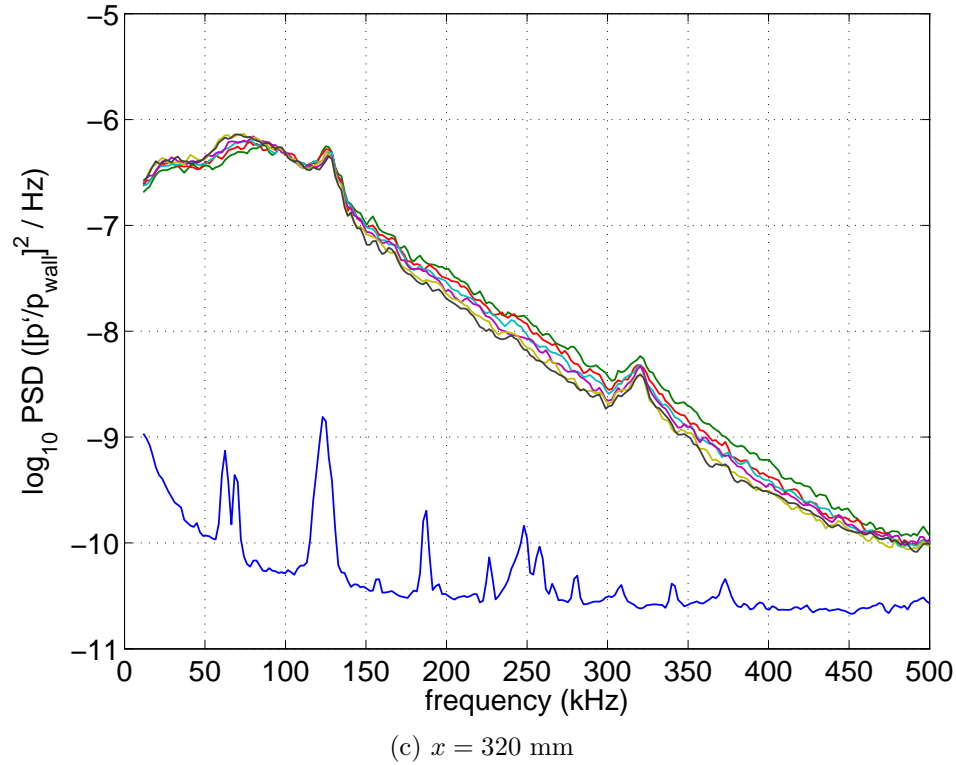


Figure 8.6.: PCB power spectra under noisy flow (continued).

### 8.4.3 Second-Mode Wave Amplitudes

The PCB power spectra were integrated to compute the amplitudes of the second-mode waves. These results should not be treated as accurately quantitative due to unresolved questions regarding the calibration of PCB sensors. The method described in Reference 91 was used to calculate second-mode-wave amplitudes, so these results should be comparable to those tests on a  $7^\circ$ -half-angle nearly-sharp circular cone.

The lower limit of integration was the local minimum in the power spectra past which the suspected second-mode waves occur. The upper limit was the frequency at which the signal returned to the power of the lower limit. The peak power was approximately an order of magnitude higher than the power at the tails of the integrated region, so the sensitivity to the bounds of integration was small.

The power for the  $\alpha = 4^\circ$  case at  $x = 220$  mm (Figure 8.3a) was integrated between 64 and 135–158 kHz. The upper limit of integration generally decreased at later times and higher  $Re$ . The resulting amplitudes  $p'/p_{\text{wall}}$  were 6.9–5.1%, decreasing at later times. For  $\alpha = 0^\circ$  at  $x = 270$  mm (Figure 8.6b), integrating between 39 and 82–94 kHz yielded  $p'/p_{\text{wall}} = 17.8$ –18.5%. The amplitudes for this case increased during the run (albeit slightly), which is surprising. For comparison, Figure 8b in Ref. 91 yields amplitudes of 5–10% prior to breakdown of second-mode waves on the cone in the Langley Mach-6 Tunnel.

### 8.5 Difficulty Interpreting PCB Sensors Under Quiet Flow

PCB data were collected under quiet as well as noisy flow. Unlike the smoothly-varying disturbance amplitudes encountered under noisy flow, for quiet flow the power spectra were much more jagged. The PCB at  $x = 220$  mm was measuring amplitudes much smaller under quiet flow than under noisy flow ( $\approx 10^{-10}$  compared to  $10^{-7}$ ), so for this sensor it is likely an issue of the sensor's sensitivity to small signals. This explanation does not suffice for the other sensors, which detected similar power levels under noisy and quiet flow.

Early analysis of quiet-flow PCB data at  $x = 320$  mm indicated that it was detecting waves at  $f \approx 125$  kHz, which seemed like a reasonable estimate for second-mode wave frequencies (Figure 8.7). However, when several PCB power spectra were compared with one another, it was realized that a peak occurred at 125 kHz regardless of Reynolds number (Figure 8.8) or angle of attack (Figure 8.9). The significance of this peak's presence even under noisy flow (Figures 8.3c, 8.4c, and 8.6c) was only then comprehended. If this frequency is constant despite changing all of these conditions, it is probably not related to second-mode waves.

This particular PCB is not the only one in the group's inventory that exhibits a large, otherwise unexplained peak at about 125 kHz. A PCB used in some early



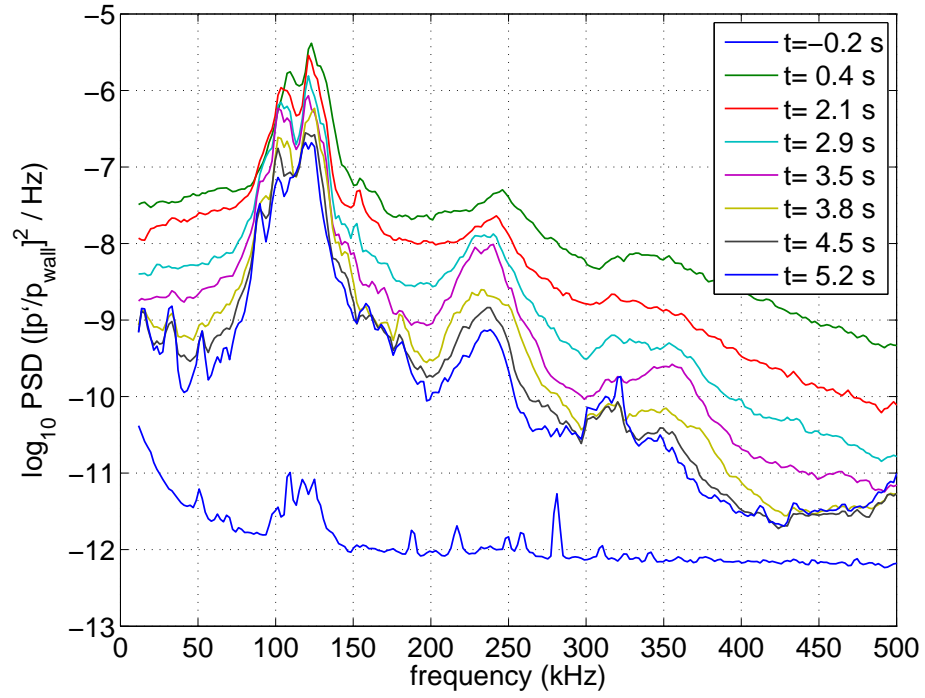


Figure 8.7.: Quiet flow,  $M = 6.0$ ,  $\alpha = 4^\circ$ ,  $Re_i = 12.0 \cdot 10^6 / \text{m}$ ,  $p_{0i} = 1120 \text{ kPa}$

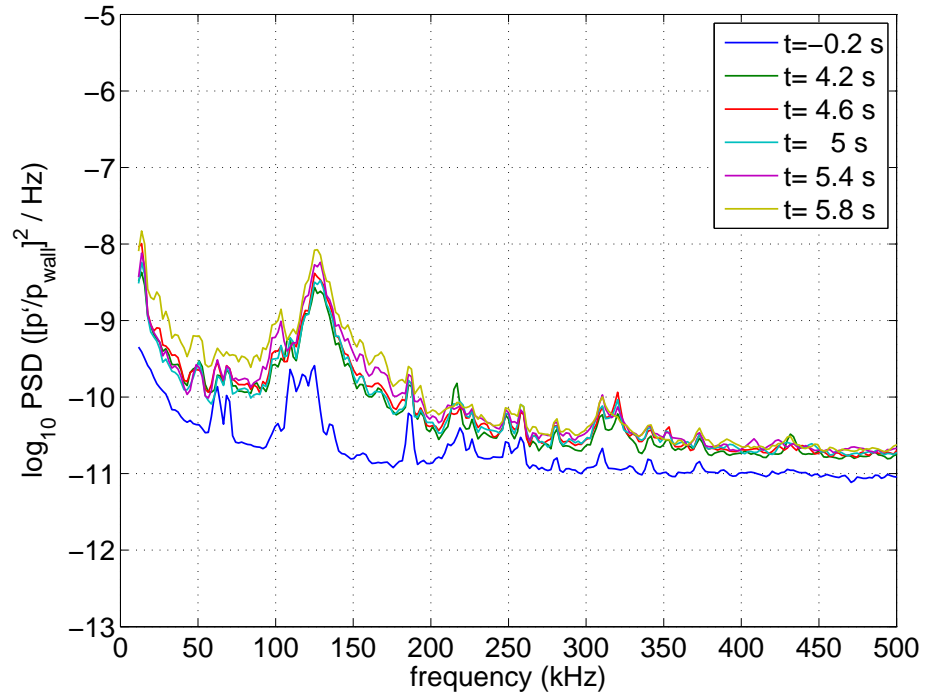


Figure 8.8.: Quiet flow,  $M = 6.0$ ,  $\alpha = 4^\circ$ ,  $Re_i = 3.0 \cdot 10^6 / \text{m}$ ,  $p_{0i} = 280 \text{ kPa}$

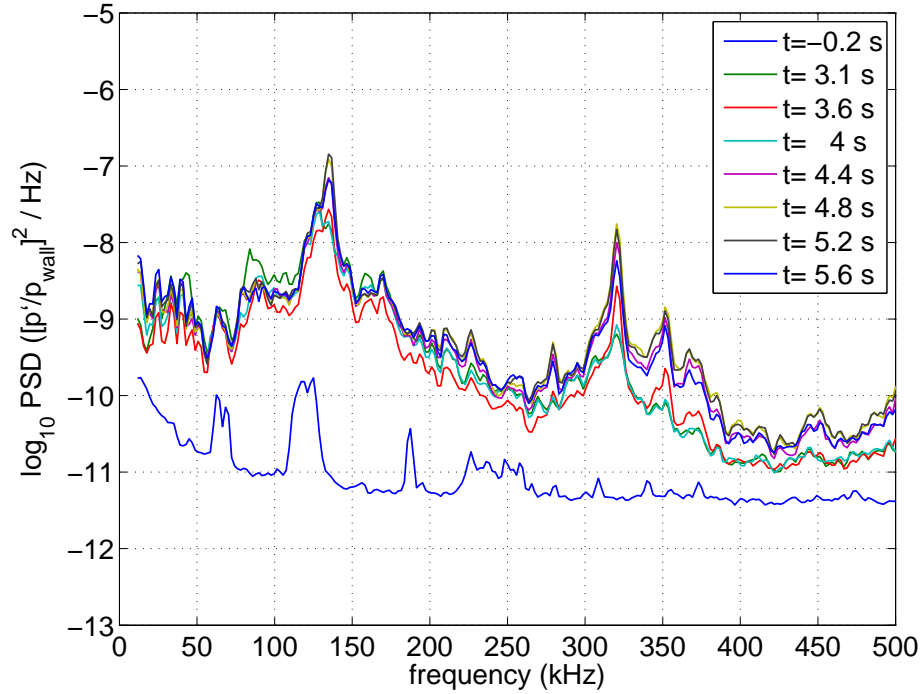


Figure 8.9.: Quiet flow,  $M = 6.0$ ,  $\alpha = 0^\circ$ ,  $Re_i = 6.7 \cdot 10^6 / \text{m}$ ,  $p_{0i} = 630 \text{ kPa}$

compression cone tests displayed similar behavior — see, for example, Figure 5b in Ref. 52.

A moderate amount of time was spent analyzing the data that was belatedly suspected to arise from a faulty sensor. The larger problem is that this error was not detected until shortly before the last set of BAM6QT HIFiRE-5 tests, which was devoted to hot-wire measurements. Therefore, a replacement set of TSP and PCB comparison data was not collected. During the second-to-last set of tests, the first and second PCBs were broken while changing angle-of-attack adapters. The sensor that had been at  $x = 320 \text{ mm}$  was moved to  $220 \text{ mm}$ . Two sensors that Berridge had used in his shock-tube calibration tests (see Ref. 89) were installed at  $x = 270$  and  $320 \text{ mm}$ .

Figure 8.10 shows the power spectra from one of these runs with the replacement sensor. The large peak that had been present at  $f = 125 \text{ kHz}$  is conspicuously absent. Instead, there is a single peak at  $90 \text{ kHz}$ . As before, spectra at a lower  $Re$

(Figure 8.11) and different angle of attack (Figure 8.12) were computed to assess whether the anticipated effects on disturbance frequency occur. All three cases show disturbances at the same frequency, once again suggesting that second-mode waves were not detected. Furthermore, the normalized amplitude increases during the run, whereas the second-mode waves are expected to remain constant or decrease. Perhaps this sensor has a similar flaw as the previous one. All three of these spectra are downstream of a hot wire. The hot wire traversed in and out of the boundary layer; at the times shown in Figure 8.10, the hot wire was out of the boundary layer. It is possible that the 90 kHz disturbance arises from the wake of that probe or that the hot wire emits electronic noise at that frequency. Therefore, no solid conclusions can be drawn but it appears that the 125 kHz peak was a result of the particular PCB used. Further work with PCBs is needed before it can be stated with certainty whether these frequencies are spurious or not.

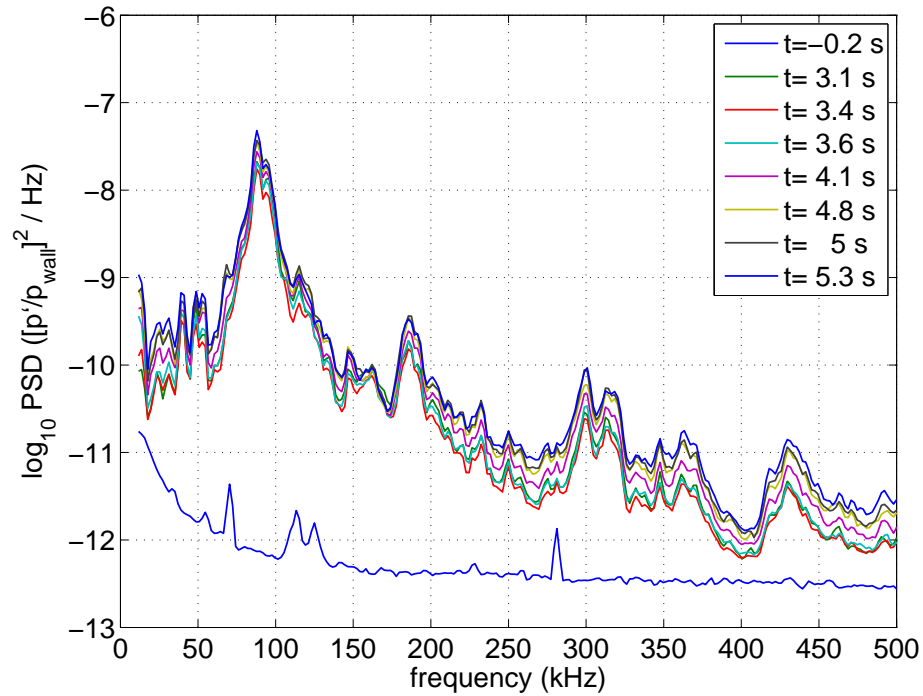


Figure 8.10.: Quiet flow,  $M = 6.0$ ,  $\alpha = 4^\circ$ ,  $Re(t = 3) = 10.3 \cdot 10^6 / m$ ,  $p_0(t = 3) = 890 \text{ kPa}$

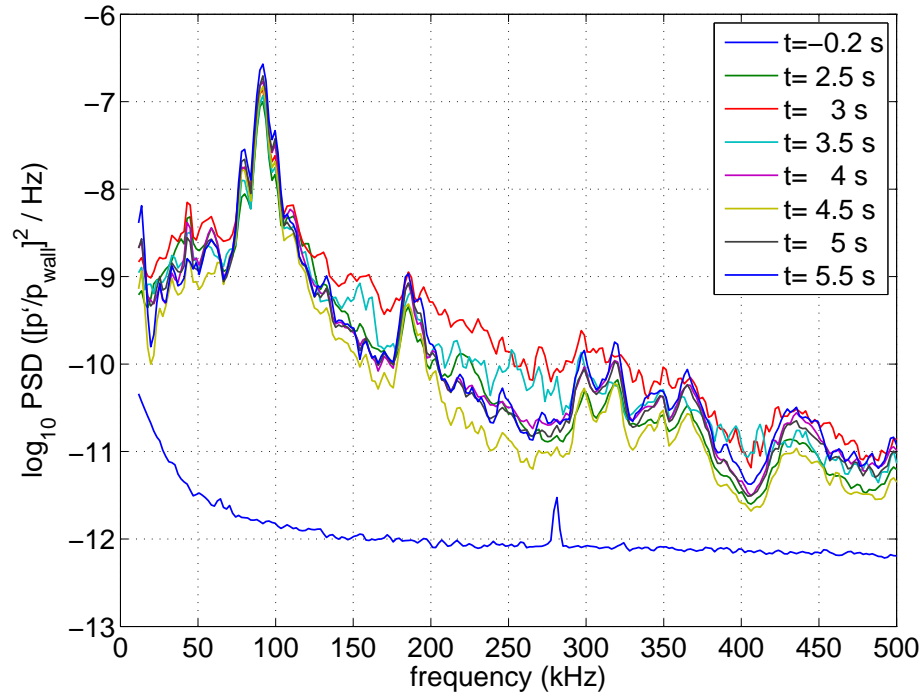


Figure 8.11.: Quiet flow,  $M = 6.0$ ,  $\alpha = 0^\circ$ ,  $Re(t = 3) = 10.2 \cdot 10^6 /m$ ,  $p_0(t = 3) = 890$  kPa

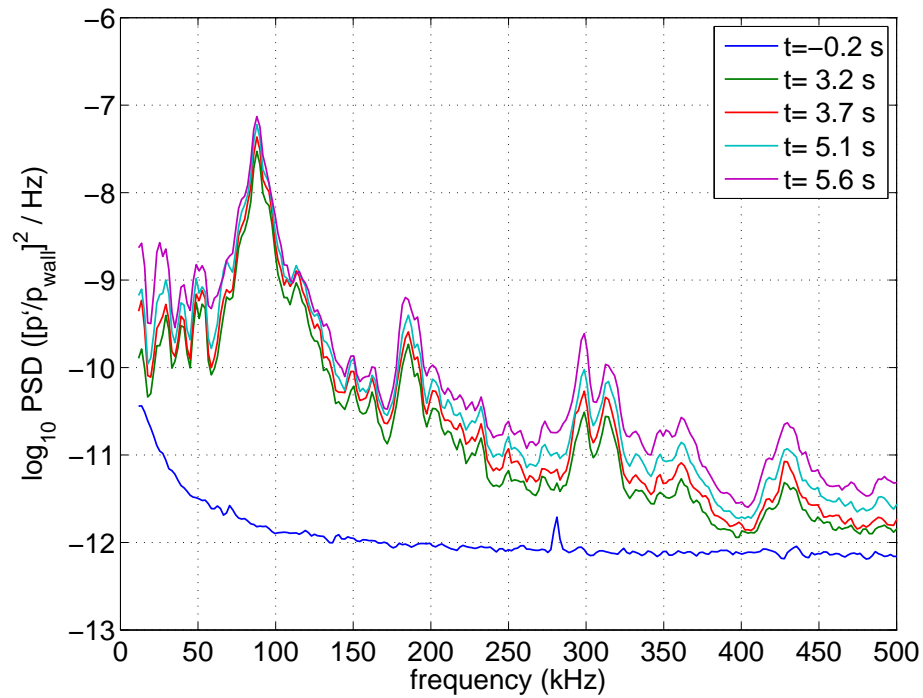


Figure 8.12.: Quiet flow,  $M = 6.0$ ,  $\alpha = 0^\circ$ ,  $Re(t = 3) = 6.9 \cdot 10^6 /m$ ,  $p_0(t = 3) = 600$  kPa

There is some information that can be salvaged from the earlier PCB tests, even if the largest peak frequencies are actually an artifact of the sensor. The difference between laminar and turbulent model boundary layers can be distinguished in the PCB data. At the time of the image in Figure 8.13a, centerline transition onset occurs at  $x \approx 280$  mm. The boundary layer above the third PCB sensor ( $x = 320$  mm) is well into transition. This state appears in the PCB power spectra as larger amplitudes ( $10^{-9}$ – $10^{-7}$ ) over a broad range of frequencies (Figure 8.14). At later times during the run, the broadband noise magnitude has receded 2–3 orders of magnitude. Significantly, the TSP indicates that at these later times the transition front has moved off the back end of the model (Figure 8.13b — note that the temperature scale was changed to better capture the  $\Delta T$  range at this time). The other sensors, which were under a laminar boundary layer, do not exhibit the same broadband amplitude reduction. The large harmonics visible in Figure 8.14b are an exception. Therefore, it appears that a turbulent boundary layer is evidenced by the larger amplitude over a broad range of frequencies on PCB power spectra under quiet as well as noisy flow. This result agrees with the observations of other PCB studies, which did not have the benefit of direct comparison to TSP (e.g., Reference 85 with a straight circular cone and Reference 51 with the compression cone).

Although several reasons have been provided above to suspect that the largest disturbances detected by the PCBs are not second-mode waves, there are several reasons to suspect that in fact they are. Alternatively, these reasons can be regarded as excuses for why the problem took so long to detect. In the PCB spectra in Figure 8.14, the sensors at  $x = 220$  and 270 mm display peaks at 125 kHz too. Perhaps the distortion in one sensor corrupted the others through an inadvertent electrical connection in the model or in the PCB signal conditioning box, or perhaps the disturbance frequency should not be expected to change much between 220 and 320 mm from the nosetip. The stability computations discussed below predict an approximately 20-kHz shift in peak frequency for this  $Re$  at  $\alpha = 4^\circ$  and no streamwise dependence for

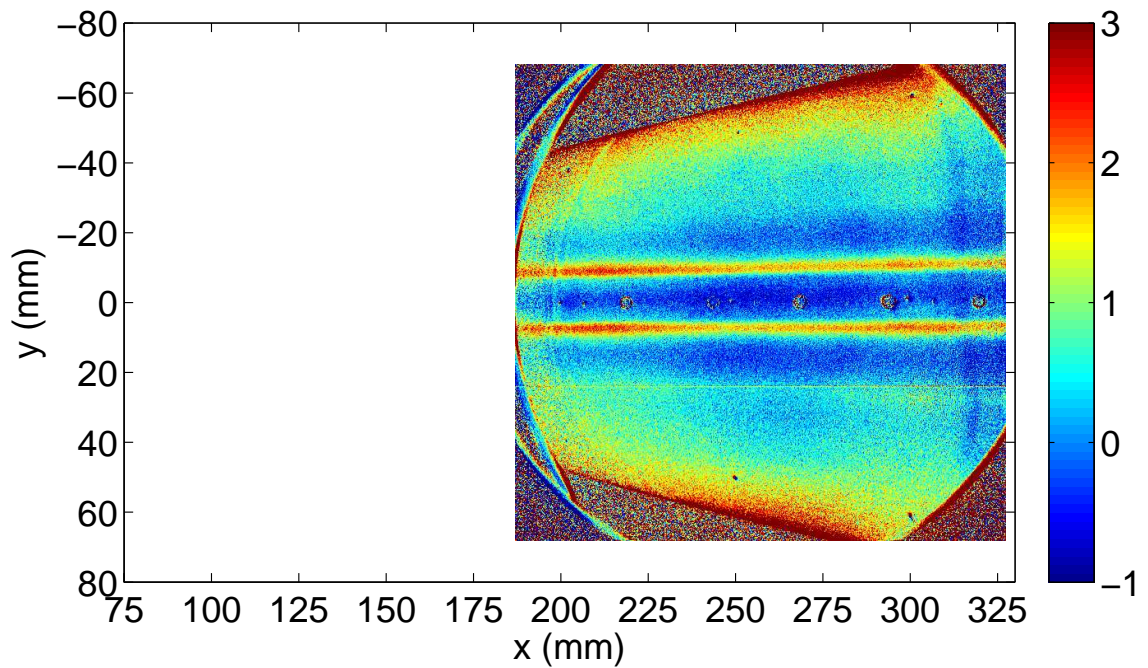
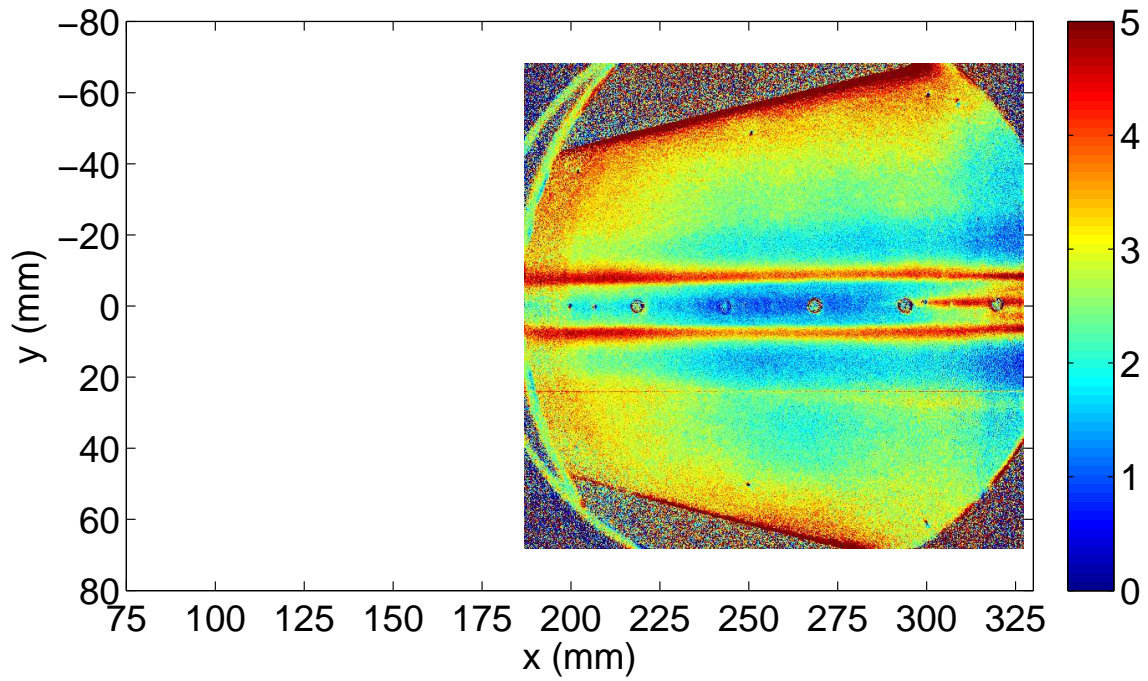


Figure 8.13.: TSP for comparison to PCB power spectra. Quiet flow,  $M = 6.0$ ,  $\alpha = 4^\circ$

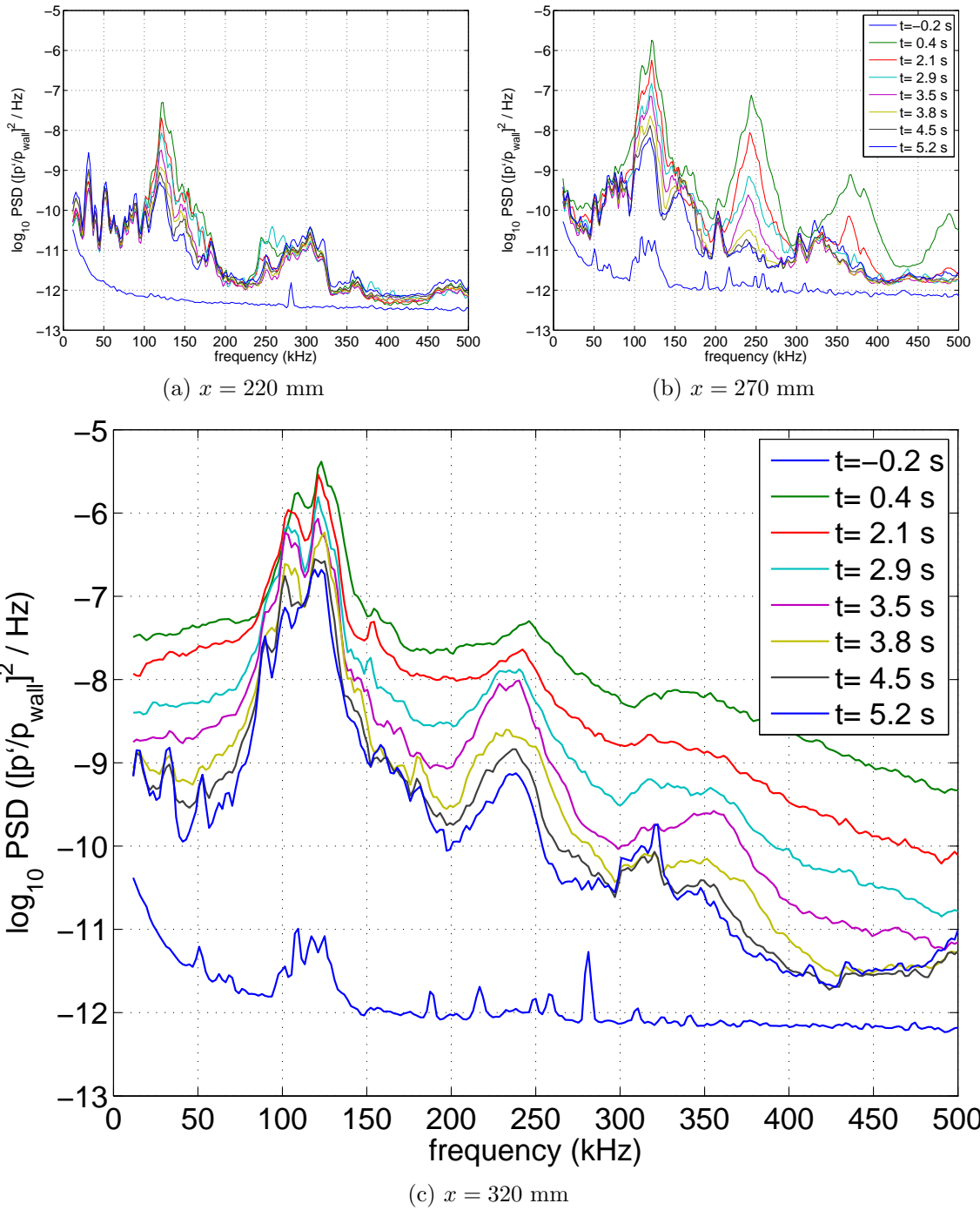


Figure 8.14.: PCB power spectra under quiet flow. Legend common to all subfigures.  $M = 6.0$ ,  $\alpha = 4^\circ$ ,  $Re_i = 12.1 \cdot 10^6$  /m,  $p_{0i} = 1140$  kPa,  $T_{0i} = 433$  K



$\alpha = 0^\circ$ . Furthermore, the amplitude diminishes as  $Re$  and  $p_0$  decrease, as expected. Additionally, several harmonics of the highest-amplitude waves are detected.

### 8.5.1 Comparison of Experimental and Computational Disturbance Frequencies

A careful examination of the PCB spectra shows a handful of disturbance peaks that do display a frequency shift as  $Re$  decreases. These peaks are partially obscured by the larger, constant-frequency signals. Figure 8.15 is a portion of Figure 8.7 with a black arrow along the peaks indicating their direction of movement as time elapses and  $Re$  decreases.

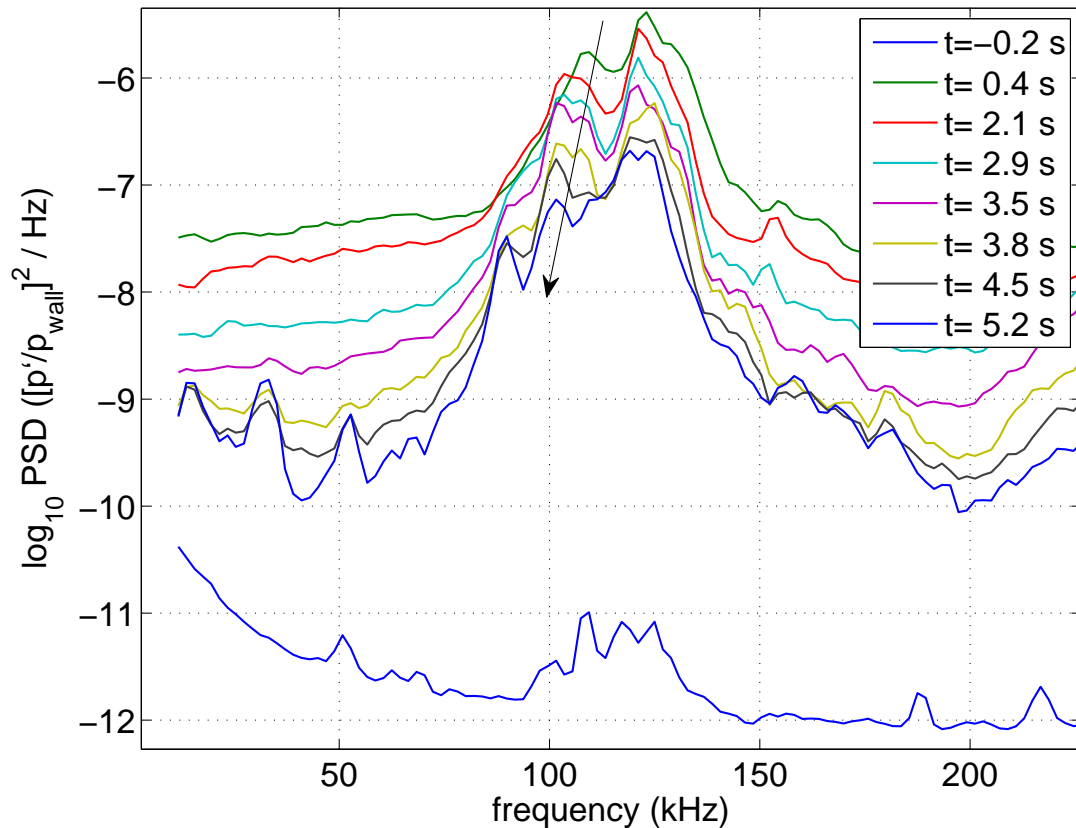


Figure 8.15.: PCB output under quiet flow,  $M = 6.0$ ,  $\alpha = 4^\circ$ ,  $Re_i = 12.0 \cdot 10^6 / \text{m}$ ,  $p_{0i} = 1120 \text{ kPa}$ ,  $x = 320 \text{ mm}$

The peak frequencies shown in Figure 8.15 ( $f \approx 95\text{--}110$  kHz) appear to agree with stability computations for this case provided by Chau-Lyan Chang and Meelan Choudhari and shown in Figure 8.16 [92]. They explain that the three disturbance peaks denote first-, second- and third-mode disturbances, respectively. The disturbances at this sensor location,  $x = 320$  mm, were computed with both Linear Stability Theory (LST) and the Parabolized Stability Equations (PSE). It is encouraging that the two computations are close to one another.

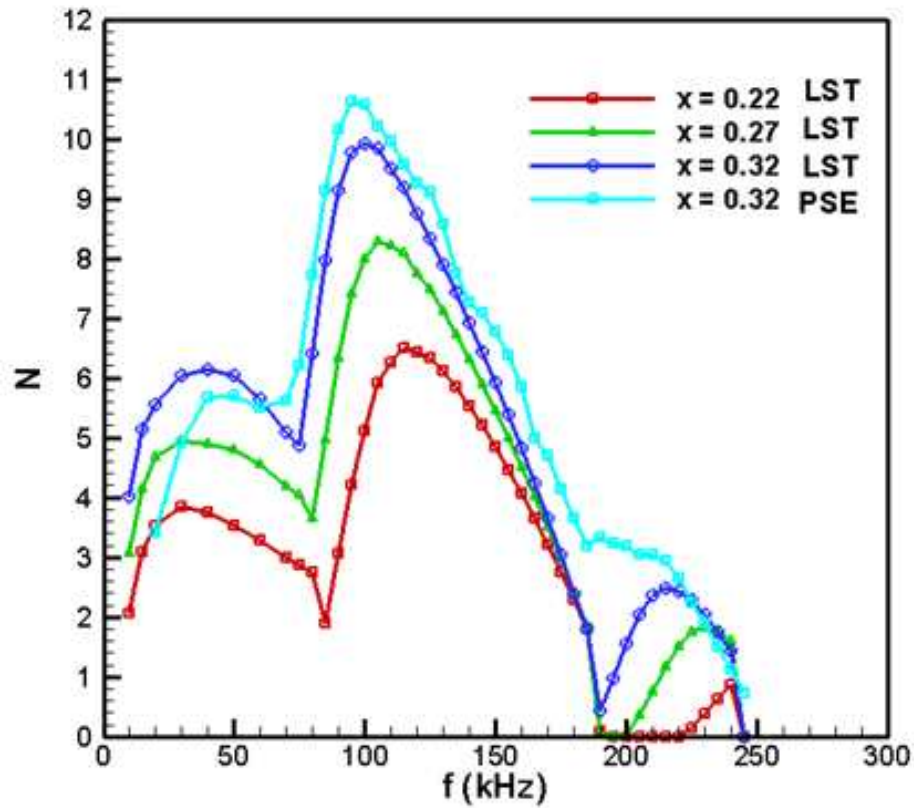


Figure 8.16.: Computational prediction of disturbance amplification spectra.  $M = 6.0$ ,  $\alpha = 4^\circ$ ,  $Re = 10.2 \cdot 10^6$  /m,  $p_0 = 970$  kPa,  $T_0 = 433$  K. From Ref. 92

The experimental and computational results for  $\alpha = 4^\circ$  are plotted together in Figure 8.17. The LST second-mode-wave amplification rates for  $x = 320$  mm from Figure 8.16 are marked by the black squares connected by the dotted line and refer to the right axis. The scales of the two vertical axes were adjusted so that the PCB and

LST peaks are near one another. The lower 100–110-kHz-peak in the experimental data is much closer than the higher 120–125-kHz-peak to the computational prediction of most-amplified frequencies.

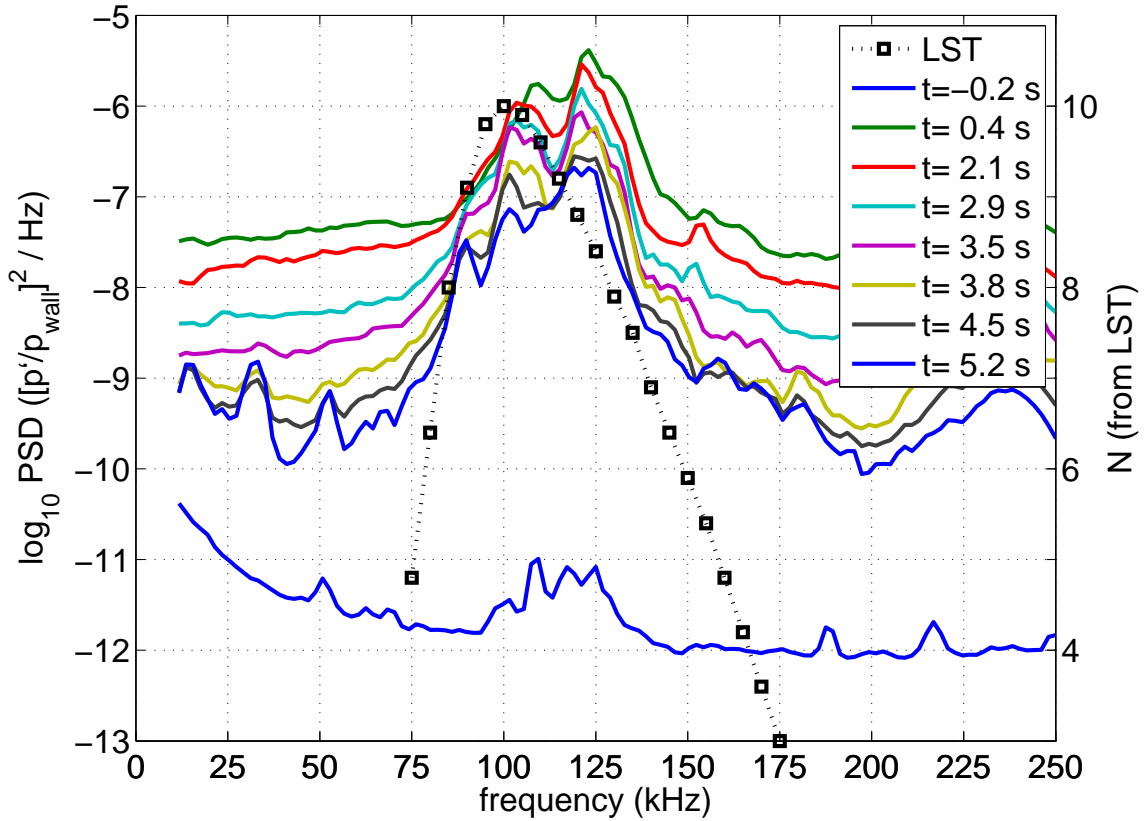


Figure 8.17.: PCB and LST comparison under quiet flow,  $M = 6.0$ ,  $\alpha = 4^\circ$ ,  $Re_i = 12.0 \cdot 10^6$  /m,  $p_{0i} = 1120$  kPa,  $x = 320$  mm

Figure 8.18 is from a test under the same conditions as Figure 8.15, except the angle of attack is  $0^\circ$  instead of  $4^\circ$ . According to the TSP (Figure 6.13), the transition front is further forward and the PCB at  $x = 320$  mm indicates turbulence. At  $x = 270$  mm, however, disturbances at  $f \approx 80$ – $95$  kHz do appear. Once again, the black arrow identifies the peak frequencies observed. At  $t = 0.2$  s, the model boundary layer is turbulent at  $x = 270$  mm, which results in the large amplitude over a wide frequency range.

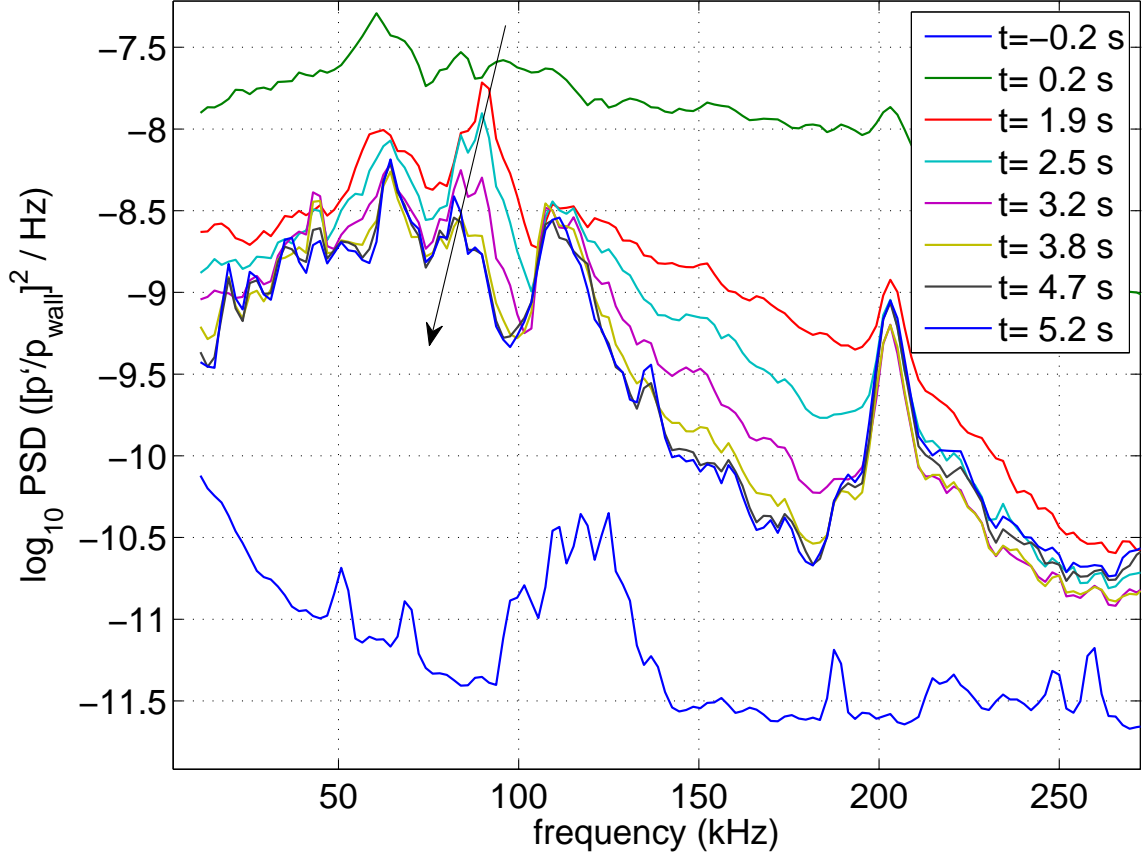


Figure 8.18.: PCB output under quiet flow,  $M = 6.0$ ,  $\alpha = 0^\circ$ ,  $Re_i = 12.0 \cdot 10^6 / \text{m}$ ,  $p_{0i} = 1120 \text{ kPa}$ ,  $x = 270 \text{ mm}$

The peak frequencies shown in Figure 8.18 also agree with stability computations for this case provided by Dr. Choudhari and shown in Figure 8.19. These amplification curves are the result of LST computations based on a preliminary mean-flow solution and should be considered approximate. First-mode waves are most amplified up to 60 kHz; second-mode waves are more amplified thereafter. The experimental  $Re$  matches that of the computation ( $Re = 10.2 \cdot 10^6 / \text{m}$ ) at  $t = 4.8 \text{ s}$ . The frequency resolution of the computational result is coarse, but it identifies the peak frequency to be about 90 kHz, which is in fair agreement with the PCB data.

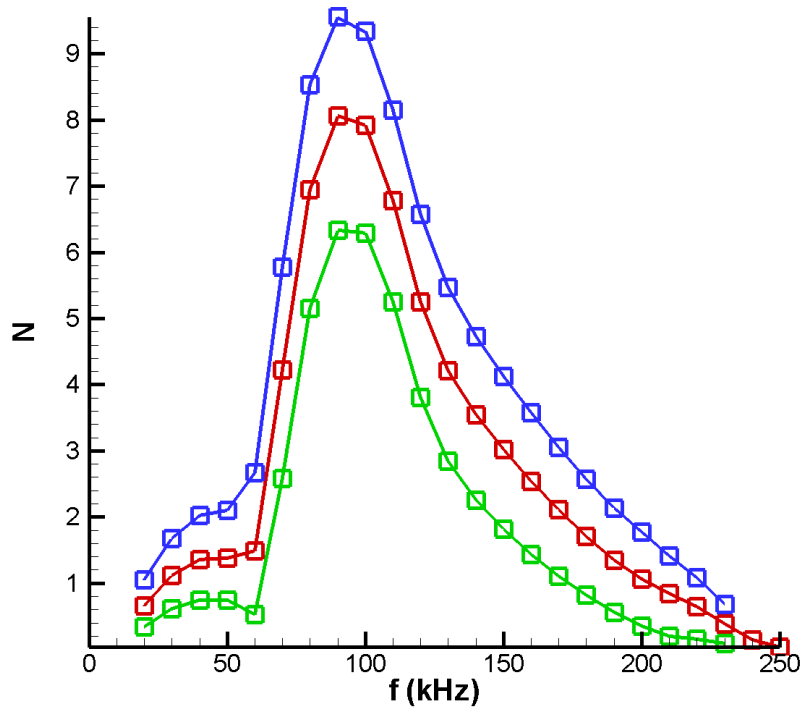


Figure 8.19.: Computational prediction of disturbance amplification spectra. Green is  $x = 220$  mm, red is  $x = 270$  mm, and blue is  $x = 320$  mm.  $M = 6.0$ ,  $\alpha = 0^\circ$ ,  $Re = 10.2 \cdot 10^6$  /m,  $p_0 = 970$  kPa,  $T_0 = 433$  K. Courtesy M. Choudhari

If the assumptions are made that the second-mode-wave disturbance frequency is inversely proportional to the boundary layer thickness, and that the boundary layer thickness is proportional to  $Re^{-1/2}$ , then the highest-amplified frequency for  $Re = 3 \cdot 10^6$  /m would be roughly 50–55 kHz, which is close to the 55–65 kHz indicated by the PCBs prior to transition under noisy flow in Figure 8.6.

Figure 8.20 shows a comparison of the experimental and computational results for  $\alpha = 0^\circ$ . The LST amplification rates for  $x = 270$  mm from Figure 8.19 are marked by the black squares connected by the dotted line and refer to the right axis. As in Figure 8.17, the scales of the two vertical axes were adjusted so that the PCB and LST peaks are near one another. The measured disturbance frequencies of 80–95 kHz are close to the computed prediction of peak amplification at  $f = 90$ –100 kHz.

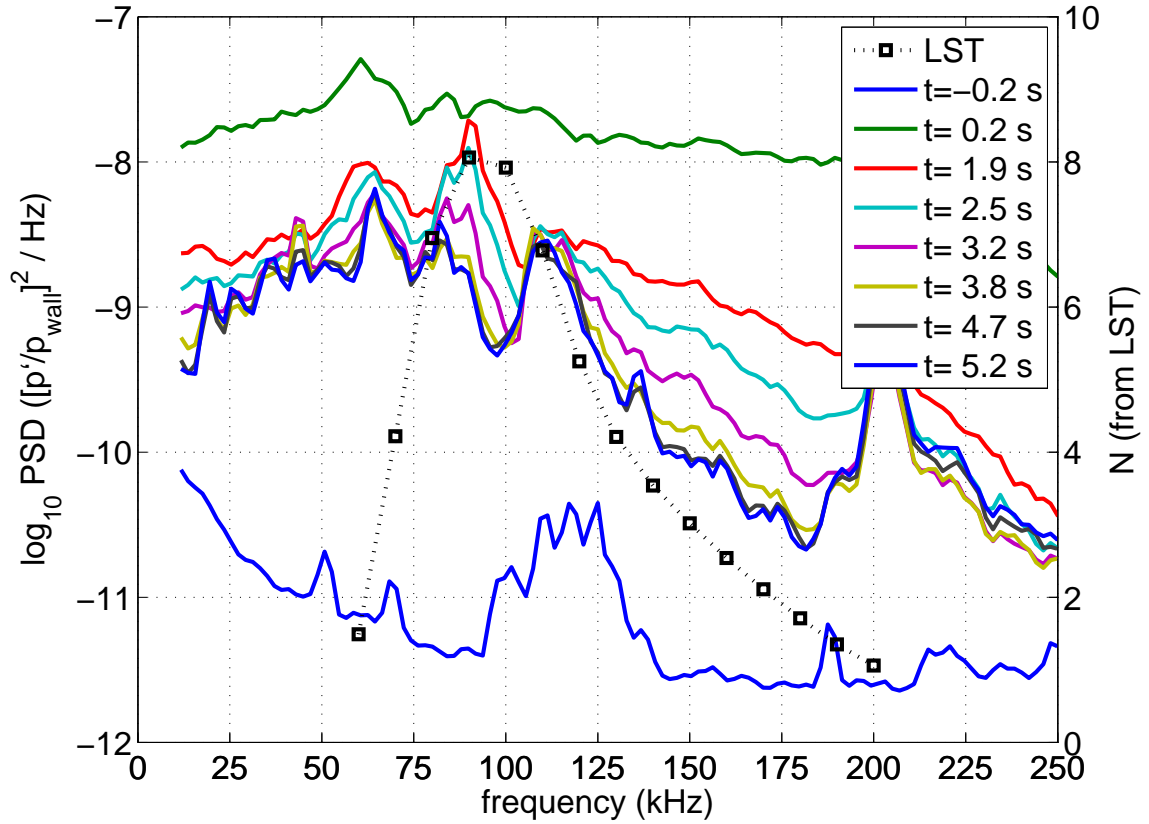


Figure 8.20.: PCB and LST comparison under quiet flow,  $M = 6.0$ ,  $\alpha = 0^\circ$ ,  $Re_i = 12.0 \cdot 10^6 / \text{m}$ ,  $p_{0i} = 1120 \text{ kPa}$ ,  $x = 270 \text{ mm}$

Figures 8.15 and 8.18 are inconclusive, but it is possible that second-mode waves were detected by PCB sensors under quiet flow prior to or during transition. Clearly, more work is needed to develop the proper technique for employing PCB sensors under quiet flow.

## 9. HOT-WIRE MASS FLUX PROFILES

### 9.1 Instrumentation

Hot wires operate on the principle that as the thermodynamic and kinematic state of their surrounding fluid changes, the heat transfer between the wire and fluid will change [93]. Two types of anemometers are primarily used: constant current anemometers (CCA) and constant temperature anemometers (CTA) [94]. Constant current anemometry is more suitable for high-frequency  $T_0$  fluctuations [95]. For supersonic flows, constant temperature anemometry is sensitive to massflux ( $\rho u$ ) fluctuations for sufficiently large overheat ratios ( $\tau \approx 1$ ) [96,97].

These measurements of mass-flux profiles on the HIFiRE-5 were suggested by Dr. Meelan Choudhari, who explained their importance for the verification of mean-flow CFD results. Dr. Shann Rufer was the first to employ hot wires extensively in the BAM6QT [98,99]. Her techniques were used as a starting point for these tests. The main difference between these tests and prior BAM6QT hot-wire experiments (e.g., References 83,99,100) is that the identification of high-frequency boundary layer disturbances was not the primary objective — that goal was addressed with the PCB sensors, as described in Chapter 8.

#### 9.1.1 Hardware

In light of the past difficulties encountered using wires with diameters  $d$  of 0.0001, 0.00015, and 0.0002 in. (2.54, 3.81, and 5.08  $\mu\text{m}$ ), 0.0004-in.- (10.16- $\mu\text{m}$ -) diameter wires were used instead. These wires sacrifice frequency response for robustness. Frequency responses of  $\approx 20$  kHz were typical, compared to 200–230 kHz often achieved with 0.0002-in.-diameter wires. The Platinum-Rhodium Wollaston wires were welded



onto the broaches of the standard hot-wire probes used in the BAM6QT for boundary-layer measurements. The probe is inserted into a double-wedge hot-wire mount that is installed in the test section traverse (see Section 3.3). The probes and probe mount are described in detail in Chapter 3 of Reference 99.

The wire length  $l$  was measured by photographing it under a microscope. Figure 9.1 shows a microscope photo of a broken hot wire superimposed on a photo of a ruler with 1/64-in. (0.397-mm) engravings. Unfortunately, when this hot wire was photographed, it was discovered that the wire had broken. The distance between the broaches where the wire had been attached is 0.338 mm. The wires are usually bowed when attached to avoid strain gauging [101], so its true length was probably slightly more. The aspect ratio  $l/d$  for this wire was 33, which is much lower than the 200 or more recommended in Reference 102. Therefore, end-conduction effects may have an influence and be a significant source of error.

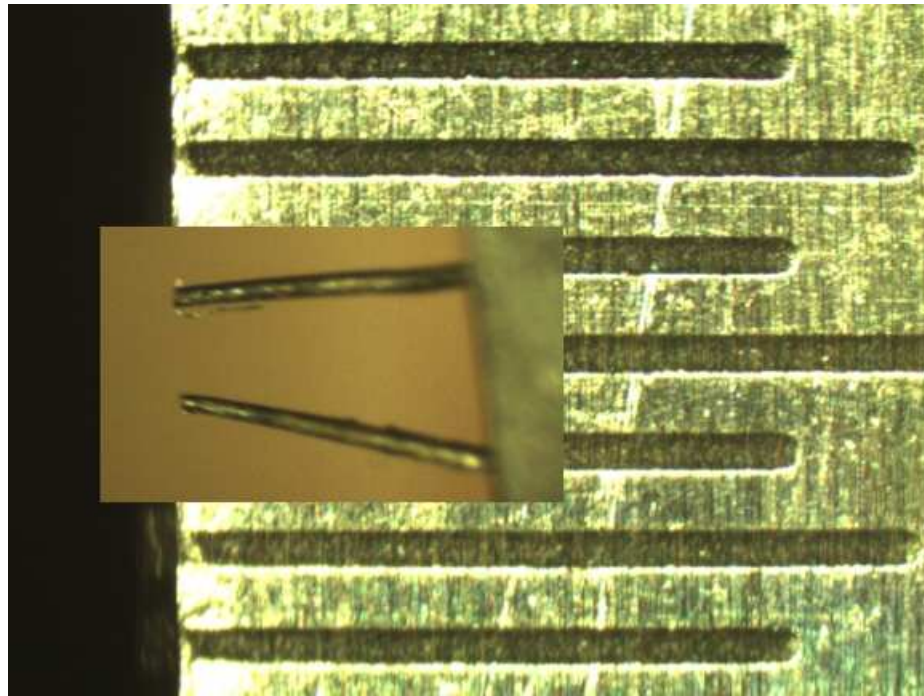


Figure 9.1.: Photograph of a broken hot wire through microscope at  $40\times$  magnification. Background image shows a ruler with 1/64-in. (0.397-mm) engravings. Wire length is estimated to have been 0.338 mm.

A TSI IFA100 constant temperature anemometer was employed for all hot-wire tests. The 1:1 bridge that enables custom selection of a bridge resistor to set properly the hot wire overheat was used. When tuned, the wires' frequency response was typically 20–25 kHz. This frequency response is too low for measurement of second-mode waves or other fast boundary-layer phenomena but is acceptable for mean-flow mass flux measurements.

### 9.1.2 Mass Flux Calibration

After measuring a wire's length, the next step in calibrating it is to measure its thermal coefficient of resistance  $\alpha$ . The relationship between a wire's temperature and resistance is described by:

$$\frac{R}{R_{\text{ref}}} = 1 + \alpha(T - T_{\text{ref}}) \quad (9.1)$$

This measurement was conducted in an oven over a temperature range of 290–450 K. A value of  $1 \cdot 10^{-3}$  /K was typical and the correlation coefficient was greater than 0.99.

The recovery temperature  $T_{\text{rec}}$  is the temperature that an unheated wire reaches when placed in a fluid flow [102]. The recovery factor  $\eta$  is defined as the ratio between  $T_{\text{rec}}$  and  $T_0$ . For a low-speed continuum flow,  $\eta = 1$ . Rufer reported  $\eta = 0.974$ – $0.987$  measured in the BAM6QT with constant-current 0.00015-in.-diameter hot wires [99]. She reports Knudsen numbers ( $Kn$ , the ratio between the mean free path and wire diameter) of 0.2–0.4, near the upper limit of continuum flow. With the larger wire diameter used in these tests (that is, lower  $Kn$ ), the assumption of continuum flow seems justified. Reference 102 reports  $\eta$  typically between 0.95 and 0.97 for a wide range of supersonic Mach numbers. Combining these two sources,  $\eta = 0.97$  was assumed for these calculations.

The basis of the hot wire calibration is the semi-empirical relation [96]:

$$Nu = C + D \cdot Re_d^n \quad (9.2)$$

The Nusselt number  $Nu$  is related to the convection of heat away from the hot wire:

$$Nu = \frac{\dot{q}}{\pi l k (T_{\text{wire}} - T_{\text{rec}})} \quad (9.3)$$

The Reynolds number is based on the wire diameter and  $\mu(T_0)$ :

$$Re_d \equiv \frac{\rho u d}{\mu} \quad (9.4)$$

In actuality  $C$  and  $D$  are functions of the overheat ratio  $\tau$ , but it is assumed here that the variation in  $\tau$  is negligible — another potential source of error considering that  $T_0$  decreases by 8% after 5 s.  $C$  and  $D$  are particular to each individual wire. The exponent  $n$  is a function of  $Re_d$  and  $M$ . Rufer refers to a figure in Reference 103 for this relation. For this case ( $Re_d \approx 50$  and  $M = 6$ ), the prescribed  $n$  is  $\approx 0.6$ . This result is approximate, but Figure 3.11 in Reference 99 illustrates the negligibly small sensitivity of the calibration to this parameter.

The Wheatstone bridge in the constant temperature anemometer ensures that  $\dot{q}$  out of the wire (convected into the fluid) is balanced by the power supplied by the electronics. Combining Joule's and Ohm's laws enables an expression of the power through the hot wire as a function of the anemometer output voltage  $V$ , CTA bridge resistance  $R_{\text{bridge}}$ , and the constant resistance  $R_a = 20 \, \Omega$  in the legs of the CTA circuit:

$$\dot{q} = \frac{V^2 R_{\text{bridge}}}{(R_a + R_{\text{bridge}})^2} \quad (9.5)$$

With these assumptions and relations established, the calibration and data reduction procedures become tractable. To calibrate a wire:

1. Measure  $l$  and  $\alpha$  with microscope and oven

2. Select appropriate  $R_b=1.7-1.9 \times R(T_{\text{ref}})$  and compute resulting  $T_{\text{wire}}$  by rearranging Equation 9.1
3. Measure a flow with a known mass flux computed from measured stagnation conditions
4. Calculate  $Re_d$  for that flow
5. Measure that flow with the hot wire CTA and record the output voltage  $V$
6. Calculate  $Nu$  from Equations 9.3 and 9.5
7. Calculate best-fit linear regression  $Nu = C + D \cdot Re_d^n$  with the assumed  $n$

To measure mass flux with a calibrated wire:

1. Measure the unknown flow with the hot wire and record the CTA output voltage
2. Calculate  $Nu$  from Equations 9.3 and 9.5
3. Calculate  $Re_d$  from  $Nu$  and Equation 9.2
4. Calculate  $\rho u$  from the definition of  $Re_d$

The only significant step listed above as yet unaddressed is the measurement of a known flow. Two different methods were attempted in support of the HIFiRE-5 tests: calibration in the Mach-4 supersonic jet, and calibration in the BAM6QT itself. The Mach-4 supersonic jet test rig at the ASL was the first method employed. This facility is described in detail in References 99 and 83. Operation of this facility poses a minor conflict with running the BAM6QT due to the shared compressed air and vacuum sources. Its stagnation temperature wanders slightly during a run ( $422 \pm 8$  K was typical).

The hot wire calibration in the supersonic jet posed one significant problem. When the supersonic jet calibration was used to compute mass flux in the BAM6QT, there was a large difference between the theoretical mass flux and the measured mass flux.

The hot wire was traversed from near the HIFiRE-5 model to outside of its shock in order to measure the shock location and angle. This pre-shock voltage was converted to mass flux to check the calibration — and it was 20% less than the theoretical value. There are several possible explanations for the discrepancy, for instance: one of the assumptions above is substantially invalid, the theoretical mass flux through the jet was inaccurate due to separation in its nozzle, and/or the hot wire suffers from serious end effects.

For the second set of HIFiRE-5 hot wire tests, the hot wire was calibrated in the BAM6QT itself. The mass flux was calculated from stagnation conditions measured in the contraction and assuming isentropic expansion in the driver tube and nozzle. According to Reference 69, the freestream Mach number in the BAM6QT is 6.1 at  $p_0 \approx 1000$  kPa under quiet flow 2.16–2.38 m downstream of the throat, so this value was used in the hot wire calculations. Slight variations in Mach number are another likely source of error. The calibration data were culled from the portions of the traverse profile that exited the oblique shock from the model. Tunnel runs were made at stagnation pressures greater and less than the primary conditions tested to extend the calibration over as wide a mass flux range as possible. The first hot wire used survived only three runs, so there was insufficient data for calibration. The second wire survived seven runs. This lifetime was just long enough to record profiles at  $\alpha = 0^\circ$  and  $4^\circ$ , one duplicate run to assess repeatability, and the necessary calibration data.

Figures 9.2 displays the data collected from three tunnel runs that were used in the calibration. The independent axis is the theoretical mass flux computed for the measured stagnation pressure. The dependent axis is the voltage output by the constant temperature anemometer. Two samples were used from each run — one early and one later in the run, in order to optimize the range and distribution of calibration data. The most important information in Figures 9.2 is that the hot wire was calibrated over a mass flux range of 18.58–52.44 kg/m<sup>2</sup>/s.

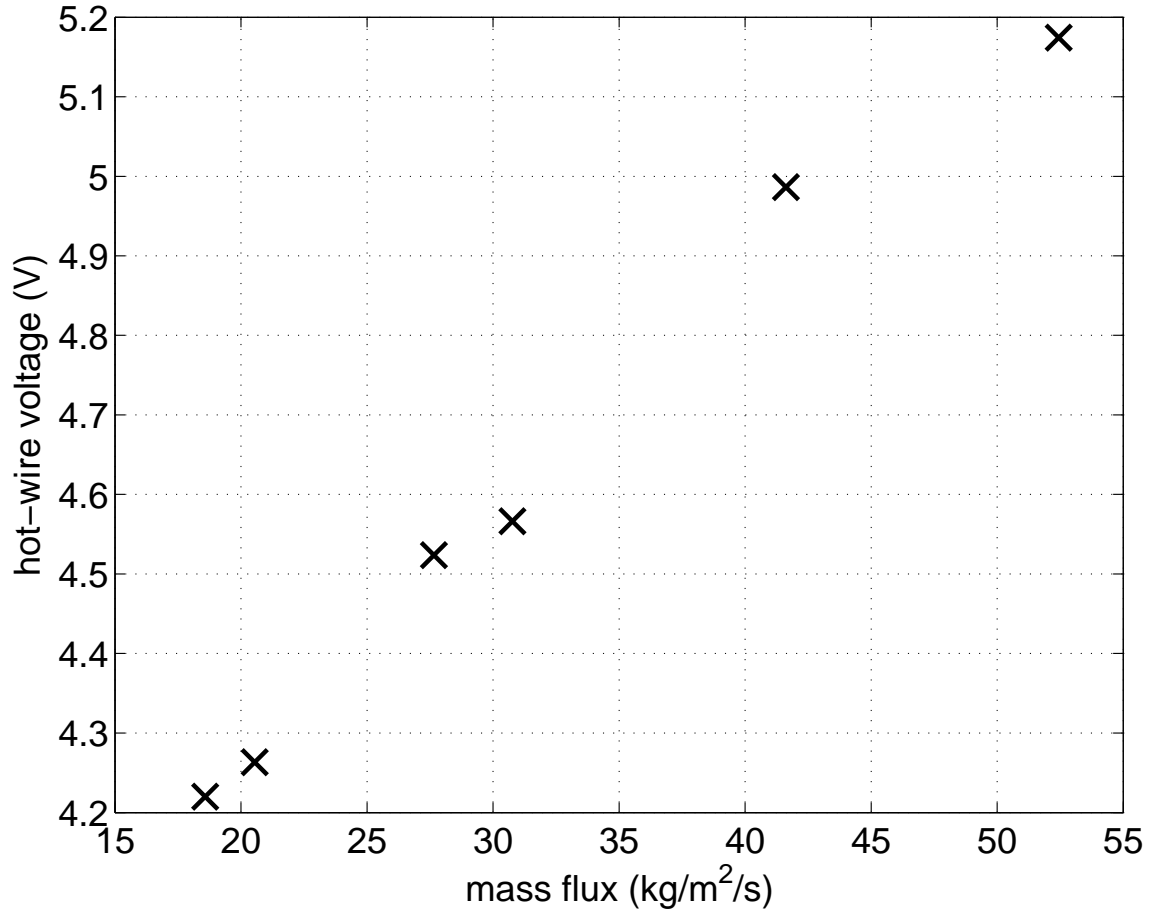


Figure 9.2.: Hot wire calibration data

Figure 9.3 shows the six data points above converted to dimensionless parameters. The Reynolds number is computed from the mass flux with Equation 9.4 and the Nusselt number is computed from the CTA voltage with Equations 9.5 and 9.3. The independent axis is  $Re_d^{0.6}$ , where  $n = 0.6$  was chosen as the exponent for  $Nu = C + D \cdot Re_d^n$ . When  $Re_d$  is scaled in this way, the calibration data is expected to lie in a straight line with slope  $D$  and intercept  $C$ . These data are indeed straight; the square of the correlation coefficient is greater than 0.99. A best-fit linear regression yielded  $D = 1.5499$  and  $C = 2.9945$ . The X-marks identify the calibration data and the solid line is the calibration curve.

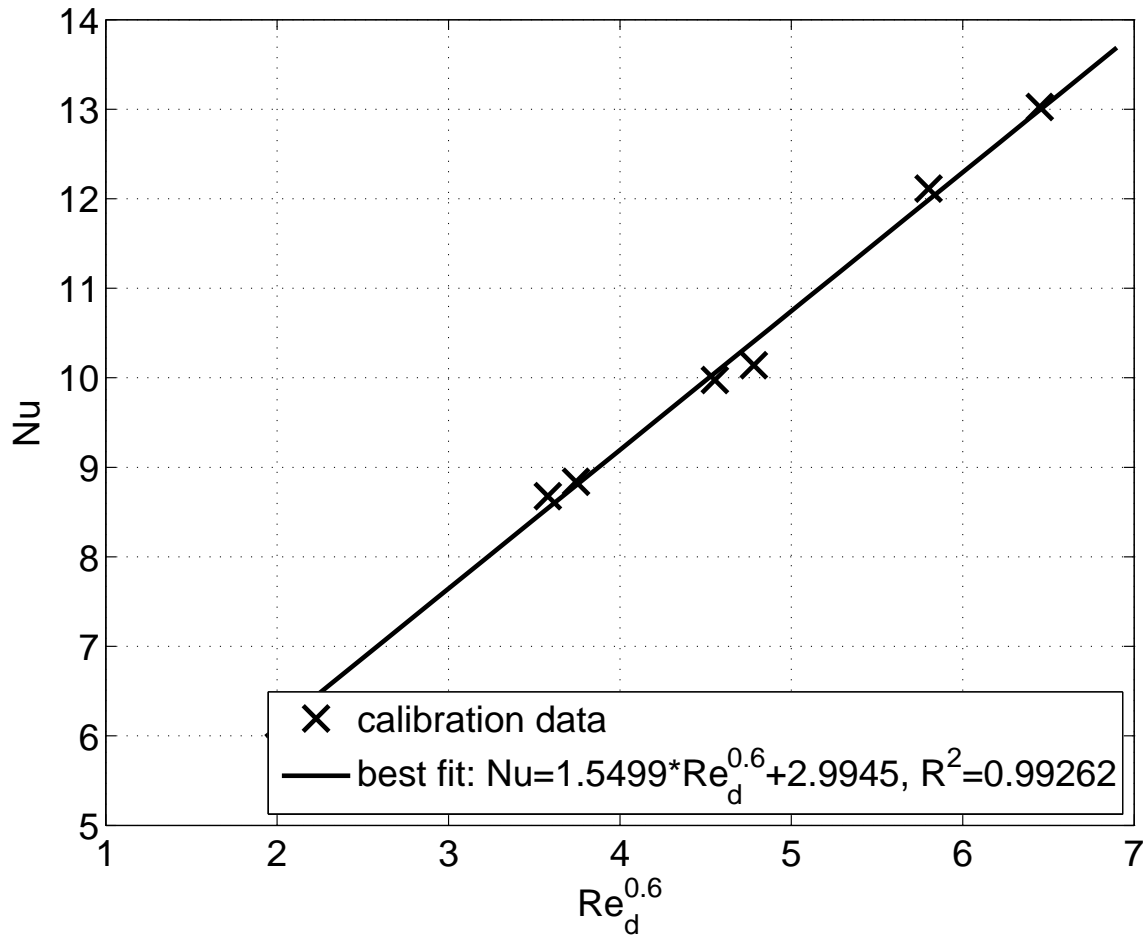


Figure 9.3.: Hot wire calibration data converted to non-dimensional parameters

Finally,  $Nu$  as a function of  $Re_d$  is shown in Figure 9.4. This calibration appears to be valid for  $Re_d \approx 8-23$ , and  $Nu \approx 8-13$ . The curve was extrapolated for data outside of this range. The hot-wire results should be regarded as merely qualitative for the extrapolated calibration curve.



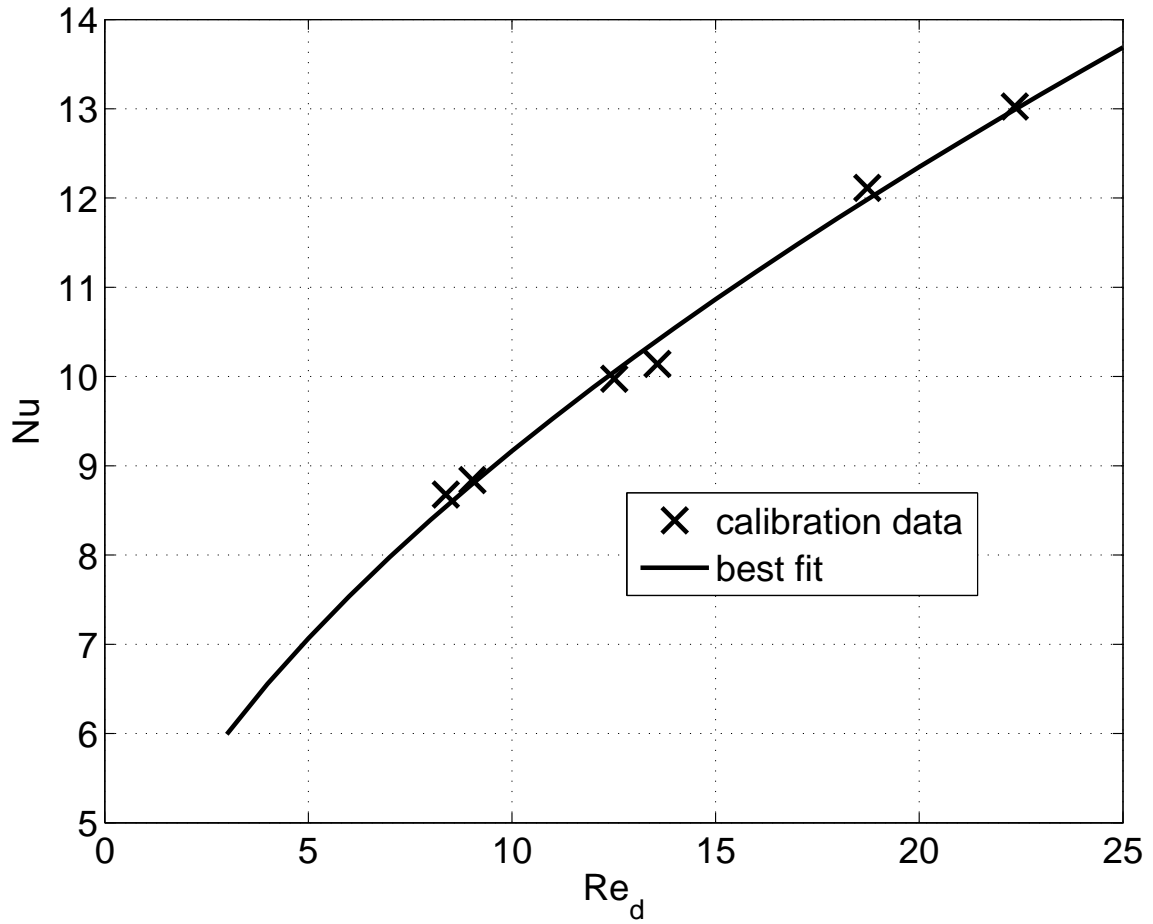


Figure 9.4.: Hot wire calibration data converted to non-dimensional parameters. Linear independent axis

### 9.1.3 Hot Wire Location and Spatial Accuracy

The first set of hot-wire data was collected at  $x = 285$  mm. This location was chosen to be ahead of transition, but as far downstream as possible to enable better probing of a thicker boundary layer. The mass flux profile at  $\alpha = 4^\circ$  seemed reasonable, but for  $\alpha = 0^\circ$  the profile had larger-than-expected fluctuations and an unusual bulged shape. After further analysis of TSP data, it was realized that the preliminary transition location assessment was incorrect and that in fact the boundary layer was

transitional under these conditions for  $\alpha = 0^\circ$  (but not  $\alpha = 4^\circ$ ). For this reason the subsequent profiles were collected at  $x = 250$  mm, ahead of the 270 mm onset location measured with TSP.

The hot wire's horizontal position was set by aligning it with the registration mark at  $x = 250$  mm. It was impossible to see the centerline mark when the model was installed in the tunnel, so the mark at  $y = 50$  mm was used instead. It was difficult to ensure there was no parallax when aligning this mark and the hotwire, so the streamwise location is estimated to be  $x = 250 \pm 2$  mm. As illustrated in Section 2.2.2, streamwise gradients of the flow properties are relatively small this far from the nose.

The hot wire's initial vertical location relative to the model was measured with an Infinity Model K2 long-distance microscope with a CF-1B objective lens and an additional set of lenses, designed by Professor Steven Collicott, to correct for the thick Plexiglas window [99]. The microscope reticle enables vertical precision of better than 0.1 mm if the hot wire and model surface can be brought into focus. This ideal condition was not achieved for these tests. The porthole window was installed for the hot wire tests. It is thinner than the large Plexiglass window, so the corrective optics on the microscope did not perfect the image. It is estimated that the error in the hot wire's initial location was  $\pm 0.2$  mm.

The hot wire's vertical position during the run was controlled and measured by the traverse system described in Section 3.3. In previous hot-wire experimentation, the traverse motion profiles typically included stationary pauses between steps to aid in establishing the probe's location and ostensibly to reduce electronic noise from the traverse in the CTA output. These pauses were not employed in the final hot-wire data shown here. The new position encoder eliminates the need to count pauses to find the probe location. The electronic noise is present whenever the traverse system is powered, whether moving or not. In fact, the preliminary hot-wire results showed increased noise when the wire was stationary. The maximum vertical velocity of the hot wire, 50 mm/s, is more than three orders of magnitude less than the streamwise

velocity ( $\approx 800\text{--}900$  m/s in the freestream, less in the boundary layer); thus, the probe velocity component of the CTA output was disregarded. The benefits of the shorter-duration profile were that the freestream conditions changed less during the measurement and that more profiles could be made during the run time.

Two different types of profile were employed. The first test for each angle of attack covered a large vertical distance (30 or 35 mm) to find the boundary layer edge, detect the shock location, and record the freestream mass flux. These longer profiles took  $\approx 2$  s to complete, so only one or two could be completed during the attached portion of a run. Their start was delayed until  $t = 2.5$  s, after the nozzle boundary layer reattached. The travel of subsequent profiles was reduced to 5–8 mm, depending on boundary-layer thickness, so that many circuits of the boundary layer could be made during the run. Both long and short profiles had 100-ms pauses after each leg. The actual profiles used are presented below, in conjunction with the mass flux data.

When analyzing the first boundary layer profiles after the linear encoder was installed, it appeared as though the oblique shock from the model nosetip and the boundary layer edge occurred at different heights depending on whether the probe was moving up or down. After studying the system and the profiles, it was eventually realized that the linear encoder's output is delayed slightly from the probe's true position. The boundary layer edge was not moving; instead, the probe position was incorrectly reported. Shifting the traverse location signal ahead 0.018 s fixed this error. John Phillips, the laboratory electronics technician, was consulted on this problem and he considers it reasonable to attribute this delay to circuitry within the encoder meter. This correction was determined by the heuristic technique of adjusting the delay until the shock location was consistent for consecutive passes by the hot wire.

## 9.2 Results and Discussion

A calibrated hot wire was used to measure the mass flux profile along the HIFiRE-5 centerline at  $\alpha = 0^\circ$  and  $4^\circ$ . Extensive hot-wire measurements over a wide range of flow conditions and locations were not made because the goal was merely to collect data for verification of CFD mean-flow results.

There were several turbulent bursts originally present in the hot-wire data. An algorithm was written to automatically remove the data segments corrupted by the bursts because the voltage spikes obscured shape of the boundary layer profile. The code searched through the nozzle-wall hot-film data for each run and discarded data whenever the voltage exceeded the mean plus three standard deviations. An extra 0.05 ms ahead of and 0.20 ms behind each segment were also excised. There were 20–40 bursts encountered during each 6-s run. This task could have been accomplished manually, but it was much easier to automate.

### 9.2.1 $4^\circ$ Angle of Attack

Figure 9.5 shows the mass flux measured by a hot wire for  $\alpha = 4^\circ$  (windward side) at  $x = 250$  mm. The black line shows the calibrated hot wire output; the blue line shows the freestream mass flux ( $\rho_\infty u_\infty$ ) computed from the stagnation conditions. The mass flux ranges from 15.6 to 57.2 kg/m<sup>2</sup>/s, a small extrapolation from the calibration (18.6–52.4 kg/m<sup>2</sup>/s). In Figure 9.5b, the mass flux has been normalized by the freestream mass flux. The red line in Figure 9.5b, which refers to the right axis, shows the distance of the hot wire above the model surface during the run. The hot wire began the run at  $z = 1$  mm and moved to  $z = 36$  mm. It had time to cover this distance slightly more than three times (more than 1.5 complete laps) before the run ended.

This run's data from  $t = 3.47$ – $3.53$  s was used in the calibration. It is the point at  $Re_d = 13.57$ ,  $Nu = 10.14$  in Figure 9.4. This point deviates the most from the calibration curve fit, which is apparent in Figure 9.5 as the difference between the

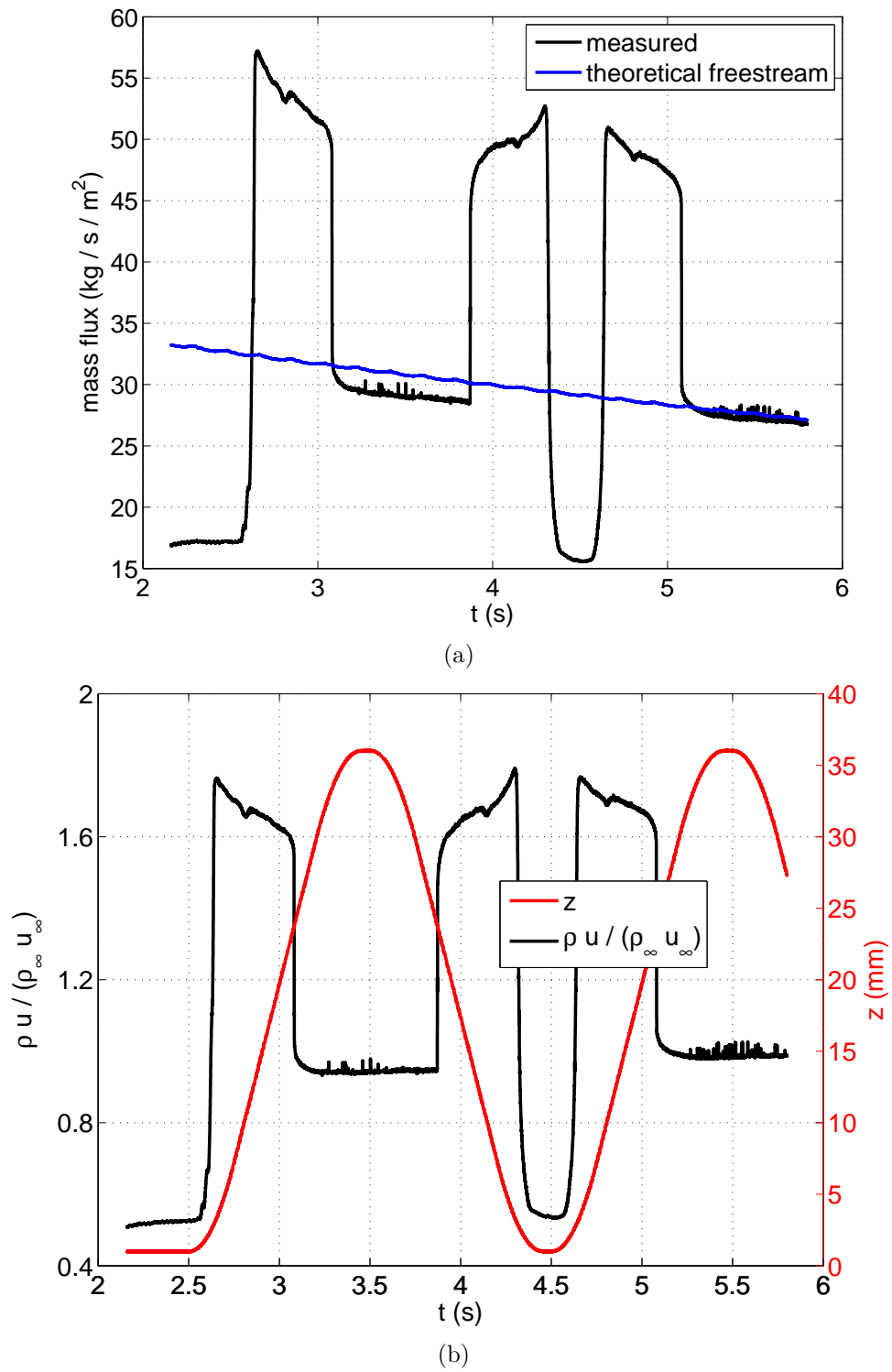


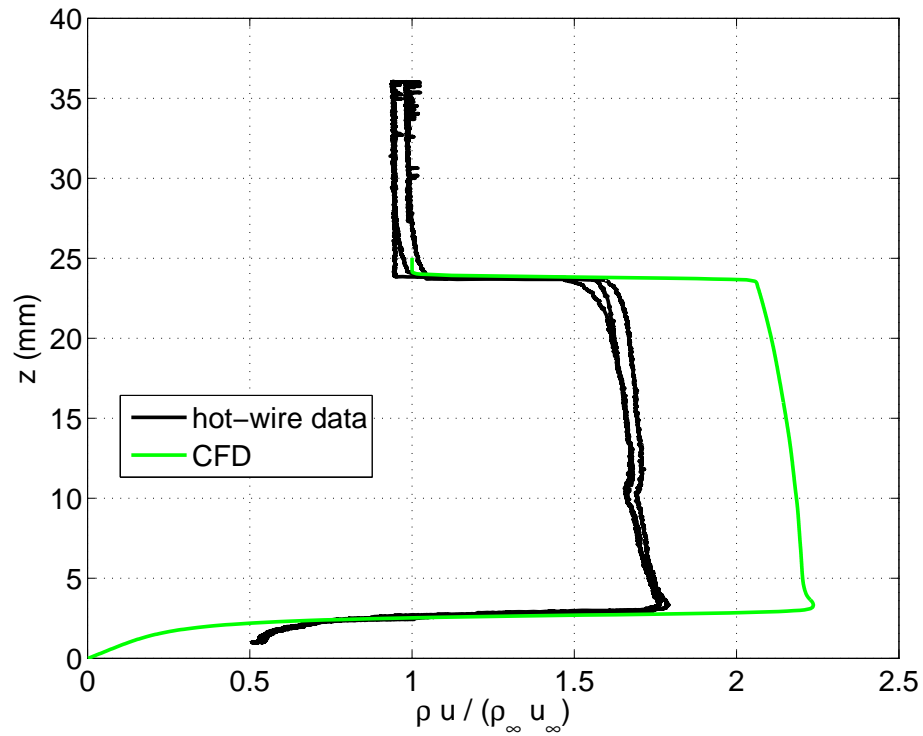
Figure 9.5.: Mass flux measured by hot wire.  $\alpha = 4^\circ$ ,  $x = 250$  mm,  $y = 0$  mm

measured and theoretical mass flux at  $t \approx 3.5$  s. The measured and theoretical freestream mass flux differ here by 6%, which is a reasonable approximation of the error within the calibration range.

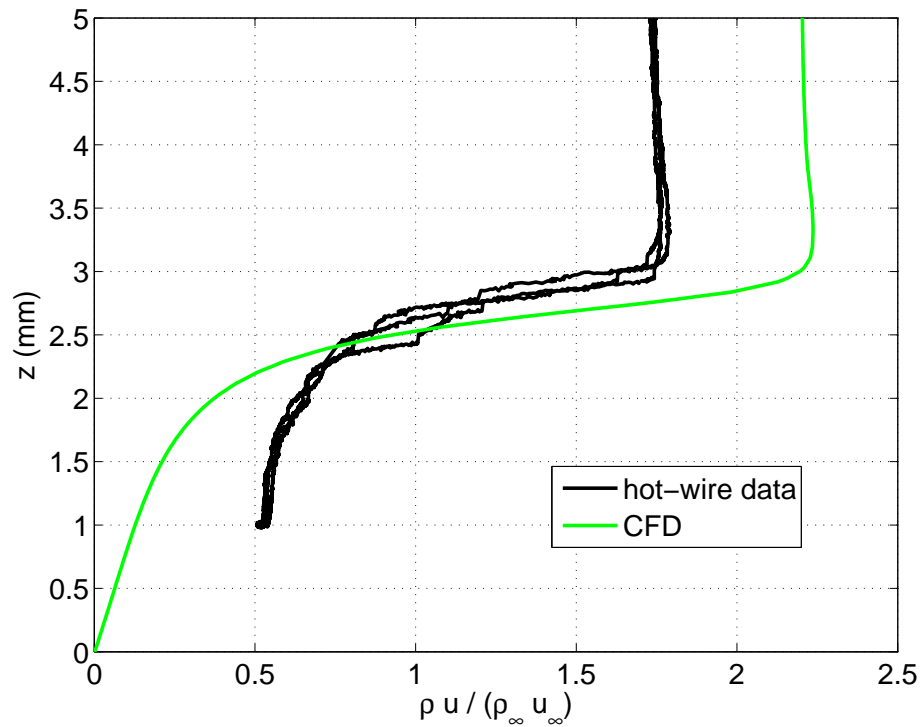
Figure 9.6 shows the mass flux boundary layer profile. As in Figure 9.5b, the mass flux has been normalized by its freestream value. All passes from the hot wire are shown to provide a picture of the scatter of the data. The green line is the boundary layer profile computed by Dr. Choudhari. Figure 9.6a shows the entire range of the profile, while Figure 9.6b shows only the boundary layer. The experimental and computational results agree well in several significant ways. Both methods locate the boundary-layer edge at  $z = 3.0$  mm and the shock at  $z = 24$  mm. They also indicate similar concavity inside the boundary layer and slopes near its edge. The mass flux exhibits the same narrow ( $\approx 1$ -mm-thick) overshoot just outside the boundary layer edge.

The main difference between the experimental and computational results is that their magnitudes are significantly different at both the low and high ends of the mass flux range. The deviation for low mass flux is not surprising because the hot wire calibration assumes  $M > 2$ , which is not valid near the wall. According to the CFD prediction, the Mach number is less than 2 within 2.2 mm of the wall at  $x = 250$  mm for these conditions, which is where the experimental and computational mass fluxes diverge. This invalid assumption explains why the profile does not extend to  $\rho u = 0$  at the wall. The differing mass fluxes between the boundary layer edge and shock location are not as easily explained. The reason for the dimple in the profile at  $z = 10$  mm is also unknown.

The computed boundary-layer edge velocity  $u_e$  is 839 m/s, 3.06 mm above the wall. Estimating the second-mode wave frequency as  $\frac{1}{2}u_e/\delta$  yields  $f = 137$  kHz, higher than the  $\approx 105$  kHz predicted as the most-amplified frequency at that location by the stability computations discussed in Section 8.5.



(a) Wide view



(b) Zoomed view

Figure 9.6.: Mass flux boundary layer profile.  $\alpha = 4^\circ$ ,  $x = 250$  mm,  $y = 0$  mm



### 9.2.2 0° Angle of Attack

Figure 9.7 displays the mass flux measured by a hot wire for  $\alpha = 0^\circ$ . In this test, the hot wire traversed from 0.5 to 8.5 mm above the model. This distance was sufficient to cover the entire boundary layer, but the shock was not reached. The probe completed four laps during the run.

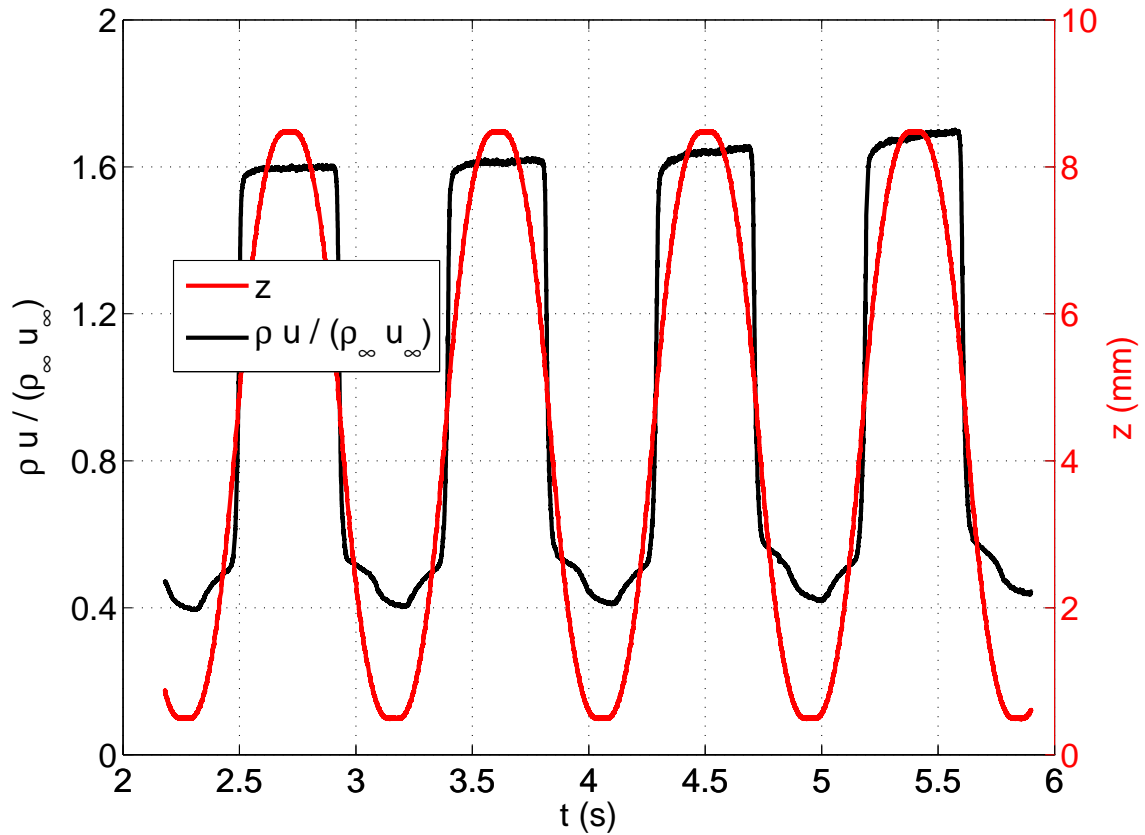


Figure 9.7.: Mass flux measured by hot wire.  $\alpha = 0^\circ$ ,  $x = 250$  mm,  $y = 0$  mm

The mass flux boundary layer profile for  $\alpha = 0^\circ$  is shown in Figure 9.8. Dr. Choudhari's computational prediction for this case is again included for comparison (green line). As in the previous  $\alpha = 4^\circ$  case, substantial agreement between the experimental and computational data is observed. The boundary layer thickness is 5.5 mm, compared to 3.0 mm for  $\alpha = 4^\circ$ . The high shear at the boundary layer edge predicted

by the CFD appears in the hot wire data. Both CFD and hot wire show a mass flux profile that is concave up nearest the wall, has an inflection point at  $z = 2$ – $3$  mm, is concave down until  $z = 5$  mm where a second inflection point exists, and is concave up thereafter. Unlike the previous case, the experimental mass flux is only 3–8% below the computed mass flux at the boundary layer edge. There is a much larger discrepancy at the low end of the mass flux range, but this difference can be attributed again to questionable extrapolation of the calibration at low mass flux and  $M$ . For the  $\alpha = 0^\circ$  case, the Mach number is computed to be less than 2 within 4.3 mm of the wall, which is once again where the computational and experimental results differ.

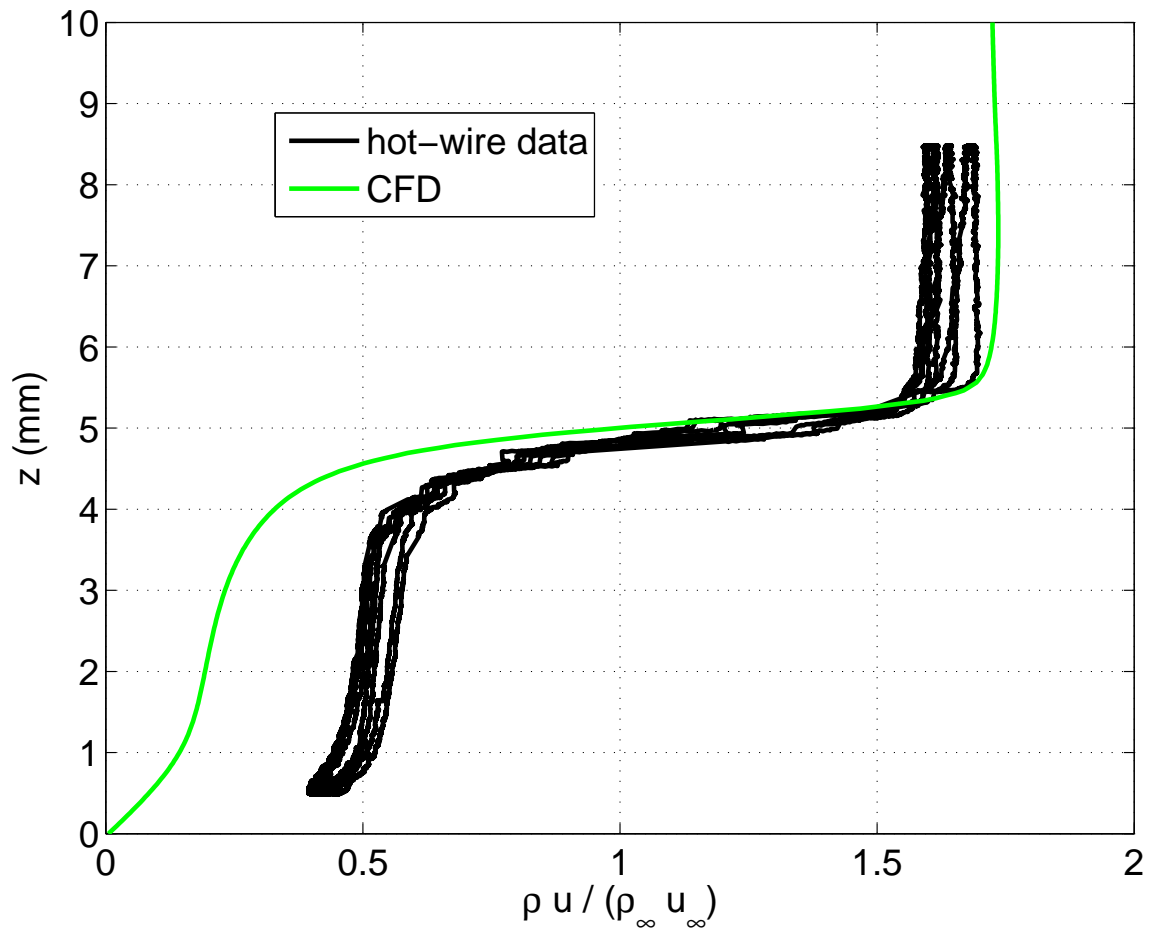


Figure 9.8.: Mass flux boundary layer profile.  $\alpha = 0^\circ$ ,  $x = 250$  mm,  $y = 0$  mm

## 10. SUMMARY AND CONCLUSIONS

A 38.1% scale model of the HIFiRE-5 blunt elliptic cone was tested under noisy and quiet flow in the Boeing/AFOSR Mach-6 Quiet Tunnel. Boundary layer transition was found to be delayed when running with low noise levels.

Two problems arose regarding the flow quality in the BAM6QT. The flow through the nozzle tended to separate under quiet flow due to the relatively large cross section of the model. The data collected during this portion of the run is unusable. Also, the spatial extent of quiet flow in the BAM6QT at high stagnation pressures is uncertain. The flow may be quiet throughout the nozzle, but conclusive measurements have not been made. Thus, it is possible that the quiet-flow transition results are contaminated by noise impinging near the aft end of the model.

Temperature-Sensitive Paint was employed to visualize the temperature rise on the frustum under quiet and noisy flow. Boundary layer transition was inferred from increases in the streamwise temperature profile. A substantial delay in transition was observed when running with a low noise level. Centerline transition occurs at both  $\alpha = 0^\circ$  and  $4^\circ$  under quiet flow near the maximum quiet pressure. If the noise level is truly low throughout the test section, then these results are the first evidence in the BAM6QT of transition under quiet flow that is not induced by deliberately-generated roughness. Until now, quiet-flow transition had been detected only on vehicles with isolated roughness elements intended to trip the boundary layer, such as the X-51 and HIFiRE-1. There was a two-fold increase of  $Re_x$  at the centerline transition location under quiet compared to noisy flow.

Transition on the HIFiRE-5 appears to arise from amplification of two different modes — second-mode waves along the centerline, and crossflow vortices between the centerline and leading edge. Transition on the windward side along the centerline was delayed slightly ( $< 10\%$ ) when increasing angle of attack from  $0^\circ$  to  $4^\circ$  under both

quiet and noisy flow. Crossflow transition was delayed substantially at higher angle of attack. This difference is attributed to the reduced spanwise pressure gradient on the elliptic cone as  $\alpha$  is increased in this range.

The first TSP application did not have the desired smooth finish; this flaw was exploited as an opportunity to investigate the effect of distributed roughness on transition. Unfortunately, the original rough ‘orange-peel’ finish was not characterized well. Compared to the relatively smooth final paint job, the temperature rise presumed to arise from crossflow vortices occurs earlier. Centerline transition is impossible to discern for the rough finish. Application of TSP also introduced a step at the leading edge of the paint. However, when a 0.33-mm forward-facing step 76.2 mm from the tip was tapered over a  $\approx 6$ -mm distance, no difference in centerline or crossflow transition was detected.

Several thermocouples and heat-transfer gauges were installed on the HIFiRE-5 to complement the TSP. The model temperature as measured on the model base was found to vary by less than 1 K during a run, but the initial model temperature varied by several K from one run to the next, and by 10–15 K during a week of testing. Coaxial thermocouples were installed flush with the model surface, but the data was unsatisfactory due to a small signal-to-noise ratio. Schmidt-Boelter and thin-film heat-transfer gauges were employed with greater success. The Schmidt-Boelter gauge, in particular, holds promise for future efforts to convert the TSP global temperature measurement to heat flux.

PCB fast-response pressure sensors were used to detect fluctuations in the boundary layer above the centerline prior to transition under noisy flow at  $Re \approx 3 \cdot 10^6$  /m, the lowest  $Re$  tested. At higher  $Re$ , the model boundary layer transitioned ahead of the farthest-upstream PCB sensor. The peak frequency was 110–115 kHz on the windward side at  $\alpha = 4^\circ$  and 55–65 kHz at  $\alpha = 0^\circ$  for  $Re = 3 \cdot 10^6$  /m. The thicker boundary layer at  $\alpha = 0^\circ$  probably accounts for this difference. Stability computations at this  $Re$  are not available. The PCB data are harder to interpret under quiet flow, probably because of the smaller amplitudes of the fluctuations. It is pos-

sible that pressure fluctuations from second-mode waves were observed under quiet flow at  $Re = 10\text{--}12 \cdot 10^6$  /m, but this conclusion cannot be made with confidence. The frequencies detected by the PCBs under quiet flow at  $\alpha = 0^\circ$  and  $4^\circ$  agree with computational predictions of second-mode disturbance frequencies.

Calibrated 0.0004-in.- (10- $\mu$ m-) diameter hot wires were used with a Constant Temperature Anemometer to measure mass flux profiles on the HIFiRE-5 centerline 250 mm downstream from the nose. The frequency response of the hot wires was only  $\approx 20$  kHz, so they were suitable only for mean-flow measurements. The qualitative shape of the hot-wire profiles agrees with computational predictions of the profile. The boundary layer contains one inflection point for  $\alpha = 4^\circ$  and two for the less-stable  $\alpha = 0^\circ$  case. The experimental and computational data do not agree as well for higher or (especially) lower mass fluxes. This discrepancy is not too surprising, considering the limited calibration range and numerous assumptions (Mach number independence, constant overheat ratio, neglect of end effects, etc.) incorporated in the calculations.

## 10.1 Recommendations for Future Work

The most important future work recommended is to improve the characterization of the noise level at the aft end of the BAM6QT test section at high stagnation pressures. This uncertainty prevents clear assessment of quiet-flow transition locations. Another recommendation is to revisit the investigation of transition on the unpainted model. Testing with coaxial thermocouples proved fruitless, but the installation of several Schmidt-Boelter heat-transfer gauges may provide an interesting comparison with the TSP results.

The agreement between TSP and PCB fast pressure sensor indications of transition onset and end locations under noisy flow is encouraging. Computational predictions of the disturbance frequencies for these low- $Re$  conditions have not been made, but are the logical next step for further verification of stability computations. Fur-

ther work is needed with the PCBs to understand and eliminate the narrow peaks in frequency spectra of surface pressure fluctuations that obscure the quiet-flow measurements of second-mode waves.

The hot-wire measurements appear to have been successful, especially considering their late addition to the test program. Qualitative agreement with the computational results was achieved throughout the profile and the quantitative results match within the calibration range. There is lots of room for improvement and expansion. The calibration should be refined and extended. Measurements at other locations and flow conditions simply require time devoted to them.

## LIST OF REFERENCES



## LIST OF REFERENCES

- [1] Eli Reshotko. Stability and transition, how much do we know? *U.S. National Congress of Applied Mechanics*, pages 421–434, June 1986. American Society of Mechanical Engineers.
- [2] John D. Anderson Jr. *Hypersonic and High Temperature Gas Dynamics*, chapter 6, Viscous Flow: Basic Aspects, Boundary Layer Results, and Aerodynamic Heating. American Institute of Aeronautics and Astronautics, Inc., Reston, VA, 1989.
- [3] Steven P. Schneider. Laminar-turbulent transition on reentry capsules and planetary probes. *Journal of Spacecraft and Rockets*, 43(6):1153–1173, November–December 2006.
- [4] Steven P. Schneider. Hypersonic laminar-turbulent transition on circular cones and scramjet forebodies. *Progress in Aerospace Sciences*, 40(1-2):1–50, February 2004.
- [5] John Laufer. Aerodynamic noise in supersonic wind tunnels. *Journal of the Aerospace Sciences*, 28(9):685–692, September 1961.
- [6] Ivan E. Beckwith. Development of a high Reynolds number quiet tunnel for transition research. *AIAA Journal*, 13(3):300–306, March 1975.
- [7] Steven P. Schneider. Effects of high-speed tunnel noise on laminar-turbulent transition. *Journal of Spacecraft and Rockets*, 38(3):323–333, May–June 2001.
- [8] S. R. Pate and C. J. Schueler. Radiated aerodynamic noise effects on boundary layer transition in supersonic and hypersonic wind tunnels. *AIAA Journal*, 7(3):450–457, March 1969.
- [9] Steven P. Schneider. Development of hypersonic quiet tunnels. *Journal of Spacecraft and Rockets*, 45(4):641–664, July–August 2008.
- [10] I. E. Beckwith, W. D. Harvey, J. E. Harris, and B. B. Holley. Control of supersonic wind-tunnel noise by laminarization of nozzle-wall boundary layers. Technical Report TM X-2879, NASA Langley Research Center, Hampton, VA 23665, December 1973.
- [11] W. D. Harvey, P. C. Stainback, J. B. Anders, and A. M. Cary. Nozzle wall boundary-layer transition and freestream disturbances at Mach 5. *AIAA Journal*, 13(3):307–314, March 1975.
- [12] Frank M. White. *Viscous Fluid Flow*. McGraw-Hill, New York, NY, 3rd edition, 2006.

- [13] Leslie M. Mack. Boundary layer stability theory. Technical Report Document 900-277, Rev. A, Jet Propulsion Laboratory, Pasadena, CA, 1969.
- [14] H. L. Reed and W. S. Saric. Linear stability theory applied to boundary layers. *Annual Review of Fluid Mechanics*, 28:389–428, 1996.
- [15] J. C. Adams Jr. and W. R. Martindale. Hypersonic lifting body windward surface flow-field analysis for high angles of incidence. Technical Report AECD-TR-73-2, Arnold Engineering Development Center, February 1973.
- [16] Steven P. Schneider. Effects of roughness on hypersonic boundary-layer transition. *Journal of Spacecraft and Rockets*, 45(2):193–209, March–April 2008.
- [17] R. H. Radeztsky Jr., M. S. Reibert, and W. S. Saric. Effect of isolated micron-sized roughness on transition in swept-wing flows. *AIAA Journal*, 37(11):1370–1377, November 1999.
- [18] Leslie M. Mack. Linear stability theory and the problem of supersonic boundary layer transition. *AIAA Journal*, 13(3):278–289, March 1975.
- [19] C. R. Alba, H. B. Johnson, M. D. Bartkowicz, and G. V. Candler. Boundary layer stability calculations of the HIFiRE Flight 1 vehicle in the LaRC 20-Inch Mach 6 Air Tunnel. AIAA Paper 2008-505, January 2008.
- [20] F.-J. Chen, M. R. Malik, and I. E. Beckwith. Boundary-layer transition on a cone and flat plate at Mach 3.5. *AIAA Journal*, 27(6):687–693, June 1989.
- [21] Eli Reshotko. Transition issues for atmospheric entry. *Journal of Spacecraft and Rockets*, 45(2):161–164, March–April 2008.
- [22] Eli Reshotko. Roughness-induced transition, experiment and modeling. AIAA Paper 2008-4294, June 2008.
- [23] K. M. Casper and B. M. Wheaton. Effect of freestream noise on roughness-induced transition at Mach 6. AIAA Paper 2008-4291, June 2008.
- [24] T. J. Horvath, A. J. Amar, N. Calvert, B. R. Hollis, J. Everhart, S. A. Berry, and P. Danehy. Experimental observations of blunt body boundary layer transition. AIAA Oral Presentation, June 2008.
- [25] S. Berry, K. Daryabeigi, K. Wurster, and R. Bittner. Boundary layer transition on X-43A. AIAA Paper 2008-3736, June 2008.
- [26] Roger L. Kimmel. Roughness considerations for the HIFiRE-1 vehicle. AIAA Paper 2008-4293, June 2008.
- [27] G. B. Schubauer and H. K. Skramstad. Laminar boundary-layer oscillations and stability of laminar flow. *Journal of the Aeronautical Sciences*, 14(2):69–78, February 1947.
- [28] M. Estorf, R. Radespiel, S. P. Schneider, H. B. Johnson, and S. Hein. Surface-pressure measurements of second-mode instability in quiet hypersonic flow. AIAA Paper 2008-1153, January 2008.

- [29] R. L. Kimmel and J. Poggie. Three-dimensional hypersonic boundary layer stability and transition. Technical Report WL-TR-97-3111, Air Force Research Laboratory, Wright-Patterson Air Force Base, OH 45433-7542, December 1997.
- [30] J. Poggie, R. L. Kimmel, and S. N. Schwoerke. Traveling instability in a Mach 8 flow over an elliptic cone. *AIAA Journal*, 38(2):251–258, February 2000.
- [31] R. L. Kimmel, M. A. Klein, and S. N. Schwoerke. Three-dimensional hypersonic boundary-layer computations for transition experiment design. *Journal of Spacecraft and Rockets*, 34(4):409–415, July-August 1997.
- [32] M. Huntley and A. Smits. Transition studies on an elliptic cone in Mach 8 flow using Filtered Rayleigh Scattering. *European Journal of Mechanics B: Fluids*, 19:695–706, 2000.
- [33] Mark B. Huntley. *Transition on Elliptic Cones at Mach 8*. PhD thesis, Princeton University Department of Mechanical and Aerospace Engineering, November 2000.
- [34] J. D. Schmisser, S. P. Schneider, and S. H. Collicott. Receptivity of the Mach-4 boundary-layer on an elliptic cone to laser-generated localized freestream perturbations. AIAA Paper 1998-0532, January 1998.
- [35] J. D. Schmisser, S. P. Schneider, and S. H. Collicott. Supersonic boundary-layer response to optically generated freestream disturbances. *Experiments in Fluids*, 33(2):225–232, August 2002.
- [36] S. L. Huang, G. K. Stuckert, and T. Herbert. Cross flow instability of the supersonic flow over a 4:1 elliptic cone. Technical Report 95-0077TR, AFOSR, 1995. DTIC citation AD-A291128.
- [37] Ian J. Lyttle. On the use of transition correlations for three-dimensional boundary layers within hypersonic, viscous flows. Master’s thesis, Arizona State University, Mechanical and Aerospace Engineering, August 1994.
- [38] H. L. Reed and T. S. Haynes. Transition correlations in three-dimensional boundary layers. *AIAA Journal*, 32(5):923–929, May 1994.
- [39] Douglas J. Dolvin. Hypersonic International Flight Research and Experimentation (HIFiRE): Fundamental sciences and technology development strategy. AIAA Paper 2008-2581, April 2008.
- [40] K. T. Berger, F. A. Green, and R. L. Kimmel. Aerothermodynamic testing and boundary layer trip sizing of the HIFiRE Flight 1 vehicle. AIAA Paper 2008-640, January 2008.
- [41] K. T. Berger, F. A. Green, R. L. Kimmel, C. R. Alba, and G. V. Candler. Aerothermodynamic testing and boundary-layer trip sizing of the HIFiRE Flight 1 vehicle. *Journal of Spacecraft and Rockets*, 45(6):1117–1124, November–December 2008.
- [42] S. H. Walker, J. Sherk, D. Shell, R. Schena, J. F. Bergmann, and J. Gladbach. The DARPA/AF Falcon program: the Hypersonic Technology Vehicle #2 (HTV-2) flight demonstration phase. AIAA Paper 2008-2539, April 2008.

- [43] Meelan Choudhari et al. HIFiRE5: boundary layer analysis. Private communication; presentation HF5\_preliminary\_results\_0309.pdf, March 2009.
- [44] M. Choudhari, C.-L. Chang, T. Jentink, F. Li, K. Berger, G. Candler, and R. Kimmel. Transition analysis for the HIFiRE-5 vehicle. AIAA Paper 2009-4056, June 2009.
- [45] F. P. Incropera, D. P. DeWitt, T. L. Bergman, and A. S. Levine. *Fundamentals of Heat and Mass Transfer*. John Wiley & Sons, Inc., New York, NY, 6th edition, 2007.
- [46] J. Lukasiewicz. *Experimental Methods of Hypersonics*. Marcel Dekker, Inc., New York, 1973.
- [47] T. J. Juliano, E. O. Swanson, and S. P. Schneider. Transition research and improved performance in the Boeing/AFOSR Mach-6 quiet tunnel. AIAA Paper 2007-0535, January 2007.
- [48] T. J. Juliano, S. P. Schneider, S. Aradag, and D. Knight. Quiet-flow Ludwig tube for hypersonic transition research. *AIAA Journal*, 46(7):1757–1763, July 2008.
- [49] Thomas J. Juliano. Nozzle modifications for high-Reynolds-number quiet flow in the Boeing/AFOSR Mach-6 Quiet Tunnel. Master’s thesis, Purdue University, School of Aeronautics and Astronautics, December 2006. Available from DTIC as ADA456772.
- [50] T. J. Juliano, R. Segura, M. P. Borg, K. Casper, M. J. Hannon, Jr., B. M. Wheaton, and S. P. Schneider. Starting issues and forward-facing cavity resonance in a hypersonic quiet tunnel. AIAA Paper 2008-3735, June 2008.
- [51] B. M. Wheaton, T. J. Juliano, D. C. Berridge, A. Chou, P. L. Gilbert, K. M. Casper, L. E. Steen, and S. P. Schneider. Instability and transition measurements in the Mach-6 Quiet Tunnel. AIAA Paper 2009-3559, June 2009.
- [52] D. C. Berridge, A. Chou, C. A. C. Ward, L. E. Steen, P. L. Gilbert, T. J. Juliano, S. P. Schneider, and J. E. Gronvall. Hypersonic boundary layer transition experiments in a Mach-6 quiet tunnel. AIAA Paper 2010-1061, January 2010.
- [53] C. A. C. Ward, B. M. Wheaton, A. Chou, P. L. Gilbert, L. E. Steen, and S. P. Schneider. Hypersonic boundary-layer transition experiments in a Mach-6 quiet tunnel. AIAA Paper 2010-4721, June 2010.
- [54] Michael J. Hannon, Jr. Evaluation of diffuser modifications for the Boeing/AFOSR Mach-6 Quiet Tunnel. Master’s thesis, School of Aeronautics and Astronautics, Purdue University, August 2008.
- [55] C. R. Skoch, S. P. Schneider, and M. P. Borg. Disturbances from shock/boundary-layer interactions affecting upstream hypersonic flow. AIAA Paper 2005-4897, June 2005.
- [56] Craig R. Skoch. *Disturbances from Shock/Boundary-Layer Interactions Affecting Upstream Hypersonic Flow*. PhD thesis, Purdue University School of Aeronautics & Astronautics, December 2005.

- [57] A. X. Cartagena, T. J. Juliano, and S. P. Schneider. Gap pressure maintenance system for the Boeing/AFOSR Mach-6 Quiet Tunnel. Unpublished SURF Program Final Report, July 2008.
- [58] Amanda Chou. Untitled master's thesis. Master's thesis, Purdue University, School of Aeronautics and Astronautics, December 2010.
- [59] Erick O. Swanson. Mean flow measurements and cone flow visualization at Mach 6. Master's thesis, Purdue University School of Aeronautics & Astronautics, December 2002.
- [60] Laurel Electronics Inc., 3183-G Airway Ave, Costa Mesa, CA, 92626, USA. *Laureate Series 2 Counter / Timer / Serial Input Meter Owners Manual*. <http://www.laurels.com/quadrature.htm>.
- [61] Matthew P. Borg. Characteristics of the contraction of the Boeing/AFOSR Mach-6 Quiet Tunnel. Master's thesis, Purdue University, School of Aeronautics and Astronautics, December 2005.
- [62] M. P. Borg, S. P. Schneider, and T. J. Juliano. Inlet measurements and quiet flow improvements in the Boeing/AFOSR Mach-6 Quiet Tunnel. AIAA Paper 2006-1317, January 2006.
- [63] E. W. Lemmon and R. T. Jacobsen. Viscosity and thermal conductivity equations for nitrogen, oxygen, argon, and air. *International Journal of Thermophysics*, 25(1):21–69, January 2004.
- [64] Peter L. Gilbert. Effect of tunnel noise on laminar stagnation point heating. Master's thesis, Purdue University, School of Aeronautics and Astronautics, August 2010.
- [65] John D. Anderson Jr. *Fundamentals of Aerodynamics*. McGraw-Hill, New York, 4th edition, 2007.
- [66] S. P. Schneider and T. J. Juliano. Laminar-turbulent transition measurements in the Boeing/AFOSR Mach-6 Quiet Tunnel. AIAA Paper 2007-4489, June 2007.
- [67] S. Aradag, D. D. Knight, and S. P. Schneider. Computational design of the Boeing/AFOSR Mach 6 wind tunnel. AIAA Paper 2006-1434, January 2006.
- [68] S. Aradag, D. D. Knight, and S. P. Schneider. Bleed lip geometry effects on the flow in a hypersonic wind tunnel. *AIAA Journal*, 44(9):2133–2136, September 2006.
- [69] Laura E. Steen. Untitled master's thesis. Master's thesis, Purdue University, School of Aeronautics and Astronautics, December 2010.
- [70] S. P. Schneider and C. E. Haven. Quiet-flow Ludwig tube for high-speed transition research. *AIAA Journal*, 33(4):688–693, April 1995.
- [71] H. Naiman, D. D. Knight, and S. P. Schneider. Computational redesign of the test section for the Boeing/AFOSR Mach-6 Quiet Tunnel. *Proceedings of the Institution of Mechanical Engineers, Part G: Journal of Aerospace Engineering*, 223(4):407–413, Special Issue 2009.

- [72] S. P. Schneider, C. Skoch, S. Rufer, E. Swanson, and M. P. Borg. Laminar-turbulent transition research in the Boeing/AFOSR Mach-6 Quiet Tunnel. AIAA Paper 2005-0888, January 2005.
- [73] Justin Rubal. Quantitative global heat transfer in a Mach-6 quiet tunnel using temperature sensitive paints. Master's thesis, Purdue University School of Aeronautics & Astronautics, December 2010.
- [74] Christopher A. C. Ward. Untitled master's thesis. Master's thesis, Purdue University, School of Aeronautics and Astronautics, December 2010.
- [75] F. L. Pedrotti, L. S. Pedrotti, and L. M. Pedrotti. *Introduction to Optics*. Pearson Prentice Hall, Upper Saddle River, NJ 07458, 3rd edition, 2007.
- [76] Erick O. Swanson. *Boundary-Layer Transition on Cones at Angle of Attack in a Mach-6 Quiet Tunnel*. PhD thesis, Purdue University School of Aeronautics & Astronautics, August 2008.
- [77] T. Liu and J. P. Sullivan. *Pressure and Temperature Sensitive Paints*. Springer-Verlag, 1st edition, 2005.
- [78] Justin Rubal. pressure-sensitive TSP. Personal communication (e-mail), February 22 2010.
- [79] Leslie M. Mack. Boundary layer linear stability theory. In *Report 709, Special Course on Stability and Transition of Laminar Flow*, pages 1–81. AGARD, March 1984.
- [80] W. S. Saric, H. L. Reed, and E. B. White. Stability and transition of three-dimensional boundary layers. *Annual Review of Fluid Mechanics*, 35:413–430, 2003.
- [81] W. Saric and H. Reed. Stability, transition, and control of three-dimensional boundary layer on swept wings. In G. E. A. Meier and K. R. Sreenivasan, editors, *IUTAM Symposium on One Hundred Years of Boundary Layer Research*, pages 177–188, 2006.
- [82] M. P. Borg, S. P. Schneider, and T. J. Juliano. Effect of freestream noise on roughness-induced transition for the X-51A forebody. AIAA Paper 2008-0592, January 2008.
- [83] Matthew P. Borg. *Instability and Transition on the X-51*. PhD thesis, Purdue University School of Aeronautics & Astronautics, August 2009.
- [84] John P. Sullivan. HiFire model 2010-2-8 run 7 & 8.docx. Unpublished report, June 2010.
- [85] K. M. Casper, S. J. Beresh, J. F. Henfling, R. W. Spillers, B. Pruett, and S. P. Schneider. Hypersonic wind-tunnel measurements of boundary-layer pressure fluctuations. AIAA Paper 2009-4054, June 2009.
- [86] Katya M. Casper. Hypersonic wind-tunnel measurements of boundary-layer pressure fluctuations. Master's thesis, Purdue University, School of Aeronautics and Astronautics, August 2009.

- [87] C. R. Alba, K. M. Casper, S. J. Beresh, and S. P. Schneider. Comparison of experimentally measured and computed second-mode disturbances in hypersonic boundary-layers. AIAA Paper 2010-897, January 2010.
- [88] Keisuke Fujii. Experiment of the two-dimensional roughness effect on hypersonic boundary-layer transition. *Journal of Spacecraft and Rockets*, 43(4):731–738, July-August 2006.
- [89] Dennis C. Berridge. Measurements of second-mode waves in hypersonic boundary layers with a high-frequency pressure transducer. Master’s thesis, Purdue University, School of Aeronautics and Astronautics, December 2010.
- [90] David Formenti. Choosing a spectral measurement for data analysis. *Sound and Vibration*, pages 2–3, June 2000.
- [91] D. C. Berridge, K. M. Casper, S. J. Rufer, C. R. Alba, D. R. Lewis, S. J. Beresh, and S. P. Schneider. Measurements and computations of second-mode instability waves in three hypersonic wind tunnels. AIAA Paper 2010-5002, June 2010.
- [92] M. M. Choudhari and C.-L. Chang. Purdue HiFire5 wind tunnel model at 4-degrees angle of attack. Private communication; document `Purdue_HiFire5_LST_PSE_results.doc`, June 2010.
- [93] Mark V. Morkovin. Fluctuations and hot-wire anemometry in compressible flows. AGARDograph 24, AGARD, November 1956.
- [94] P. C. Stainback and K. A. Nagabushana. Review of hot-wire anemometry techniques and the range of their applicability for various flows. In ASME, editor, *Thermal Anemometry*, volume FED167, pages 93–133. ASME, New York, 1993.
- [95] P. C. Stainback and R. D. Wagner. A comparison of disturbance levels measured in hypersonic tunnels using a hot-wire anemometer and a pitot pressure probe. AIAA Paper 72-1003, September 1972.
- [96] A. J. Smits, H. Hayakawa, and K. C. Muck. Constant-temperature hot-wire anemometry practice in supersonic flows. *Experiments in Fluids*, 1:83–92, 1983.
- [97] A. J. Smits and J. P. Dussauge. Hot-wire anemometry in supersonic flow. In *AGARDograph 315*, chapter 5. AGARD, 1989.
- [98] S. J. Rufer and S. P. Schneider. Hot-wire measurements of instability waves on a blunt cone at Mach 6. AIAA Paper 2005-5137, June 2005.
- [99] Shann J. Rufer. *Hot Wire Measurements of Instability Waves on Sharp and Blunt Cones at Mach 6*. PhD thesis, Purdue University School of Aeronautics & Astronautics, December 2005.
- [100] Thomas J. Juliano. Laminar-turbulent transition on the HTV-2 in a Mach-6 quiet tunnel. DTIC number ADB352458, June 2009. 132 pages. Unclassified; distribution limited to U.S. Government agencies and contractors.
- [101] Richard Shau. Hot-wire anemometry for supersonic flows. University of Texas at Austin Wind Tunnel Laboratory, August 1991.

- [102] E. F. Spina and C. B. McGinley. Constant-temperature anemometry in hypersonic flow: Critical issues and sample results. *Experiments in Fluids*, 17(6):365–374, October 1994.
- [103] C. Forbes Dewey. Hot-wire measurements in low Reynolds number hypersonic flow. *ARS Journal*, pages 1709–1718, December 1961.



## APPENDIX

## A. Figure Source Data

Table A identifies which tunnel runs were used to create the figures presented herein. The tunnel session is identified by the year, month, and day of the first run in that set. The photograph frame number is only applicable to TSP results.

Table A.1: Figure source data

Figure	Tunnel Session	Run No.	Frame
4.2	2006-9-18	2	
4.3	2009-11-17	6	
4.6	2010-2-8	10	14, 57
4.7	2010-2-8	10	
6.7	2010-2-8	13	160
6.8	2010-2-8	8	91
	2010-2-8	7	11
6.9	2009-11-17	9	101
	2009-11-17	7	11
6.10	2009-11-17	7	11
6.11	2010-2-8	11	151
	2010-2-8	10	57
6.12	2009-11-17	10	91
	2009-11-17	6	11
6.13, 6.14	2009-11-17	7	11
	2009-11-17	6	11
6.15	2010-2-8	8	160
	2010-2-8	11	151

*Continued on next page*

Figure	Tunnel Session	Run No.	Frame
6.16	2010-2-8	7	11
	2010-2-8	10	57
	2010-2-8	8	91
	2010-2-8	11	151
6.17, 6.18	2010-2-8	1	91
	2010-2-8	3	71
	2010-2-8	5	61
	2010-2-8	7	11
6.19, 6.20	2009-11-17	7	11
	2010-2-8	2	160
	2010-2-8	4	160
	2010-2-8	6	160
6.21, 6.22	2010-2-8	8	91
	2009-11-17	9	101
	2010-2-8	16	85
	2010-2-8	14	73
6.23, 6.24	2010-2-8	12	61
	2010-2-8	10	57
	2009-11-17	6	11
	2010-2-8	17	160
6.25, 6.26	2010-2-8	15	160
	2010-2-8	13	160
	2010-2-8	11	151
	2009-11-17	10	91
6.27	2010-2-8	7	11
	2009-1-28	5	141

*Continued on next page*

Figure	Tunnel Session	Run No.	Frame
	2009-12-15	2	11
7.2	2009-12-15	3	
7.3	2010-2-8	1–20	
7.4	2010-5-5	8	
7.6	2009-7-7	6	
7.7	2009-7-7	6	21
7.8, 7.9	2010-2-8	8	91
7.10, 7.11	2010-2-8	7	11
8.1	2010-2-8	7	
8.2, 8.3	2010-2-8	17	160
8.4	2010-2-8	15	160
8.5, 8.6	2010-2-8	2	160
8.7	2009-11-17	6	
8.8	2010-2-8	16	
8.9	2010-2-8	3	
8.10	2010-5-5	5	
8.11	2010-5-5	4	
8.12	2010-5-5	6	
8.13, 8.14	2009-11-17	6	11, 77
8.15, 8.17	2009-11-17	6	
8.18, 8.20	2009-11-17	2	
9.5, 9.6	2010-5-5	5	
9.7, 9.8	2010-5-5	4	

## B. Model Final Drawings

The design of the BAM6QT HIFiRE-5 model was originally created by the author using Pro/E. Mike Gideon of Tri-Models, Inc. made minor revisions to the originals and converted them to English units for fabrication. These images are excerpted from the final drawings. All dimensions are inches.

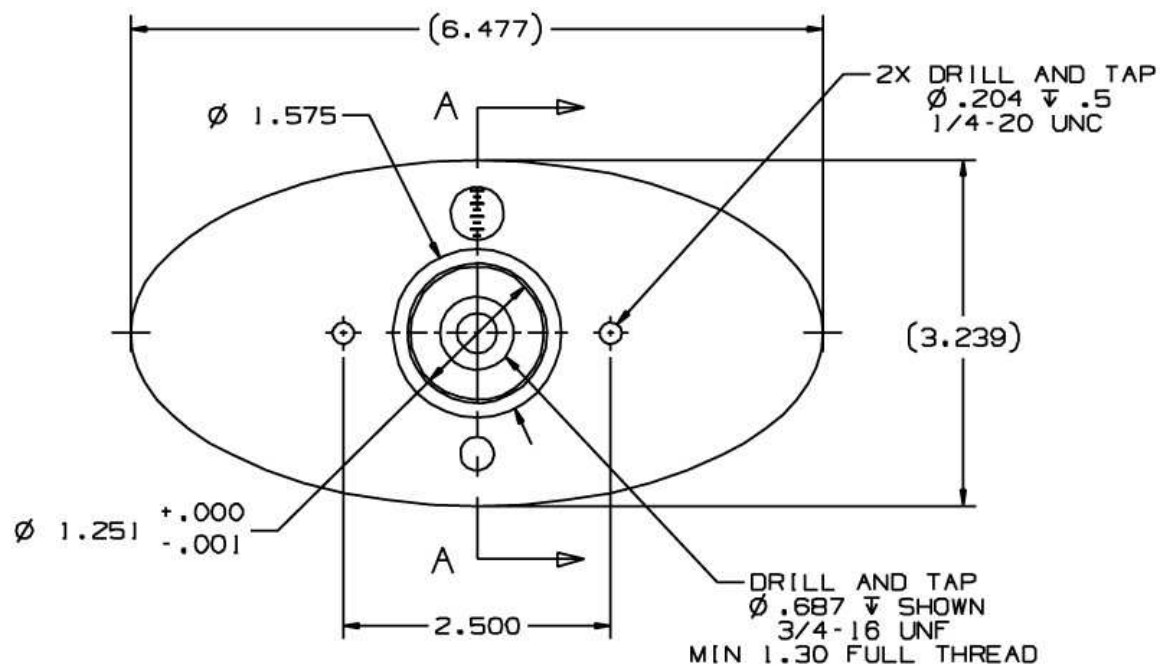


Figure B.1.: Frustum end view

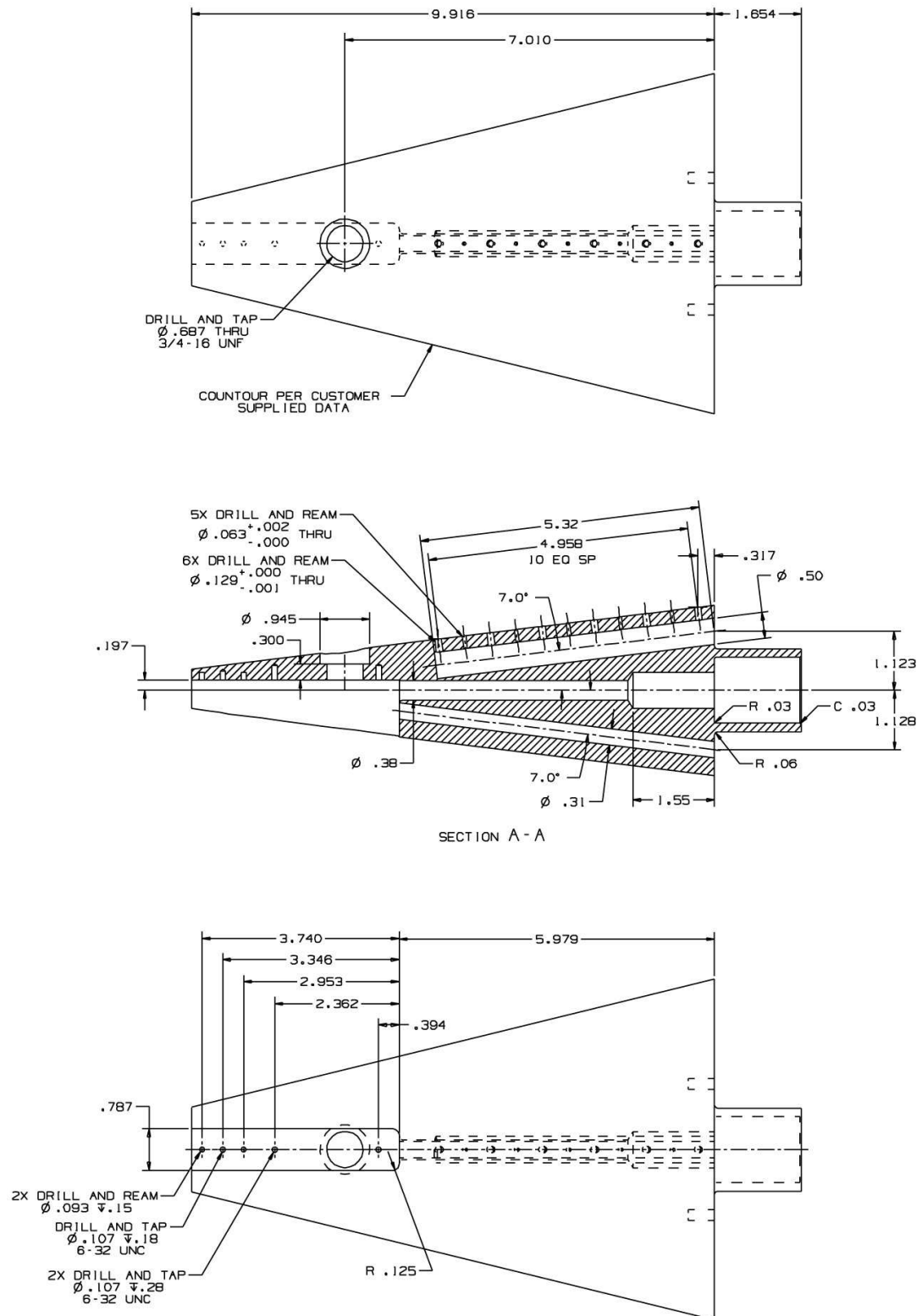


Figure B.2.: Frustum top and side views

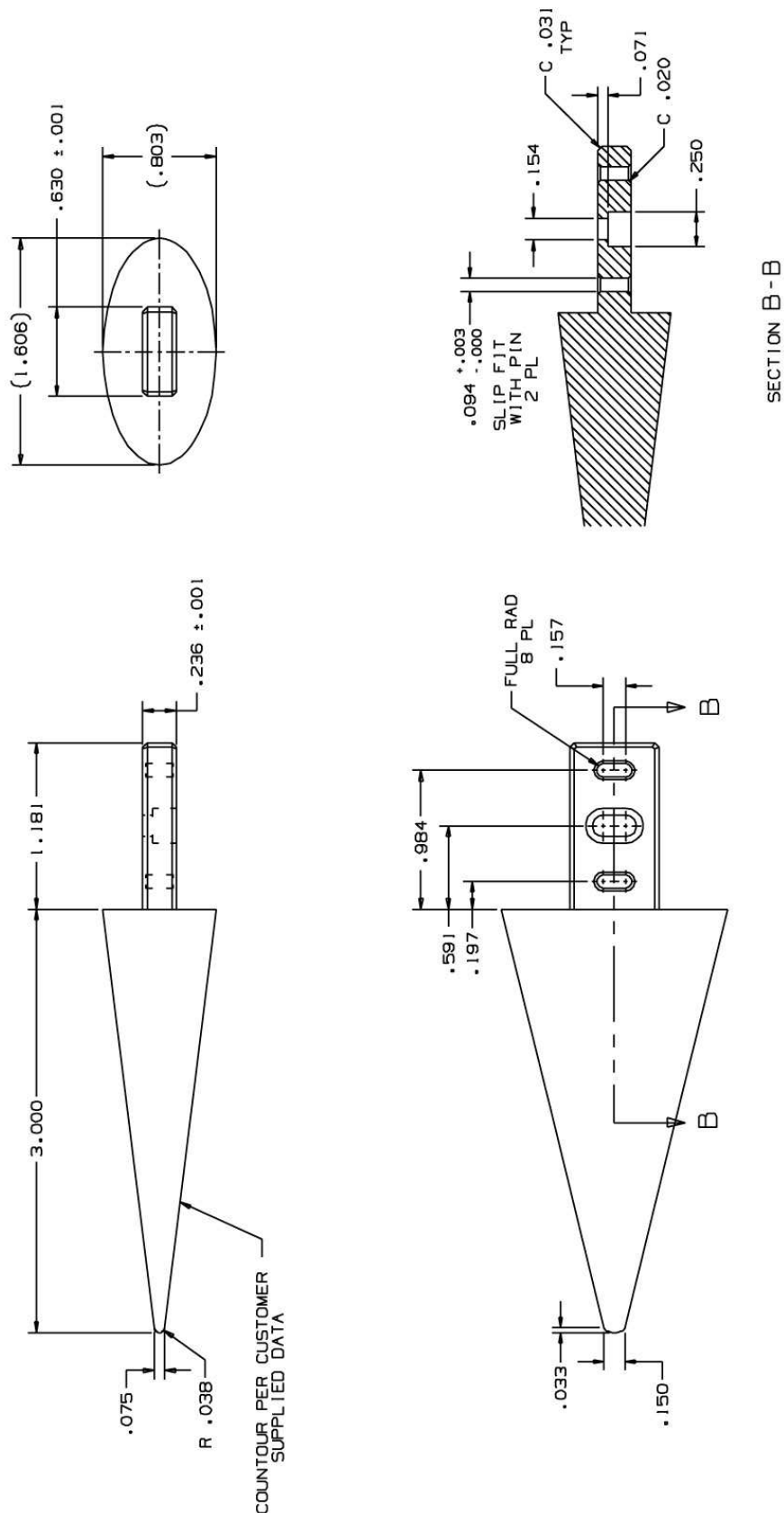


Figure B.3.: Nositip

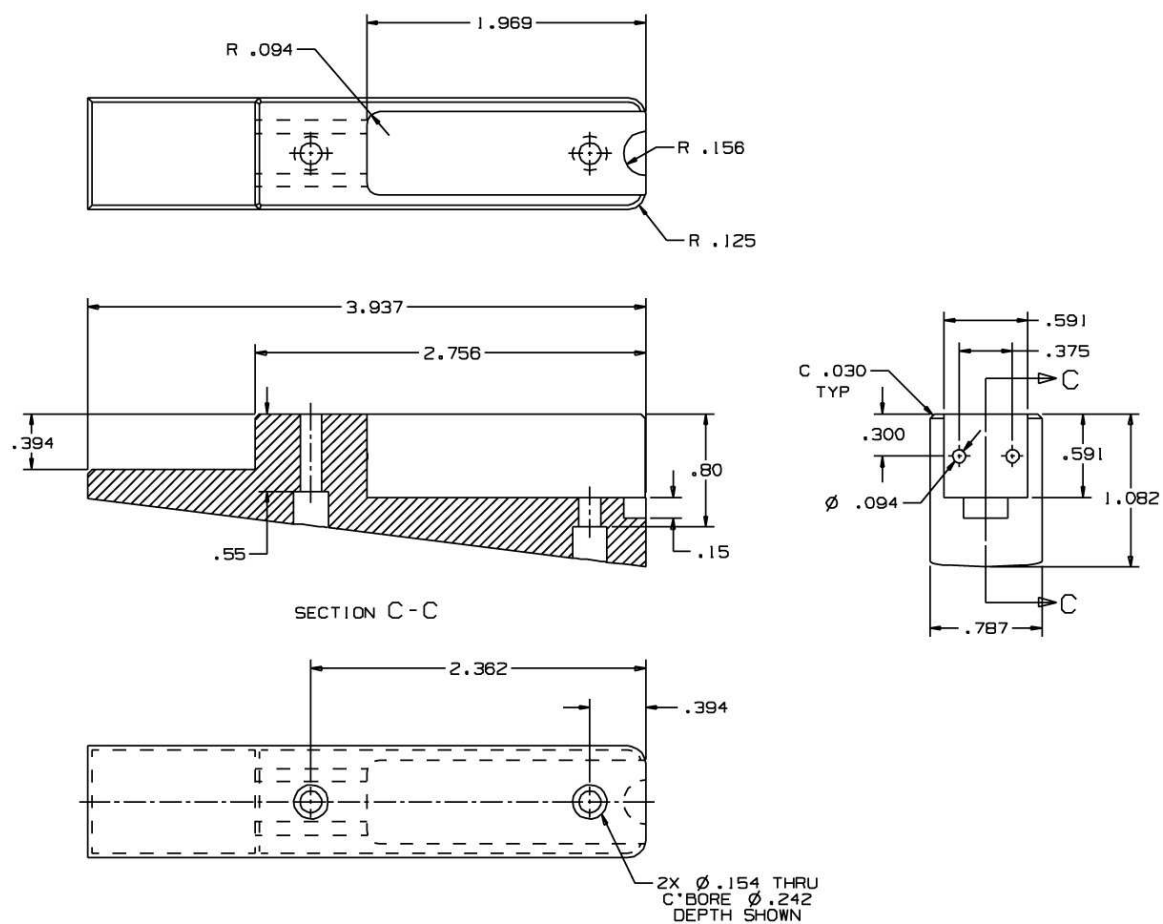


Figure B.4.: Nosetip and glow perturber access hatch

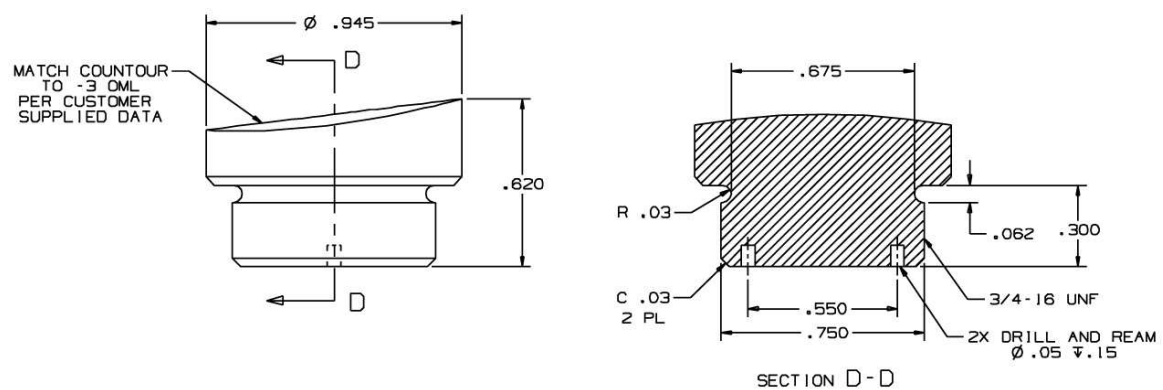


Figure B.5.: Glow perturber insert



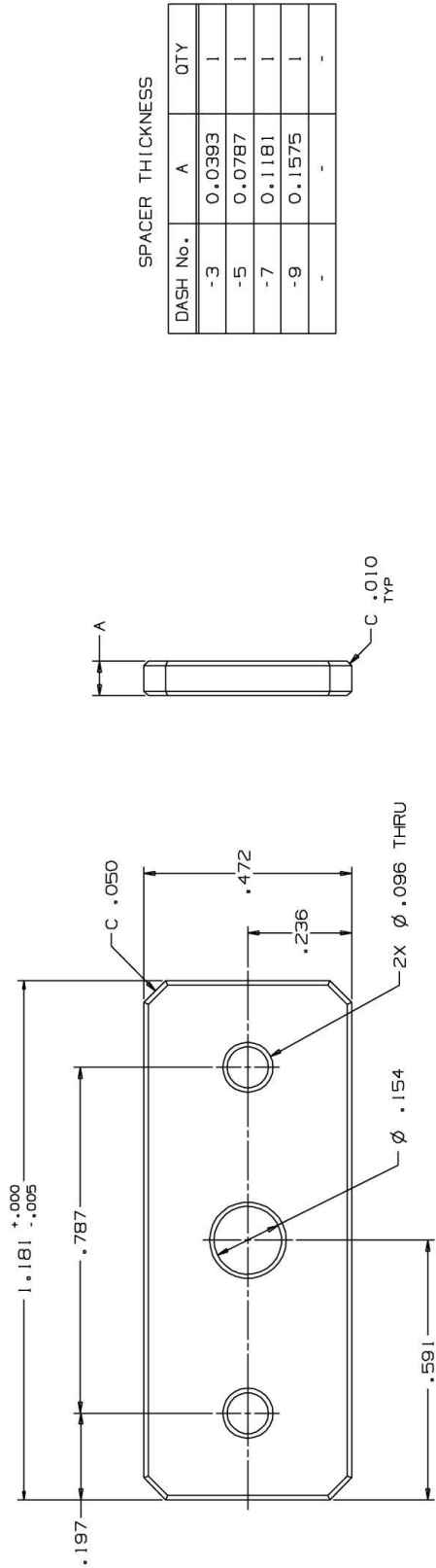


Figure B.6.: Top spacer for vertical nosetip steps

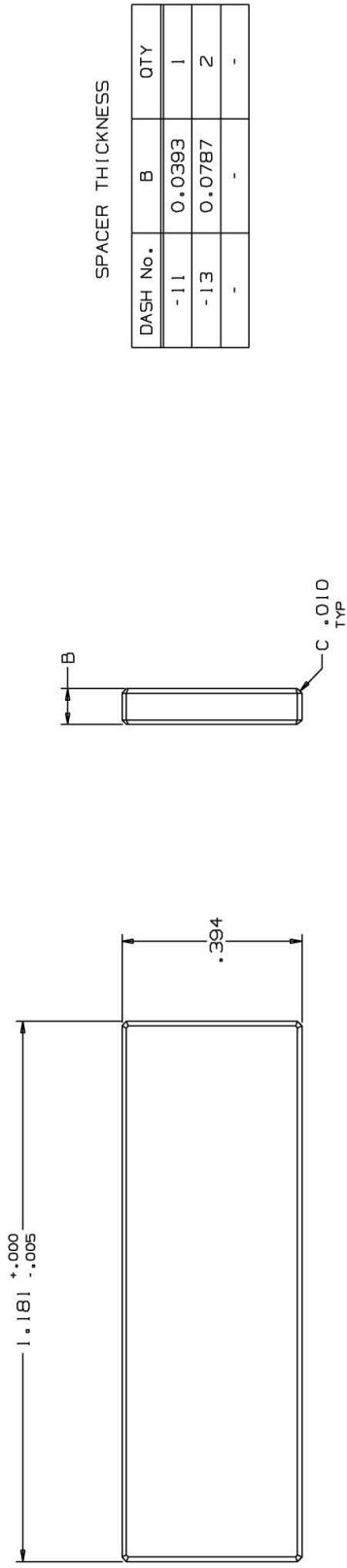


Figure B.7.: Side spacer for horizontal nosetip steps

VITA

## VITA

Thomas J. Juliano was born in Cleveland, Ohio. He graduated from Orange High School in 2000. He then attended the California Institute of Technology, graduating with a B.S. in Aeronautics in 2004. He worked as an intern at the NASA Glenn Research Center in the microgravity fluids branch during the summers of 2001 and 2002. In the summer of 2003, he worked for the Equity Engineering Group, Inc. in Shaker Heights, Ohio. Tom received his M.S. in Aeronautical and Astronautical Engineering from Purdue University in 2006 and his Ph.D. in 2010.